Study of Directed Flow in Au+Au Collisions at 11.5 A·GeV/c

by

Yi Dai

A thesis submitted
to the Faculty of Graduate Studies and Research
in partial fulfillment of the requirements
of the degree of

Doctor of Philosophy
in Physics

Physics Department, McGill University, Montréal, Canada.

To my dear parents

for their caring and love...

Abstract

This thesis presents the systematic analysis of azimuthal distributions of identified charged particles produced in Au+Au collisions at 11.5 A·GeV/c at the AGS measured with respect to the reaction plane. A Fourier expansion is used to describe the azimuthal anisotropy in particle production. Directed flow of protons, deuterons, $\pi^{\pm}$, K$^{\pm}$ and antiprotons is presented as a function of transverse momentum for different particle rapidities and collision centralities. Directed flow of protons and that of deuterons are well described by a simple sideward moving and radially expanding thermal source model; the observed behavior of the directed flow of $\pi^{\pm}$ indicates the interplay between shadowing and expansion; direct flow of K^{+} and K^{-} is observed to be anti-correlated to that of protons at low p_t, implying that the role of absorption and rescattering is significant for kaons in the dense nuclear medium; the first observation of a large "antiflow" signal for antiprotons suggests that a strong annihilation process occurs in heavy-ion collisions at the AGS. The experimental results are compared to the predictions of the event generator RQMD (version 2.3) in both the mean-field and cascade modes.

Résumé

Cette thèse présente une étude systématique de la distribution angulaire relative au plan de réaction des particules chargées produites dans les collisions Au+Au à 11.5GeV/c à l'AGS. La distribution angulaire des particules produites est décrite en terme d'une expansion de Fourier. Le premier moment de ces distributions pour les protons, deutérons, $\pi^{\pm}$, $K^{\pm}$ et les antiprotons est présenté en fonction du moment transverse pour diverses centralités de la réaction et rapidités des particules. Le flot des $\pi^{\pm}$ montre l'intéraction entre les effects de l'absorption et ceux dus à l'expansion de la boule de feu. On observe qu'à basse valeur du moment transverse le flot des kaons est de signe opposé à celui des protons, suggérant que le role de l'absorption et de la diffusion multiple dans la matière chaude est important pour ces particules. On rapporte la première observation d'un fort "anti-flot" des antiprotons, observation qui suggère un effect d'annihilation important dans les collisions d'ions lourds à l'AGS. Les résultats expérimentaux sont comparés aux prédictions du modèle RQMD(version 2.3) dans le mode "cascade" et dans le mode ou l'on tient compte de l'effet du champ nucléaire moyen.

Contents

List of Figures

List of Tables

Acknowledgments

I thank my dear parents for their love and support. Their caring and encouragement inspired me to get through each moment of depression and difficulty to reach the goal of today. I am deeply indebted to my elder brother and younger sister for their sharing my responsibility of taking care of my parents during the past five years. This thesis is my dedication to them.

I would like to express my sincere gratitude to my thesis supervisor Prof. Jean Barrette for his financial support during my stay at McGill. I am very impressed by his amazing memory and deep insight into problems. I believe that his integrity and enthusiasm for physics are examples for young physicists today.

I am grateful to Prof. S. K. Mark for his help and encouragement. I treasure the friendship with my colleague Dr. R. Lacasse and thanks to him for his help during my first year in the experiment. I want to thank the other members of our small data analysis team for the E877 1995 data set: K. Filimonov, Yujin Qi and Thongbay Vongpaseuth. Thank them for having shared the huge responsibility in the software construction and data production. I keep the memory of lots of pleasant moments when we worked and traveled together. I also want to thank Dr. Vasile Topor Pop and Francois Vincent for their help during my writing period.

I feel indebted to Dr. Jean-Yves Ollitrault. His generous theoretical assistance has made Chapter 6 of this thesis possible. I have obtained a better understanding of the flow phenomena in heavy-ion collisions from the numerous discussions with him. I am also grateful to the McGill technical staff Leo Nikkinen for his help in the design and construction of the new double-sided microstrip silicon detector. I also want to thank Steve Kecani for his help in achieving the high precision machining of the printing circuit boards. I would like to thank Prof. J. K. P. Lee for his sincere advice about life. I have benefited a lot from numerous discussions with him. I also would like to thank Prof. J. Crawford for his help during my first semester at McGill.

I was particularly impressed by the E877 spokesman Dr. Peter Braun-Munzinger and Prof. Johanna Stachel for their integrity and professionalism in physics. I cherish the friendship with Nu Xu, S. Voloshin, Yinchao Zhang, W. C. Chang, M. Pollack, S. Panitikin, U. Sonnadara, M. Rosati, C. M. Zou. As my final words of this acknowledgment, I would like to present the list of the E877 members as my thanks to all of them.

The E877 Collaboration: J. Barrette[4], R. Bellwied[8], S. Bennett[8], R. Bersch[5], P. Braun-Munzinger[5], W. C. Chang[5], W. E. Cleland[6], M. Clemen[6], J. D. Cole[3], T. M. Cormier[8], Y. Dai[4], G. David[1], J. Dee[5], O. Dietzsch[7], M. W. Drigert[3], K. Filimonov[4], A. French[8], J. R. Hall[8], T. K. Hemmick[5], N. Herrmann[2], B. Hong[5], C. L. Jiang[5], S. C. Johnson[5], Y. Kwon[5], R. Lacasse[4], A. Lukaszew[8], Q. Li[8], T. W. Ludlam[1], S. McCorkle[1], S. K. Mark[4], R. Matheus[8], D. Miśkowiec[5], J. Murgatroyd[8], E. O'Brien[1], S. Panitkin[5], P. Paul[5], T. Piazza[5], M. Pollack[5], C. Pruneau[8], Y. Qi[4], M. N. Rao[5], M. Rosati[4], N. C. da Silva[7], S. Sedykh[5], J. Sheen[8], U. Sonnadara[6], J. Stachel[5], N. Starinski[4], E. M. Takagui[7], M. Trzaska[5], S. Voloshin[6], T. Vongpaseuth[5], G. Wang[4], J. P. Wessels[5], C. L. Woody[1], N. Xu[5], Y. Zhang[5], C. Zou[5]

[1]Brookhaven National Laboratory, Upton, New York 11973

[2]Gesellschaft für Schwerionenforschung, Darmstadt, Germany

[3]Idaho National Engineering Laboratory, Idaho Falls, Idaho 83402

[4]McGill University, Montreal, Canada

[5]SUNY, Stony Brook, New York 11794

[6]University of Pittsburgh, Pittsbrugh, Pennsylvania

[7]University of São Paulo, Brazil

[8]Wayne State University, Detroit, Michigan 48202

Chapter 1

Introduction

1.1 The Quark-Gluon Plasma

Ultra-relativistic heavy ion physics emerged around 1986 as an interdisciplinary field from the traditional domains of particle physics and nuclear physics. The primary goal of the ultra-relativistic heavy ion experiments carried out at the Alternating Gradient Synchrotron (AGS) of the Brookhaven National Laboratory (BNL) and the Super Proton Synchrotron (SPS) of CERN, and the future experiments at the Relativistic Heavy Ion Collider (RHIC, 1999 at BNL) and the Large Hadron Collider (LHC, ~2005 at CERN), is the creation and experimental observation of the Quark-Gluon Plasma (QGP) in heavy nucleus-nucleus collisions.

1.1.1 The QCD phase transition and the QGP

Quantum chromodynamics (QCD) describes strongly interacting matter as the interaction of quarks through the exchange of gluons[1]. According to the theory of QCD, at large distances and small momenta q, the effective coupling constant $\alpha_s(q^2)$ is strong. This strong coupling results in that quarks do not appear isolated in nature but only in hadronic bound states as baryons and mesons. This phenomenon is called *quark confinement*. The strong coupling also brings out *chiral symmetry breaking* which is manifested in large, dynamically generated quark masses. At short distances and large momenta, the effective coupling constant decreases logarithmically. And at low energies, the QCD vacuum is characterized by vacuum condensates such as quark condensate and gluon condensate etc.

Normal nuclear matter is made up of protons and neutrons, which are themselves made up of quarks and gluons. It is known that at low temperatures, nuclear matter exists in a dense liquid phase. It has been observed in nuclear collisions at intermediate energies that nuclear matter transforms into a dilute gaseous phase when the temperature becomes higher than 5 MeV [2]. Phenomenologically, the hadronic gas becomes denser and the interaction distances among quanta become ever shorter with the increase of the temperature. The long-range interactions between quarks thus become dynamically screened. As a consequence, quarks break up the boundaries of hadrons and become free within a larger volume (*quark deconfinement*). A new phase of QCD matter, the quark-gluon plasma (QGP), is thus formed. The transition between the low-temperature (hadronic, chirally broken, confined) and high-temperature (QGP, chirally symmetric, deconfined) phases of QCD matter is predicted to exhibit a rapid discontinuity (phase transition). Numerical calculations of lattice gauge theory indicate that the transition occurs in the vicinity of a critical temperature $T_c \sim 150{\sim}160$ MeV at zero net baryon density[3]. Up to date, whether the phase transition is first-order, or second-order, or simply a rapid crossover, is not established yet.

Chiral symmetry restoration is another equally important feature of QCD. Chiral symmetry is the conservation of the helicity of the quarks. Chiral symmetry is spontaneously broken in QCD vacuum and normal nuclear matter (low temperature), and is restored at high temperatures. The restoration results in the formation of do-

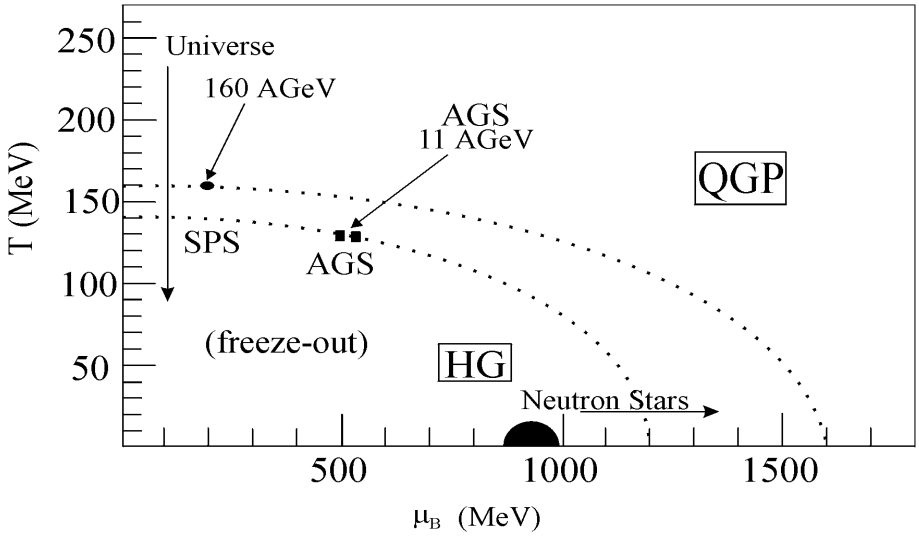

Figure 1.1: Phase diagram of nuclear matter. The horizontal axis represents the baryon chemical potential μ_B, which is a measure of the baryon density. The two dashed lines indicate the expected phase boundary with its uncertainty. Thermal freeze-out parameters deduced from AGS and SPS experimental results are shown. The arrows (Universe, SPS and AGS) imply how the freeze-out may be approached during the expansion of the fireball. For neutron stars, the arrow indicates how the QGP could be formed in the core of these stars.

mains of disoriented chiral condensate (DCC)[4]. Chiral symmetry restoration is also expected to occur at high baryon density even at zero temperature.

Abnormal nuclear matter is also an interesting issue of ultra-relativistic heavy ion physics. It is speculated that additional phases of baryon-rich nuclear matter might exist such as pion condensates, kaon condensates and strange quark matter, density isomers and others[5, 6, 7]. Kaon condensates and strange quark matter (strangelets) appear to be the most interesting one. Some models predict that strange quark matter might be more stable than non-strange quark matter and could be the true ground state of nuclear matter[8, 9]. The search for strange quark matter in heavy ion collisions has just began[10, 11].

1.1.2 The QGP signatures

According to the standard cosmological model[12], the universe started from a Big Bang of an infinite hot and dense point. In the very early period ($\sim 10\mu$s after the Big Bang) the universe was filled with a quark-gluon plasma. Presumably the matter in the core of neutron stars of the universe today could still exist in this form.

It is believed that QGP can be recreated in the laboratory by colliding two heavy nuclei together at ultra-relativistic energies. Fig. 1.1 shows the predicted phase diagram of nuclear matter. From a phenomenological point of view, when two nuclei collide together, they overlap and compress each other, creating a highly excited and strongly interacting zone. Large amount of the longitudinal beam momentum is transformed into other degrees of freedom (transverse momenta, thermal energy, entropy, etc.) due to violent inelastic nucleon-nucleon interactions and hadronic rescattering inside the collision zone. Thermal and chemical equilibrium are built up to a large extent and the state of an equilibrated QGP may be formed as a result. All these processes happen very quickly (approximately the order of 1 fm/c in duration). The QGP state is similar to a meta-stable state in some respects. QGP could live as long as 10 fm/c. Then the system begins to expand and cool until the hadronization takes place when the temperature reaches the critical temperature T_c. It is possible that QGP and strongly interacting hadrons could coexist for a short period of time (a few 10 fm/c in duration). In the end, the hadronized system expand and cool until freeze-out, i.e. until hadrons cease to interact strongly with each other (when the mean free path is larger than the dimension of the system). After that, hadrons just stream away into vacuum.

Experimental observation and exploration of QGP is unprecedentedly challenging because of the elusive characteristics of QGP. There exist several major difficulties for experimentalists to observe the QGP signals in the laboratory: the small size (a few fermi in diameter) and very short lifetime (5-10 fm/c in duration) of QGP; the competition between signals of QGP and backgrounds emitted from the hot hadronic gas phase; the effect on the QGP signals due to the final-state interactions during the hadronization of the plasma. For this reason, many ideas have been put forward to explore the short-lived QGP such as kinematic probes, electromagnetic probes, deconfinement probes, chiral symmetry restoration signatures (DCC and medium effects on hadrons) and hard QCD probes, etc. I will briefly describe below the first three probes. For a more detailed and complete description of the QGP signatures, the reader is refered to Ref. [13].

The basic concept of kinematic probes is the determination of the energy density ϵ, pressure P, and entropy density s of superdense hadronic matter as a function of the temperature T and baryon-chemical potential μ_B. The QCD phase transition would lead to an observation of a rapid rise of ϵ or s as a function of T over a small temperature range. The variables T, s and ϵ are related to the experimental observables of the average transverse momentum $\langle p_T \rangle$, the hadron rapidity distribution dN/dy, and the transverse energy distribution dE_T/dy, respectively[14]. One possible consequence from the formation of QGP could be a plateau-like behavior of the excitation function of the pion multiplicity in central heavy-ion collisions[15]. However, no such discontinuities have been observed by experiments yet[16]. Theoretical studies in the context of the hydrodynamical model have shown that the transverse signal would be enhanced by the formation of a detonation wave during the hadronization transition[17]. The effect of QGP on collective flow will be discussed in more details later. Identical-particle interferometry of pions, kaons and nucleons provides also important information on the reaction geometry and the space-time dynamics of nuclear collisions[18].

Electromagnetic probes (lepton pairs, direct photons) are penetrating probes. Leptons and photons emitted from QGP are associated with electro-magnetic interactions and are virtually unaffected by the final-state interactions of hadronization. However, their yields are quite low and the relatively large backgrounds from hadronic processes create serious background problem for their experimental identification.

The observation of the anomalous particle production such as J/ψ suppression[19] in relativistic heavy ion collisions becomes one of the hottest topics in ultra-relativistic heavy-ion physics. The production of J/ψ in a quark-gluon plasma is suppressed because a $c\bar{c}$ pair formed by the fusion of two gluons from the colliding nuclei do not bind inside QGP. Recently the NA50 Collaboration at SPS reported their observation of the measured J/ψ suppression in Pb+Pb collisions at 158A GeV/c[20] as the evidence of the first observation of QGP. However, there exist other possibilities such as the absorption by the co-moving freeze-out nucleons, which could also lead such suppression. The mechanisms of the suppression are still under study.

1.2 Collective Flow in Heavy Ion Collisions

As is discussed in the previous section, the major goal of ultra-relativistic heavy-ion physics is to study the properties of highly excited and dense nuclear matter, and possibly the QGP formation and/or the chiral symmetry restoration. At the AGS, nuclei are found to stop each other completely and create a dense hadronic system; the system formed in the collision is found to be thermalized at a temperature of $\sim$140MeV[40]; the high pressure built up in the hot and dense system (fireball) induces a significant collective expansion[40]. On the one hand, the information from the earlier stages of the collision is likely to be smeared out because of the strong thermalization processes occurring before/at freeze-out. On the other hand, the study of collective motion driven by the pressure gradient, provides a powerful diagnostic tool to study the compressibility of nuclear matter and thus furthers our understanding of the nuclear equation of state; moreover, since different particles species subject to different interactions are created at different stages of the collision, a systematic study of the collective behavior for different particle species would reveal important aspects of the evolution of the collision system as well as particle production and absorption mechanisms.

The concept of flow from macroscopic classical hydrodynamics describes the globally co-moving behavior of a system in space and time relative to its center of mass. As is described in the previous section, when two heavy nuclei collide with each other, the collision zone is highly compressed and heated. The compression and heating build up a high pressure (or energy density) which induces additional collective motion (flow) superimposed on the thermal motion at the stage of expansion. For a pure thermal source, no flow will be present since the thermal motion of particles is completely random (net current is zero everywhere at any time).

From a hydrodynamical point of view, nuclear matter is described by the equation of state (EoS): the relationship specifying the dependence of the pressure (or alternatively the energy per particle) on the density and temperature. Flow conceptually links conservation laws (mass, momentum, energy) with fundamental properties of the fluid: the equation of state and transport coefficients (viscosity, heat conductivity, etc). Flow is directly sensitive to the compressibility K [1], which measures resistance against compression and is one of the properties characterizing the EoS.

A fluid-dynamics model was first applied by Belenkij and Landau[22] to the description of nuclear collisions. A few years later, Glassgold et al.[23] predicted that shock waves could be formed in nuclear matter when the relative velocity of two colliding nuclei exceeds the velocity of sound. Flow in heavy-ion collisions was first introduced by Scheid, Müller, and Greiner[21]. In their ideal-fluid hydrodynamics calculation, they found out that the transverse border of the collision zone is expanding faster than the longitudinal border when nuclear shock waves occur. They

[1] It is also often called incompressibility in many references.

concluded that the stopped and shocked "*matter is pushed outwards perpendicular to the relative motion of the two nuclei*" (*squeeze-out* or sideward flow). This prediction stressed the importance of transverse expansion in heavy nuclear collisions.

Sideward flow was first observed in experiments with the so-called 4π detectors (the Streamer Chamber and the Plastic Ball) at the Bevalac in the Lawrence Berkeley Laboratory[24, 25]. Since then, a large amount of experimental data on flow has been accumulated in the beam energy from 30A MeV up to 200A GeV in the past decade. The results have systematically established collective flow as an experimental observation in heavy-nucleus collisions.

Recent results from the AGS experiments have shown[26, 27, 28, 29] that a nearly complete stopping of baryons occurs in heavy nuclear collisions. This stopping scenario indicates that during the compression stage, energy and baryon densities up to 10 times that of nuclei in their ground state could have been reached . Such high compression would produce a high pressure in the collision region and the pressure-induced collective flow effects should occur. Jean-Yves Ollitrault[30] pointed out that anisotropies in transverse-momentum distributions provide an unambiguous signature of transverse collective flow in ultra-relativistic nucleus-nucleus collisions. Collective flow can be separated into two parts in the transverse plane (perpendicular to the beam axis): the azimuthal isotropic part which is called the radial flow, and the azimuthal anisotropic part. The first-order component of the anisotropy is the so-called directed flow [2] and the second-order component the elliptic flow [3].

1.2.1 Radial flow

In a simple fireball model, the emitted particles from the breakup of the hot equilibrated system are expected to exhibit a pure thermal distribution[36] and to have

[2] At lower energies, the directed flow is also called *bounce-off* or *sideward flow*

[3] It is commonly known as *squeeze-out* at Bevalac energies

the same average energy.

$$E\frac{d^3N}{d^3p} \propto Ee^{-\frac{E}{T}} = m_t\cosh(y)e^{-\frac{m_t\cosh(y)}{T}} \tag{1.1}$$

where m and $m_t = \sqrt{m^2+p_t^2}$ are respectively the mass and transverse mass of the particle, and all kinematic variables are evaluated in the nucleon-nucleon center of momentum frame. The integration of Eq. (1.1) over m_t gives out the expected rapidity distribution,

$$\frac{dN_{iso}}{dy} \propto m^2T(1+2\chi+2\chi^2)\exp(-1/\chi) \tag{1.2}$$

with $\chi = T/(m\cosh(y))$.

The observed p_t spectra of identified particles, however, do not show the characteristic Boltzmann-like shape expected for a thermal emission, but rather a shoulder arm shape[37]. Furthermore, a quasi-linear dependence of the average kinetic energy on the mass (or charge) of the emitted fragment has been observed[38]. The so-called blast-wave picture[39] was therefore introduced, in which it was assumed that an isotropic hydrodynamical expansion that converted part of the initial thermal energy into radial flow kinetic energy. In the center of mass for particles emitted from a thermally equilibrated and radially expanding source with a temperature T and a mean radial flow velocity β_f, the energy distribution is given by

$$\frac{dN}{dEd\Omega} \propto pe^{-\gamma_f\frac{E}{T}}\{\frac{\sinh\alpha}{\alpha}(\gamma_fE+T)-T\cosh\alpha\} \tag{1.3}$$

where E and p are the total energy and momentum of the particle in the center of mass, $\gamma_f = (1-\beta_f^2)^{-1/2}$, and $\alpha = \gamma_f\beta_f p/T$. While a common temperature for the radial flow was justified experimentally, the local flow velocity β_f was found to approximately follow the Hubble-like relation $\beta_f = hr$ at all times, where h is a constant. All observables (density, temperature, entropy, pressure, flow energy. etc.) are found to be functions of the scaled radius r/R, where R is the time-dependent outer radius of the expanding system.

At energies much higher than 1A GeV, the isotropic expansion scenario becomes improper simply because of the significant Lorentz contraction. At the AGS energies ($\sim$10A GeV), the Lorentz contraction factor is about 5:1 and becomes even bigger at higher bombarding energies (10:1 at SPS energies). This effect alone will lead to non-spherical collective expansion. Decoupling the collective expansion into longitudinal and transverse flow becomes necessary and also provides a convenient way in the comparison between experimental results and theoretical predications[40].

Longitudinal flow is manifested by the widening of the rapidity distributions. Analyses on the experimental data from the AGS and SPS, using ideal-gas thermodynamics with chemical equilibrium and strangeness conservation, give quite satisfying fits to the rapidity distributions of the produced particles at both energies[40]. The deduced average transverse flow velocity is $\langle \beta_l \rangle = 0.50$ ($T = 130MeV$) for Au+Au collisions at the AGS and $\langle \beta_l \rangle = 0.76$ ($T = 160MeV$) for Pb+Pb at SPS[41]. A preliminary result from the E895 Collaboration shows $\langle \beta_l \rangle = 0.4$ ($T = 110MeV$) in Au+Au at 6A GeV[45].

Transverse flow is a result of rescattering during the expansion stages of a collision. Transverse flow has been studied using particle transverse-momentum spectra,

$$\frac{dN}{m_t dm_t} \propto \int_0^R r dr m_t I_0\left(\frac{p_t \sinh(\varrho)}{T}\right) K_1\left(\frac{m_t \cosh(\varrho)}{T}\right) \tag{1.4}$$

where I_0 and K_1 are Bessel functions and $\varrho = \tanh^{-1}(\beta_t)$ and β_t is given by a transverse velocity profile $\beta_t(r) = \beta_t^{max}(r/R)^{\alpha}$ (usually α is chosen to be 1). In a hydrodynamical picture, particles of different mass all move with the same velocity. The collective kinetic energy is then dependent on the particle mass: particles with heavier mass carry more collective energy. The inverse slope (or effective "temperature") parameter T extracted from the measured transverse-momentum spectra is dependent on both the random thermal (T_0) and collective contributions ($\langle \beta_t \rangle$). The relationship between the inverse slope parameter and particle mass m can be described qualitatively as[43]

$$T = T_0 + \frac{1}{2} m \langle \beta_t \rangle^2. \tag{1.5}$$

Fig. 1.2(a) shows the observed average transverse flow velocity extracted from experimental measurements based on a expansion thermal model, as a function of beam energy. The transverse velocity seems to saturate at a bombarding energy of ~10A GeV, indicating that the conversion of additional thermal energy into transverse direction stops at higher beam energies. Fig. 1.2(b) shows the freeze-out temperature extracted from experimental measurements as a function of beam energy. The temperature increases dramatically with the beam energy in the beam energy range 0.2~5A GeV, then saturates at about 140 MeV. This behavior implies that additional energy goes primarily into heat at lower energies and into other degrees of freedom like particle production at higher energies. Interestingly, the saturation of the temperature and collective transverse velocity happens at roughly the same energy.

1.2.2 Directed flow

When two colliding nuclei compress each other at a non-zero impact parameter, a higher pressure is built up in the reaction plane. Consequently nuclear matter is pushed more outwards in that direction at the subsequent exploding stage. Viewed in the transverse plane on the projectile (or target) side, the matter is being pushed to move sideward nearly in parallel (or anti-parallel) with the reaction plane direction. This phenomenon is the so-called directed flow [4].

In contrast to the transverse radial flow, directed flow is dominated by the interactions occurring near the projectile (or target) region. It is strongly correlated

[4] It is also commonly called sideward flow or bounce-off

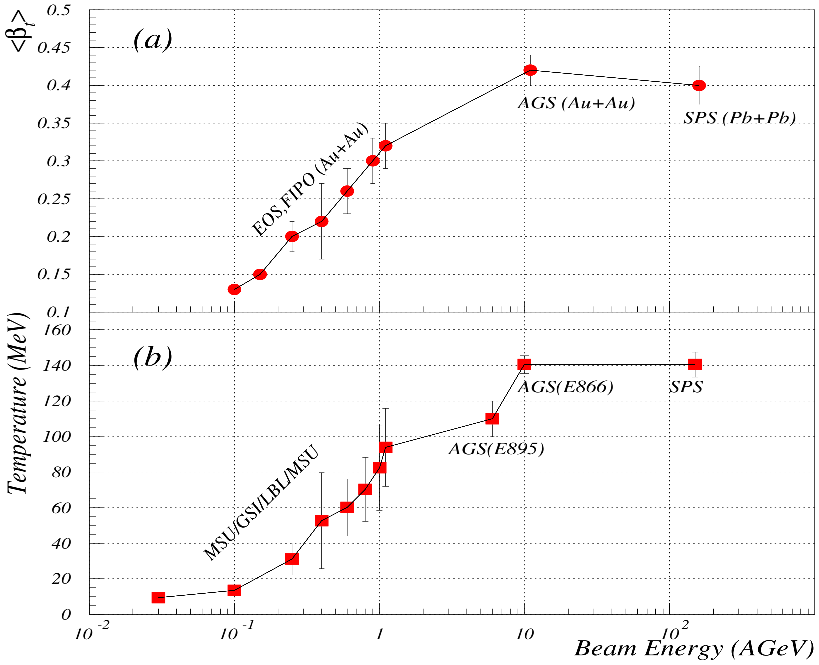

Figure 1.2: Average transverse flow velocity and freeze-out temperature as a function of beam energy. Data points are extracted from [42, 43, 44, 45].

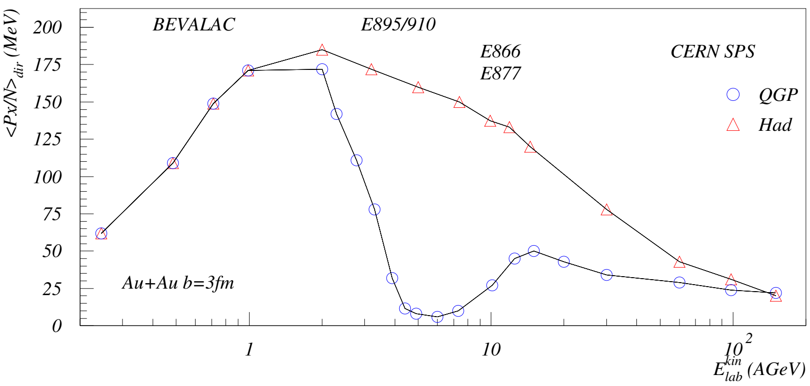

Figure 1.3: The excitation function of the directed flow calculated by one-fluid hydrodynamic model for Au+Au at b = 3fm. Triangles represent the predictions by using the normal hadronic processes only and circles the predictions by the inclusion of the QGP phase transition. The figure is reproduced from Ref. [49].

with the collision geometry (the impact parameter) and principally reflects the non-equilibrium aspects of the collision.

Nucleons are the major carriers of the flow signal. The behavior of the nucleon directed flow is strongly affected by the compressibility of the nuclear matter. Because of nucleons' large mass and stability, they are less affected by the thermal motion. Therefore, the directed flow pattern of nucleons straightforwardly reflects the collision geometry and the hydrodynamic aspects of the collision system. Study of the nucleon directed flow is important for the understanding of the nuclear mean-field properties[47] described by the nuclear equation of state.

The energy dependence of directed flow is interesting because the onset of new phases or new and exotic forms of matter is reflected in the EoS. It is expected that, at around 1A GeV the EoS will soften due to the onset of copious particle and resonance production. Hung and Shuryak[3] pointed out that the softest point in the EoS, where the lifetime is the longest, could be used as a way to search for the QCD phase transition in experiments. The balance between the prolonged compression and expansion leads to a local minimum of directed flow. Rischke[49] calculated the excitation function of directed flow with an ideal one-fluid hydrodynamic model by including the QCD phase transitions. He predicted that a well-pronounced minimum at 6A GeV could be the onset of the QGP occurrence (Fig. 1.3).

Directed flow at ultra-relativistic energies was first observed by the E877 Collaboration at the AGS in Au+Au collisions at 10.8A GeV[31]. An anticorrelation of the azimuthal distributions of transverse energy measured by the E877 calorimeters between forward and backward hemispheres, which is most pronounced at intermediate impact parameters and vanishes for very peripheral and central collisions, has clearly demonstrated the existence of a directed flow component at the AGS. This directed flow is small compared to what was observed at Bevalac energies. The signal decreases even further at SPS energies, but is still observable[34, 35]. Fig. 1.4

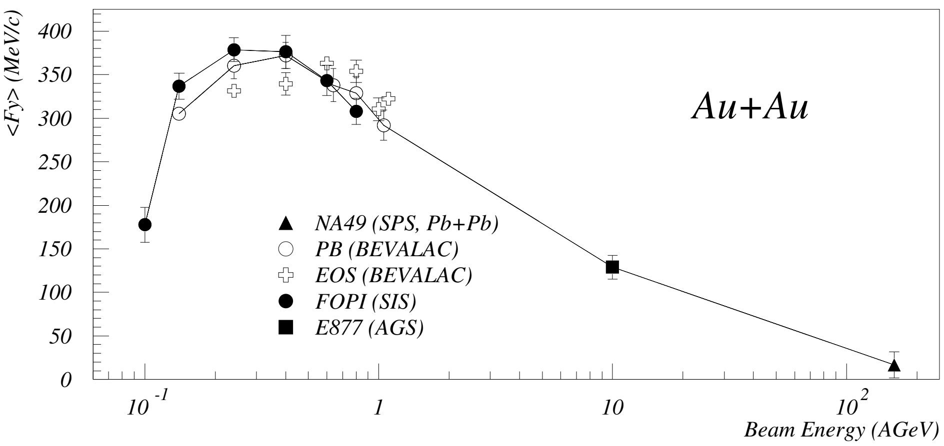

Figure 1.4: The excitation function of directed flow for Au+Au system (Pb+Pb at SPS). F_y is defined as the slope of $\langle p_x \rangle$ at mid-rapidity normalized by projectile rapidity in the center of mass frame[94].

shows the excitation function of directed flow measured by various experiments from Bevalac energies up to SPS energies. The observation of directed flow at all these energies demonstrates the persistence of hydrodynamical behavior of heavy nuclear collisions from relativistic to ultra-relativistic energies. Recent results from the E895 Collaboration (EOS)[45] and the E917 Collaboration[46] at the AGS show a smooth decrease in $\langle p_x \rangle$ (the transverse momentum projected in the reaction plane) [5] from 2 up to 10.6 GeV/c per nucleon. This observation possibly indicates that nuclear matter created in Au+Au collisions at the AGS energies still remains in the hadronic phase.

Generally, different particle species are produced at different stages of the collision by different mechanisms. A comprehensive study of the directed flow of different particles would provide us a systematic and detailed information about the collective evolution of the collision system, and would be helpful for us to understand

[5] Here x represents the orientation of the reaction plane.

the in-medium effects such as absorption, rescattering, and possibly the QGP phase transition.

Light nuclei (deuterons, tritons, helium-3, helium-4,..., etc) can not be formed inside the hot and dense collision zone. Instead they are formed through fragmentation and/or coalescence[108] of nucleons at/after freeze-out. Directed flow of light nuclei is helpful for the understanding of these production mechanisms and non-equilibrium influence.

Pions are mainly produced through the inelastic processes and decays of baryon resonances[115, 117]. Due to their large interaction cross section, most of the pions cannot escape from the collision zone until the zone starts to freeze out. The study of the directed flow of pions would reveal the space-momentum correlation properties of the fireball at freeze-out. Also, due to their small mass, pions are sensitive to Coulomb interaction and their flow signal would help us to understand the role of this interaction in the collision.

Kaon directed flow is a promising probe of the dense matter formed in the initial stage of the collision because of kaon's comparatively small interaction cross-section with nucleons. The study of kaon flow would be important to understand the properties of kaons in the dense nuclear medium. This comprehension is crucial to understand the role of KN potentials[122] and possibly chiral symmetry restoration[120] in the dense nuclear matter existing in neutron stars[124] and formed in NN collisions.

The production of antiprotons becomes significant at the AGS and SPS energies. Antiprotons only contain newly produced anti-quarks and may present a rather clean probe of the hot and dense matter. The enhanced production of antiprotons has been proposed as a signature for the formation of QGP[48]. However, the actually measurable antiprotons may be greatly reduced due to their large annihilation cross section. If true, this would result in a strongly anti-correlated azimuthal distribution ("antiflow")[132] of antiprotons with that of nucleons for non-central collisions. Also, the comparison of the directed flow of antiprotons ($\bar{p}$) with that of anti-lambda ($\bar{\Lambda}$) could give us crucial information to understand the high $\bar{\Lambda}/\bar{p}$ ratio[134, 135, 136, 137] observed at the AGS and SPS, and the production of anti-quarks ($\bar{u}$ and $\bar{s}$) in hot and dense nuclear matter.

1.2.3 Elliptic flow

Elliptic flow represents a deviation from a spherical shape of the ellipsoid and defines a second direction of preferred emission. Different from directed flow, elliptic flow reflects the equilibrium aspects of the collision, and is sensitive to the pressure development of the collision system in the expansion stage. Elliptic flow can occur either in the reaction plane (in-plane flow) or out of the reaction plane (out-of-plane flow or squeeze-out).

The magnitude and the sign (in-plane or squeeze-out) of elliptic flow depend on the pressure built up in the compression stage, the energy density in the collision zone and the influence of the shadowing due to the projectile and target spectators. At energies lower than Bevalac/SIS energies (2A GeV), the transit time of spectators is longer than that needed for the speed of sound to pass the collision region; the matter in the collision zone is blocked by the spectators during most of the expansion stage, and as a consequence, is observed to emit preferentially out of the reaction plane. This is the squeeze-out phenomenon first observed at Bevalac [51, 52].

At higher energies, the blocking of the spectators still induce squeeze-out in the very early stage (∼5.4 fm/c for the AGS and ∼1.4 fm/c for SPS), but spectators pass each other very quickly and leave the collision zone to explode freely. A higher pressure is built up in the direction of the reaction plane due to compression and consequently this higher pressure leads to a preferential emission in the reaction plane. The final elliptic flow is actually a time integration of these two contributions[53].

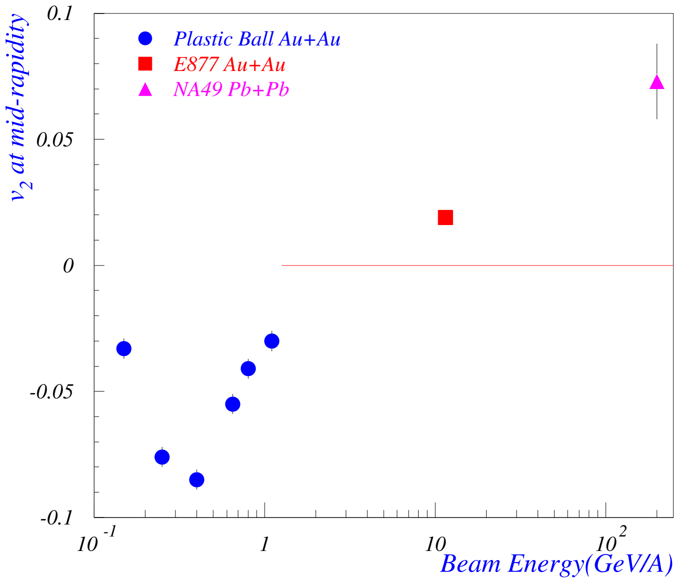

Figure 1.5: The observed excitation function of elliptic flow measured by experiments (from Ref.[55]). v_2 is the second Fourier component which quantifies the elliptic flow.

At the AGS and SPS energies, the second contribution dominates and in-plane flow has been observed[32, 33, 34]. Fig.1.5 shows the excitation function of elliptic flow measured by various experiments[55, 56].

The sensitivity of elliptic flow to the early pressure evolution of the collision system provides a good probe to the EoS. The elliptic pattern can be used to distinguish different expansion scenarios[53]. Interestingly, from Fig.1.5, one notices that elliptic flow could disappear somewhere between the AGS and the Bevalac/SIS energies. This is the point where the early squeeze-out contribution balances the later in-plane one. The experimental determination of the point where elliptic flow disappears could be used to distinguish the different EoS models and possibly become a potential probe for the onset of QGP phase transition[54].

Interpreting the result of experimental flow measurements is usually a difficult task because of the presence of the interplay between different flow components: the measurement of directed flow would be subject to the radial expansion; the measurement of elliptic flow would be complicated by the coupling from radial and directed motions. Keeping this in mind is important to establish a correct and comprehensive picture of flow phenomenon in heavy-ion collisions.

1.3 Outline

This thesis attempts to present a systematic study of directed flow in Au+Au collisions at the AGS. This is done by taking advantage of the azimuthal distributions relative to the reaction plane of various particle species (protons, deuterons, charged pions, charged kaons and antiprotons) measured by the E877 experiment in 1995. In the next chapter, an overview of the E877 experimental setup will be presented. In Chapter 3, the design and construction of the new two-dimensional beam vertex detectors used in the 1995 experiment of E877 will be described. In Chapter 4, the details of the data analysis strategy and software for the 1995 data set will be given; also, the event selection criteria used in the analysis for the 1995 data will be discussed. In Chapter 5, the identification criteria for charged particles measured by the E877 spectrometer will be presented; particularly, the track matching and the occupancy correction due to the presence of two close-tracks in the spectrometer will be discussed. In Chapter 6, the strategy in determining the reaction plane will be reviewed and the estimation of the reaction plane resolution will be discussed in a systematic way. In Chapter 7, the directed flow results of identified particles from the 1995 data set, particularly, the first directed flow results of antiprotons and antikaons measured at the AGS, , will be presented. The data will be compared to the predictions from RQMD model (version 2.3) both in the cascade and mean-field modes. Finally, summary and conclusions will be given.

Chapter 2

E877 Experimental Setup

Experiment E877 is a fixed target experiment located on the C5 beam line of the Alternating Gradient Synchrotron (AGS) at the Brookhaven National Laboratory (BNL) on Long Island, New York. It is an upgrade of the previous Experiment E814 to study Au+Au collisions at an energy of approximately 10 GeV/c per nucleon. The data taking began in 1993 and continued until 1995. The data presented in this thesis are from central Au+Au collisions at 11.5 GeV/c per nucleon obtained in the last E877 running period in the fall of 1995.

A schematic view of the E877 setup is shown in Fig. 2.1. A right-handed coordinate system centering at the target is used for the setup. The z axis is defined as the beam trajectory starting from the left hand side of the figure; the y axis points upward out of the page and the x axis points to the top of the page.

The E877 experimental setup consists of three major groups of detectors: the beam definition detectors, the calorimeter and the forward spectrometers. Due to the long history of E814/E877, many references are available which describes in details each component of the experimental setup. I will here only give a brief description of the experimental setup as it was used in 1995 and refer readers to the references

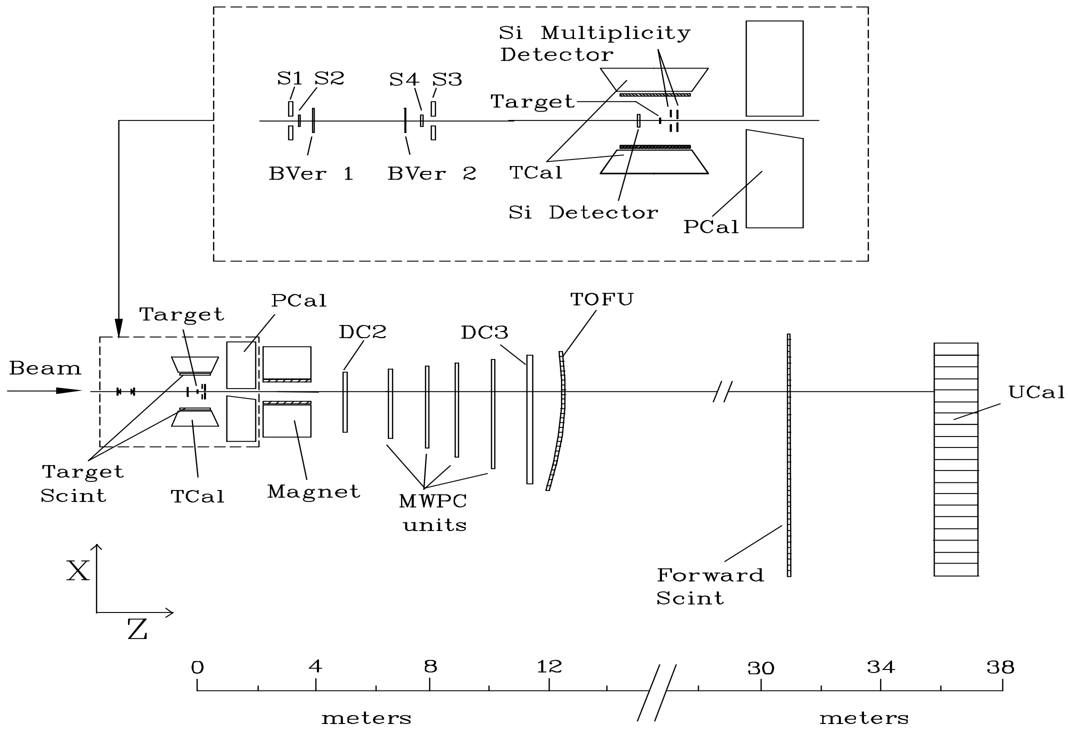

Figure 2.1: The E877 experimental setup

for more detailed explanations.

2.1 Beam Definition Detectors

Beam definition detectors consists of two groups of detectors: the beam scintillators(BSCI) and the beam vertex detectors(BVER). Both BSCI and BVER were upgraded in 1995. BSCI is comprised of four scintillators: S1, S2, S3 and S4 (see Appendix C). S2 and S4 were used to define a 'good' beam particle while S1 and S3 are used as veto counters. Each of S2 and S4 is a Čerenkov quartz radiator equipped with two photomultipliers. BSCI generates the start time signal of each incident beam particle. It also provides a rough collimation of the beam by eliminating stray particles. BVER measures the angular orientation of the incident beam particle and its position on the target. More detailed information about BSCI can be found in

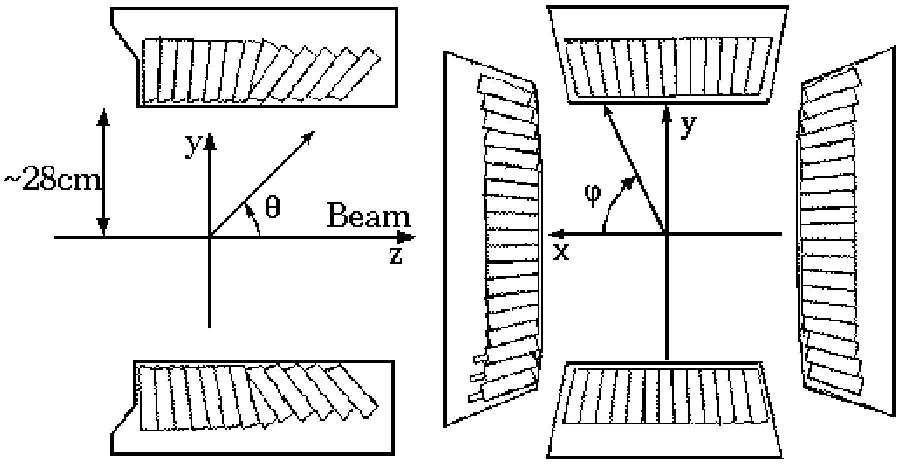

Figure 2.2: Schematic view of the Target Calorimeter (TCAL).

Ref.[59]. An extensive description of BVER is provided in Chapter 3.

2.2 Calorimeters

One of the main features of the E877 apparatus is its calorimeters which provide a nearly 4π coverage. The calorimeter group consists of three parts: the target calorimeter (TCAL), the participant calorimeter (PCAL) and the uranium calorimeter (UCAL). The data measured by these calorimeters are used to describe the global characteristics of the collision event, such as the centrality and the reaction plane orientation of the collision. In the present work, UCAL is not used. Interested reader can refer to Ref.[60] for information.

2.2.1 Target Calorimeter

The TCAL is an electromagnetic calorimeter which measures the energy flow of particles(neutrals, charged particles and gamma rays) produced near target pseudorapidity ($-0.5 < \eta < 0.8$ or $48° < \theta_{lab} < 117°$ in angular coverage) with a nearly full

2π azimuthal coverage. The geometry of the TCAL shown in Fig. 2.2. The TCAL is composed of 832 NaI(Th) crystals [1] arranged in a quasi-projective geometry facing the target and contained in 4 side walls parallel to the beam trajectory. Each crystal is 13.8 cm in depth (5.3 radiation length or 0.34 hadronic interaction length in equivalence) and 3.8 cm on each side. The produced light of each crystal is detected and read out by photodiodes. The responses of the photodiodes are very stable. The energy calibration was done using cosmic rays in 1993 over a period of several weeks. This calibration has been used in the present data analysis.

The transverse energy measured by TCAL is used for triggering and the event selection because of its high segmentation and stable performance. However, its relatively short radiation length limits its usefulness in highest centrality event selection and the reaction plane determination. This issue will be discussed in Chapter 4 in more details.

2.2.2 Participant Calorimeter

The participant calorimeter is a Lead/Iron/Scintillator sampling calorimeter. It is sketched in Fig. 2.3. The PCAL measures energy flow into the forward angular region and has an polar angular coverage of $1° < \theta_{lab} < 47°$ (or $0.83 < \eta < 4.7$ in pseudo-rapidity).

The PCAL is divided into two electromagnetic(EM1 and EM2) and two hadronic segments(HAD1 and HAD2) segments. The equivalent depth of each electromagnetic and hadronic segment is 10 and 40 radiation lengths respectively and their corresponding energy resolutions are $45/\sqrt{E}(GeV)$ and $28/\sqrt{E}(GeV)$ [61]. Looking downstream on x-y plane, the PCAL consists of four identical quadrants with each

[1] A previous back wall which is composed of 160 crystals and has a pseudorapidity coverage of $-2.3 < \eta < -0.5$ was removed for the experimental run of 1995 and is not used in the measurements described in this thesis.

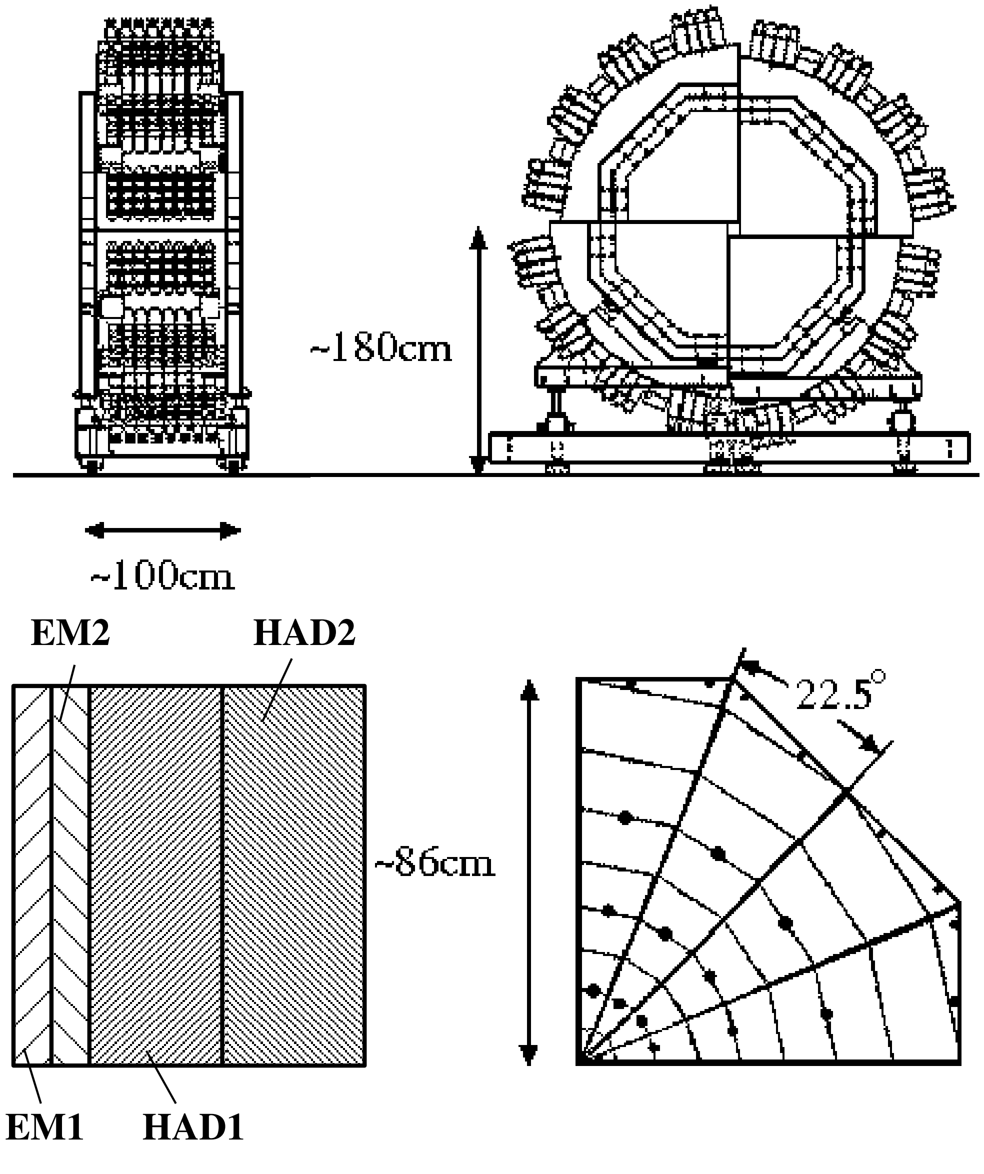

Figure 2.3: Schematic view of the Participant Calorimeter (PCAL).

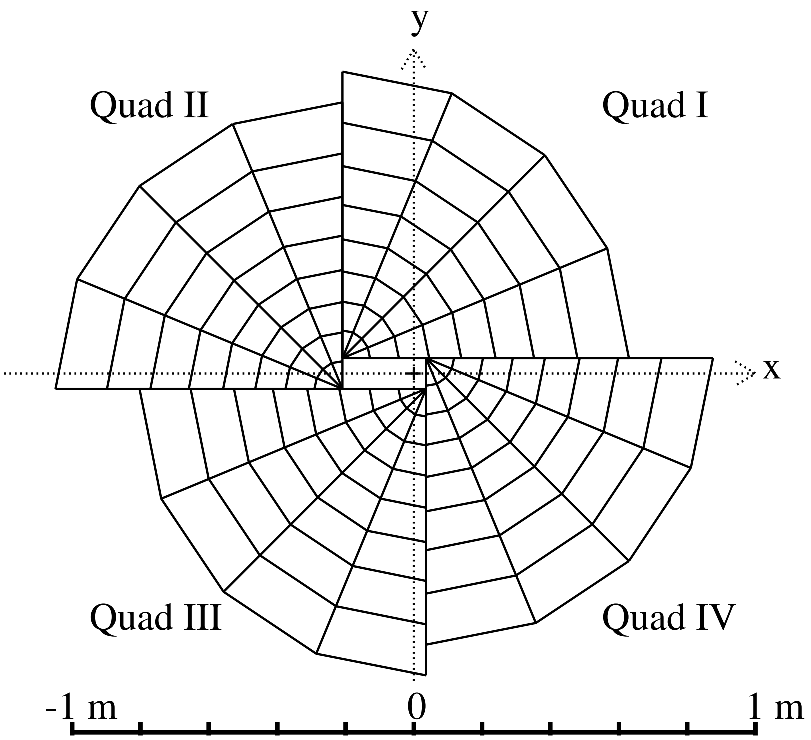

Figure 2.4: View of the PCAL cross-section along the beam axis. The origin (denoted by a cross) is the position of the beam. The positional fluctuation of the beam axis at PCAL is small (less than ~2 mm).

quadrant segmented laterally into 8 radial and 4 azimuthal cells. The total number of cells is 512. In the 1995 running period, the four quadrants were arranged slightly asymmetrically in x direction to increase and optimize the acceptance of the E877 forward spectrometer (see Fig. 2.4). The geometrical acceptance of particles measured by the spectrometer is determined by a wedged collimator installed in the hole at the center of the calorimeter. It has an opening of $-115 < \theta_{xz}^{lab} < 14$ mrad in x-z plane and $-21 < \theta_{yz}^{lab} < 21$ mrad in y-z plane.

In the fall of 1995, the PCAL was carefully recalibrated with ^{60}Co γ-source cell by cell[66]. The PCAL is used as the basis of the centrality dependence and the study of the reaction plane due to its much lower energy leakage. This issue will be further discussed in Chapter 4 and Chapter 6. Further information about the PCAL can be found in references:[68, 61, 65].

2.3 Forward Spectrometer

The forward spectrometer is a magnetic spectrometer designated to analyze the charged particles passing through the collimator in the PCAL. It is composed of an analyzing magnet, the upstream tracking pad chambers, the drift chambers, the multiwire proportional chambers, and the time-of-flight hodoscope. The spectrometer simultaneously measure the charge, the momentum and velocity of the produced charge particles and is able to identify proton, $\pi^{\pm}$, $K^{\pm}$, $\bar{p}$ and light nuclei such as d, ^{3}He, etc. The particle identification will be discussed in details in Chapter 5.

2.3.1 Upstream Cathode Pad Chambers

During 1995 run, two highly segmented cathode pad chambers (vertex detectors) were added between the collimator and the magnet as shown in Fig. 2.5. The implementation of these two chambers was originally motivated by the measurement of the hyperon Λ decay vertex and therefore they are abbreviated as VTXs(VTX A/B). In this work, they are used for improving track selection in the study of rare particles such as $K^{\pm}$ and $\bar{p}$. A drawing of the cathode pad plane is sketched in Fig. 2.6. The active area of each pad chamber consists of 10 rows of chevron-like shape pads with each row having 53 chevron shape pads and one anode wire placed above. The position resolution measured by these two detectors is approximately 300 μm along x direction. The spacing between the anode wires is 5 mm and this provides the

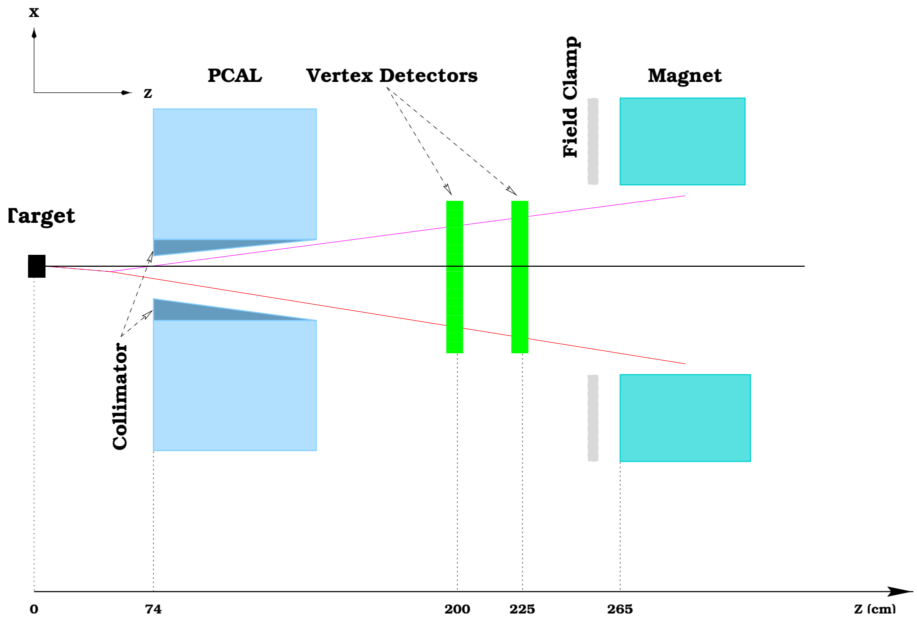

Figure 2.5: Schematic view of the cathode pad chambers layout.

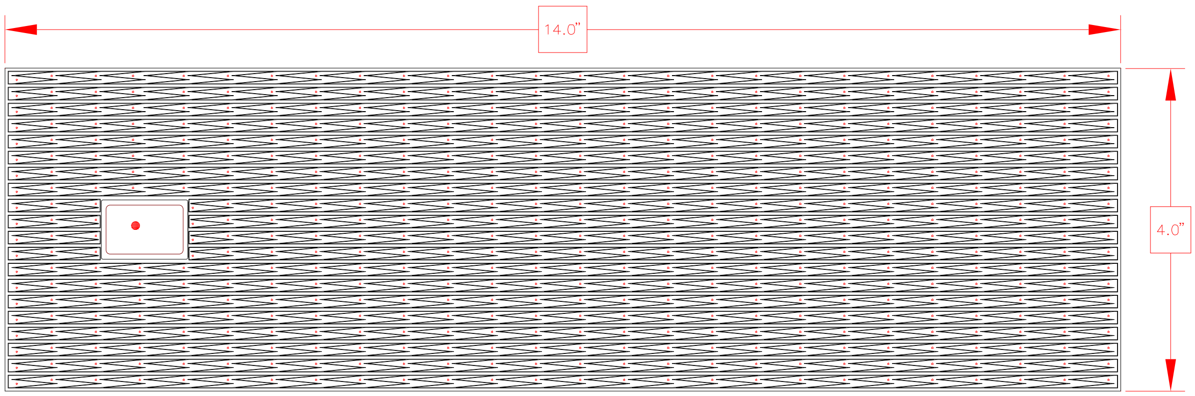

Figure 2.6: The cathode pad plane of the VTXs.

position resolution along y direction. The analysis of VTXs' data is discussed in Chapter 5. More detailed description of the technical part of the detector can be found in Ref. [57, 67].

2.3.2 Drift Chambers and Multi-wire Proportional Chambers

The two drift chambers(DCs) and four multi-wire proportional chambers(MWPCs) make up the main tracking system of the spectrometer.

The two drift chambers(DC2 and DC3) provide the precision measurement of the particle trajectories and they are located at 5.4 m and 11.5 m downstream from the target. Both chambers are designed in similar way except that DC3 is twice as big as DC2. Each chamber has 6 independent drift planes with vertically strung anode wires arranged in a "staggered" geometry and one wire plane with a cathode readout (see Fig. 2.7). The anode wire spacing is 6.35 mm in DC2 and 12.7 mm in DC3. The differences in geometries of DC2 and DC3 are dictated by the projective geometry of the spectrometer to maintain the similar occupancy on wires of DC2 and DC3. The staggering pattern of the plane wires are to aid the resolution of the left-right ambiguity and to provide enough redundancy to guarantee the nearly 100% efficiency. The wires in the regions where the beam passes through are not biased to avoid high voltage breakdown. The resolution in the horizontal (x) direction of DC2 and DC3 is 300 μm and 600 μm respectively. The vertical (y) position of a track is determined from measurements of the charge shared by the chevron shaped pads on the cathode pad plane. Both of the chambers have three pad density regions(fine, medium and coarse regions). The fine region is closest to the beam and has the highest pad density to handle a higher occupancy. The y resolutions in DC2 are estimated 2.3 mm, 5.1 mm and 15.0 mm for the three regions respectively; for DC3, the resolutions are 4.3

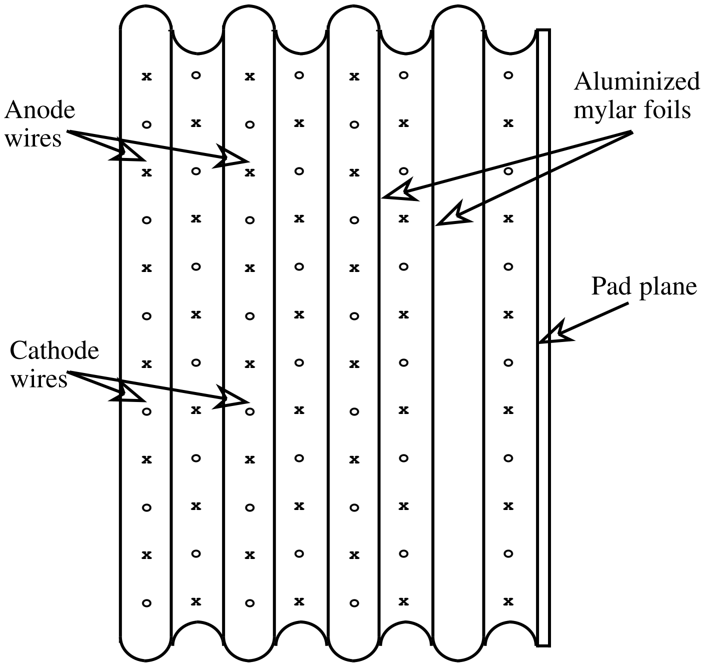

Figure 2.7: Schematic view of the drift chambers. The beam direction (z-axis) is the horizontal direction (from left to right) and the x-axis is along the vertical direction (from bottom to top).

mm, 7.0mm and 36.0 mm[62].

The four multiwire proportional chambers are installed between DC2 and DC3. They are built in a similar design with differences in sizes to maintain the projective geometry of the spectrometer. The tracking redundancy obtained by the addition of MWPCs is used to improve the pattern recognition ability of DCs to cope with the high particle multiplicity in Au+Au collisions at AGS energies. The spacing between vertically strung anode wires on each MWPC is 5.08 mm. The detection efficiency of MWPCs is about 97% with three out of four planes required for track confirmation. In the fall of 1995, the MWPCs were also implemented with tracking trigger system to provide simple on-line tracking [58]. Th reader is referred to Ref.[63] for more details about the design and operation of the MWPCs.

2.3.3 Time-Of-Flight System

A high granularity time-of-flight wall located at ~12 m from the target provides the time of flight of particles accepted by the spectrometer. It is abbreviated as TOFU (Time-Of–Flight Upgrade).

The TOFU consists of 148 vertical plastic scintillators having a full coverage of the projection area of the collimator aperture. The photons produced in each scintillator are readout by two photomultipliers mounted on both the top and bottom end. All scintillators have a length of 70 cm and a thickness of 15 mm. The whole wall is divided into two density regions. The region near the beam ($-21.0cm < x < 17cm$) consists of 39 slats which are 10 mm wide. The rest of scintillators have a width of 17 mm. The 148 scintillators are stacked in a staggered fashion in the z-direction with an overlap of 0.25 mm to provide complete geometrical acceptance. The overall layout of the whole wall is arranged along an arc centered at the magnet with a radius of 9.5 m. This curvature reduces the probability of a hit being shared by two scintillators due to their overlap in x-direction, and thus reduces the effective occupancy. The pulse height information from both photomultipliers gives the energy loss of the particle in the scintillator and hence is used to determine the charge of the particle. The overall TOF resolution is 85 ps.

Besides charge and TOF measurement, the TOFU also provides a vertical (y-direction) position measurement from the measured time differences between the signals at the two photomultipliers. This useful information provides a way to enhance the tracking efficiency by reconstructing the y-information of those tracks where such information is missing either at DC2 or at DC3. The overall y-resolution of the TOFU is about 1.7 cm. Characteristics of the TOFU calibration for 1995 data will be discussed in Appendix C. A full description of TOFU can be found in Ref. [64].

2.4 Forward Scintillators and Uranium Calorimeter

The forward scintillators is another time-of-flight system located at about 31 m from the target. It consists of 39 10cm-wide vertical plastic scintillators with a TOF resolution of 350 ps. The uranium calorimeter is a Uranium/Iron-scintillator sampling calorimeter located approximately 35 m from the target. It is used to measure the energy flow of forward particles including neutrons. Both detectors are not used in this analysis. Interested readers are referred to Ref. [69] for detailed information.

The gaps between detectors (DCs, MWPCs and TOFU) are filled up with large helium bags. The purpose is to reduce multiple scattering and downstream interactions.

2.5 Trigger and the Data Acquisition System

The digitized information (the ADCs, TDCs,etc.,) of all detectors is readout in parallel by FASTBUS and CAMAC electronics, then collected in sequence and built as one event. The built event is then sent to to the 8 MB circular memory shared by a Motorola 68040 CPU running OS-9 operating system [2] and a Silicon Graphics UNIX workstation which is used for on-line monitoring and analysis. The events collected in the buffer memory are then finally written to two Exabyte 8500 8mm magnetic tapes in a data stream fashion. The average event size is 21 kbytes. In 1995, the DAQ software was rewritten and optimized. Due to the improvement both in hardware and software in 1995, the DAQ was able to take up to $\sim$220 events per AGS spill compared to 60-70 events per spill in 1994[72].

The DAQ is controlled by the trigger system. The trigger decision is made at

[2] In 1993 and 1994, a Motorola 68030 with 4MB memory was used.

three different levels: the pre-trigger, the level-1 trigger and the level-2 trigger. The pre-trigger decision requires the presence of a valid beam particle determined by the BSCI detector and a minimal amount of transverse energy ($>$ 1 GeV) present in PCAL. The pre-trigger also issues the START signal for all the ADCs and TDCs for digitization. The level-1 trigger serves as an "after-protection" , rejecting the current event if another beam particle is present within 1μs. The level-2 trigger makes the final decision which is based on the centrality (the transverse energy) measured by TCAL and PCAL. At this stage, three different thresholds are applied to each calorimeter measurement (PCAL threshold-1,2,3 and TCAL threshold-1,2,3) [3] and corresponding down-scaling is chosen. In the experimental run of 1995, the data taking was focused on central collisions and carried out with a mixed central trigger (a logical ORs of PCAL3, TCAL3 and other down-scaled triggers or thresholds). The down-scaling factors of triggers or thresholds relevant to the present work will be discussed in Chapter 4. For more details of the E877 trigger and data acquisition system, readers are referred to Ref.[70, 71].

In the fall of 1995, a third level "tracking-trigger" was partly implemented during the experimental run. The original goal of the implementation of this trigger is to achieve a tracking pattern recognition by utilizing part of the E877 tracking facilities to enhance the measurement sensitivity for rare particles such as negative kaons and antiprotons. Due to the enhancement of the DAQ performance in 1995, all events decided by level-2 trigger were recorded onto tapes and the third level became unnecessary. The data set used for analysis (including this thesis) doesn't contain this portion. Interested readers can refer to Ref.[72] for more details.

[3]The terms of PCAL1,2,3 and TCAL1,2,3 will be used in the following chapters of this thesis. When used in such way, they are actually referred to PCAL threshold-1,2,3 or TCAL threshold-1,2,3.

Chapter 3

Two-dimensional Beam Vertex Detector

3.1 Introduction

A new two-dimensional Beam VERtex (BVER) detector was built as part of the upgrade of the E877 experiment in 1995 to study rare particles produced in Au+Au collisions. In 1993's and 1994's experimental runs of the E877, a one-dimensional BVER was used. This detector was made of two single-sided microstrip silicon detectors, each of which has 320 strips with a pitch of 50 μm[64]. It provided the beam position at the target only in the x-direction and the beam angle in the x-z projection. The tracking efficiency of this detector was $\sim$70%[77]. To study hyperon production such as Λ in the reconstruction of its decay vertex, it is useful to know the beam position and angle relative to the target in both x- and y-directions; the availability of the beam information in the y-direction would help to improve the momentum resolution in p_y and hence to achieve a better tracking quality. This is helpful for the study of kaons ($K^{\pm}$) and antiprotons ($\bar{p}$), and also helpful for the understanding of the effect of the beam angle on the determination of the reaction plane.

To achieve these new physics goals, a new two-dimensional beam vertex detector was designed at McGill University. This design is based on the previous years' operational experience of the one-dimensional BVER and the recent technology development in microstrip silicon detectors. The new detector system consists of two double-sided microstrip silicon detectors located at 2.8 m and 5.8 m upstream of the target. The pitch size of each silicon detector is 200 μm and the inferred positional and angular resolutions in both x-z and y-z projections at the target are $\sim$280μm and $\sim$60μrad respectively. The tracking efficiency for both the x- and y-dimensions is better than 90%. The contents of this chapter are arranged as follows: a brief review of the development and working principle of double-sided microstrip silicon detectors will be introduced; then the technical details in the design and construction of the new two-dimensional beam vertex detector system will be described and the test results of this detector with the Au beam from the AGS will be presented; finally, the performance of the new detector will be discussed.

3.2 Principle of a Double-sided Microstrip Silicon Detector

Microstrip detectors have been developed to give high precision measurements of the positions of single particles incident on, or traversing the detectors. The first microstrip silicon detectors appeared in the early 1980s when the demand for vertex detectors to filter the decays of relatively long-lived charmed particles out of the huge debris of hadrons produced in proton-nucleus interactions[73]. Since then, silicon microstrip detectors were used widely in many fixed-target and collider experiments. However, most of them were single-sided detectors. The first application of double-

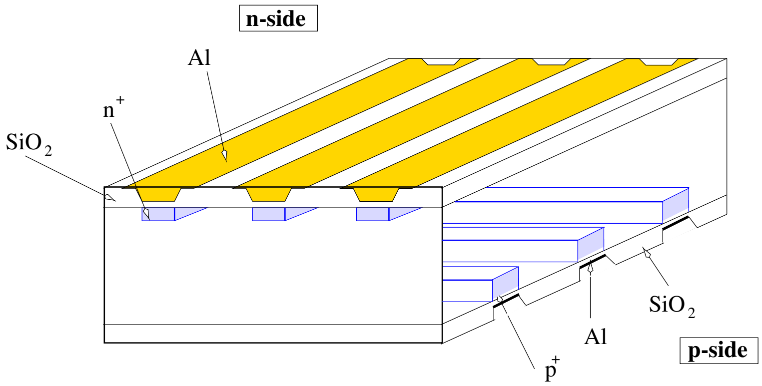

Figure 3.1: Cross section 3D view of the double-sided detector

sided microstrip detectors in high-energy physics experiments had not been realized until 1990 in the ALEPH experiment at LEP[74].

Fig. 3.1 shows schematically the cross-section of a double-sided microstrip silicon detector. The lower strips (junction side) are boron implanted p^+n junctions on a n-type silicon substrate. The upper n^+-strips (phosphorous implanted, ohmic side) provide an ohmic contact to the bulk. The strips are electrically isolated from one another, under operating conditions once all free charge carriers are removed.

The principle of single-sided strip detectors is simple. A single-sided strip detector is just the division of the large area p^+n junction side (p-side) into narrow strips. Each strip acts as a single p-n diode. The position of the ionizing particle incident on, or traversing the detector is given by the location of the strip carrying the signal. Due to the charge diffusion during signal collection, the signal might spread to several neighboring strips.

The realization of double-sided microstrip detectors is technologically more complicated. The n^+-strips cannot be a simple division of the ohmic side into narrow strips. The presence of a positive oxide charge in Si-$Si0_2$ interface on the ohmic side causes an accumulation layer of electrons underneath. These electrons lead to a very low inter-strip resistance and position information is lost as a result. With the development of semiconductor technologies, several kinds of techniques have been applied to solve this problem. This electron layer can be interrupted either by a large-area compensation implant of p-doped insulation strips between n^+-strips [74], or by properly biased MOS barriers[75]. A detailed review of the development of silicon detectors and their applications is given in Ref.[73, 76].

3.3 Design of the Two-dimensional Beam Vertex Detector

3.3.1 Double-sided microstrip silicon chip

Fig. 3.2 depicts the schematic layout of the n-side of the double-sided microstrip silicon chip used in the present detector. The p-side has a similar layout except that the strips are orthogonal to those of n-side. The chip was manufactured by Hamamatsu Corporation in Japan. The wafer is made of high-resistivity ($\sim$5 kΩ) n-type silicon and has a thickness of 300 μm which is equivalent to 0.3% radiation length. The chip has a size of 22.0mm by 22.0mm and a 1.2mm wide boundary for mounting. The active area is 19.2mm$\times$19.2mm and surrounded by a 50 μm wide guard ring which serves as the bias bus for each strip as well as a measure to stop edge currents. On both sides, a capacitor is integrated under the readout pad of each strip to allow AC coupling to the readout electronics. Bias is provided through individual integrated polysilicon resistors ($\sim$10 MΩ) between the strips and the bias bus. There are 384 strips on each side of a chip with a pitch of 50 μm. Each AC coupling capacitor has been under a strict test at 100 V by Hamamatsu.

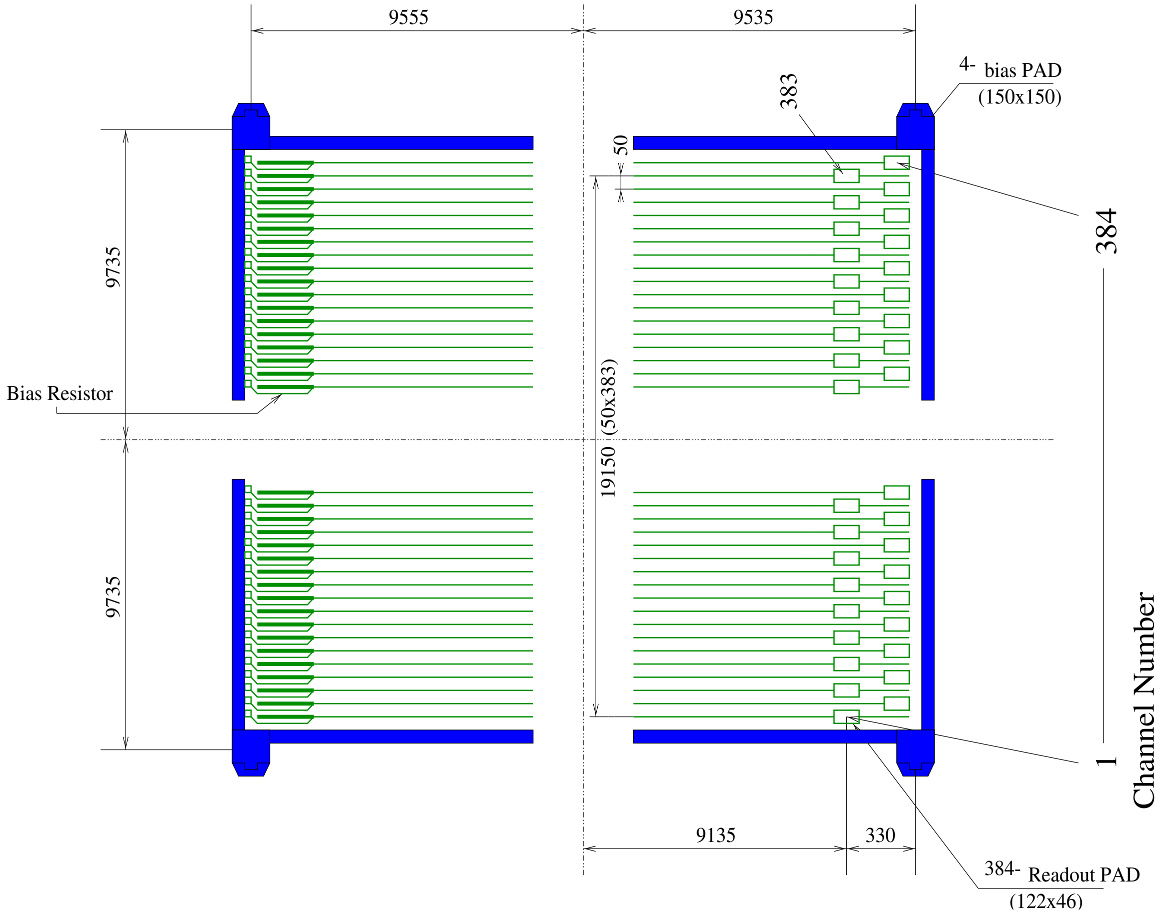

Figure 3.2: Schematic layout of n-side of a silicon chip(units are in μm)

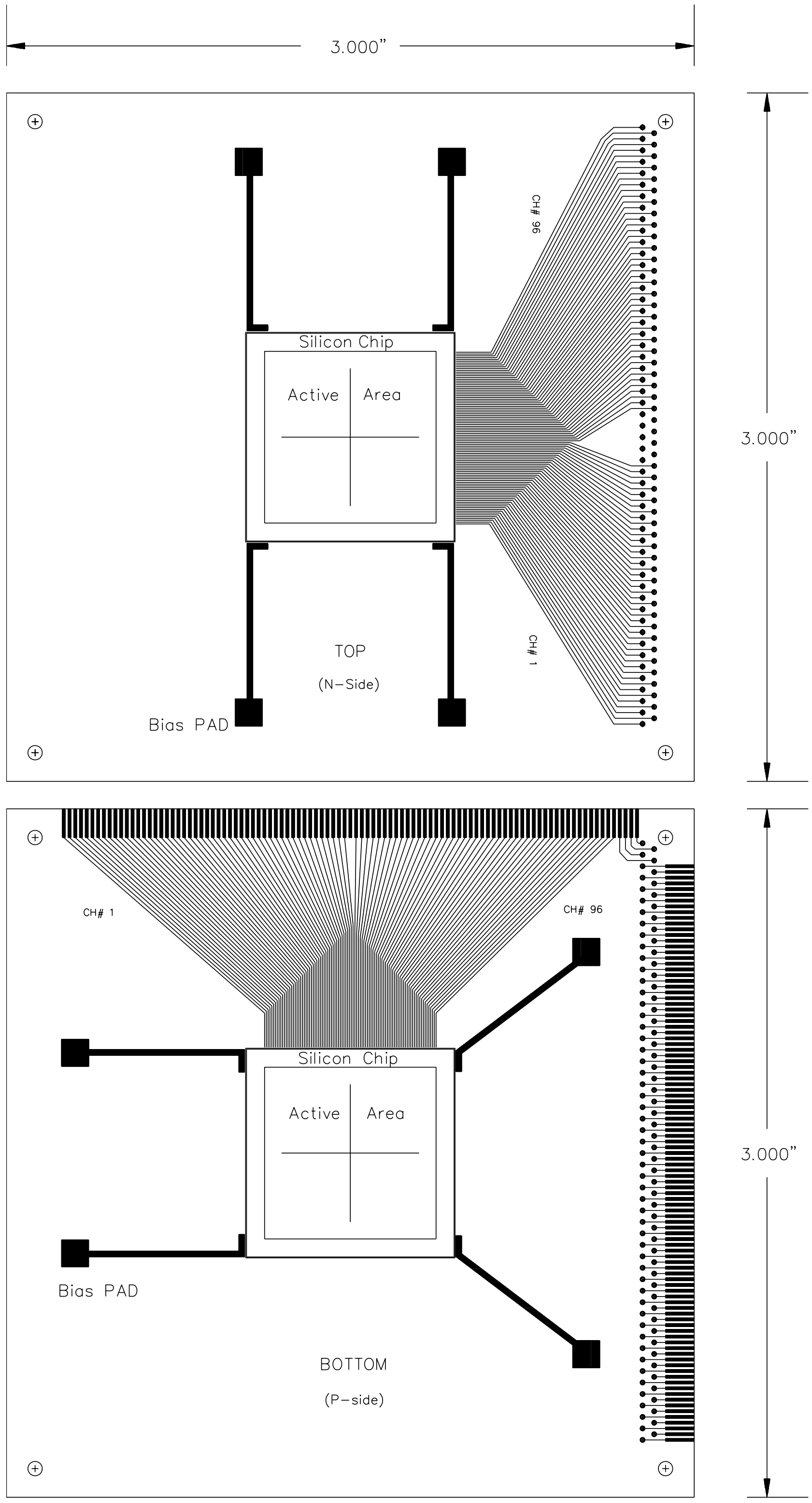

Figure 3.3: Daughter printing circuit board

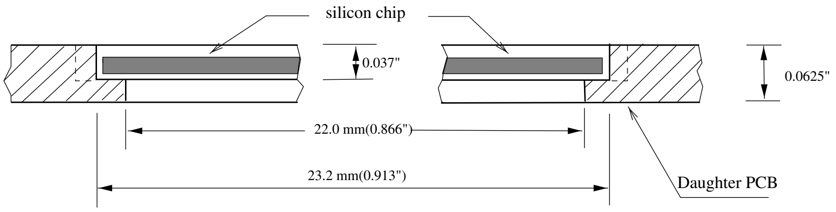

Figure 3.4: Cross-section view of a silicon chip mounted on a daughter PCB

3.3.2 Daughter printing circuit board

The daughter printing circuit board (PCB) serves as an interface between the silicon chip and the front-end electronics on the motherboard (Fig. 3.3). Two identical daughter PCBs have been used for two identical silicon chips. Each daughter board is a 3 inch by 3 inch two-sided PCB with a thickness of 1/16 inch. Each side has 96 readout traces for a total of 192 traces in each detector. The traces are connected to the motherboard through the connection pads on the bottom side as shown in Fig. 3.3. The width of each readout trace is 100 μm. Each connection pad is 1/8 inch long and 1/80 inch wide. Traces on the top side are connected to the connection pads on the bottom side through VIAs [1] (0.012 inch in diameter) and connection donuts (0.025 inch in diameter). All traces, pads and VIAs are coated with gold for good electric connection.

3.3.3 Mounting and bonding

Fig. 3.4 shows a silicon chip mounted on a daughter PCB. The silicon chip is glued to the center of the daughter board with a precision of ± 0.001 inch (or $\sim \pm 25$ μm). Every four neighboring readout pads of the silicon chip are bonded together with aluminum bonding wires to connect to one readout trace of the daughter board

[1] A VIA is a plate-through hole bringing the electric conduction from one side (layer) of the PCB to the other side (layer).

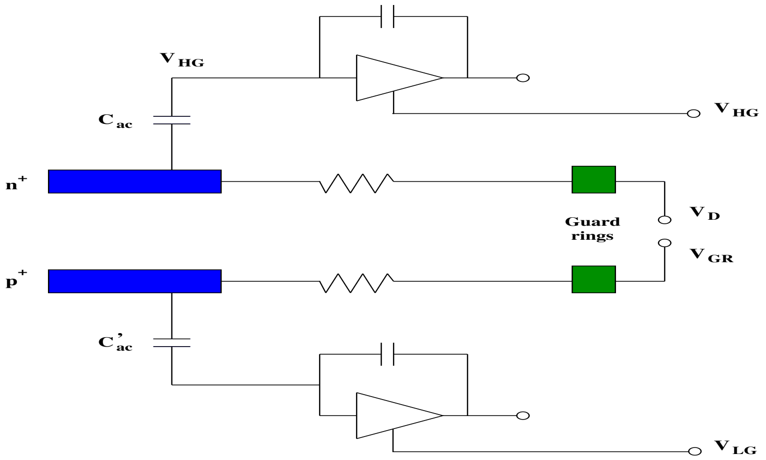

Figure 3.5: Bias scheme for the double-sided microstrip silicon detector. C_{ac} and C'_{ac} are built-in capacitors for AC-coupling to preamplifiers. Two bias voltages are applied to n^+-side and p^+-side strips independently through guard rings and built-in polysilicon resistors.

. There are two major considerations for selecting this bonding scheme. (1). The tracking capability of the E877 magnetic spectrometer requires a positional resolution of $\sim$300 μm at the target, and the average cluster size (due to electric diffusion) of an Au beam particle on a silicon detector is between 200μm and 400μm, shown by the previous single-sided BVER. A readout pitch of 200 μm is sufficient to meet both needs. (2). Bonding four strips into one readout channel reduces the number of electronics by a factor of 4. The total number of readout channels required for two silicon detectors is thus 384. The readout channel would recognize a signal whenever any of the four bonded strips is fired. This makes us less dependent on a small fraction of dead strips.

3.3.4 Bias and leakage current

Fig. 3.5 shows the bias scheme of the double-sided microstrip silicon detector. A positive bias voltage is applied to the n^+-side strips and a negative one to the p^+-side

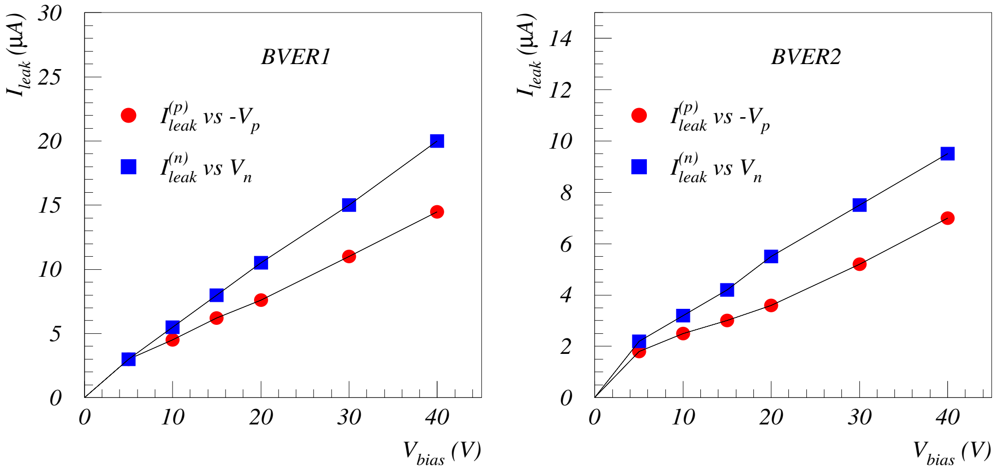

Figure 3.6: Total leakage currents as a function of bias voltages for BVER. V_p(negative) and V_n(positive) are the respective bias voltages applied to p-side and n-side of each silicon detector. $I^{(p)}_{leak}$ and $I^{(n)}_{leak}$ are their leakage currents.

strips. The leakage current as a function of bias voltage on each side of each detector is shown in Fig. 3.6. The average leakage current for each working channel (four original microstrips bonded together) is not greater than 200 pA for BVER1 and not greater than 100 pA for BVER2 at an equivalent bias voltage of 80 volts.

Fig. 3.7 is a photo showing one of the two double-sided microstrip silicon detectors installed onto the C5 beam line at the AGS. The two detectors were installed onto the light-tight beam pipeline and kept in vacuum. They are located at 2.8m (BVER2 as shown in Fig. 3.7) and 5.8m (BVER1) from the target respectively. Each silicon chip of each detector was precisely aligned to the center of th beam line. p-side strips go vertically and give the x-position measurement of an incident beam particle; n-side strips go horizontally and give the y-position measurement.

Figure 3.7: A photo showing one of the two E877 double-sided microstrip silicon detectors installed onto the AGS C5 beam line. The detector was mounted on a solid steel frame. The silicon chip is not visible due to the presence of the beam pipeline connector (seen in the center of the picture with two handles). The small chips around the beam pipeline connector are the preamplifiers. The twist pair cables send the preamplifier signals from the mother board to the discriminators (not shown in the photo). The AGS beam comes from the left. Part of the beam pipe was removed when the picture was taken.

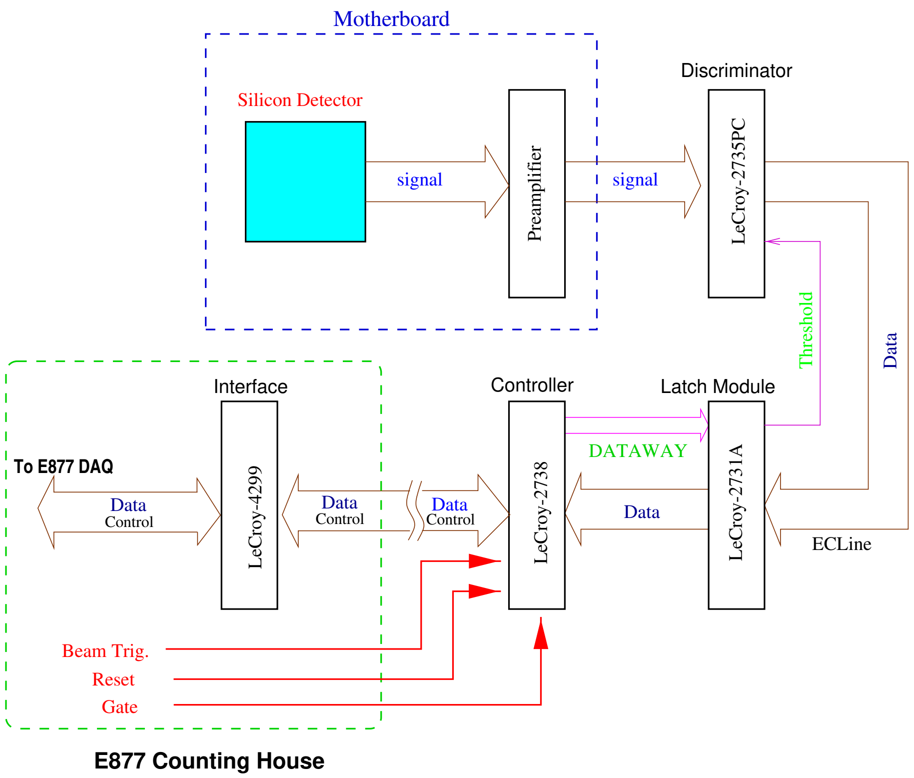

Figure 3.8: Readout system of E877 2D Vertex Detector

3.4 Readout Electronics

A block diagram of the BVER readout electronics system is schematically shown in Fig. 3.8. Charge sensitive preamplifiers (low noise, high performance BNL-IO-456-3 [67]) are used at the second stage of strip signal processing. Signals from the preamplifiers are processed by a LeCroy PCOS (multiwire Proportional Chamber Operating System). The signals from the preamplifiers are discriminated by LeCroy Model 2735PC (16-channel Chamber Card), then delayed and stored as 32-bit word by LeCroy Model 2731A (32-channel Delay and Latch Module). LeCroy Model 2731A (Crate Readout Controller) scans the status of 2731A modules and encodes the addresses of of hit patterns into a look-up memory. Event data from BVER is buffered at CAMAC Model 4299 (DATABUS-CAMAC Interface) via LeCroy DATABUS and

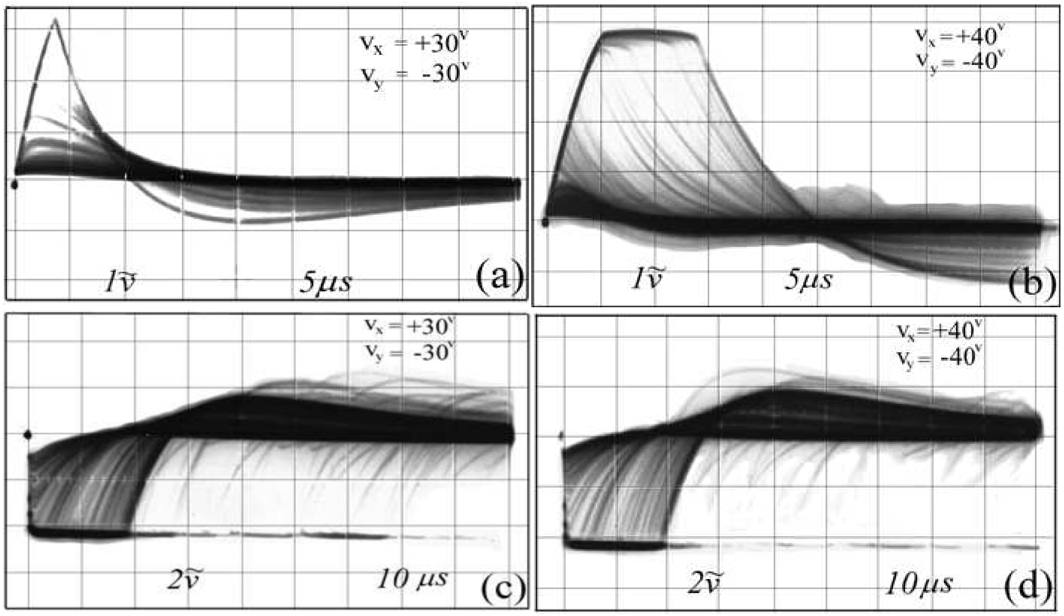

Figure 3.9: Typical BVER signals after preamplifiers. (a) and (b) are the signals from y-side under two different sets of bias voltages; (c) and (d) are the signals from x-side under the same settings. The polarity of the signals was reversed after the preamplifiers.

transferred to the E877 DAQ system whenever a beam trigger from the beam scintillator is present. The threshold of 2735PC and the delay of 2731A are programmable. Interested readers can refer to Ref.[78] for a complete description of PCOS electronics.

3.5 Performance

Fig. 3.9 shows typical preamplifier signals from one of the two BVER detectors hit by the AGS Au beam particles (11.5 A·GeV/c). The polarity of the signals was reversed after the preamplifiers. One notices that signals from both sides suffer from a significant saturation when the biases get higher. Since the number of electron-hole pairs produced in the silicon wafer is approximately proportional to Z^2 (Z is the charge state of the incident particle), a lower bias ($V_x = -15V$, V_y=+15V) was

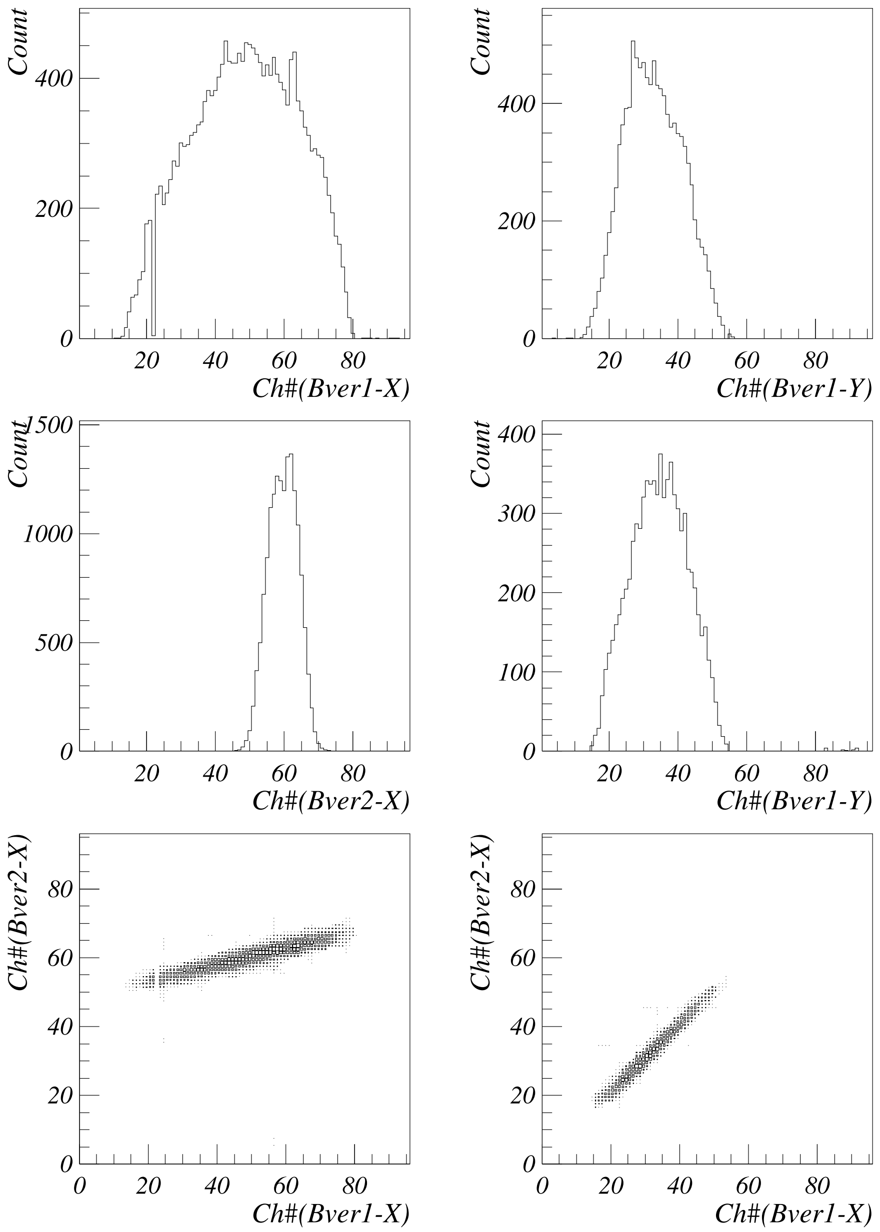

Figure 3.10: Hit patterns on the two detector of the BVER. The top two histograms show the hit pattern on the x- and y-side of BVER1; the middle two histograms are for BVER2. The bottom two figures show the corrections between BVER1 and BVER2.

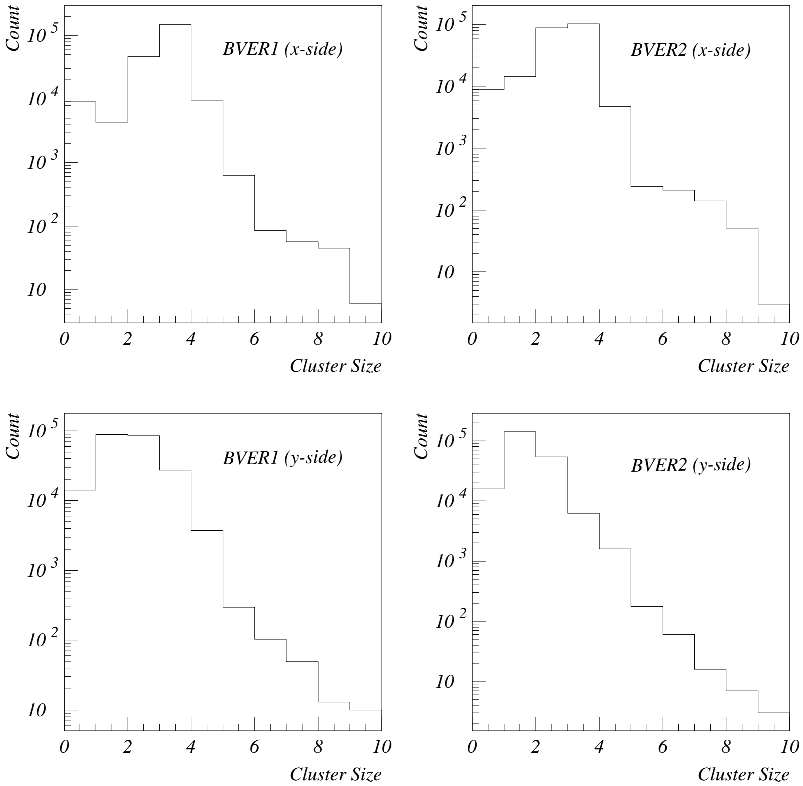

Figure 3.11: Distributions of the cluster size of BVERs. Distributions for two sides of each detector are illustrated. The unit of cluster size is the size of one BVER readout channel (200μm pitch size).

chosen to avoid causing signal saturation at preamplifiers due to the high charge state of Au ($Z = 79$).

Fig. 3.10 shows typical hit patterns of Au beam particles on the two detectors of the BVER. One notices that both x- and y-projections of the AGS beam profile show distributions close to Gaussians; a narrower x-distribution is observed at BVER2, indicating the beam is focusing towards the target (BVER2 sitting closer to the target), whereas the y-distributions remain nearly unchanged from BVER1 to BVER2.

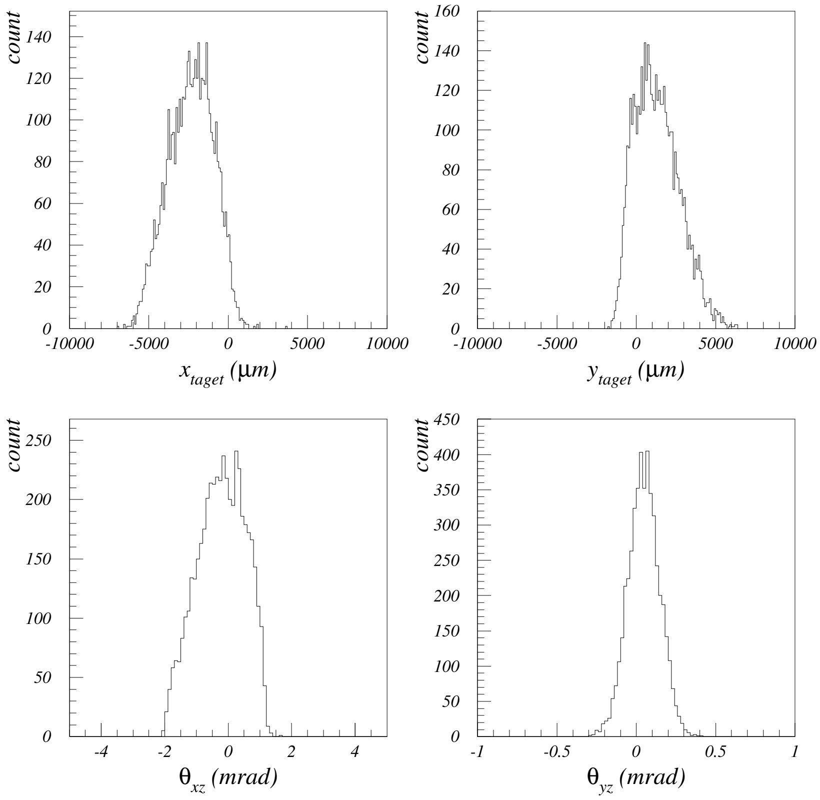

Figure 3.12: AGS Au beam profile measured by the BVER. The top two panels are respectively the beam profile projected in the x- and y-directions at the target; the bottom two panels show the beam angular distributions projected in x-z and y-z planes.

As shown at the bottom of the figures, the position measurement at BVER1 and BVER2 are strongly correlated in both x- and y-directions.

When an incident beam particle passes through a BVER detector, a few number of strips are fired due to charge diffusion and induction during the collection of the produced electrons and holes. The size of cluster is usually between 1$\sim$4 readout channels. Fig. 3.11 displays the cluster size distributions of all the four sides of the BVER. On average, for each incident Au beam particle, $\sim$3 channels are fired on the BVER1-X (x-side of BVER1), 1~2 channels on the BVER1-Y, 2~3 channels on the BVER2-X and ~1 channels on the BVER2-Y. The position of an incident beam particle is calculated as the geometric center of its cluster. Two adjacent clusters which are separated by more than three readout channels are treated as the hits from double beams.

The trajectory of an incident beam particle in the x-z (or y-z) projection can be uniquely reconstructed when the x-side (or y-side) of each detector records one and only one cluster. Multiple clusters on any side of any detector creates ambiguity in beam track reconstruction, and events of such kind are discarded. At a beam rate of less than 2×10^5 per spill (the length of per AGS spill is ~1.4 second), the tracking efficiency of the beam vertex detector is better than 95% in the x-z projection and 92% in the y-z projection (see Table 3.1). [2] The overall efficiency requiring both x-z and y-z tracking information over the whole running period of 1995 was ~90%.

Table 3.1: Average number of clusters per event in the two detectors of the BVER. The numbers are from the data taken during the E877 operating period of 1995.

Number of clusters	BVER1X	BVER2X	BVER1Y	BVER2Y
0	0.033	0.035	0.059	0.065
1	0.959	0.960	0.935	0.928
2	0.008	0.005	0.006	0.007
3	< 0.0001	< 0.0001	< 0.0001	< 0.0001

Fig. 3.12 shows the Au beam profile from the AGS C5-line at the target. These distributions are extrapolated from the measurements by the BVER. Both positional

[2] Since BVER1 and BVER2 are strongly correlated, the tracking efficiency using the two detectors is higher than a simple product of each detector's efficiency. The efficiency of 95% in x-z and 93% in y-z were obtained from separate study of the data. This is also true for the ~90% efficiency requiring both x-z and y-z information.

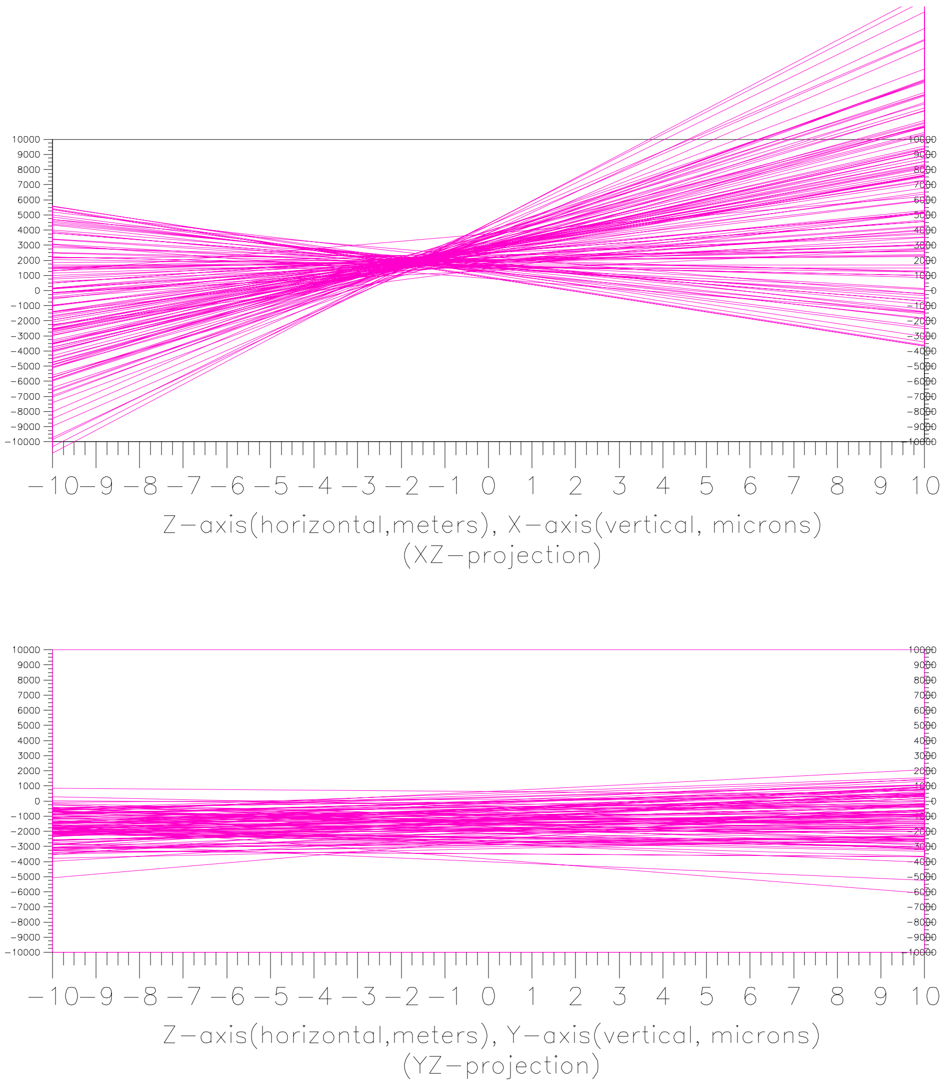

Figure 3.13: AGS C5-line beam trajectories reconstructed using the BVER. The top panel shows the beam trajectories in the x-z projection and the bottom one shows the beam trajectories in the x-z projection. In both panels, the horizontal axis is the beam axis (z-axis) with the target located at $z = 0$. BVER1 and BVER2 are located at $z = -5.8$m and $z = -2.8$m respectively.

and angular profiles of the AGS beam show distributions close to Gaussians. The beam positional dispersion width in both x- and y-directions is $\sim$3.5mm; the beam angular dispersion is $\sim$2.5mrad in the x-z projection and $\sim$0.3mrad in the y-z projection.

During the experimental running period of the E877 experiment in 1995, the BVER was also used as a real-time beam optics monitor to help the AGS C5-line beam tune-up. Fig. 3.13 shows the typical C5-line beam trajectories in both x-z and y-z projections reconstructed with the measurements from the BVER. The target is located at $z = 0$m position. The trajectories are extended to the downstream region ($z > 0$) to give a symmetric view. On notices that the beam particles are focusing near the target in the x-z plane whereas they are almost parallel in the y-z plane. The beam was actually focused at $z \sim -2$ (where one of the beam scintillators S4 is located) to get a maximum acceptance for the incoming beams.

The beam angles measured by the double-sided BVER are used in correcting the incident beam angles in the study of the reaction plane. This application will be discussed in Section 6.3. For the application of the BVER information in the study of Λ decay and the improvement on p_y measurement, readers are referred to Ref. [79].

Chapter 4

Data Reduction and Event Characterization

4.1 Data Reduction

4.1.1 Strategy

The total amount of data collected by the E877 in 1995 corresponds to approximately 1600 GB, or about 80×10^6 central events. The raw data are distributed into nearly 400 magnetic tapes (8mm Exabyte). Each tape sequentially stores $\sim$200k events. Each event archive on tape begins with an event header, followed by the data section for each detector (the beam definition detectors, the event characterization detectors and the tracking detectors in sequence). The length of a typical event is $\sim$16 KB. The event header indicates the beginning of an event and contains some basic information (sequence number, event length, scalers, etc.) about the event. Each data section is a self encoding segment, beginning with a detector header followed by the ADC or TDC signals of the detector. The detector header contains the number of ADC (or TDC) channel of the detector.

One sequential reading of these raw data tapes normally takes few months of time [1]. Obviously, this huge amount of data should be reduced to a level that data analysis can be carried out repeatedly in a more reasonable period of time. Furthermore, the raw ADC/TDC information of detectors should be transformed into physically important variables such as positions, momentum and energy for each particle after the data reduction.

Proper data structure formats are crucial to data transformation, reduction and analysis. There are two major requirements from the point of view of data analysis. The first requirement is that the size of each data file must not be too large. This issue is directly related to the efficiency of I/O bound data analysis. The second requirement is that the relationships between physics variables must be retained. Based on these demands, we chose the HBOOK CWN (Column-Wise-Ntuple) provided by CERN [80] as the reduced data format. Ntuple is a data structure designed on the basis of a relational database model. An Ntuple is a list of identical data structures with each variable being kept as one column and each event as one row. The data storage and management strategy of Nutples thus preserves the correlations between variables and provides a convenient and efficient way for such study. In a CWN, the elements of each column are stored sequentially. A major advantage of CWN is its on-the-fly compression mechanism and variable length arrays. Variables in CWNs are typed and their ranges can be specified. This provides an efficient and flexible way to store data and is particularly important for large data files as in our case. The storage feature of CWNs also enhances the system performance when only a small fraction of variables are accessed in a query. For the data analysis and presentation system, we adopted from CERN the PAW[81] package equipped with the new query processor which supports the features of CWNs.

[1] The maximum reading speed of an Exabyte drive is 500 KB per second.

4.1.2 Off-line software

An block diagram depicting the architecture of the E877 off-line data analysis system is shown in Fig. 4.1. This system inherits most of the features of the E877 off-line software developed in the previous years [70, 71], and was redesigned for the data set of 1995. It primarily consists of three major parts: the data reduction package, the end-user package and the database monitor.

Data reduction package

This package accomplishes the task of data reduction. The data reduction is done in two steps: STEP1 and STEP1.5. At each step, there is an auxiliary calibration sub-package. Each calibration sub-package generates the detector calibration data files for the main package (STEP1 or STEP1.5).

- **STEP1**

  STEP1 is the main data reduction/reconstruction software written in FORTRAN and C. It serves as the basis for unpacking and calibration of raw data, reconstruction of tracks, monitoring display and the creation of the reduced data set. The CWN produced by STEP1 from each raw data tape, the fat (it was named "fat" because of its large size), has 131 variables with 2462 columns in maximum and is about 180 MB. Each "fat" contains the global information (such as beam angles, PCAL/TCAL transverse energies(un-calibrated), etc) for each event and the track information (p_x,p_y, p_z, time-of-flight, etc) of each particle reconstructed in the spectrometer. Also contained in each "fat" is the necessary tracking information which might potentially be used in the later analysis. A parallel CWN for PCAL was also generated. The production of parallel CWNs is to save the effort of resorting to the raw data tape for the option of the detector re-calibration at STEP1.5 and in case a new scan is nec-

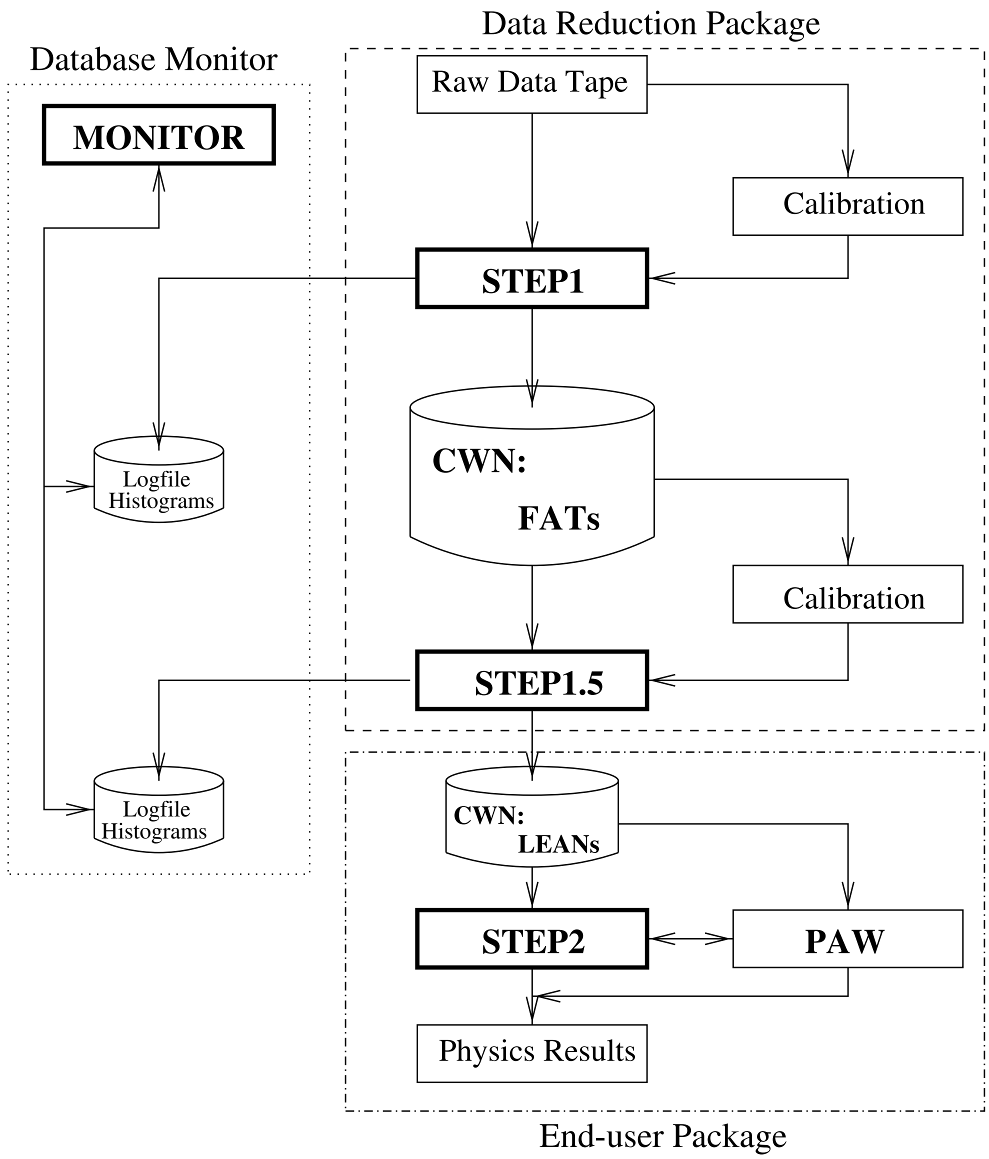

Figure 4.1: Architecture of the E877 off-line data analysis system. The components of the data reduction package is enclosed by the dashed square, those of the database monitor package by the dotted square and those of the end-user package by the dot-dashed square.

essary. After STEP1, most of the redundant global and tracking information has been removed and the whole raw data set has been reduced to ~70 GB in addition to ~80 GB of parallel CWNs. The produced "fat" and parallel ntuples are stored in nearly 40 DSTs (Data Summary Tape).

- **STEP1.5**

  A data set of 70 GB is still too large for our I/O bound data analysis system. The second step of data reduction called STEP1.5 was therefore introduced. The structure of STEP1.5 is similar to that of STEP1 except that the input is not the original data tapes but the "fats" produced by STEP1. In STEP1.5, the PCAL/TCAL transverse energies were calibrated to provide the reaction plane and centrality information of each collision; particle identification (mass) and relevant other tracking information (such as VTX matching, occupancy correction,etc) were derived; variables were digitized in accordance with the needs of our final physics analysis. The CWNs produced by STEP1.5 are called "leans" because of their much smaller size (~60 MB each). Each "lean" CWN contains 50 variables with 411 columns in maximum and the total amount of "lean" CWNs is ~22 GB.

End-user package

After the two steps of data reduction, the raw data set of 1600 GB has been downsized by a factor of 70 to a set of 22 GB. Final physics analysis now proceeds with the 22 GB "leans" being kept in a pool of NFS [2] disks. Simple physics analysis can be interactively performed with embedded FORTRAN (or C) programs under PAW. STEP2 was designed to handle complicated physics analysis with batch jobs. In order to take the advantage of the rich FORTRAN CERN libraries, an interface

[2] The acronym for Network File System.

inside STEP2 is provided to transform CWN data objects into objects of FORTRAN data structure. A pass of full statistics based on STEP2 batch job usually takes a few hours on an ALPHA/533MHz machine running Digital UNIX.

Database monitor

The database monitor package assures the production quality of database files (fats and leans) by monitoring the production processes using log files and monitoring histograms. The package was designed and developed in CGI [3] Perl, HTML and C-shell scripts under the client/server environment with the Netscape graphics user interface. Since the package is a small database system itself, it also serves as a management and maintenance tool for the production and storage of the CWNs.

4.2 Event Characterization

In the E877 experiment, a 'good' event is selected with the measurements made in the two groups of detectors: the beam definition detectors and the calorimeters. The beam definition detector group defines a 'good' beam particle and the energy measured by the calorimeter group characterizes the collision.

4.2.1 Event characterization by beam definition detectors

In 1995, the beam definition detector group consists of two detectors: the beam scintillator (BSCI) and the beam vertex (BVER) detectors (see Chapter 2). These two detectors provide the arriving time and incident angle of the incoming beam particle from the AGS. Additional information from these detectors can be used as selection criteria for event characterization.

[3] The acronym for Common Gateway Interface.

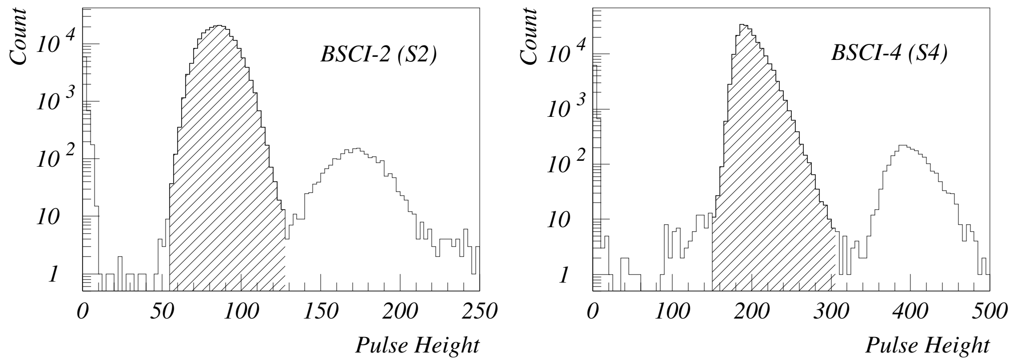

Figure 4.2: Pulse height distributions of BSCI S2 and S4. The pulse heights are in ADC channels. The hatched areas indicate the ranges for selecting a 'good' beam particle.

- **Event selection using beam scintillator detector**

The pulse height produced by an incident beam particle in S2 or S4 can be described by

$$ph^{(i)} = \sqrt{ph_1^{(i)} \cdot ph_2^{(i)}}, \qquad i = S2, S4, \tag{4.1}$$

where $ph_j^{(i)}$ ($i = S2, S4,\ j = 1, 2$) represents the pulse height measured by the photomultiplier j of detector i. Fig. 4.2 shows the pulse height distributions as observed by S2 and S4. The hatched areas indicate the ranges for selecting events with 'good' beam definition. In each plot, the narrow peak in the lower pulse height range is from noise. The secondary peak in the higher pulse height range is due to double beam. The double beam effect is produced when the arriving time difference between two incoming beam particles is less than the ADC gate width of the detector. Both noise and double beam effects were removed by requiring events falling within the selected pulse height ranges.

- **Event selection using beam vertex detector**

To obtain unambiguously the incident angle of the beam particle, it is required that each side of each detector of the BVER see one and only one beam particle at a time. This issue has already been discussed in Section 3.5. The overall efficiency for requiring both x- and y-information is better than 90%. Also, additional requirement that the reconstructed positions (x_{target} and y_{target}) of the beam particle at the target be within the geometric dimensions of the target:(-10000μm,+10000μm), has been applied in the event selection.

4.2.2 Event Characterization by the Calorimeters

The three calorimeters of the E877 experiment (TCAL, PCAL and UCAL) cover different angular regions and provide for each event the measured energy distributions, the centrality and reaction plane orientation information. In this section, we will first discuss the trigger down-scaling and the construction of the unbiased transverse energy distributions measured by TCAL and PCAL. Then we will discuss the event selection criteria. The determination of the reaction plane will be presented in Chapter 6.

- **E_T spectra and down-scaling factors**

The data collected by the E877 experiment in 1995 rely on the use of the combination of multilevel and multi-threshold triggers (Section 2.5), along with various down-scaling factors to produce approximately equal statistical weight for the sample over the entire transverse energy spectrum. The down-scaling technique is commonly exploited in experiments that measure cross sections varying by orders of magnitude over the range covered by the experiments. To get the real physics results free of these experimental biases, it is important to reconstruct the natural distributions

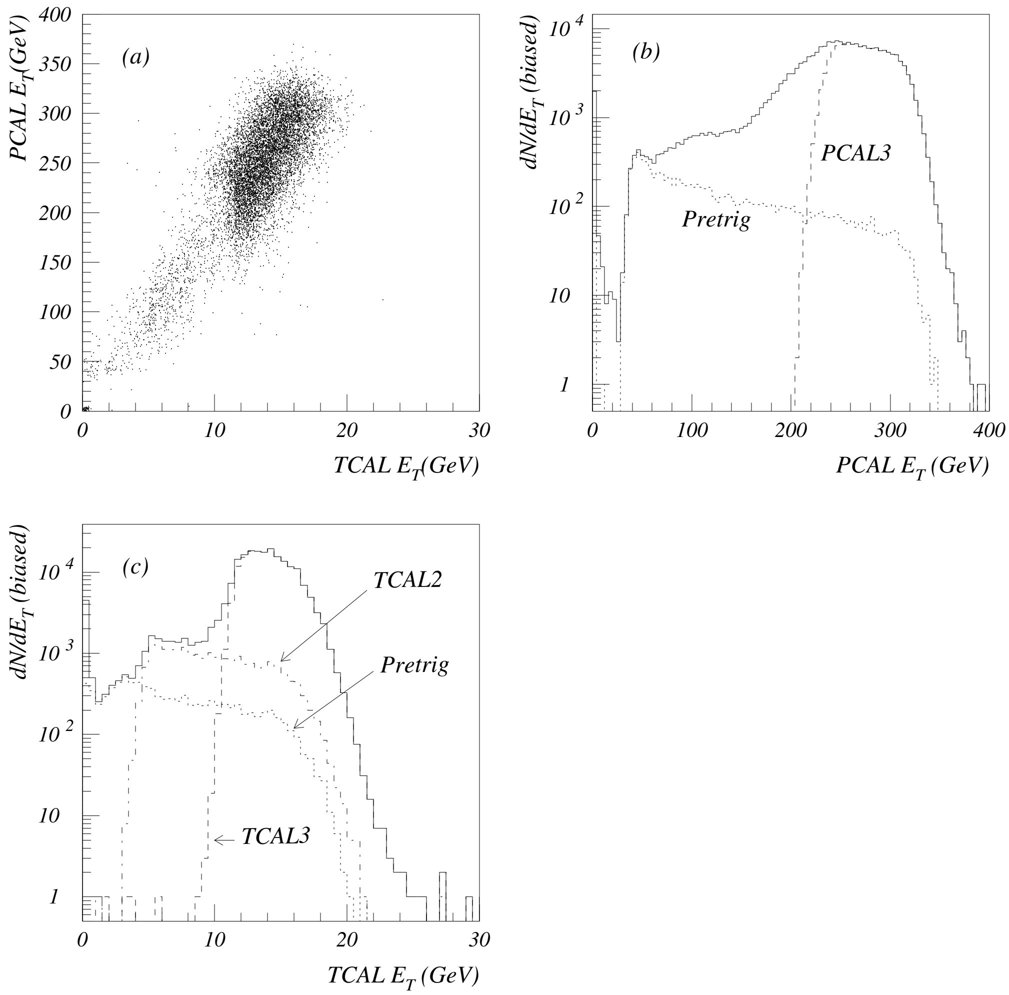

Figure 4.3: Measured PCAL and TCAL E_T distributions of various triggers. (a) shows the correlation between PCAL E_T and TCAL E_T. (b) and (c) are the E_T distributions measured in the PCAL and TCAL. E_T distributions of pre-trigger (dotted line), TCAL2(dot-dashed line in (c)), TCAL3(dashed line in (c)), PCAL3(dashed line in (b)) and the mixed trigger(solid line) are shown. The mixed trigger is the logical ORs of all available triggers.

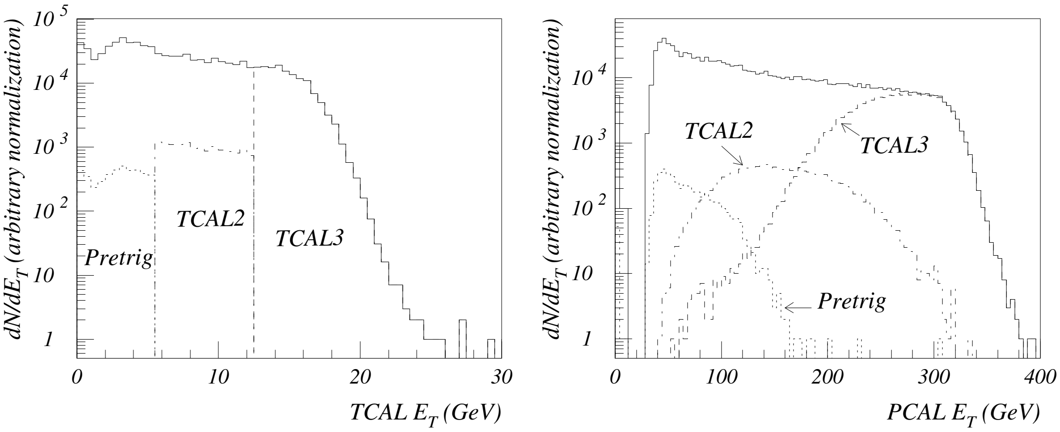

Figure 4.4: Unbiased E_T distributions obtained by the PCAL and TCAL. The left panel shows the unbiased TCAL E_T spectrum (solid line histogram) constructed from the distributions of pre-trigger, TCAL2 and TCAL3; the unbiased PCAL E_T distribution (solid line histogram) on the right panel is constructed with the same trigger data.

from the biased ones.

In 1995, not all data of the level-2 trigger were written to tape. Only data above the thresholds of TCAL2, TCAL3 and PCAL3 (see Section 2.5 of Chapter 2) were recorded. The data of TCAL2 are down-scaled. The pre-trigger data retains the natural shape of the distributions but are down-scaled even more.

Fig. 4.3 shows the correlation between the transverse energy measured by PCAL and TCAL, and their E_T distributions for the various triggers. In principle, there exist many ways of constructing unbiased distributions by a proper combination of distributions of different triggers and their corresponding down-scaling factors. We choose TCAL3 to select the central collision events, TCAL2 to select mid-central events and pre-trigger for peripheral ones. This choice is based on the consideration of keeping the total statistics as much as possible.

Fig. 4.4 shows the unbiased E_T spectra measured by the TCAL and PCAL constructed from the distributions of pre-trigger and TCAL triggers. Different threshold regions are correlated to different triggers. The conclusion from this procedure is that the unbiased PCAL E_T distribution is recovered with TCAL triggers [4]. This is based on the fact that PCAL E_T is closely correlated with TCAL E_T (Fig. 4.3(a)). The unbiased distributions are consistent with the up-scaled pre-trigger distributions. This consistency proves the effectiveness of this method. This technique of removing experimental bias will be used for the following analysis.

- **Centrality determination**

The centrality of the collision is directly connected to the impact parameter and a reflection of the violence of the collision, which shows up in observables such as multiplicity, transverse energy, etc. In principle, the centrality of a collision can be directly estimated from the constructed unbiased E_T distribution (PCAL or TCAL E_T spectra) obtained in the previous section, by calculating the ratio of the number of events above the transverse energy E_T^0 produced in the collision to the total number of events of the unbiased distribution.

Unfortunately, the constructed distributions from experimental data are incomplete. The very low E_T portions are quite difficult to construct because of the incomplete information about triggers and threshold cuts (Fig. 4.4). Instead, a simple geometrical model was used. The total number of collisions for the number of defined beam particles B is estimated using the geometrical cross section of the Au+Au collision as

$$N_{geo} = B \cdot \sigma_0 \cdot \lambda_{target} \tag{4.2}$$

[4] In principle, this PCAL E_T spectra could be reconstructed with the PCAL3 and pre-trigger data, but such spectra would have less statistics since the data of pre-trigger is more down-scaled than that of TCAL2.

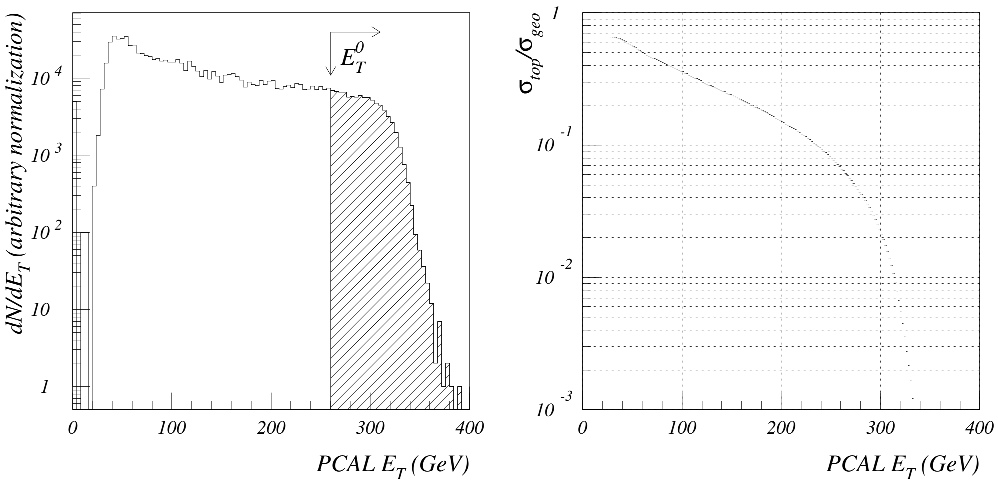

Figure 4.5: Centrality function determined from PCAL E_T distribution. The hatched area in the unbiased PCAL dN/dE_T distribution on the left panel represents the number of events with $E_T > E_T^0$, where E_T^0 is the transverse energy measured by PCAL for the collision. The right panel shows the centrality as a function of PCAL E_T.

where σ_0 is the geometrical collision cross section of two Au nuclei, $\sigma_0 = \pi(2R)^2 = 6127$mb with $R = 1.2A^{1/3}$ fm and $A = 197$. λ_{target} is the number thickness of the Au target, whose value was equivalent to about 2% of interaction probability.

The centrality cut for events with $E_T > E_T^0$ is calculated, with the number of events falling in that range from the constructed PCAL E_T distribution and the total number of collisions estimated by the geometrical cross section, as

$$\frac{\sigma_{top}}{\sigma_{geo}} = \frac{N_{top}}{N_{geo}} = \frac{\int_{E_T=E_T^0}^{\infty} \frac{dN}{dE_T} dE_T}{N_{geo}} \tag{4.3}$$

Fig. 4.5 shows the calculated centrality function using the geometrical model. This was done for every run to take into account probable shift between runs. A similar calculation can be done with the unbiased TCAL E_T distribution. We choose PCAL because of its larger acceptance(Table 6.1).

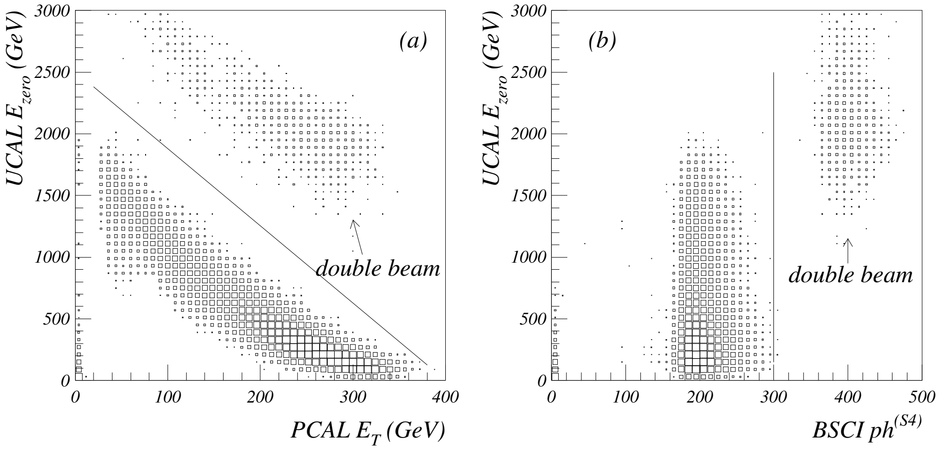

Figure 4.6: Correlation distribution between UCAL E_{zero} and PCAL E_T. The distribution below the straight line in (a) shows the correlation between the energies measured by PCAL and UCAL; the distribution above the straight line is due to double beam hits. The double beam effect is confirmed by the correlation distribution between UCAL E_{zero} and the BSCI (S4) pulse height shown in (b).

- **Correlation between UCAL and PCAL**

UCAL covers the most forward direction and measures the energy flow of produced particles and spectators in this direction. The energy measured in UCAL is well correlated with that measured in TCAL and PCAL. Fig. 4.6(a) shows the correlation distribution between the energy measured in UCAL along the beam direction (E_{zero}) and the transverse energy measured in PCAL. The contribution from double beam is removed by applying a cut (indicated by the straight line in Fig. 4.6(a)) to the correlation distribution. This cut is consistent with the cut on the pulse height of the beam scintillator (for example, S4) signal as discussed in Section 4.2.1.

Fig. 4.7 shows the UCAL E_{zero} distribution after removing trigger biases. The

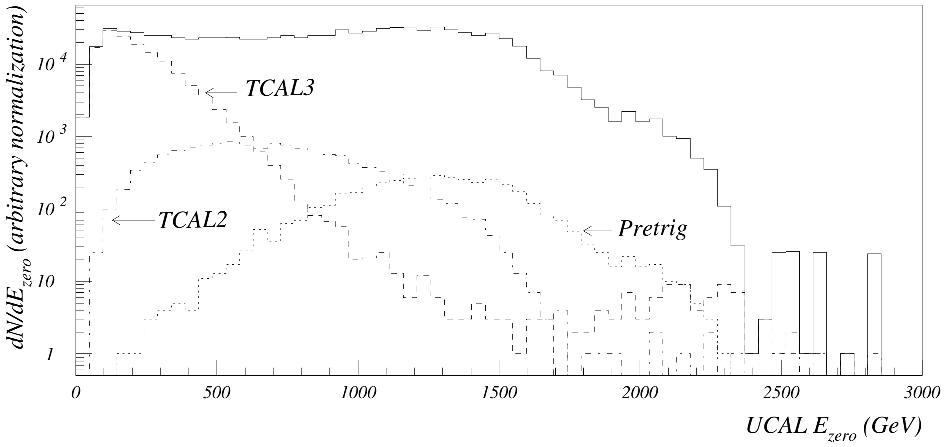

Figure 4.7: Unbiased UCAL E_{zero} distribution. This distribution was obtained from the construction of the biased distributions of pre-trigger, TCAL2 and TCAL3.

distribution of dN/dE_{zero} also reflects the violence of the collision: central collisions usually have smaller E_{zero} while peripheral ones have bigger E_{zero}. In principle, the dN/dE_{zero} of UCAL can also be used as a measure of centrality in a similar fashion to the PCAL dN/E_T. In the present analysis we did not use the UCAL information because of its worse energy resolution compared to that of PCAL.

Chapter 5

Particle Identification

Charged particles emitted from the target into the PCAL collimator opening ($-115 < \theta_{xz}^{lab} < 14$mrad and $-21 < \theta_{yz}^{lab} < 21$mrad) are analyzed by the forward spectrometer (Section 2.3). Particles are identified by a combination of momentum, charge and time-of-flight measurements. In this section, we will describe various issues involved in the particle identification and selection criteria.

5.1 Particle Identification Criteria

5.1.1 Track reconstruction

The trajectories of the charged particles passing through the collimator are reconstructed using the E877 track reconstruction software called "Quanah"[70, 83]. First, wire hits on each drift chamber are reconstructed into line "elements" using a "tree" algorithm[82] to resolve the left-right ambiguity of the hit position. Associated with each element is the y position measured by the cathode plane of each drift chamber. All possible links between elements in DC2 and DC3 are labeled as "segments". A segment is assumed valid if at least 3 MWPC hits lie along its path. For valid seg-

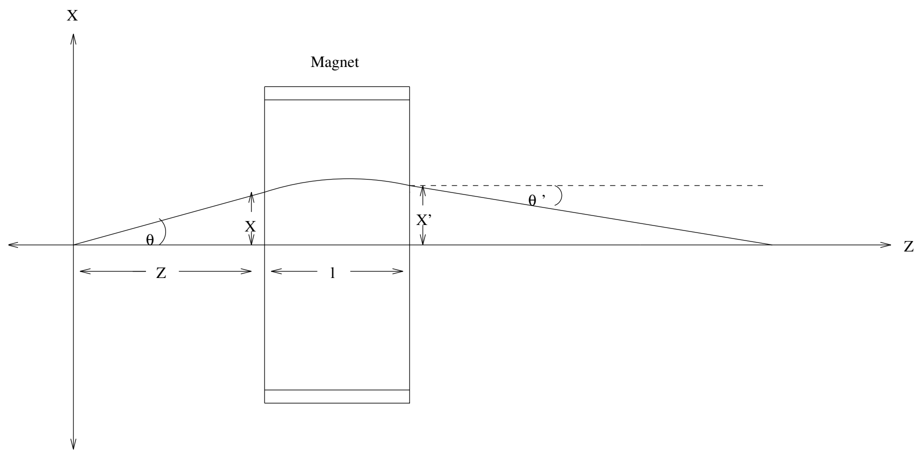

Figure 5.1: Bend-plane geometry of a track passing through the E877 spectrometer. The plot shows the projection on the x-z plane.

ments it is then checked if they are pointing back through the open region of the spectrometer magnet, and those which have passed this check are promoted to "candidates". The candidates are further inspected if they have shared hits in the drift chambers or TOFU. Those which have such sharing are eliminated. Finally, the surviving candidates become tracks. Additional associations with the tracks are the x-y positions in the two cathode pad chambers (VTXs) and the TOFU slat number. The efficiency of track reconstruction is better than 95% for events with PCAL $E_T > 150$ GeV[66].

5.1.2 Momentum determination

The momentum of each track is calculated based on an uniform magnetic field model and the assumption that every particle originates from the target. The effect of the edge field of the magnet is accurately accounted for by using an effective length slightly greater than the physical length[71],

$$\int_{-\infty}^{+\infty} B \cdot dz = B_{eff} \cdot \ell$$

where the integral on the left side which represents the real field profile can be equivalently described as the product of the effective field (B_{eff}) and the effective length (ℓ).

Fig. 5.1 schematically illustrates the bending trajectory (x-z projection) of a track passing through an uniform magnetic field. From this simple geometry, we have

$$R(\sin\theta' - \sin\theta) = -\ell \tag{5.1}$$

and

$$x = z\tan\theta \qquad , \qquad x' - x = R(\cos\theta' - \cos\theta), \tag{5.2}$$

where R is the radius of the circular curvature projected onto the x-z plane; θ and θ' are the angles of the trajectory with the beam axis (z) before and after the magnet respectively. $R > 0$ designates the case that a positively charged particle is deflected in the $-x$ direction. In principle, R and θ can be analytically determined from Eq. (5.1) and Eq. (5.2) with the measured values of x' and θ'. They were actually numerically calculated using an iterative method. The rigidity of a particle is then given by

$$p_{xz}/Z = e \cdot R \cdot B_{eff}, \tag{5.3}$$

where $p_{xz} = \sqrt{p_x^2 + p_z^2}$, Z is the charge of the particle and e stands for the unit charge. Therefore, $p_x = p_{xz}\sin\theta$ and $p_z = p_{xz}\cos\theta$. p_y can be reconstructed from the vertical position measurements by

$$p_y = p_{xz}\arctan(\varphi), \tag{5.4}$$

where φ is the out-of-plane angle (between the trajectory and the bend-plane). p_y is conserved since the magnetic field is parallel with the y direction. The angles of the incident beam particle and its positions at the target change from event to event. The actual p_x, p_y and p_z are calculated by taking into account the beam particle angle and position at the target.

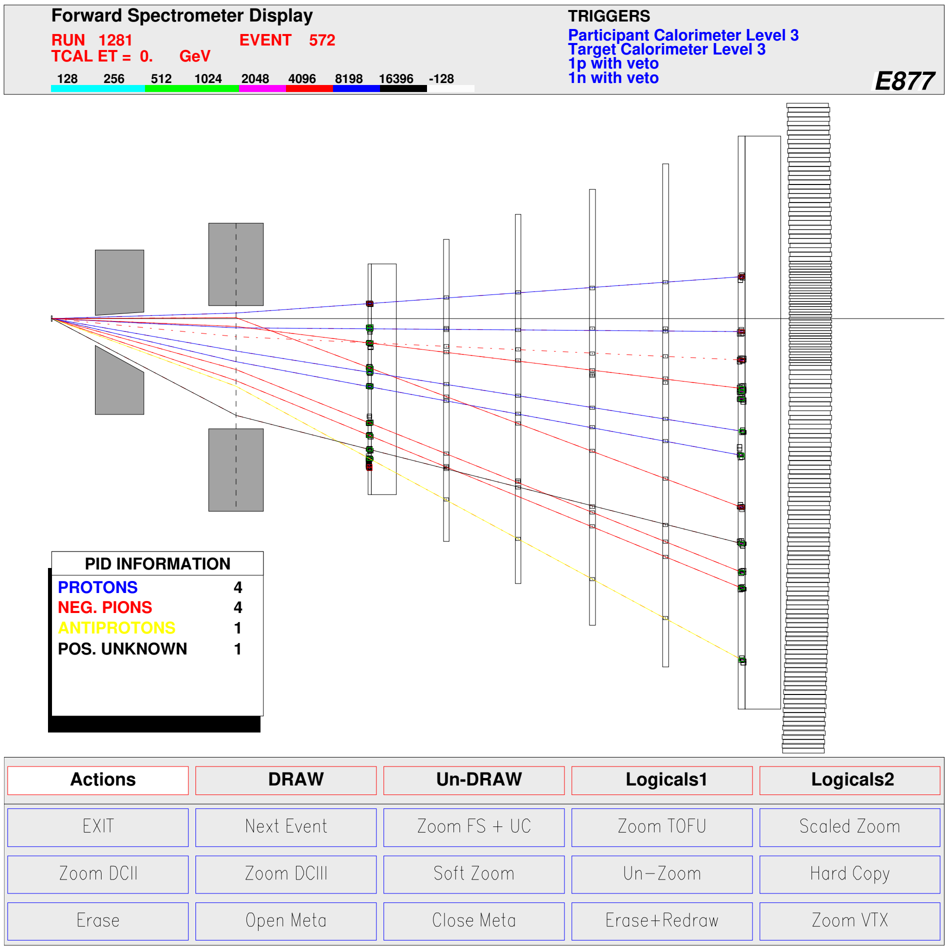

Figure 5.2: Event display of a typical central Au+Au event measured in the E877 spectrometer. Shown from left to right are the collimator, magnet, DC2, MWPC1-4, DC3 and TOFU. For 1995 magnetic polarity configuration, positive charged particles are bent upward (x direction) whereas negative charged particles are bent downward ($-x$ direction).

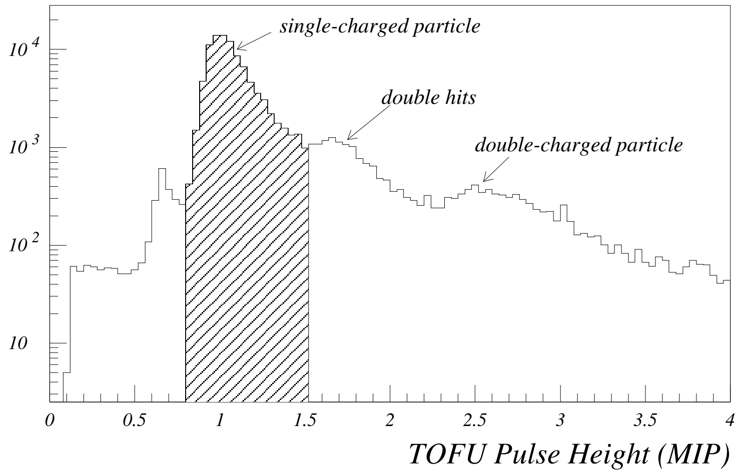

Figure 5.3: Pulse height distribution in TOFU. The pulse height is normalized to the unit of minimized ionization particle (MIP). The shaded region is the selection range of single charged particles.

Fig. 5.2 illustrates a typical central Au+Au collision event measured in the E877 forward magnetic spectrometer. From left to right, the produced charged particles which pass through the collimator are bent at the magnet, then intersect with the six tracking detectors (DC2, MWPC1-4 and DC3), and finally reach TOFU. The time-of-flight of each track is obtained by matching the extrapolated position of the reconstructed trajectory with a hit on TOFU. The average time-of-flight resolution is better than $\sim$ 90 ps (see Fig. C.15 in Appendix C).

The energies deposited in the TOFU scintillators by the traversing particles are used to determine the charge state Z of the particles. Fig. 5.3 shows the TOFU pulse height distribution for the particles detected by TOFU. The distribution has been normalized to the peak pulse height for a minimum ionization particle (MIP). The spectrum corresponds to the superimposition of Landau distributions of various charged particles. For the analysis of the single-charged particles, the double hits have been rejected by requiring the TOFU pulse height be between 0.8 and 1.5 in the case of protons, $\pi^{\pm}$ and deuterons. The tracking efficiency loss due to this cut is less than 2%[64]. For the analysis of $K^{\pm}$ and $\bar{p}$, a more stringent selection criteria requiring the TOFU pulse height to be between 0.9 and 1.2, has been applied.

For more descriptions of the track reconstruction, momentum determination and tracking detector calibrations, readers are referred to [83, 84, 85, 70, 64] and Appendix C for more details.

5.1.3 Mass resolution and cut criteria

After the momentum and the time-of-flight of a particle are determined, the mass of the particle can be calculated. The squared mass m^2 is given by

$$m^2 = p^2 \cdot \left(\frac{1}{\beta^2} - 1\right), \tag{5.5}$$

where p is the measured momentum, and the Lorentz factor is given by

$$\beta = \frac{v}{c} = \frac{t_{v=c}}{t_{track}},$$

where t_{track} is the measured time-of-flight and $t_{v=c}$ is the time that a $v = c$ particle would take to traverse the same flight path.

Due to the finite resolution of the momentum and time-of-flight measurements, the m^2 of each particle species is characterized by a broadened distribution peaked at the real mass. Fig.5.4 shows as an example the two dimensional m^2 distribution versus momentum for positively charged particles. The ridges corresponding to π^+ ($m^2 \sim 0.0\mathrm{GeV}^2/\mathrm{c}^4$), K^+ ($m^2 \sim 0.2\mathrm{GeV}^2/\mathrm{c}^4$), proton ($m^2 \sim 0.9\mathrm{GeV}^2/\mathrm{c}^4$) and deuteron ($m^2 \sim 3.4\mathrm{GeV}^2/\mathrm{c}^4$), are clearly observed.

The resolution of m^2 can be approximated by[86]

$$\sigma^2_{m^2} = 4m_0^4\left(\frac{\sigma_p}{p}\right)^2 + \frac{4p^4}{\beta^2}\left(\frac{\sigma_{TOF}}{L}\right)^2, \tag{5.6}$$

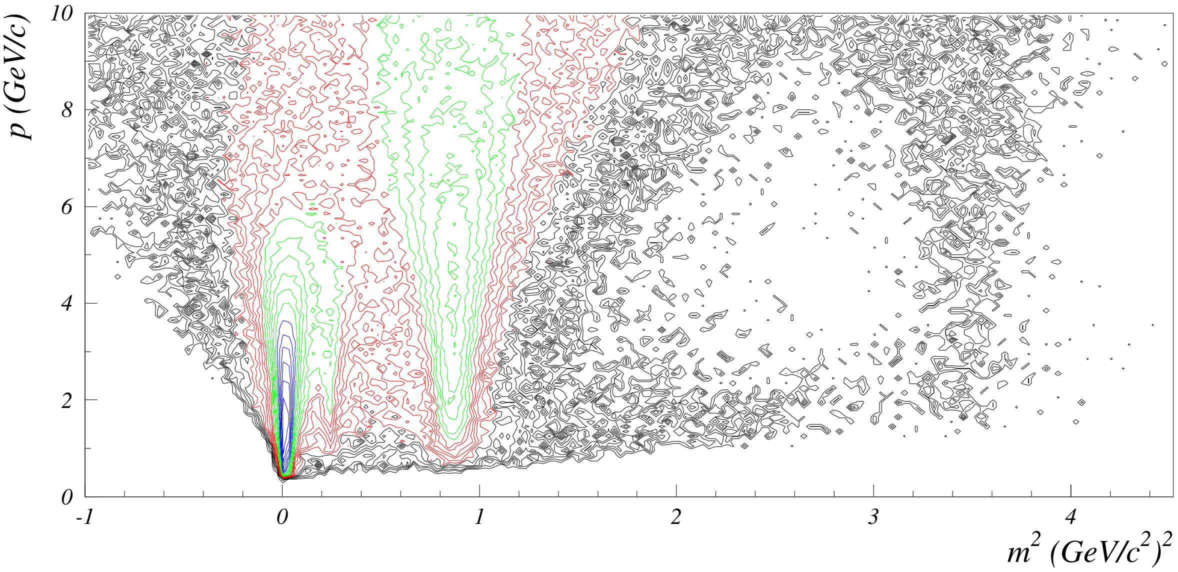

Figure 5.4: The squared-mass distribution for positive charged particles.

where m_0 represents the real mass of the particle; σ_p is the resolution of momentum measurement; σ_{TOF} is the resolution of the time-of-flight measurement and L the length of the flight path. This approximate expression is valid since in the E877 spectrometer, σ_{TOF} is nearly constant ($\sigma_{TOF} \simeq 90 \pm 10$ps, see Appendix C) and the error in the flight path length is negligible ($\triangle L/L \ll 10^{-3}$).

The momentum resolution consists of two contributions: the intrinsic angular resolution of the spectrometer ($\sigma_p(\theta)$) and the spread due to multiple scattering in the detector ($\sigma_p(\theta_{m.s.})$)[87].

$$\left(\frac{\sigma_p}{p}\right)^2 = \left(\frac{\sigma_p(\theta)}{p}\right)^2 + \left(\frac{\sigma_p(\theta_{m.s.})}{p}\right)^2 \tag{5.7}$$

with

$$\sigma_p(\theta) = C_1 p^2 \qquad \sigma_p(\theta_{m.s.}) = C_2 p/\beta$$

The final form of the resolution of m^2 as a function of momentum can thus be

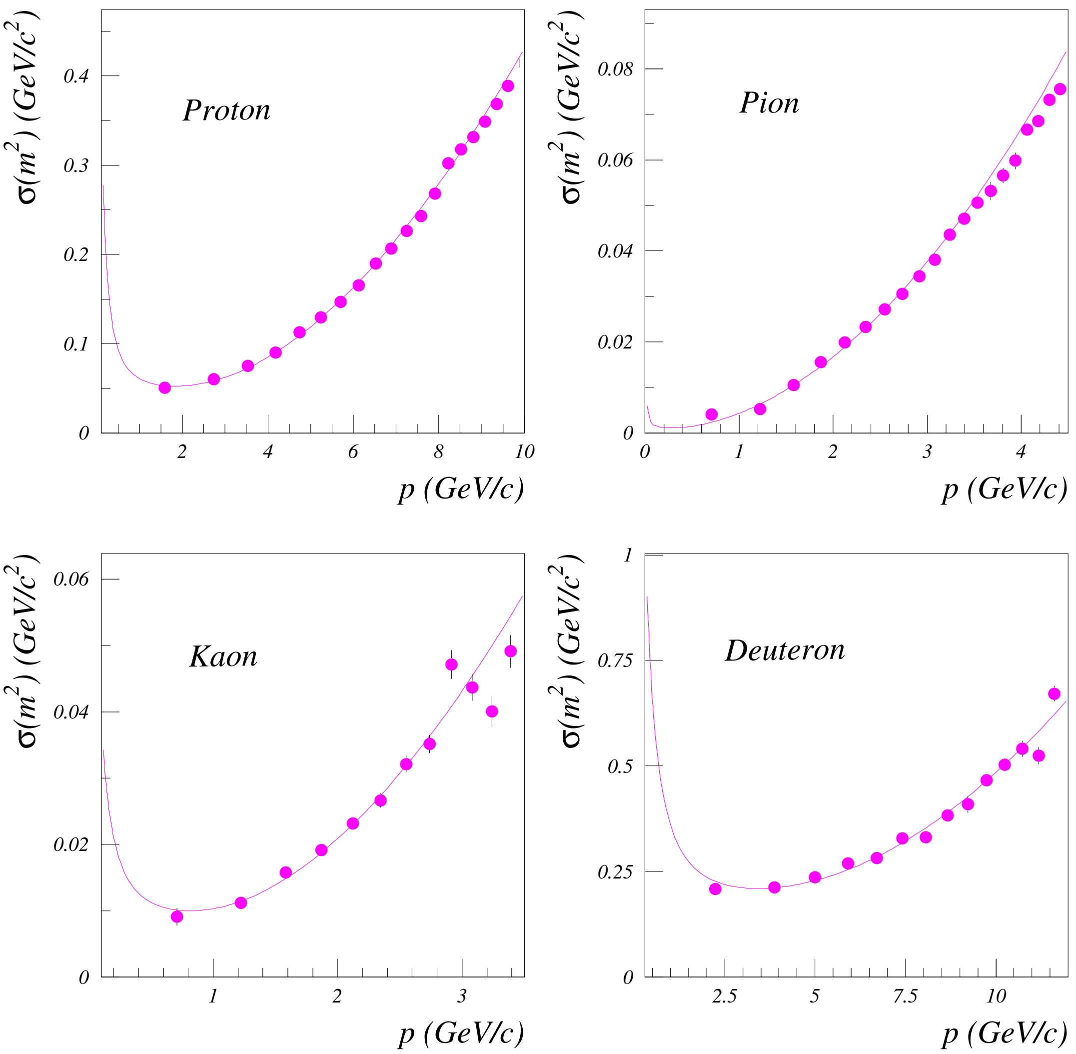

Figure 5.5: The resolution of squared-mass as a function of momentum. Resolutions for proton, pion, kaon and deuteron are shown. The curves overlaid on data points are the functions fitted with the parameters given in Table 5.1.

expressed as

$$\sigma^2_{m^2}(p) = C_1^2(4m_0^4p^2) + C_2^2\left[4m_0^2\left(1+\frac{m_0^2}{p^2}\right)\right] + C_3^2\left[4p^2(m_0^2+p^2)\right] \qquad (5.8)$$

where C_1, C_2 and $C_3 = \sigma_{TOF}/L$ are constants representing the contributions from the angular, multiple scattering and time-of-flight resolution, respectively. To determine the various contributions, the distribution of m^2 vs p were divided into many momentum slices. For each slice, the mass distribution was fitted with Gaussians. The plots in Fig. 5.5 show the extracted widths of m^2 drawn as a function of momentum for different particle species. The data points are fitted with the function given by Eq. (5.8). C_1 was fixed during the fit and its value was estimated in[88]. The values of the fit parameters are summarized in Table 5.1.

In our analysis, a preliminary identification is assigned to a track if its measured m^2 fall within a certain amount of σ_{m^2} of an expected particle species. Table 5.2 presents the parameters of the identification cuts on m^2 versus p distribution for different particles. Additional requirements for particle identification such as VTX matching, y-matching and occupancy correction, will be discussed in the following sections.

Table 5.1: The fit parameters of the squared-mass peak for different particles. Eq.(5.8) was used in the fitting with C_1 fixed. The numbers inside the brackets are estimated errors.

Particle	C_1(GeV/c)$^{-1}$	C_2(GeV/c^2)	$C_3(c^{-1})$	$\sigma_{TOF}(ps)$
Proton	0.0025	0.027(0.001)	0.0021(0.0001)	84(5)
Pion	0.0025	0.025(0.001)	0.0021(0.0001)	84(5)
Kaon	0.0025	0.017(0.001)	0.0021(0.0001)	85(5)
Deuteron	0.0025	0.026(0.001)	0.0020(0.0001)	80(5)

Table 5.2: Particle identification criteria for different particle species. σ_{m^2} is given by Eq. (5.8) for each particle species using the parameters from Table 5.1.

Particle	identifying range	momentum range
Proton	$\lvert m^2 - m_p^2\rvert < 2.0\sigma_{m^2}$	$p < 10.0$GeV/c
$\pi^{\pm}$	$\lvert m^2 - m_\pi^2\rvert < 2.0\sigma_{m^2}$	$p < 6.0$GeV/c
K^+	$\lvert m^2 - m_K^2\rvert < 2.0\sigma_{m^2}$	$p < 3.5$GeV/c
K^-	$\lvert m^2 - m_K^2\rvert < 2.0\sigma_{m^2}$	$p < 3.5$GeV/c
Deuteron	$\lvert m^2 - m_d^2\rvert < 1.5\sigma_{m^2}$	$p < 25.0$GeV/c
$\bar{p}$	$\lvert m^2 - m_{\bar{p}}^2\rvert < 1.5\sigma_{m^2}$	$p < 4.0$GeV/c

5.2 Vertex Chamber Matching

The positional measurements provided by the two vertex chambers (VTX) located before the magnet are used in a confirmation mode to remove background tracks generated before the magnet. The difference in x-position between the position measurement as given by VTX and the expected position of a track reconstructed by the downstream tracking chambers is calculated as

$$dx^{(i)} = x^{(i)} - (z^{(i)} \cdot \tan\theta + x_{target}) \qquad i = A, B \tag{5.9}$$

where $x^{(i)}$ $(i = A, B)$ represents the x position measured by VTX-i, $z^{(i)}$ $(i = A, B)$ is the z position of the VTX-i with respect to the target, θ is the emission angle of a reconstructed track in the x-z plane and x_{target} is the x position of the incident beam particle at the target.

Fig. 5.6 displays the dx distributions for the two VTX detectors. The correlation between the x position measurements of VTXA and VTXB shown in Fig. 5.6(a) indicates that there are two components. The width of the component projected onto the x_{narrow} axis (Fig. 5.6(b)) is nearly constant with respect to momentum (solid

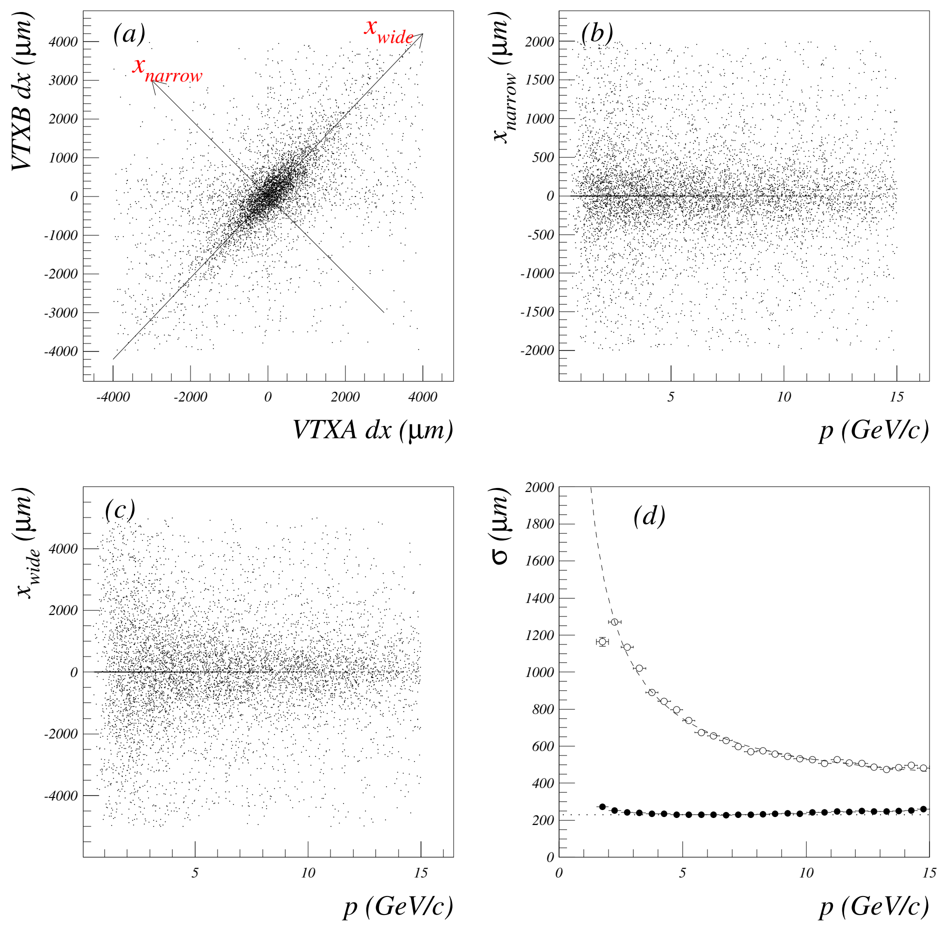

Figure 5.6: Track matching at vertex chambers. (a) shows the correlation between VTXA dx and VTXB dx; (b) and (c) show the positional match as a function of momentum projected on the x_{narrow} and x_{wide} axis respectively; (d) presents the width of positional match of the distribution of (b) (empty circles) and (c) (solid circles) as a function of momentum. x_{wide}-axis and x_{narrow}-axis are perpendicular to each other.

Table 5.3: Parameterization of the width of VTX dx.

VTX confirmation	width function (σ_{dx} in μm, p in GeV/c)
VTXA only	$\sigma_{dx}^{(A)} = 293 + 1350/p$
VTXB only	$\sigma_{dx}^{(B)} = 313 + 1400/p$
Both VTXs	$\sigma_{narrow} = 230$ $\sigma_{wide} = 320 + 2140/p$

circles shown in Fig. 5.6(d)), indicating that the broadening is due to the intrinsic resolution of the detectors; the width of the second component which is projected onto the x_{wide} axis (Fig. 5.6(c)) exhibits a strong $1/p$ dependence on momentum (empty circles shown in Fig. 5.6(d)), indicating the dominant influence from multiple scattering. The widths of the projected distributions shown in Fig. 5.6(d) were obtained by dividing each distribution into momentum slices and by fitting each sliced distribution with Gaussians. The distribution for each individual VTX is similar to the one shown in Fig. 5.6(c). Their widths were extracted using the same technique.

The track matching before the magnet is then performed by requiring the track has a VTX matching measurement falling within a certain value of dx expressed as a number of σ_{dx}. In our analysis, the VTX matching is used in three different ways depending on the level of the background reduction and efficiency desired: only VTXA matching required, only VTXB required and both VTXs required. The parameterization of the detector response for these three cases used in this analysis is summarized in Table. 5.3. In the event that both VTXs are enforced, the matching is performed by first converting $dx^{(A)}$ and $dx^{(B)}$ into x_{narrow} and x_{wide} and then by requiring a track be within a certain range of x_{wide} and x_{narrow}. Since the resolutions of both VTXs in the y direction are very coarse ($\sim$2000μm), no matching in that direction for both VTXs is applied in this analysis. The application of VTX matching in the study of kaons and antiprotons is described in Chapter 7.

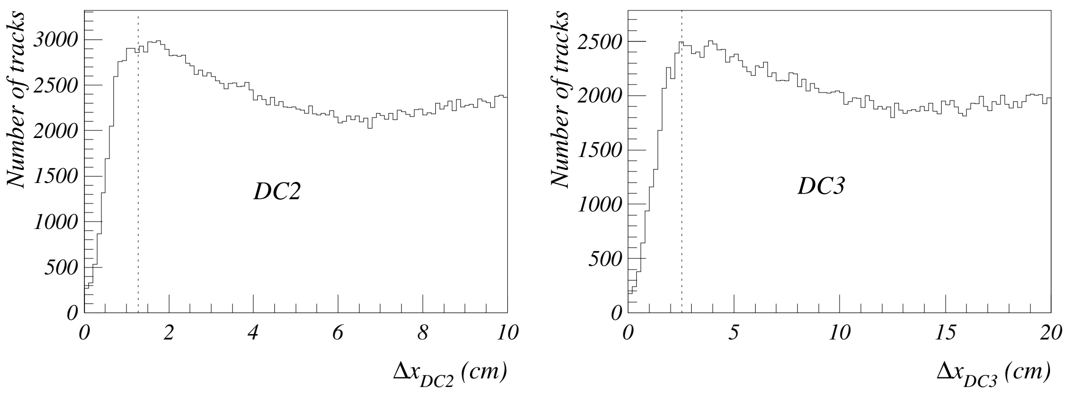

Figure 5.7: Distributions of two-track separation in DC2 and DC3.

5.3 Occupancy Correction

For a tracking detector like DC2 or DC3, when the hits of two passing particles on the detector are closer than the granularity of the detector, the position of each individual hit will not be resolved. In this case, either the trajectories of the two tracks are taken as one track if they share elements both in DC2 and DC3, or they will both be eliminated according the reconstruction criteria (Section 5.1) if they share elements only in one of the two chambers. Tracking inefficiency is thus introduced. This inefficiency is directly related to the distribution of particles (occupancy) across the detectors. The corresponding correction is thus called the occupancy correction.

Fig. 5.7 shows the two-track separation distributions in the two drift chambers. $\triangle x$ represents the separation between two tracks in x. The tracking efficiency drops dramatically when $\triangle x$ gets smaller than $\sim$1cm in DC2 or $\sim$2cm in DC3. As expected, the critical value is nearly twice the cell size (6.35mm for DC2, 12.7mm for DC3).

It is rather difficult to calculate exactly the tracking inefficiency due to occupancy because of the complication from the other effects which are unknown or difficult

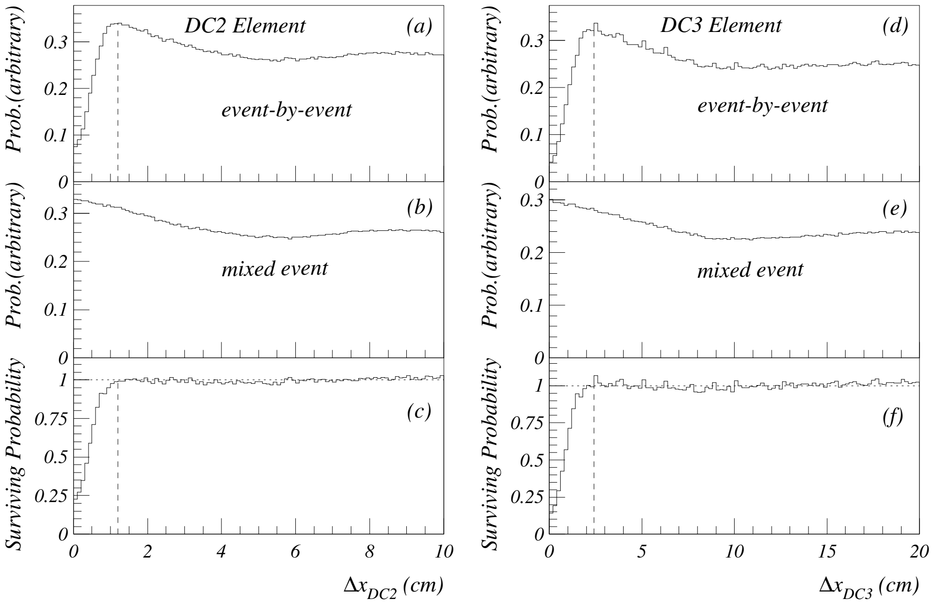

Figure 5.8: Distributions of two-element separation in DC2 and DC3. (a) and (d) are for tracks from the same event; (b) and (e) are for tracks from different events (mixed event); (c) and (f) correspond to the ratios between the same-event distributions and the mixed-event distributions.

to evaluate, such as fragment effects, detector imperfections and tracking software limitations, etc. Several approaches to the occupancy corrections have been developed in the data analysis history of E877[64, 77, 89]. They are designated for the specific physics aim of each particular analysis. In the analysis of particle correlations using pairs[77, 66], those tracks whose separations in the two drift chambers are closer than the minimum separations (∼1cm in DC2 and ∼2cm in DC3) were removed with the software cuts and the inefficiency were accounted for using the acceptance estimated with the same cutting criteria. In the analysis of single particle spectra in central collisions[64, 85], event-averaged occupancy correction functions of DC2 and

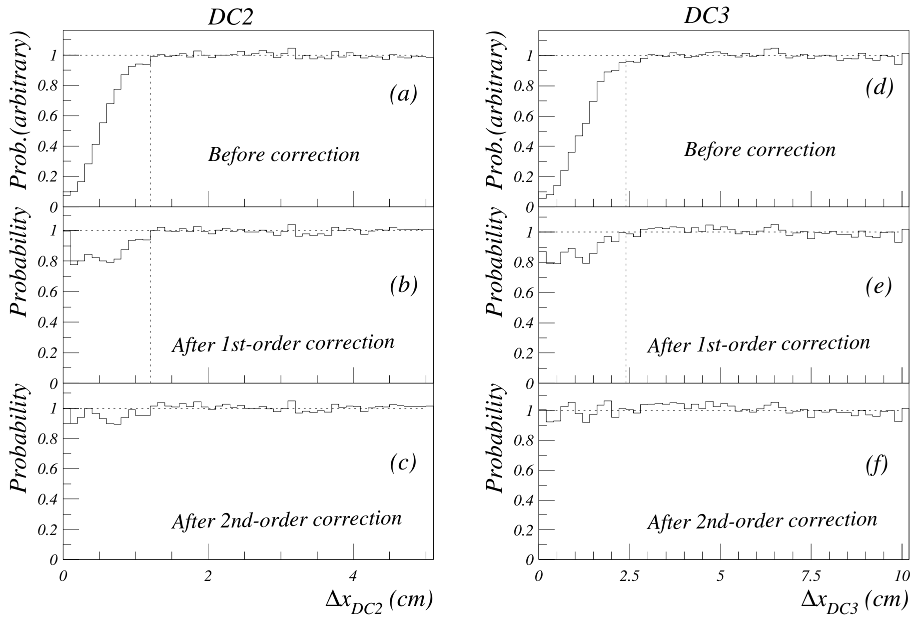

Figure 5.9: Recovering of the tracking inefficiency due to occupancy. (a) shows the surviving probability of a track as a function of track separation in DC2; (b) shows the probability function after the first-order efficiency recovery using Eq.(5.11); (c) shows the probability function after the second-order efficiency recovery. (d),(e) and (f) show the same procedure for DC3.

DC3 were extracted from the occupancy distributions of the two chambers. The first approach is simple but with a big sacrifice on the data statistics; the second approach is only valid for particular event sample and cannot be applied to flow analysis since the occupancy distributions of the detectors depend not only on the centrality but also on the reaction plane orientation and they both change from event to event.

A new occupancy correction method on an event-by-event basis was thus introduced in the flow analysis for the 1995 data set. Assuming that other effects are negligible, the tracking inefficiency due to occupancy is actually an intrinsic effect from the finite granularity of the detectors. Since every track is reconstructed using the elements measured by DC2 and DC3, we first take a look at the influence of occupancy on each detector independently. Fig. 5.8(a) and (d) show the distributions of the separation between elements formed in DC2 and DC3 respectively. One observes that tracking efficiency falls down when $\triangle x_{DC2}$ (or $\triangle x_{DC3}$) gets smaller than twice the cell size. Fig. 5.8(b) and (e) are similar separation distributions of elements in DC2 and DC3 respectively but with mixed event method. The mixed event method uses two different elements of a detector from two different events. In practice, it was done by fetching one element from the current event and the other element from the next event. The mixed event distribution reflects the response of the detector free from the influence of occupancy, i.e., the response when one and only particle impacts on the detector at a time. The surviving probability functions from occupancy are thus derived from the ratio between the event-by-event distributions and the mixed event ones, as shown in Fig. 5.8(c) and (f). These surviving probability functions are the intrinsic responses of the detectors and independent of any particular occupancy distribution.

Given the element surviving probabilities at DC2 and DC3, denoted by $P_2(\triangle x_{DC2})$ and $P_3(\triangle x_{DC3})$ respectively, the surviving probability $P_{trk}(\triangle x_{DC2}, \triangle x_{DC2})$ of a track constructed from the two elements in DC2 and DC3 is given as

$$P_{trk}(\triangle x_{DC2}, \triangle x_{DC3}) = P_2(\triangle x_{DC2}) \cdot P_3(\triangle x_{DC3}). \tag{5.10}$$

And consequently the probability for a track being lost is $1 - P_{trk}$. To account for the tracking inefficiency due to occupancy, a weight is assigned to each track according to its $\triangle x_{DC2}$ and $\triangle x_{DC3}$

$$w(\triangle x_{DC2}, \triangle x_{DC3}) = 1 + \frac{1 - P_{trk}}{P_{trk}} = 1 + \frac{1 - P_2 \cdot P_3}{P_2 \cdot P_3}. \tag{5.11}$$

This weighting assignment is performed by looping all the tracks of each event. This correction is based on the assumption that the particle distribution in reality can be approximated by the distribution of the reconstructed tracks. This assumption is valid in first-order since the tracking efficiency of the spectrometer is over 95%[66] for the centrality region of interest. Fig. 5.9 (a) and (d) display respectively the tracking efficiency functions in DC2 and DC3 before the occupancy correction. Fig. 5.9 (b) and (e) are the functions using the weight given by Eq.(5.11) as the first-order correction. Most of the efficiency has been recovered after this step. The residual effect is then recovered in an empirical way by using Fig. 5.9 (b) and (e) as the probability correction functions as it is done in the previous step. The completely corrected efficiency function after the two steps are drawn in (c) and (f). All distributions in Fig. 5.9 have been normalized to the mixed event distributions. Monte Carlo simulations indicate that ~10% of tracks are lost due to occupancy effect for Au+Au collisions.

The tracking inefficiency due to occupancy at TOFU has already been taken into account in the correction for the inefficiency at DC3. Since TOFU ($z \sim$ 12.3m) is located closely to DC3 ($z =$ 11.546m), the occupancy distributions of these two detectors are closely correlated. Tracks lost in DC3 will be lost in TOFU. The second order correction takes into account the additional effect due to TOFU itself.

5.4 y-position Matching

As described in Section 5.1, the track reconstruction algorithm only depends on the measurements in the x-z plane, and the y position information is optional depending on its availability. If available, the angle of a track in the y-z plane is reconstructed using the origin (after correcting for the beam angle and position) and the measurements from DC2 and DC3. Fig. 5.10 shows the y position matching at DC2, DC3 and TOFU. Δy_i ($i = dc2, dc3, tofu$) are given by

$$\Delta y_i = y_i^{(elem)} - y_i^{(fit)} \qquad i = dc2, dc3, tofu, \tag{5.12}$$

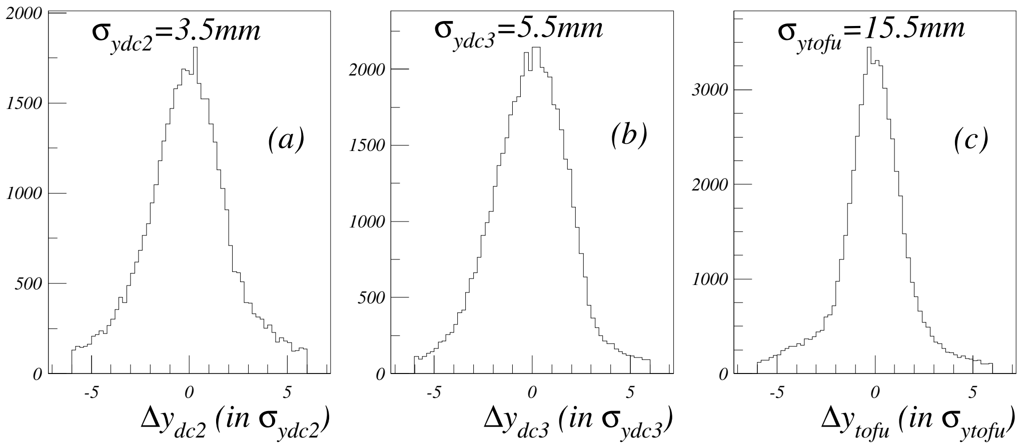

Figure 5.10: The y-position matching at (a) DC2, (b) DC3 and (c) TOFU, respectively. Each distribution is plotted in the unit of σ_y of each detector. The definition of Δy is given by Eq. 5.12.

where $y_i^{(elem)}$ and $y_i^{(fit)}$ are respectively the measured position of the element and the fitted value of the track at the detector i. The Δy distribution of each detector consists of two components: a narrow Gaussian (dominant) resulting from good tracks and a wide Gaussian due to background. The distributions are plotted in the unit of the width of the narrow Gaussian component.

Those tracks which have incomplete (at least one out of $y_{dc2}^{(elem)}$, $y_{dc3}^{(elem)}$ and $y_{tofu}^{(elem)}$ is missing) or bad y position information are one of the major sources of background in particle identification. In the analysis of protons, deuterons and $\pi^{\pm}$, we require that the y position given by TOFU and at least one of the two y position measurements given by DC2 and DC3 be available and within $\pm 3\sigma_y$ of the Δy distribution on the required detector; in the analysis of $K^{\pm}$ and $\bar{p}$, all three y position measurements are required to be within the range of $\pm 3\sigma_y$.

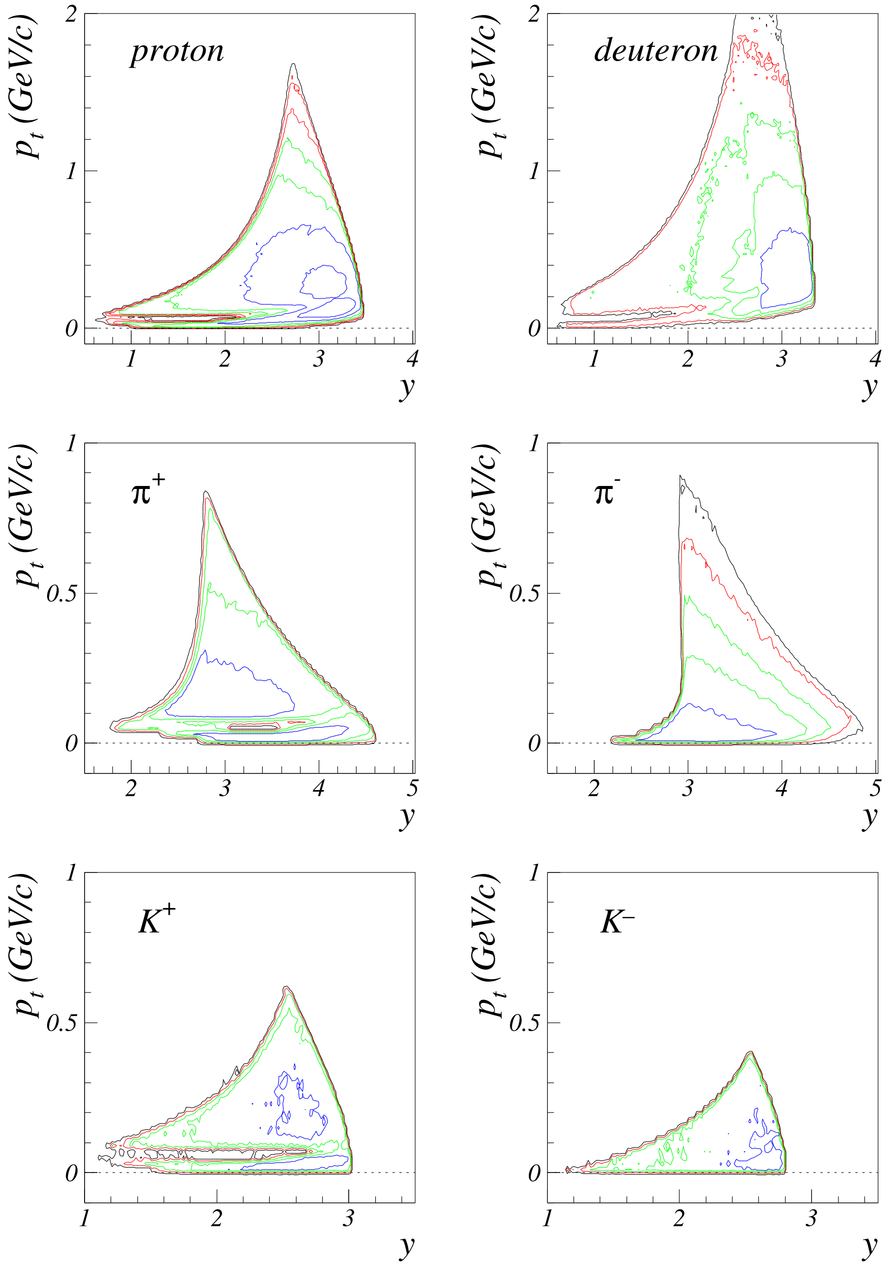

Figure 5.11: The acceptance in rapidity and transverse momentum for protons, deuterons, $\pi^{\pm}$ and $K^{\pm}$.

5.5 Acceptance

Fig. 5.11 shows the acceptance in the phase space of rapidity and transverse momentum for protons, deuterons, $\pi^{\pm}$ and $K^{\pm}$. The combination of the opening of the collimator, the magnetic field (polarity and strength) and the dimensions of the tracking detectors, determines the acceptance shape of each particle species. Most of the rapidity coverage for all the particles is in the projectile rapidity region. For each particle species, the clear cut at high p_t (left edge) is because of the efficiency of track reconstruction falling to zero at the edges of each tracking detector; the edges at high rapidity comes from the limit in particle momentum imposed on the analysis (see Table 5.2). Due to the high ionization of Au beam particles, the regions where the beam passes through were turned off in each tracking detector to avoid high voltage tripping. The deadened beam regions introduces efficiency holes in the acceptance near low p_t for positive charged particles (protons, deuterons, π^+ and K^+) in the 1995's magnetic field configuration. To avoid the difficulty in correcting for the lower efficiency at edges and the efficiency loss in beam regions as well as the inefficiency due to dead or inefficient regions in each detector, a software collimator and additional geometric cuts are used for each detector in the analysis.

Chapter 6

Flow Analysis Relative to the Reaction Plane

6.1 Introduction

The study of event anisotropy requires the definition of a preferential direction, with respect to which the preferred motion of some subset of emitted particles can be explored. Generally, what one chooses is the reaction plane. The reaction plane is spanned by the impact parameter vector and the beam axis. The first observation of directed flow in Au+Au collisions at the AGS by the E877 experiment [31] was based on a Fourier analysis of the event-by-event azimuthal distribution of the transverse energy E_T. A pronounced dipole moment, which vanishes for peripheral and central collisions and maximizes in semi-central collisions, clearly demonstrates the existence of directed flow in heavy nucleus-nucleus reactions at the AGS energies. In this pioneering analysis, the reaction plane is not explicitly determined.

The existence of directed flow provides the possibility of the reconstruction of the reaction plane event by event. One of the major features of the E877 setup is its two calorimeters with a nearly 4π coverage. The reaction plane is reconstructed and its resolution is studied using the measured transverse energy distribution. Identified particles measured by the forward magnetic spectrometer are then studied with respect to the reaction plane. In this chapter, we will give a full description of the methodology for flow analysis employed in this thesis. First, we will review briefly the various methods for the determination of the reaction plane and introduce the transverse energy method. Then we will illustrate the reaction plane flattening procedures which correct for beam, geometrical acceptance and detector biases. We will introduce the Fourier analysis method which serves as the core of the methodology used in the flow analysis of this thesis. Finally, we will discuss our estimation of the reaction plane resolution and the correction method for nonflow correlation effects.

6.2 The Reaction Plane

6.2.1 The sphericity method

Directed flow is correlated to the orientation of the impact parameter. The orientation of the impact parameter can be estimated event-by-event from the particles produced in the collision. These estimates are generally subject to large statistical fluctuations due to the finite multiplicity. The first method of determining the reaction plane was introduced in the early 1980s[90]. It is the so-called sphericity method. For each event the 3×3 sphericity tensor is defined as:

$$S_{ij} = \sum_{\nu} \omega_{\nu} p_i(\nu) p_j(\nu) \qquad i, j = x, y, z \tag{6.1}$$

with $p_i(\nu)$ being the components of the momentum vector of the individual particle ν and ω_{ν} being a weighting factor [1]. Usually ω_{ν} is chosen as $1/m_{\nu}$ (m_{ν}: mass of parti-

[1]The coordinated system for the discussion above could be arbitrary. In this thesis, unless redefined or stated otherwise, x,y and z are referred to the E877 coordinate system as defined in

cle) so that S_{ij} is proportional to the kinetic energy in the non-relativistic limit. The sum runs over all particles in the entire event. The sphericity matrix is symmetric by construction and is defined by six independent variables. Diagonalization of the matrix gives out three eigenvalues $\lambda_1 \leq \lambda_2 \leq \lambda_3$ which geometrically represent the three major axes of an ellipsoid, and three other angular variables which gives the orientation of the ellipsoid in space. The overall shape is constrained by momentum conservation and the absolute overall scaling quantity is determined by energy conservation. The angle between the eigenvector $\hat{e}_3$ (associated with the largest eigenvalue λ_3) and the beam axis is called the flow angle θ_f. The orientation of $\hat{e}_3$ is the so-called flow axis which corresponds to the preferred orientation of matter flow in space. The reaction plane is spanned by the flow axis and the beam axis. This analysis method has been successfully applied to the first experimental observation of the collective flow at Bevalac[24, 25]. The limitation of this method is that it requires an apparatus with a momentum measurement over 4π coverage and that details of the event shape, such as the rapidity dependence of azimuthal anisotropy, can not be revealed.

The flow angle θ_f is beam-energy dependent and is estimated as

$$\theta_f \approx \tan^{-1} \frac{\langle p_x \rangle_{y_{beam}}}{p_{beam}} \tag{6.2}$$

where the x-axis is the direction of the impact parameter vector. In collisions at ultra-relativistic energies, the flow axis merges with the beam axis. Assuming a typical value of $\langle p_x \rangle_{y_{beam}} \simeq 0.1$ GeV/c, one gets $\theta_f \simeq 2.5°$ at the AGS ($p_{beam} \simeq 11$ GeV/c) and $\theta_f \simeq 0.2°$ at SPS ($p_{beam} \simeq 160$ GeV/c). At these higher energies the longitudinal component of the flow becomes much stronger than the transverse one and these two components are well decoupled. Consequently the study of the collective flow in three dimensions is reduced to the study in the transverse directions. This leads to the sphericity being simplified to the 2-D transverse sphericity[91]. The 2×2

Chapter 2.

transverse tensor $S^{\perp}$ is defined by

$$S^{\perp}_{ij} = \sum_{\nu} \omega(\nu) u_i(\nu) u_j(\nu) \tag{6.3}$$

with $(u_1(\nu), u_2(\nu))$ being the unit vector parallel to the transverse momentum of the νth particle and $\omega(\nu)$ being the weight factor. The sum runs over all the particles detected in a given rapidity interval. $S^{\perp}_{ij}$ is fully determined by its two eigenvalues λ_1 and λ_2 (choosing $\lambda_1 \geq \lambda_2$) and the azimuthal angle ψ between the x-axis and the eigenvector associated with λ_1 with $-\pi/2 \leq \psi \leq \pi/2$. This method is sensitive to the elliptical component of the azimuthal distributions. The ellipticity of the event azimuthal distribution can be described by

$$\alpha = \frac{\lambda_1 - \lambda_2}{\lambda_1 + \lambda_2} \tag{6.4}$$

and the orientation of the major axis λ_1 in the transverse plane is estimated by [2]

$$2\psi = \tan^{-1} \frac{\sum_{\nu} \omega_{\nu} \sin 2\phi_{\nu}}{\sum_{\nu} \omega_{\nu} \cos 2\phi_{\nu}} \tag{6.5}$$

with the weighting factor ω_{ν} being chosen as the squared transverse momentum $p_t^2(\nu)$ or the transverse energy $E_T(\nu)$ of the particle depending on the characteristics of the experimental apparatus. An event plane spanned by the eigenvector of λ_1 and the beam axis can be used as the reference plane for the study of the flow distribution.

6.2.2 The directivity method

The most commonly used method to determine the reaction plane and quantify directed flow is the so-called $\vec{Q}$ vector or directivity method. The reaction plane is estimated by the event plane defined by the $\vec{Q}$ vector

$$\vec{Q} = \sum_{\nu} \omega_{\nu} \vec{u}(\nu) \tag{6.6}$$

[2]Here 2ψ has a range of 2π with the sign of x and y components being taken into account. This convention stays through the rest of this thesis unless stated otherwise.

and the beam direction. $\vec{u}(\nu)$ is a unit vector parallel to the transverse momentum of the particle and the sum runs over all the detected particles in the event. ω_ν is a weighting factor which may depend on the type of the particle, its rapidity and transverse momentum. The choice of ω_ν is to a large extent arbitrary. In the original work of Danielewicz and Odyniec[92], ω_ν was chosen to be equal to the transverse momentum $p_t(\nu)$ for $y > 0.3$, $-p_t(\nu)$ if $y < -0.3$ and 0 if $|y| < 0.3$. This method of determining the reaction plane is commonly referred to as the transverse momentum method. In contrast to the sphericity method which explores the single-particle aspect of the particle distribution associated with the reaction plane, the transverse method explores the two-particle correlation induced by the existence of the reaction plane, amplified by summation over many particles. The greatest advantage of this method is that it decouples the transverse motion (p_t) from the longitudinal one (rapidity y) and avoids possible effects due to nuclear transparency and corona effects from the longitudinal motion. The average transverse momentum (per nucleon) in the $\vec{Q}$ direction in different rapidity regions can be calculated as

$$\langle P_x(y)/A\rangle = \frac{1}{N(y)}\left[\sum_\nu(\frac{\vec{p}_\nu\cdot\hat{Q}}{A})\right], \tag{6.7}$$

where the x-axis stands for the direction of the unit vector $\hat{Q}$. When the projected average transverse momentum is plotted as a function of rapidity one obtains the so-called directed flow or S-curve plots. The transverse momentum method has been widely used in the flow analysis of intermediate energy as well as ultra-relativistic energy heavy-ion collisions.

The directivity method discussed above relies on particle identification and momentum measurement over a large acceptance. In many experiments at the AGS and SPS, one may have over a large acceptance only calorimetry or multiplicity information . Furthermore, one needs an analysis tool which is most sensitive to the specific harmonic of the flow distribution that one is interested in[96, 34]. In this case, the directivity defined by Eq. (6.6) needs to be generalized such that $\vec{u}_\nu$ can also be a unit vector giving the transverse direction of the hit or of the calorimeter cell and the weight is taken as a function of multiplicity or the transverse energy.

In general, an event plane can be determined for each harmonic of anisotropic flow. The general directivity vector $\vec{Q}_n$ is defined as

$$\vec{Q}_n = \begin{pmatrix} Q_n \cos n\psi_n \\ Q_n \sin n\psi_n \end{pmatrix} = \sum_\nu \omega_\nu \begin{pmatrix} \cos n\phi_\nu \\ \sin n\phi_\nu \end{pmatrix} \tag{6.8}$$

and the orientation of the event plane is estimated by

$$\psi_n = \frac{1}{n} \tan^{-1} \frac{\sum_\nu \omega_\nu \sin n\phi_\nu}{\sum_\nu \omega_\nu \cos n\phi_\nu} \tag{6.9}$$

The magnitude of the n-th harmonic is

$$v_n = \frac{|\vec{Q}_n|}{Q_0}. \tag{6.10}$$

The sums run over all ν particles and the range of ψ_n is $0 \leq \psi_n \leq 2\pi/n$. The n-th ambiguity of the orientation can be solved by the study of its correlations with the event planes determined from lower harmonics. The weight ω_ν should be optimized for the best event plane determination. It can be chosen to be some characteristic variables of the particle such as the transverse momentum, the transverse energy, etc. It can also be chosen to be related to the type of the particle. When $n = 1$ and ω_ν is chosen to be equal to $p_t(\nu)$, the general directivity method reduces to the case of the transverse momentum method; when $n = 2$, Eq. (6.8) and Eq. (6.9) become equivalent to Eq. (6.3) and Eq. (6.5) given by the transverse sphericity method. The reaction plane is directly related to directed flow. The event plane determined from higher harmonic could coincide with the reaction plane, but in general they are different.

6.2.3 The transverse energy method

The two calorimeters TCAL and PCAL (see Section 2.2 of Chapter 2) of the E877 experiment measure the energy distribution of produced particles in the collisions with a full 2π azimuthal coverage and a very large polar coverage ($-0.5 < \eta < 4.7$ or $1^\circ < \theta_{lab} < 117^\circ$). In our analysis, the pseudorapidity η coverage is divided into four windows (Table 6.1). [3] The region around mid-rapidity ($1.4 < \eta < 2.0$) is intentionally skipped as the dipole component is expected to cross zero in that region.

Table 6.1: Definitions of the four pseudorapidity windows of the E877 calorimeters

Window Index	1	2	3	4
Window Name	TCW1	PCW2	PCW3	PCW4
η range	[-0.5,0.7]	[0.8,1.4]	[2.0,2.7]	[2.7,4.5]
θ_{lab} range	[117°,53°]	[48°,28°]	[15°,8°]	[8°,1°]
θ_{CM} range	[166°,136°]	[131°,101°]	[67°,37°]	[37°,7°]

From the data, for each η window i, the azimuthal angle $\psi_n^{(i)}$ of the n-th moment of the transverse energy distributions is given by

$$\psi_n^{(i)} = \frac{1}{n}\tan^{-1}\frac{\sum_j (\pm) E_T^j \sin n\phi_j^{lab}}{\sum_j (\pm) E_T^j \cos n\phi_j^{lab}} = \frac{1}{n}\tan^{-1}\frac{\sum_j (\pm)(E_T^j)_x}{\sum_j (\pm)(E_T^j)_y} \qquad (6.11)$$

where E_T^j is the energy measured in the calorimetric cell-j and phi_j^{lab} is the azimuthal angle of the cell. The sums run over all the calorimetric cells within the η window-i of the detector with the sign being positive (negative) for cells at η forward (backward) of mid-pseudorapidity ($\simeq 1.6$ in our case).

For $n = 1$ this is the equivalent of the transverse momentum method except that p_t is replaced by E_T. This method is called the transverse energy method and was

[3] θ_{CM} represents the polar angle in the center-of-mass frame. The relationship between θ_{lab} and θ_{CM} is given in Appendix A.

first used by the E877 experiment to reconstruct the reaction plane for the study of energy and charged particle flow[32]. This analysis method is also adopted in this thesis for the reconstruction of the event plane for the case of directed flow ($n = 1$). A transverse energy directivity vector $\vec{E}_T^i$ in the case of $n = 1$ of the i-th η window is defined as

$$\vec{E}_T^{(i)} = (E_x^{(i)}, E_y^{(i)}) \tag{6.12}$$

$$E_x^{(i)} = \sum_j \pm E_T^j \cos(\phi_j^{lab}) \tag{6.13}$$

$$E_y^{(i)} = \sum_j \pm E_T^j \sin(\phi_j^{lab}) \tag{6.14}$$

$$\psi_1^{(i)} = \tan^{-1} \frac{E_x^{(i)}}{E_y^{(i)}} \tag{6.15}$$

In the estimation of the transverse directivity vector for each η window, the energies measured by the 832 TCAL cells were used for TCW1 and those measured in the 512 PCAL cells were used for PCW2, PCW3 and PCW4. For the geometrical arrangement of the cells of these two detectors, readers are referred to Chapter 2.

6.3 Flattening the Reaction Plane Distribution

For an ideal calorimeter with a full acceptance coverage, the distribution of the directivity $\vec{E}_T$ over many events is expected to be isotropic because of the randomness of the orientation of the collision geometry. Consequently a flat distribution of $dN/d\psi_1$ over the full azimuthal angular range is expected. However, biases due to detector effects such as the finite geometric acceptance of the detector, imperfection in gain calibrations and the change of the incident beam axis etc, could cause the distribution of the transverse energy to be azimuthally anisotropic in the laboratory and resulting in a nonflat $dN/d\psi_1$ distribution.

The non-flatness in the reaction plane distribution propagates and affects the

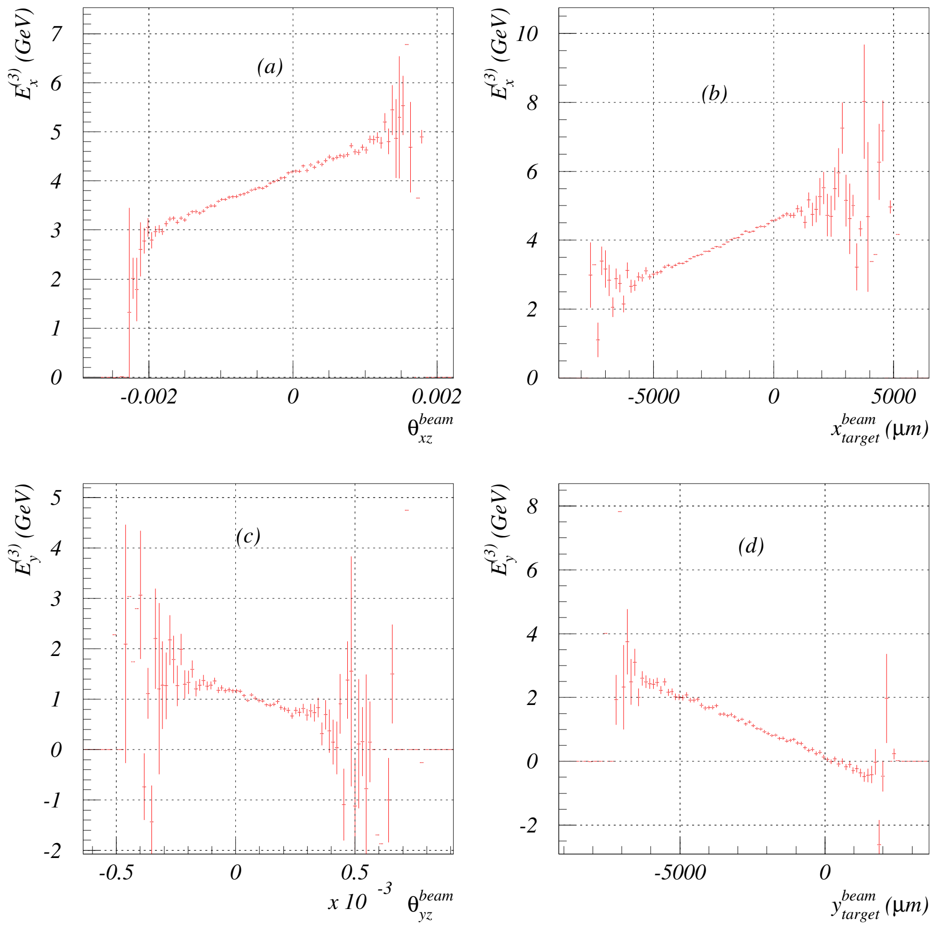

Figure 6.1: Correlations between the transverse energy directivity components and the incident beam angle and position. Correlation profiles of η window PCW3 show the dependence of the directivity components ($E_x^{(3)}$ and $E_y^{(3)}$) on the incident beam angle and position at the target.

measurement of the flow signal[94]. To study particle distributions with respect to the reaction plane in experiments, it is necessary to account for this effect. Several techniques, such as re-centering, weighting, method of mixed events and method of Fourier expansion, etc[93], have been developed for the flattening the $dN/d\psi_n$ distributions [32, 33, 34, 35]. The flattening method employed in the present analysis is a combination of re-centering, weighting and shifting with Fourier expansion technique. The correction on the reaction plane is done on an event-by-event basis.

- **Correction for the beam effect**

  The incident angle and momentum of the beam particle from AGS fluctuates within a certain range. Therefore the beam axis changes from event to event. This would affect the determination of the reaction plane even with a perfect symmetric calorimeter. One major feature of the E877 setup upgrade in 1995 is the implementation of a new two-dimensional beam vertex detector (see Chap. 3). This 2-D detector provides full spatial information of the incident beam particles. As an example, Fig. 6.1 are profiles, showing the correlations of the components of the directivity vector reconstructed from the measured transverse energy in PCW3, with the angle and the position (at the target) of the incident beam particle . $E_x^{(3)}$ and $E_y^{(3)}$ are the components of the directivity vector $\vec{E}_T^{(3)}$ directly calculated from the raw data. A nearly linear dependence of both components on the beam angle (θ_{xz}^{beam} and θ_{yz}^{beam}) and the beam position at the target (x_{target}^{beam} and y_{target}^{beam}) is observed. The correction for the beam effect on the directivity construction is done on an event-by-event basis using the profiles collected over the statistics of each run ($\sim$200k events) as the correction functions. The fact that the mean values of $E_x^{(3)}$ and $E_y^{(3)}$ significantly deviate from zero (see also Fig. 6.2(a)) is due to the biases from the calorimetric acceptance and gain. Corrections for this deviation will be discussed in the following two sections.

- **Geometry/gain symmetrization of PCAL E_T distribution**

  TCAL is designed to be symmetric around the beam axis and its performances are quite stable (see Chapter 2). Unlike TCAL, the four quadrants of PCAL are shifted asymmetrically in order to optimize the acceptance of the downstream forward spectrometer (see Fig 2.4). Also, the gain of the phototube of each segment is comparatively unstable. For this detector a first symmetrization procedure is applied that works as follows: each η window is divided equally into 16 azimuthal towers; the average E_T of each tower is first calculated over a whole run's statistics (~200k events) and its inverse is then used as a weighting factor for the E_T measured by each cell of each event. This process corrects mainly for the asymmetry in the geometry of each η window and also partly for the gain equalization (see Fig. 6.2(b)).

- **Re-centering E_T distribution**

  After the correction for the beam effect and the geometry/gain equalization, the distribution of ($E_x^{(i)}$, $E_y^{(i)}$) is re-centered to make the average of both components over all events to be zero by

  $$E'^{(i)}_{x,j} = E^{(i)}_{x,j} - \langle E^{(i)}_x \rangle, \qquad E'^{(i)}_{y,j} = E^{(i)}_{y,j} - \langle E^{(i)}_y \rangle \tag{6.16}$$

  with $\langle E^{(i)}_x \rangle$ ($\langle E^{(i)}_y \rangle$) being the average value over all events of a run and j being the event index. This correction correspond mainly to a gain equalization. However, more higher harmonics from the resulting ψ_1 distribution are partly removed by this procedure (see Fig. 6.2(c)).

- **Flattening with Fourier expansion**

  The correction for higher harmonics in the ψ_1 distribution is completed with the Fourier expansion technique[94, 32, 33]. The flattening of ψ_1 distribution is achieved by applying a correction $\Delta\psi_1$ on ψ_1, where $\Delta\psi_1$ is determined by requiring a vanishing n-th Fourier moment of the new distribution. This gives

$$\psi_1' = \psi_1 + \Delta\psi_1 \tag{6.17}$$

where

$$\Delta\psi_1 = \sum_n \frac{2}{n}\left[-\langle\sin(n\psi_1)\rangle\cos(n\psi_1) + \langle\cos(n\psi_1)\rangle\sin(n\psi_1)\right]. \tag{6.18}$$

$\langle\sin(n\psi_1)\rangle$ and $\langle\cos(n\psi_1)\rangle$ are average values over all events. The correction is carried out event-by-event. In practice, a correction up to the fourth harmonic ($n = 4$) is used (see Fig. 6.2(e)).

Fig. 6.2 shows as an example the distributions of the transverse energy directivity vector $\vec{E}_T$ and the corresponding determined reaction plane angle ψ_1 after each step of the corrections for the pseudorapidity window PCW2 ($0.8 < \eta < 1.4$). The distributions shown in Fig. 6.2 are without centrality cuts, however, the actual analysis takes into account the centrality dependence of the directivity. In order to eliminate the nontrivial 2nd harmonics propagating from the residual in the gain equalization, an additional gain equalization (namely "reshaping") is applied (see Fig. 6.2(d)). And in order to achieve a clearer elimination of the higher harmonics, the second step Fourier expansion is applied iteratively. After this global correction, the residual nonflatness is small (less than 0.1% for the first harmonic). The residual nonflatness propagates into the analysis of the flow signal but the effect is negligible(see Chapter 4 of [94]). One effect of flattening the reaction plane is a reduction of the reaction plane resolution. The width of the angle shift due to flattening after symmetrization ranges from $10°$ to $20°$ depending on the η window and centrality. This would contribute a few percent increase to the width of the reaction plane angular resolution.

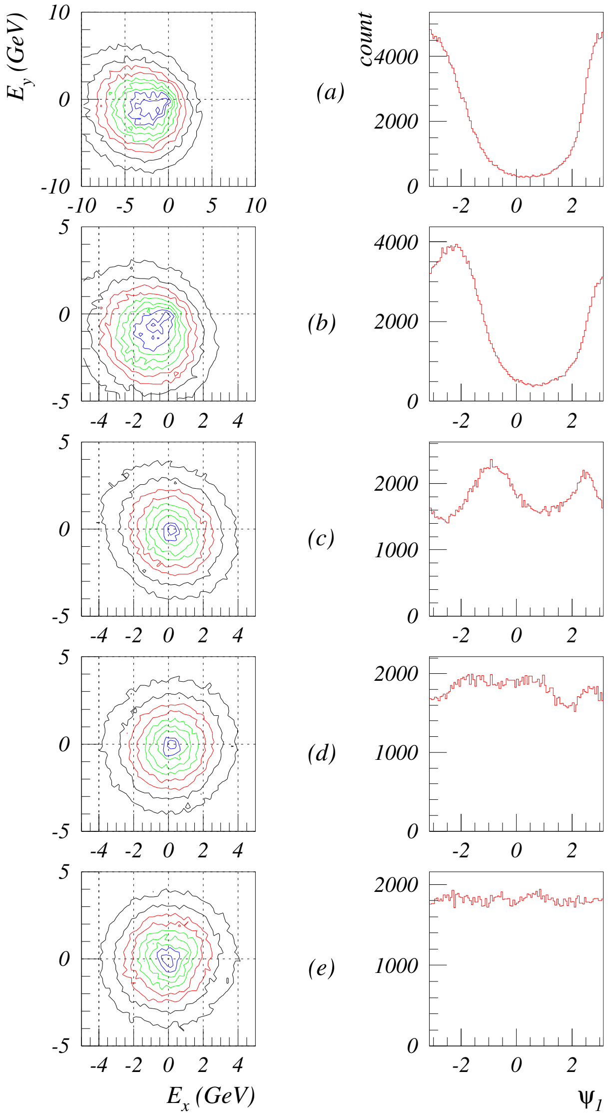

Figure 6.2: The distributions of the transverse energy directivity vector (left panel) and the determined reaction plane angle (right panel) after each step of correction. The distributions from uncorrected raw data(a), after beam effect correction and symmetrization(b), after re-centering(c), after reshaping(d) and after elimination of all harmonics up to 4-th order (e) are shown in this figure respectively. The η window here is PCW2 ($0.8 < \eta < 1.4$) and all distributions are without centrality cuts.

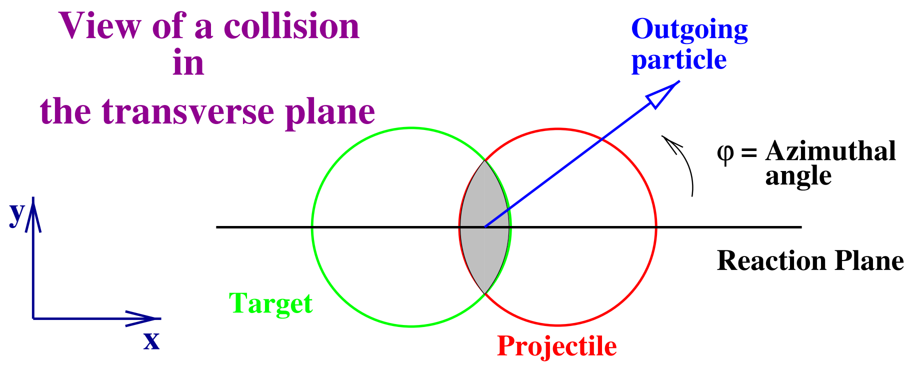

Figure 6.3: View of a collision in the transverse plane. The transverse plane is a plane which is perpendicular to the beam axis. $\varphi = \phi - \psi_R$ with ϕ and ψ_R being the azimuthal angle of the emitted particle and the reaction plane angle in the laboratory respectively.

6.4 Flow Analysis with Respect to the Reaction Plane

The appearance of transverse anisotropic flow is expected for a nonzero value of an impact parameter. A special coordinate system is defined for the convenience of flow analysis [4]: the beam axis is defined as z-axis and the transverse plane as x-y plane (see Fig. 6.3); the x-axis is defined in such way that it points in the direction of the transverse flow at forward rapidities. The reaction plane is defined by the impact parameter vector in the x-y plane together with the z-axis and the reaction plane angle ψ_R $(0 < \psi_R < 2\pi)$ is the angle between x-axis and the reaction plane.

In order to study the complex three-dimensional flow phenomena, it is suggested to slice longitudinal variables, e.g. rapidity (or pseudorapidity), into different ranges and perform analysis in each range[95]. Fourier coefficients have a clear physical meaning . In fact, Ollitrault[96] pointed out that the Fourier coefficients are the best

[4]To avoid possible confusion, we name this coordinate system the flow coordinate system. In other parts of this thesis, the default coordinate system refers to the E877 coordinate system in the laboratory defined in Chapter. 2.

observables to characterize azimuthal anisotropies because they can be reconstructed accurately.

In general, the dependence on the particle emission azimuthal angle measured with respect to the reaction plane can be described by a triple differential distribution in a form of Fourier series

$$E\frac{d^3N}{d^3p} = \frac{d^3N}{p_t dp_t dy d\phi} = \frac{1}{2\pi}\frac{d^2N}{p_t dp_t dy}\left(1 + \sum_{n=1}^{\infty} 2v_n \cos(n(\phi - \psi_R))\right), \tag{6.19}$$

where ψ_R represents the (true) reaction plane angle and the sine terms vanish due to the reflection symmetry with respect to the reaction plane. In experiments, however, the estimated reaction plane has a finite resolution due to detector resolution and the fluctuations from the finite particle multiplicity. The measured triple differential distributions with respect to the reaction plane angle determined in the i-th η window is described by

$$E\frac{d^3N}{d^3p} = \frac{d^3N}{p_t dp_t dy d\phi} = \frac{1}{2\pi}\frac{d^2N}{p_t dp_t dy}\left(1 + \sum_{n=1}^{\infty} 2v'_n \cos(n(\phi - \psi_r^{(i)}))\right), \tag{6.20}$$

where $\psi_r^{(i)}$ denotes the measured reaction plane angle in i-th η window and v'_n is the measured Fourier coefficient.

The true values of Fourier coefficients v_n are obtained from the measured coefficients v'_n by unfolding for the finite resolution with which ψ_R is measured, using:

$$v_n = \frac{v'_n}{|\langle\cos(n(\psi_r^{(i)} - \psi_R))\rangle|}. \tag{6.21}$$

The brackets indicating the event average evaluated for a given rapidity and centrality window. The measured Fourier coefficients are evaluated over events by

$$v'_n = \langle\cos(n(\phi - \psi_r^{(i)}))\rangle. \tag{6.22}$$

The great value of this method is that it allows for the direct comparison of the results for particles in a certain phase space region to theoretical predictions or to simulations without the necessity to un-filter the detector acceptance.

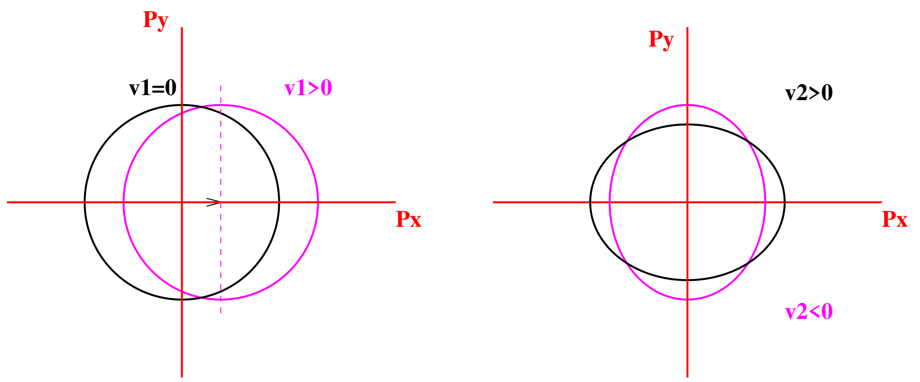

Figure 6.4: Physical meaning of the first two Fourier coefficients v_1 and v_2. v_1 indicates the shift in the reaction plane and v_2 the eccentricity of an ellipse-like distributions.

The Fourier coefficients corresponding to different harmonics have a clear physical meaning (see Fig. 6.4). The first moment coefficient v_1, which quantifies the so-called directed flow, is determined by $\langle p_x/p_t \rangle$ in a certain p_t and rapidity (y) window. A positive (negative) v_1 indicates that the shift of the particle distribution is in parallel (antiparallel) with the x-axis. The second moment coefficient v_2 represents the eccentricity (or ellipticity) of the particle distribution and is given by $\langle (p_x/p_t)^2 - (p_y/p_t)^2 \rangle$. A positive v_2 indicates the major axis of the ellipse-like distribution lies in the reaction plane and such phenomenon is called *in-plane* flow. A negative v_2 is for the case of the major axis perpendicular to the reaction plane and is commonly known as *squeeze-out*. Higher order coefficients also have their physical meaning[95] but have been rarely studied due to statistics and resolution limitation in the present experiments.

Special precautions must be paid for the possibility of autocorrelation arising from the improper practice in the experimental data analysis. The autocorrelation effects, which normally as an artifact enhances the flow signal, are generated when a particle being studied relative to the reaction plane is itself involved in the same event used for the estimation of the reaction plane. The autocorrelation effect can be avoided by

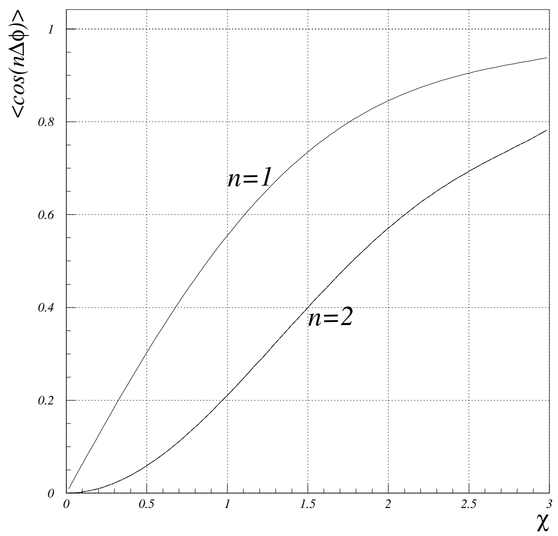

Figure 6.5: The reaction plane resolution for the n-th harmonic of the particle distribution as a function of χ.

excluding the particle of interest from the event in the reaction plane determination. Since the coverage of the calorimeters (PCAL and TCAL) used for the reaction plane determination does not overlap with the spectrometer coverage, the flow analysis of identified particles presented in the next chapter is free from effects related to such autocorrelations.

6.5 Reaction Plane Resolution and Nonflow Effects

6.5.1 The reaction plane resolution

In experiments, due to the finite multiplicity of the produced particles, the estimated transverse energy vector $\vec{Q}$ is different from the true reaction plane by an angle $\Delta\phi$.

Considering a large sample of events with the same magnitude of impact parameter (within the same centrality window), according to the central limit theorem, we get the two-dimensional distribution of $\vec{Q}$

$$\frac{d^3N}{QdQd\Delta\phi} = \frac{1}{\pi\sigma^2}\exp\left(-\frac{|\vec{Q}-\langle\vec{Q}\rangle|^2}{\sigma^2}\right) = \frac{1}{\pi\sigma^2}\exp\left(-\frac{Q^2+\bar{Q}^2-2Q\bar{Q}\cos(\Delta\phi)}{\sigma^2}\right) \tag{6.23}$$

with $\vec{Q} = Q(\hat{x}\cos(\Delta\phi)+\hat{y}\sin(\Delta\phi))$ and $\langle\vec{Q}\rangle = \bar{Q}\hat{x}$, where the flow coordinate system is chosen (i.e., the impact parameter direction is chosen as the x-axis) and the fluctuations are assumed to be isotropic. Integration of Eq. (6.23) over Q yields

$$\frac{dN}{\Delta\phi} = \frac{1}{\pi}\exp(-\chi^2)\left\{1+z\sqrt{\pi}\,[1+\mathrm{erf}(z)]\exp(z^2)\right\}, \tag{6.24}$$

where $z = \chi\cos(\Delta\phi)$, $\chi \equiv \bar{Q}/\sigma$ and $\mathrm{erf}(x)$ is the error function [5]. Integration of Eq. (6.23) over both $\Delta\phi$ and Q gives[96]

$$\langle\cos(n\Delta\phi)\rangle = \frac{\sqrt{\pi}}{2}\chi\exp\left(-\frac{\chi^2}{2}\right)\left[I_{\frac{n-1}{2}}\left(\frac{\chi^2}{2}\right)+I_{\frac{n+1}{2}}\left(\frac{\chi^2}{2}\right)\right] \tag{6.25}$$

where I_ν is the modified Bessel function of order ν.

Usually Q scales like the multiplicity N while σ scales like $\sqrt{N}$. Therefore χ scales like $\sqrt{N}$. Eq. (6.25) indicates that the accuracy of the reaction plane for any harmonic moment can be estimated as long as the universal parameter χ is known. The reaction plane resolutions for the first two harmonics of the particle distribution as a function of χ are plotted in Fig. 6.5.

The value of χ can be determined from the study of the correlations due to flow between independent subsets of particles from an event. Considering the event planes $\psi_r^{(I)}$ and $\psi_r^{(II)}$ estimated from two independent subevents (or η windows) [6] (I) and (II), and assuming no other correlations except the ones due to flow, one can write

[5] The error function erf$x$ is defined as $\mathrm{erf}(x) = \frac{2}{\sqrt{\pi}}\int_0^x e^{-t^2}dt$

[6] The measurement in an η-window is equivalent to a subevent.

the following simple relation

$$\langle\cos(n(\psi_r^{(I)} - \psi_r^{(II)}))\rangle = \langle\cos(n(\psi_r^{(I)} - \psi_R))\rangle\langle\cos(n(\psi_r^{(II)} - \psi_R))\rangle, \qquad (6.26)$$

where ψ_R is the true reaction plane angle.

The most commonly used method to estimate the reaction plane resolution, which was first suggested by Danielewicz and Odyniec[92], is to divide each event randomly into two subevents containing half of the particles each, and to construct $\vec{Q}$ vector for each subevent. Two vectors $\vec{Q}_I$ and $\vec{Q}_{II}$ are therefore obtained. The distributions of $\vec{Q}_I$ and $\vec{Q}_{II}$ are described by an equation similar to Eq. (6.23). $\bar{Q}_I = \bar{Q}_{II} = \bar{Q}/2$, $\sigma_I = \sigma_{II} = \sigma/\sqrt{2}$, and therefore $\chi_I = \chi_{II} = \chi/\sqrt{2}$ since the multiplicity of each subevent is only half of the total multiplicity of the whole event. In this case, an analytical form of Eq. (6.26) is developed by Ollitrault[96]

$$\langle\cos(\psi_r^{(I)} - \psi_r^{(II)})\rangle = \frac{\pi}{8}\chi^2 e^{-\chi^2/2}\left[I_0\left(\chi^2/4\right) + I_1\left(\chi^2/4\right)\right]. \qquad (6.27)$$

The value of χ can be determined by measuring $\langle\cos(\psi_r^{(I)} - \psi_r^{(II)})\rangle$. Alternatively, the value of χ can also be obtained by measuring the fraction of events for which $|\psi_r^{(I)} - \psi_r^{(II)}| > 90°$

$$\frac{N(|\psi_r^{(I)} - \psi_r^{(II)}| > 90°)}{N_{total}} = \frac{e^{-\chi_I^2}}{2} = \frac{e^{-\chi^2/2}}{2}. \qquad (6.28)$$

Generally, the above method cannot be applied to the case where the independent subevents (or η-windows) are not equal. In such case, at least three independent subevents are needed for the estimation of the reaction plane resolution obtained from each subevent. For the three independent η-windows i, j and k, the resolution in the η-window i can be derived from the correlations between the three windows as

$$\langle\cos(n(\psi_r^{(i)} - \psi_R))\rangle = \sqrt{\frac{\langle\cos(n(\psi_r^{(i)} - \psi_r^{(j)}))\rangle\langle\cos(n(\psi_r^{(i)} - \psi_r^{(k)}))\rangle}{\langle\cos(n(\psi_r^{(j)} - \psi_r^{(k)}))\rangle}} \qquad (6.29)$$

6.5.2 Nonflow correlations between subevents

Eq. (6.29) provides a direct way to estimate the reaction plane resolution from experimental data. Unfortunately, in reality, the subevents are usually not completely independent of each other because of the existence of correlations other than flow and these correlation effects may not be neglected under some circumstances.

One of such correlations is from the overall transverse-momentum conservation constraint. Let us consider the azimuthal distribution $dG/d\phi$ [7] in a general reaction with N particles in the final state. The transverse-momentum conservation gives the condition

$$\sum_{\nu} p_{\nu}^2 + \sum_{\mu \neq \nu} \vec{p}_{\nu} \cdot \vec{p}_{\mu} = 0 \tag{6.30}$$

where $\vec{p}_{\nu}$ denotes the transverse-momentum of the νth particle. Upon averaging over all events, we find

$$N \langle p_{\nu}^2 \rangle + N(N-1) \langle \vec{p}_{\nu} \cdot \vec{p}_{\mu} \rangle = 0, \tag{6.31}$$

which suggests

$$\langle \cos\phi \rangle \approx -\frac{1}{N-1}. \tag{6.32}$$

Eq. (6.32) indicates that the distribution of $dG/d\phi$ is asymmetric about $\phi = 90°$ (peaking at $\phi = 180°$) and the asymmetry becomes less pronounced as N increases. This anti-correlation behavior due to transverse-momentum conservation have been observed in the high-energy hadron-hadron collisions and have been used for estimating the number of missing neutrals in the final state of the reaction[97, 98].

This idea was applied by [99] to the case of the correlation between independent subevents. Considering subevents of two rapidity (or pseudorapidity) windows (a) and (b), two vectors $\vec{Q}^a$ and $\vec{Q}^b$ are constructed. If there are no correlations except

[7] G is a global observable (multiplicity, transverse energy,etc) and ϕ is the azimuthal angle between two particles.

flow, the following relation holds

$$\langle \vec{Q}^a \cdot \vec{Q}^b \rangle = \langle \vec{Q}^a \rangle \langle \vec{Q}^b \rangle = \langle Q^a_x \rangle \langle Q^b_x \rangle, \tag{6.33}$$

where Q^a_x (Q^b_x) is the x-component of $\vec{Q}^a$ ($\vec{Q}^b$) in the flow coordinate system. However, the transverse-momentum conservation modified Eq. (6.33) to[93]

$$\langle \vec{Q}^a \cdot \vec{Q}^b \rangle \simeq \langle Q^a_x \rangle \langle Q^b_x \rangle - \alpha \langle (\vec{Q}^a)^2 \rangle \langle (\vec{Q}^b)^2 \rangle. \tag{6.34}$$

where α is a correction coefficient. The correction term in Eq. (6.34) is of the order of Q^2/N, where N represents the multiplicity.

The Eq. (6.34) can be understood in a more general context. The correction term can include other nonflow correlation effects as well as the one due to transverse-momentum conservation constraint. Effects such as particle decays, two- and many-particle correlations, jet production, etc., induce correlations between subevents (or η-windows). In the case of calorimeters, the incident energetic hadron induces the production of a shower of particles which are generally shared by neighboring calorimetric cells. This kind of sharing creates correlation between calorimetric η-windows. The nonflow correlation contribution can be characterized by the parameter[100]

$$c \equiv \frac{\langle \vec{Q}^a \cdot \vec{Q}^b \rangle - \langle Q^a_x \rangle \langle Q^b_x \rangle}{\sqrt{\langle (\vec{Q}^a)^2 \rangle} \sqrt{\langle (\vec{Q}^b)^2 \rangle}}. \tag{6.35}$$

The influence of nonflow correlations is reflected by a change in the σ of the distribution Eq. (6.25) (in the case of multiplicity distribution)[93]

$$\langle Q_n^2 \rangle = \langle N \rangle + \bar{v}_n^2 \langle N^2 \rangle + 2c \langle N \rangle \tag{6.36}$$

where the three terms on the right side represent respectively the contributions to the broadening from finite multiplicity fluctuation, the non-vanishing flow and the nonflow correlations to the resolution of the event plane. The event flow distribution could be significantly biased when c is relatively large[101, 93].

6.5.3 Correction for the nonflow correlations

The study of the nonflow correlation effects in real data is rather complex. Some studies have been done with Monte Carlo simulations. In the case that the effect of momentum conservation dominates other nonflow ones, the bias in the reaction plane determination can be removed by the so-called recoil correction method[102]. Because of momentum conservation, the remaining particles in the event recoil away from the particle of interest (POI). As a result, an enhanced emission in the reaction plane could be observed. This spurious enhancement can be canceled in the first order by boosting the transverse momenta of the remaining particles by the boost velocity

$$\vec{v}_b = \frac{\vec{p}_{POI}}{m_{total} - m_{POI}} \tag{6.37}$$

where m_{totoal} is the total mass of the system, $\vec{p}_{POI}$ and m_{POI} are respectively the transverse momentum and mass of the POI. This technique has been used in the analysis of the light nucleus system at low energies[102, 103].

The recoil correction technique is not applicable to the present data analysis using calorimeters because of two reasons. First, particle momentum and identification information is not available in the transverse energy measured by PCAL and TCAL. Secondly, other nonflow effects such as shower sharing between windows are strong and cannot be separated from the one due to momentum conservation. Therefore, a semi-empirical approach is proposed for the correction of nonflow effects in data.

For simplicity, an alternative notation is introduced. We define

$$C_{ij} \equiv \langle \cos(\psi_r^{(i)} - \psi_r^{(j)}) \rangle. \tag{6.38}$$

Ideally, assuming that windows are independent except for flow, the correlation factorizes as Eq. (6.26) ($n = 1$ case) or

$$C_{ij} = \langle \cos(\psi_r^{(i)} - \psi_R) \rangle \langle \cos(\psi_r^{(j)} - \psi_R) \rangle. \tag{6.39}$$

In the case of four "independent η-windows" (Table 6.1), the following constraints must be satisfied

$$C_{12}C_{34} = C_{13}C_{24} = C_{14}C_{23}. \tag{6.40}$$

Eq. (6.40) is the presumption upon which Eq. (6.29) holds.

In practice, Eq. (6.39) is not valid anymore because of the existence of nonflow correlations between windows and generally Eq. (6.40) is also not satisfied. The deviation from the constraints can be measured by

$$\Delta \equiv (C_{12}C_{34} - C_{13}C_{24})^2 + (C_{12}C_{34} - C_{14}C_{23})^2 + (C_{13}C_{24} - C_{14}C_{23})^2. \tag{6.41}$$

$\Delta = 0$ is equivalent to the constraints given by Eq. (6.40).

In our approach, Eq. (6.39) now is replaced by

$$C_{ij} = \langle \cos(\psi_r^{(i)} - \psi_R) \rangle \langle \cos(\psi_r^{(j)} - \psi_R) \rangle + f_{ij}, \tag{6.42}$$

where f_{ij} represent the nonflow contributions. The constraint equation Eq. (6.40) still holds, but with C_{ij} replaced by $C_{ij} - f_{ij}$. Generally, f_{ij} originates from many sources. Here we only focus on the effect from showering ($f_{ij}^{(shower)}$) and that from momentum conservation ($f_{ij}^{(mom)}$), which are believed to be the two most significant factors:

$$f_{ij} \simeq f_{ij}^{(shower)} + f_{ij}^{(mom)}. \tag{6.43}$$

- **Showering effect $f_{ij}^{(shower)}$**

  High-energy hadrons create showers while passing through the calorimeters. Shower sharing is expected to occur between neighboring cells and thus between adjacent η-windows. Therefore, $f_{23}^{(shower)}$ and $f_{34}^{(shower)}$ are expected to be nonzero. Shower sharing between the two most forward η-windows (Window-3 and Window-4) could be strong since the dimensions of hadronic showers is comparable to the physical dimension of Window-4 at the calorimeter and the two windows share a significant portion of calorimetric cells. $f_{ij}^{(shower)}$ is expected to be a *positive* contribution since showering, if exists, would enhance the correlation. Also, $f_{ij}^{(shower)}$ is expected to be independent of the multiplicity in the first order since the value of $f_{ij}^{(shower)}$ is related to the ratios $M_{shower}^{(i)}/M^{(i)}$ of the η-windows, where $M^{(i)}$ and $M^{(i)_{shower}}$ are respectively the multiplicity and shower multiplicity of Window-i.

- **Momentum conservation effect** $f_{ij}^{(mom)}$
  Obviously, $f_{ij}^{(mom.)}$ depends on the size of the η-windows. This dependence is similar to the dependence on the particle multiplicity as indicated by Eq. (6.32). The increase in the acceptance of each window would result in a stronger correlation due to momentum conservation. However, $f_{ij}^{(mom)}$ doesn't depend on the multiplicity for a symmetric collision. This is because the value of $f_{ij}^{(mom)}$ is proportional to $\sqrt{x_i x_j}$, where x_i is the fraction of the total number of particles that go into Window-i[104]. The contribution of $f_{ij}^{(mom)}$ is expected to be *negative*.

A very important conclusion can be drawn from the above discussion: f_{ij} is independent of the total multiplicity or the centrality of the collision, at least as a first-order approximation. This means we can establish enough number of relations like Eq. (6.40) in different centrality intervals (E_T intervals) so as to determine f_{ij} from the values of C_{ij}. A more general method to calculate f_{ij} is to do a minimization fitting of the following error function

$$\Delta_{total} = \sum_{E_T bin} \Delta(E_T) \tag{6.44}$$

where $\Delta(E_T)$ is the error in a given centrality (E_T) bin, given by Eq. (6.41), with C_{ij} replaced by $C_{ij}^{(meas)} - f_{ij}$. Here $C_{ij}^{(meas)}$ is the measured value of the variable defined by Eq. (6.38).

Table 6.2: The 6 correction parameters for nonflow correlations between PCAL/TCAL η-windows

Parameter Name	f_{12}	f_{13}	f_{14}	f_{23}	f_{24}	f_{34}
Parameter value	-0.037	-0.118	-0.078	-0.093	-0.008	0.121
Parameter error	0.006	0.007	0.006	0.008	0.005	0.007

Table 6.2 shows the results of the six parameters f_{ij} derived from numerical minimization of the six-parameter polynomial Eq.(6.44). Fig. 6.6 presents the values of C_{ij} before and after being corrected for nonflow correlation effects. The magnitude of the correction is generally significant. Except for f_{34}, all other f_{ij} are *negative*, which suggests the dominant role of the momentum conservation constraint in the nonflow correlations between these η-windows. The big, *positive* f_{34} is consistent with the existence of a strong correlation from showering between Window-3 and Window-4.

The reaction plane resolution of each η-window can be calculated using Eq. (6.29) ($n = 1$) by combining this η-window with any two, out of the other three η-windows. This method allows three ways to determine the resolution functions for the same η-window. The consistency between the three calculations for the same η-window becomes an effective way of checking the effect of nonflow correlations and corresponding corrections. Fig. 6.7 shows the reaction plane resolution functions of the four η-windows calculated with the C_{ij} without nonflow correlation correction. For each η-window, significant discrepancies between the three options are observed. Fig. 6.8 shows the resolution functions with the same technique but using the value of C_{ij} that undergoes the nonflow correction. The discrepancies have been removed. The final reaction plane resolution functions for directed flow (v_1) of the four pseudorapidity windows are plotted in Fig. (6.9). The convention that the directed flow in the forward (pseudo)rapidity hemisphere ($\eta > 1.6$) is defined to be positive, has been

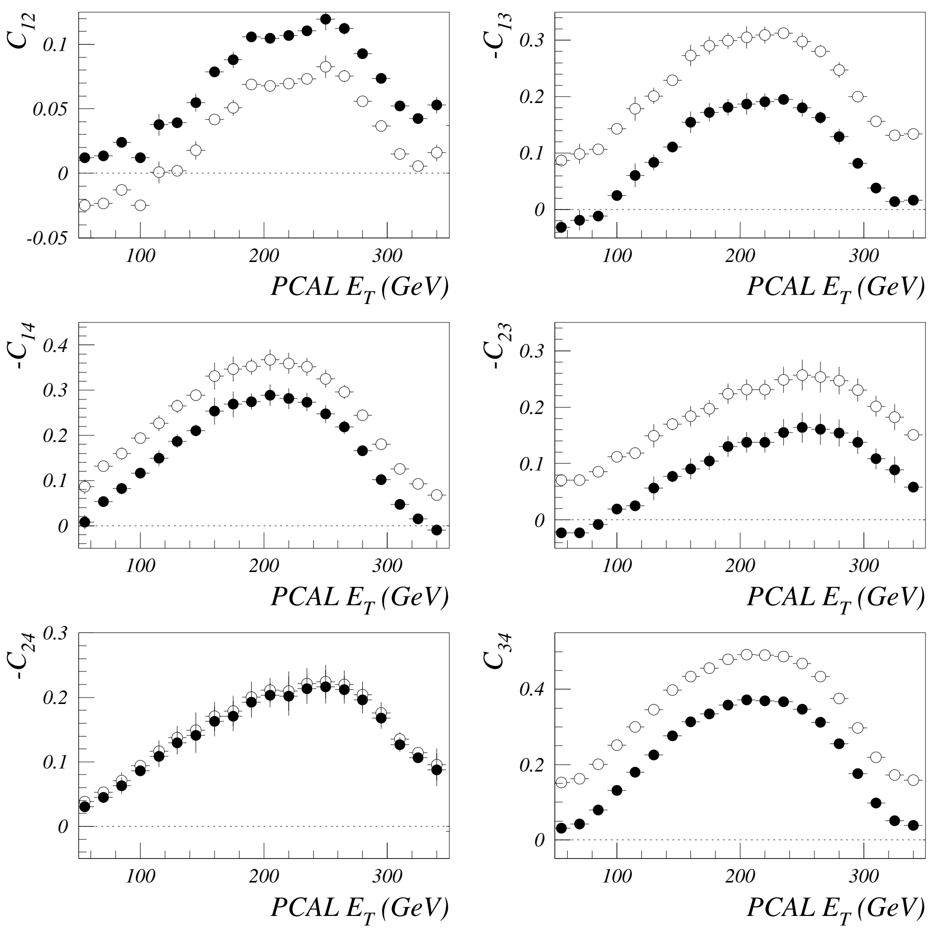

Figure 6.6: Comparison of C_{ij} before (empty circles) and after (filled circles) nonflow correlation correction. Note that the signs of C_{13}, C_{14}, C_{23} and C_{24} have been inverted since the reaction plane determined from Window-1 (or Window-2) is shifted from that determined from Window-3 (or Window-4) by π. Window-1 and Window-2 are located in the backward (pseudo)rapidity hemisphere (with respect to the projectile rapidity) while Window-3 and Window-4 are located in the forward (pseudo)rapidity hemisphere (see Table 6.1).

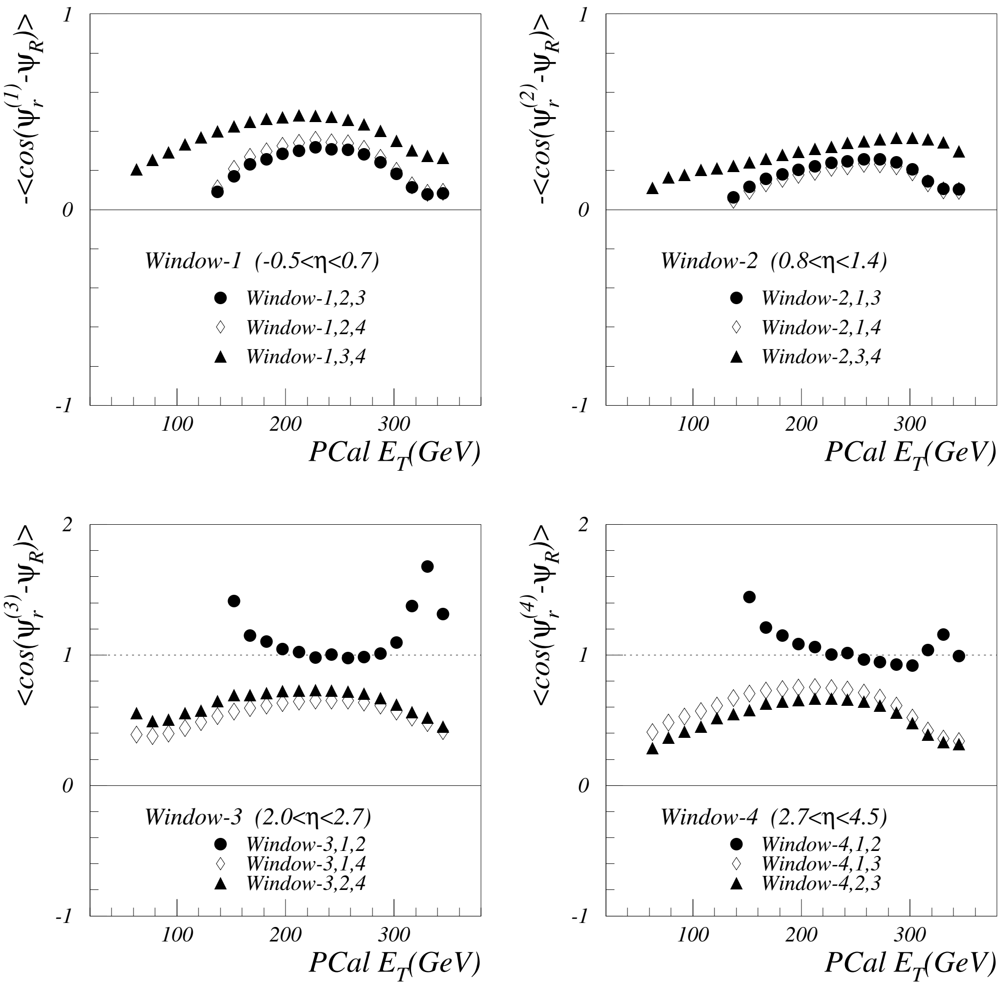

Figure 6.7: The calculated reaction plane resolution functions of the four η-windows without nonflow correlation correction. For each window the results are shown for the three possible combinations that can be used to determine the resolution function. The points at low PCAL E_T not shown in the figure are due to the negativeness of the values under square-root in Eq. (6.29). Those non-physical points larger than 1 (Window-3 and Window-4), are due to the presence of strong nonflow correlations.

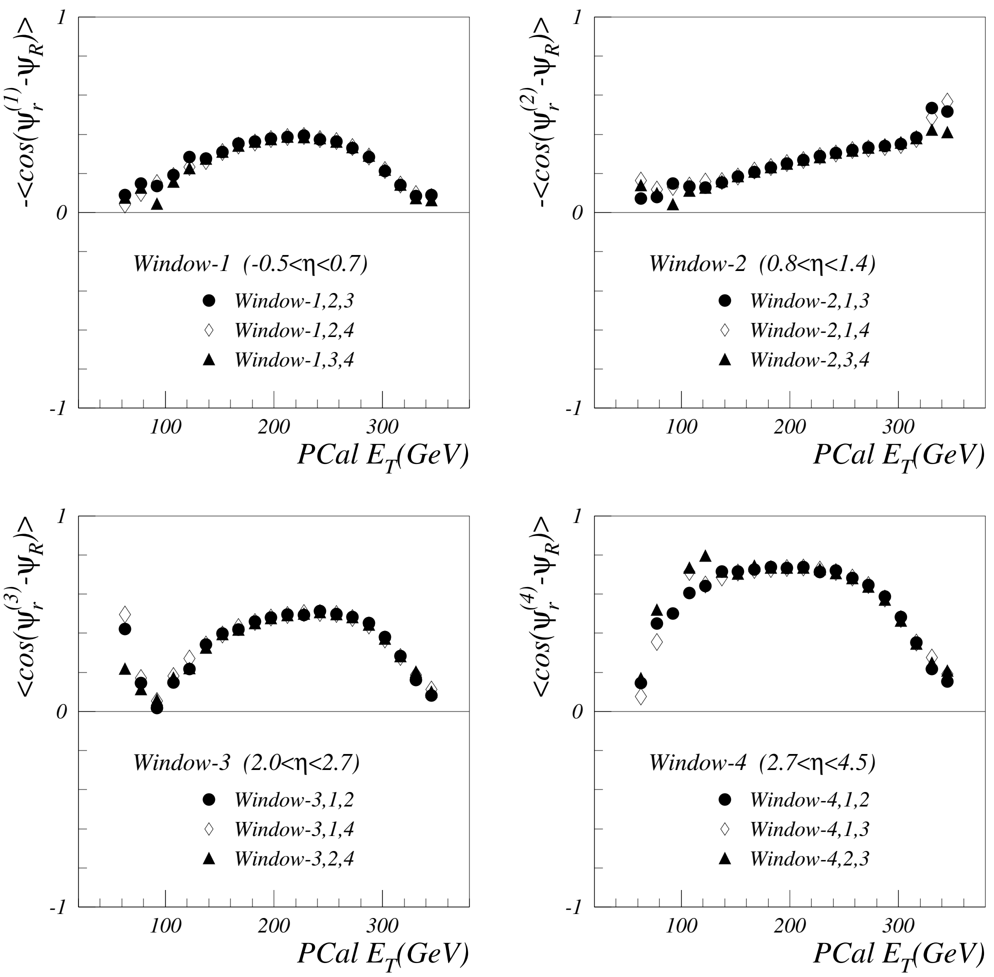

Figure 6.8: The calculated reaction plane resolution functions of the four windows after nonflow correction. The remaining discrepancies for points at very low and high PCAL E_T are due to statistical and systematic errors (see also Fig. (6.9).

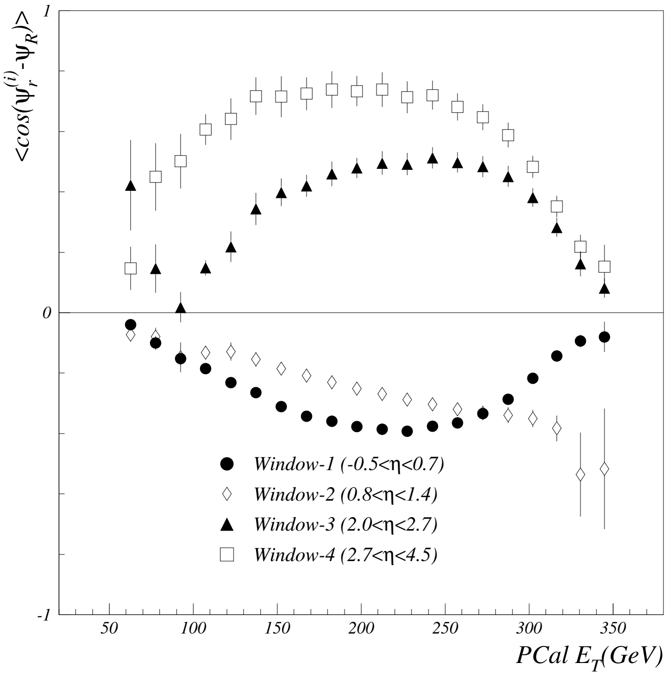

Figure 6.9: The reaction plane resolution functions of the four η windows. Positive values for Window-3 and -4 and negative ones for Window-1 and -2 are due to the convention adopted in the present analysis (see the text).

adopted in the present analysis. Therefore, the reaction plane resolutions determined by Window-3 and -4 are defined to be positive and those determined by Window-1 and -2 (in the backward (pseudo)rapidity hemisphere) become negative. Errors in the plot include the systematic one and the statistical one. The systematic error is based on the estimation of $\langle \sin(\psi_r^{(i)} - \psi_r^{(j)}) \rangle$.

6.5.4 Combining two η-windows

Since the reaction plane resolution of each window has been understood, one might consider to combine these results in order to achieve a better estimation of the reaction

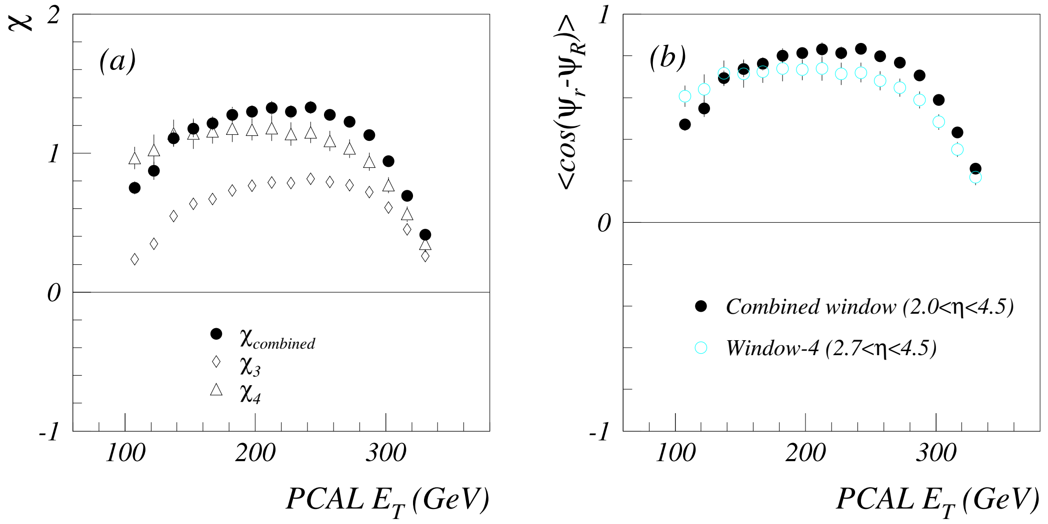

Figure 6.10: Reaction plane resolution correction function for v_1 of the combined η-window. (a) shows the χ values calculated by Eq. (6.25) from Fig. 6.9 for the combined η-window, Window-3 and Window-4. (b) shows the deduced resolution for v_1 of the combined η-window as a function of centrality. As a comparison, the resolution of Window-4 from Fig. 6.9 is replotted.

plane. PCAL can absorb nearly all the energy of an incident particle. In contrast, TCAL only absorbs part of incident particle energy due to its limited absorption length. The different responses of the two calorimeters makes the combination of them as a whole unit rather complicated. Also, from our operation experience of PCAL, Window-2 is comparatively unstable. Therefore, in this section, we will discuss only how to estimate the reaction plane resolution of the combination of the results for Window-3 and Window-4.

For estimating the reaction plane resolution of the combined η-window, so-called "weighted angles" method based on the maximum likelihood technique has been suggested in reference [105]. Here we propose a much simpler strategy which is based on the techniques that we have developed in previous sections of this chapter. First, we use Eq. (6.25) or Fig. 6.5 to find out the value of the corresponding χ for each known $\langle\cos(\psi_r^{(i)} - \psi_R)\rangle$ of each Window-i ($i = 3, 4$); then we construct the χ values for the combined η-window; and finally, we use Eq. (6.25) or Fig. 6.5 again to obtain the resolutions of the combined η-window.

Let's construct the value of χ for the combined window as

$$\chi_{combined} = \frac{\chi_3 + \chi_4\sqrt{\lambda}}{\sqrt{1+\lambda}} \tag{6.45}$$

where χ_i ($i = 3, 4$) is the value of Window-i and λ is the weighting factor. Since χ is the ratio of the average flow by fluctuations: $\chi = \bar{Q}/\sigma$ where

$$\bar{Q} = \langle \sum E_T \cos(\phi - \psi_R) \rangle$$

is the averaged flow and

$$\sigma = \sqrt{\sum(\langle E_T^2 \rangle - \langle E_T \rangle^2)}$$

the magnitude of finite multiplicity fluctuations. Both $\bar{Q}$ and σ^2 are proportional to the average transverse energy deposited in the η-window. We can therefore deduce that λ can be chosen as the ratio of the multiplicities in the two η-windows ($\lambda = \langle M_4 \rangle / \langle M_3 \rangle$) or $\lambda = \langle E_T \rangle_4 / \langle E_T \rangle_3$.

For simplicity, assuming that the particle distribution in the center-of-mass frame is isotropic, the value of λ can be estimated to be the ratio of the solid angles of Window-3 and Window-4.

$$\lambda \approx \frac{(SolidAngle)_{Window-4}}{(SolidAngle)_{Window-3}} = \frac{2\pi(\cos 7^\circ - \cos 37^\circ)}{2\pi(\cos 37^\circ - \cos 67^\circ)} \approx 0.5$$

where the angular values for cosine are taken from Table. 6.1.

Fig. 6.10 shows the deduced reaction plane resolution function of the combined window for the directed flow analysis. The resolution has been slightly improved

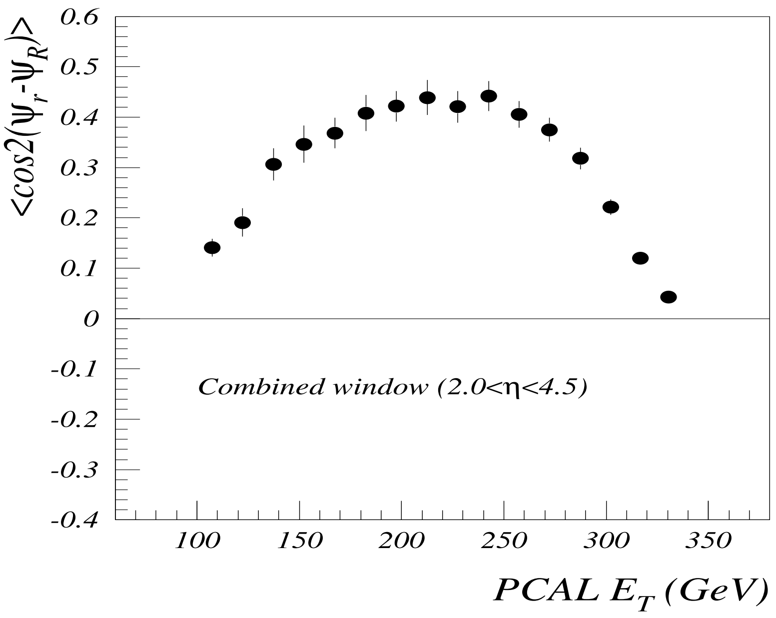

Figure 6.11: Reaction plane resolution correction function for v_2 of the combined window.

compared to that of any single window. The worse values at PCAL E_T <150 GeV is due to our approximation of using a centrality-independent weight. In peripheral collisions, the E_T distribution deviates from a symmetric one and the weighting factor λ should be different from that for central events. The E_T distribution measured by the combined window is used to determine the reaction plane for the flow analysis presented in Chapter 7 and the values given by Fig. 6.10 will be used as the correction function for directed flow results (v_1).

A similar approach can be used to evaluate the correction factor for the second component. Fig. 6.11 shows the resolution for the elliptic flow analysis deduced by Eq. (6.25) with the χ values obtained above. Data points with PCAL $E_T < 100$GeV have not been conducted in the analysis because of their large errors.

Chapter 7

Directed Flow of Identified Particles

In this chapter, we will study the azimuthal anisotropy of particle production relative to the reaction plane, as a function of particle rapidity, particle transverse momentum and collision centrality. We will use the Fourier decomposition technique discussed in Section 6.4 of Chapter 6 as the basic analysis tool. The Fourier coefficients, which represent different components of the azimuthal anisotropy, are to a large extent independent of the complications from the experimental systematics such as the uncertainties in spectrometer efficiency and acceptance. More importantly, in this way, we can easily unfold the effect of the finite resolution of the reaction plane from the coefficients. This analysis strategy simplifies the problems in data analysis and provides a direct and convenient way of comparing experimental data to model calculations. Also, since there is no overlap between the geometric coverages of the calorimeters and the spectrometer, the results are automatically free from complications due to auto-correlations.

The contents of this chapter are arranged as follows. We will first present the results for protons and deuterons. Due to the strong flow signals carried by these two particle species, they are ideal to be used to understand the flow systematics. We will use a simple transverse moving thermal source model combined with the transverse expansion thermal model to decouple radial and directed flow. We will use this method to try to understand the influence of coalescence and fragmentation in the deuteron flow. Then we will present the results for charged pions which are the typical thermalized particle species. We will present results for charged kaon flow, which largely reflects the non-equilibrium aspect of the collision system. Finally, we will present the first observation of the strong "antiflow " of antiprotons. A detailed comparison of the experimental results with the predictions from the theoretical RQMD models will be given [1]. Discussions will be focused on the results of the first Fourier coefficient (directed flow). Results of the second Fourier coefficient (elliptic flow) will be discussed briefly whenever applicable. Part of a study on elliptic flow can be found in Ref. [106].

7.1 Directed Flow of Protons and Deuterons

7.1.1 Directed flow of protons

Protons are one of the most copious particle species produced in heavy-ion collisions at the AGS; protons are stable and less affected by effects such as absorption; also, protons carry large flow signal and suffer less from thermal disturbance because of their relatively heavy mass. Therefore, directed flow of protons is a clean probe and is the best candidate for the study of the basic hydrodynamic aspect of flow in heavy ion collisions.

Fig. 7.1 shows the transverse momentum dependence of the first moment ($v_1(p_t)$)

[1]See Section 7.1.3 in this chapter for a brief description of the RQMD model.

of the proton azimuthal distributions with respect to the reaction plane for different particle rapidities (ranging from $y = 2.0$ to $y = 3.4$) and centralities of the collision. The results are presented for four centrality regions in accordance with PCAL E_T: $150 < E_T < 200GeV$, $200 < E_T < 230GeV$, $230 < E_T < 270GeV$ and $E_T > 270GeV$, corresponding to the values of $\sigma_{top}/\sigma_{geo}$ ≈23-13%, 13-9%, 9-4% and < 4% (see Section 4.2.2 in Chapter 4) respectively. These results are corrected for the reaction plane resolution. The missing data near $p_t = 0$ is due to the lack of acceptance of the spectrometer in the 1995 configuration. The results are consistent with those obtained from 1993's and 1994's data[71, 94] except for a less than 10% systematic difference due to the reevaluation of the reaction plane resolution (see Chapter 6).

The errors on data shown in Fig. 7.1 are statistical only. The systematic errors come mainly from the uncertainty in the reaction plane resolution (less than 10% for v_1, see Section 6.5 in Chapter 6) and the uncertainty in the occupancy correction. The uncertainty in the occupancy correction for two close-tracks is less than 10% for v_1 (see Section 5.3 in Chapter 5). The occupancy correction due to fragments from the collision is difficult to estimate. However, since these fragments move along the beam they only affect the $p_t \approx 0$ region near beam rapidity.

One observes that the emission of protons is strongly correlated with the orientation of the reaction plane. This correlation is observed to diminish at mid-rapidities and to be most significant at higher rapidities. v_1 grows with increasing p_t and tends to saturate at highest p_t. The nearly linear dependence of v_1 on p_t suggests to us a simple picture of a thermalized source moving in the transverse direction (or sideward moving thermal source) as is described below.

Considering the motion in the transverse plane of a source thermalized with a temperature T, localized at a rapidity y^* and moving with a transverse velocity β_x

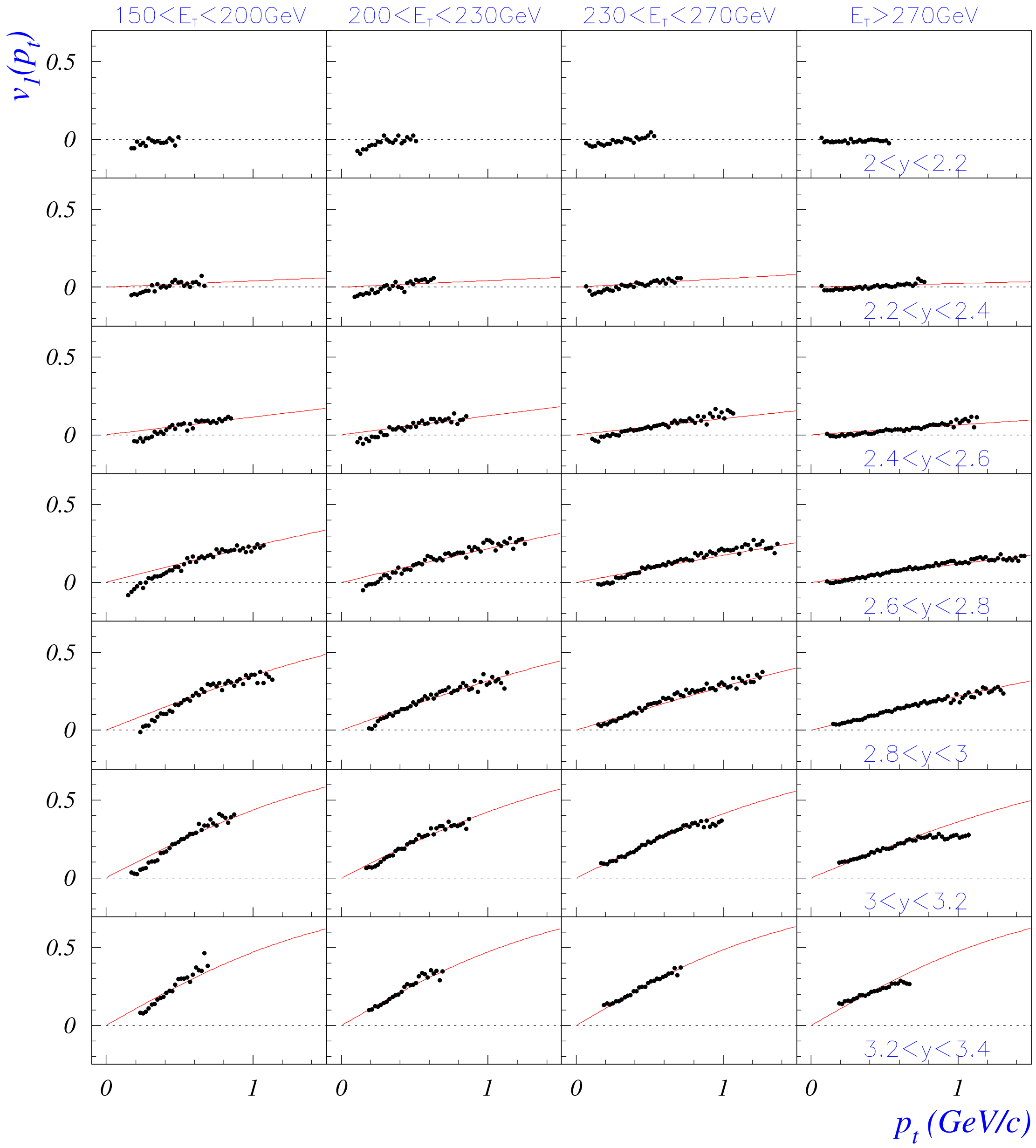

Figure 7.1: The dependence of $v_1(p_t)$ for protons. $v_1(p_t)$ is plotted for different particle rapidities and collision centralities. Each row represents a rapidity range (*e.g.*, $2 < y < 2.2$) while each column represents a centrality region (*e.g.*, $150 < E_T < 200GeV$). The values of $v_1(p_t)$ are corrected for the reaction plane resolution. The curves are the results of the fits using the function given by Eq. (7.5). The size for each p_t bin is 20 MeV/c.

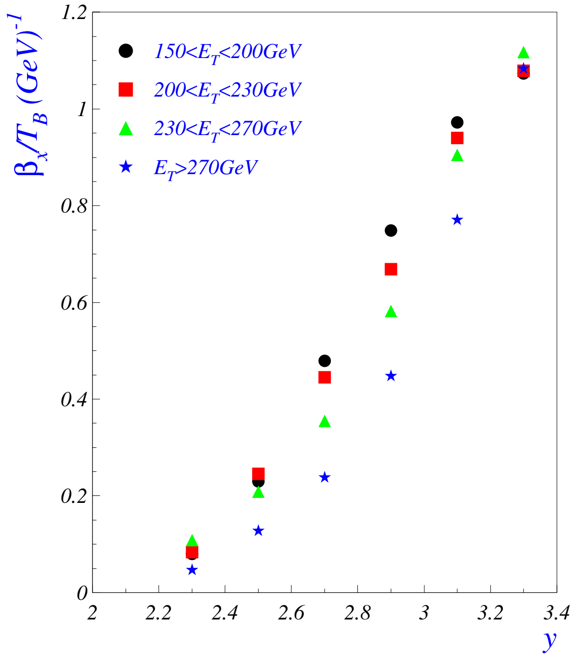

Figure 7.2: Fitted values of the β_x/T_B ratio of a proton moving thermal source. Values are extracted from the fits shown in Fig. 7.1.

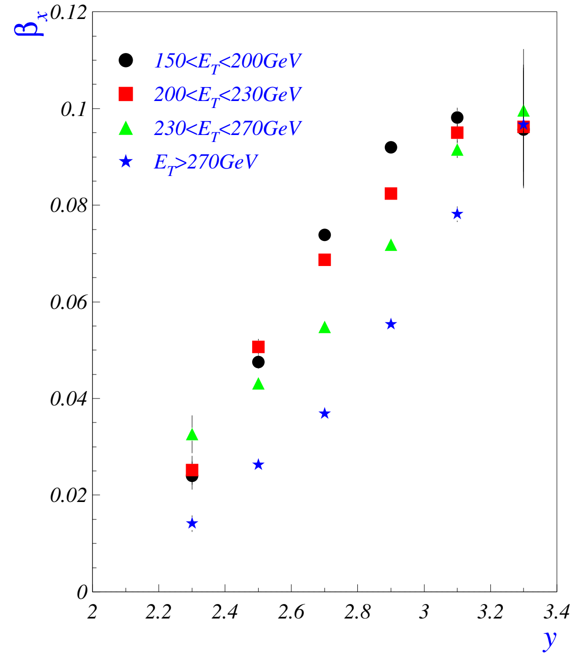

Figure 7.3: Estimated transverse velocity β_x of a proton moving thermal source. Values are evaluated from the fitted results shown in Fig. 7.2 with the parameters T_B taken from Ref. [64].

(along the x direction), the emission of particles from such a source is described by

$$\frac{1}{m_t}\frac{dN}{dm_t dy d\phi} \propto E^* \exp(-\frac{E^*}{T}), \tag{7.1}$$

where E^* is the particle's energy in the rest frame of the source. E^* is given by

$$E^* = \gamma\tilde{E} - \beta_x\gamma_x p_t \cos(\phi)$$

with $\tilde{E} = m_t \cosh(y - y^*)$ which is the energy evaluated in the frame moving longitudinally along with the source. The value of v_1 due to the moving source is given by[33]

$$v_1 = \frac{I_1(\xi) - [\xi I_0(\xi) - I_1(\xi)]T/\tilde{E}}{I_0(\xi) - \xi I_1(\xi)T/\tilde{E}} \tag{7.2}$$

where $\xi = p_t\beta_x\gamma_x/T$, $\gamma_x = 1/\sqrt{1-\beta_x^2}$, $I_0(\xi)$ and $I_1(\xi)$ are the modified Bessel functions. For heavy particles such as protons and deuterons, since $m_t \gg T$, β_x is expected to be small and v_1 does not depend on the generally unknown value of y^*, Eq. (7.2) is approximated for relatively small p_t to a quasi-linear function of p_t:

$$v_1(p_t) \approx \frac{I_1(\xi)}{I_0(\xi)} \approx \frac{\beta_x}{2T}p_t. \tag{7.3}$$

The slope of the p_t dependence of v_1 depends on two parameters: the sideward velocity β_x and the temperature of the moving thermal source.

The production of particles in heavy-ion collisions at the AGS and SPS is observed to be different from that expected from a pure thermal model[41]: the thermal source also expands radially in the transverse plane. This transverse expansion (radial flow), which is most violent at mid-rapidity and vanishes at beam rapidity, pushes particles towards higher p_t, resulting in an "effective temperature" T_B (or inverse slope parameter) extracted from the measured p_t spectra larger than the thermal temperature T. T_B is determined by the thermal energy as well as the collective energy of the particle. Also, as a consequence of the radial flow, the observed value of v_1 which is given by

$\langle p_x \rangle / \langle p_t \rangle$ would be smaller for a thermal source having both a radial expansion and a sideward movement, than that for a thermal source having only the sideward motion.

Base on the sideward moving thermal source model, Voloshin[107] added a radial expansion component (velocity β_t) to this model and studied the interplay between the radial flow and directed flow. In the non-relativistic limit, v_1 is expressed as a function of β_x, β_t and T as[107]

$$v_1(p_t) = \frac{p_t \beta_x}{2T} \left(1 - \frac{m\beta_t}{p_t} \frac{I_1(\xi')}{I_0(\xi')} \right). \tag{7.4}$$

where $\xi' = \beta_t p_t / T$ and m is the mass of the particle. v_1 generally reflects the interplay between sideward motion and radial expansion. One prediction of this model is that v_1 could become negative at very low p_t for strong radial expansion.

The thermal source model with a sideward motion and radial expansion (for simplicity, we call this model the *modified sideward moving thermal source model* from now on) in the transverse plane provides us a way to decouple the effects of directed flow from those of radial flow. However, the values of β_x, β_t and T obtained from data using Eq. (7.4) have large uncertainties due to the strong coupling between the three parameters.

Eq.(7.4) can be approximated for relatively small p_t and β_t by:

$$v_1(p_t) \approx \frac{p_t \beta_x}{2T} \left(1 - \frac{\tilde{E}_t}{T} \right) \approx \frac{p_t \beta_x}{2(T + \tilde{E}_t)} \equiv \frac{\beta_x}{2T_B} p_t \approx \frac{I_1(\xi_B)}{I_0(\xi_B)} \tag{7.5}$$

where $\tilde{E}_t = m\beta_t^2/2$ is the transverse expansion kinetic energy, $\xi_B = p_t \beta_x / T_B$ and $T_B = T + \tilde{E}_t$ is the "effective temperature" or the inverse slope parameter of the particle p_t spectra. It should be pointed out that the approximation given by Eq. (7.5) breaks down at very low p_t [2] and for relatively large $\tilde{E}_t$ (compared to T). It is interesting to notice that, even the magnitude of v_1 is reduced because of the increase of the

[2] The particle production spectra at very low p_t exhibits a shoulder arm shape and can not be approximated by a Boltzmann-like shape with T_B.

"effective temperature" T_B due to radial expansion, the quasi-linear p_t dependence of v_1 is retained. Eq. (7.5) provides us a simple and direct way to extract the sideward motion parameter (β_x) from the p_t behavior of v_1. On the other hand, with the prior knowledge (or assumption) of β_x, we can extract the "effective temperature" from the same measurement. This point will be discussed in the study of the directed flow of deuterons.

The full lines in Fig. 7.1 are the fits using the function given by Eq. (7.5). Fig. 7.2 shows the results of the fitted β_x/T_B for different centralities as a function of rapidity. β_x/T_B is small close to mid-rapidity, then rises almost linearly with increasing rapidity. The centrality dependence of β_x/T_B is most significant in the rapidity range $y = 2.6 \sim 3.0$.

Fig. 7.3 shows the extracted values of β_x of the proton moving source from Fig. 7.2 for different collision centralities as a function of rapidity. The inverse slope parameters T_B from Table A.4 of Ref.[64] are used in evaluating the values of β_x from the measured β_x/T_B ratio shown in Fig. 7.2. In the fitting, the same value of T_B is applied to all the four centrality regions for each rapidity bin since the centrality dependence of T_B for protons is negligible over the centrality range of interest[64]. One observes that, β_x is small close to mid-rapidity, then rises almost linearly with increasing rapidity and reaches its maximum value around beam rapidity. The value of β_x also becomes smaller for increasing collision centrality. The maximum source transverse velocity is about 10% of the speed of light.

With the help of this simple modified sideward moving thermal source model, we can better understand the systematic behavior of v_1 for protons. The slope of the p_t dependence of v_1 actually reflects the competition between the sideward motion (β_x) and the transverse expansion (β_t) of the source. For the Au+Au central collision at the AGS, the transverse expansion velocity β_t reaches its maximum value (~50% of the speed of light) at mid-rapidity ($y \sim 1.6$) and vanishes at beam rapidity ($y \sim$

3.2)[41]. The general feature of Fig. 7.1 can be understood as follows: close to mid-rapidity, the slope of $v_1(p_t)$ tends to vanish because of the smallness of β_x and the strong suppression from the dominant transverse expansion; away from mid-rapidity, v_1 increases because of the the increase in the sideward motion and the decrease in the suppression from radial expansion; at beam rapidity, v_1 reaches its maximum value due to the maximum sideward motion and the disappearance of transverse expansion.

Looking more closely at the fits in Fig. 7.1, one notices that the fits deviate slightly from the data at low p_t (approximately $p_t < 0.4$ GeV/c). One observes first that v_1 goes negative at $p_t < 0.3$ GeV/c for rapidity $y < 2.8$. One sees also that the difference between the fits and the data is most significant in semi-central collisions ($E_T < 230$ GeV) around beam rapidity. The first effect could be an indication of the influence from radial expansion as suggested by Voloshin[107] since this influence maximizes close to mid-rapidity; the second effect might be due to the shadowing from spectators, which sit close to the beam rapidity region where the influence of radial expansion becomes minimal. The interplay between these two effects combined with the radial expansion and sideward movement of the thermal source determines the behavior of v_1 at low p_t.

7.1.2 Directed flow of deuterons

As is pointed out in the study of the proton directed flow, the measured v_1 is actually sensitive to the interplay between the sideward motion and radial expansion in the transverse plane. In this section, we will apply the modified sideward moving thermal source model developed in the previous section to study the directed flow of deuterons.

Shown in Fig. 7.4 is the transverse momentum dependence of v_1 of the deuteron azimuthal distributions relative to the reaction plane for different rapidities and centralities. The missing data near $p_t = 0$ is because of lack of acceptance in the spec-

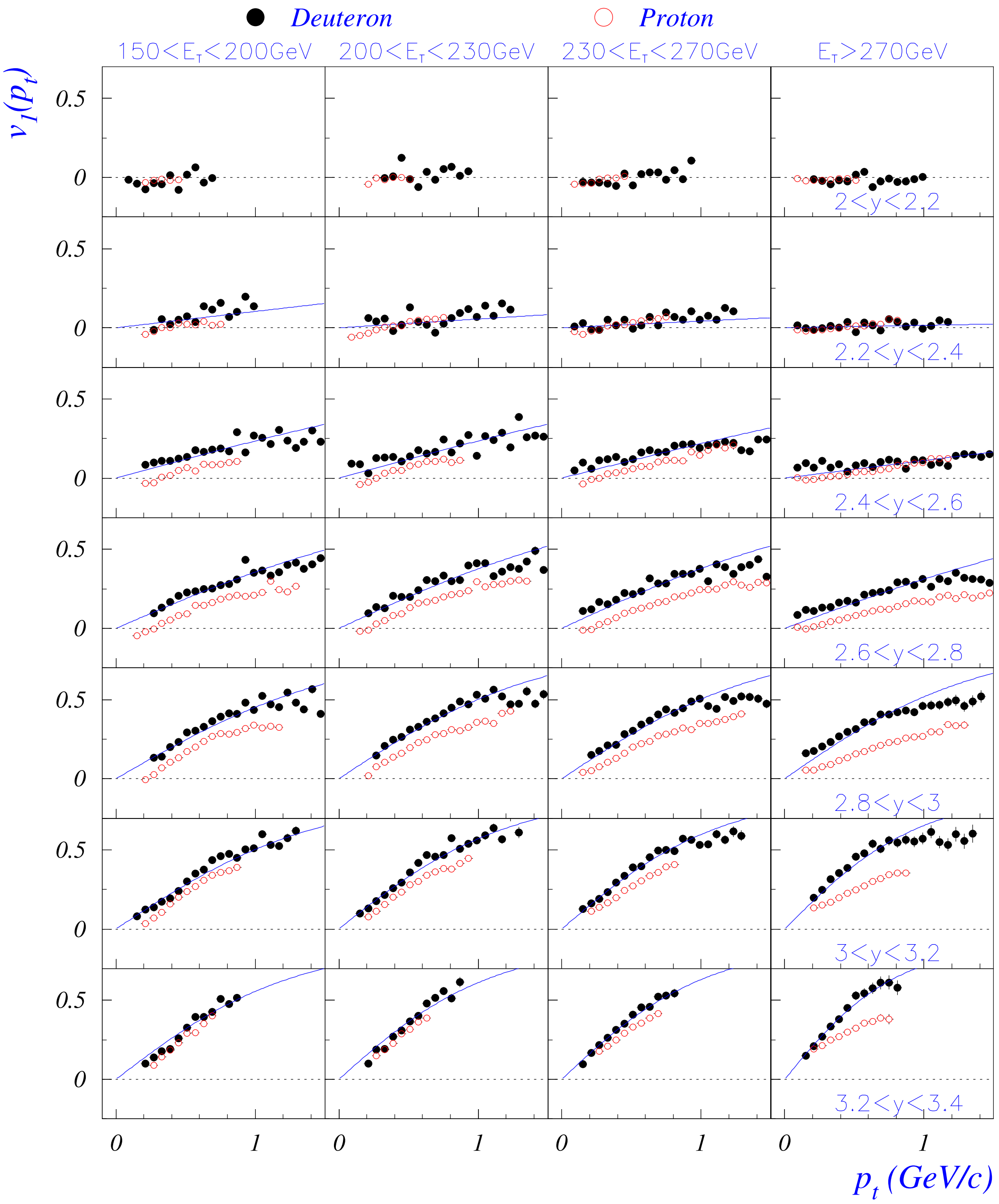

Figure 7.4: The p_t dependence of v_1 for deuterons. For comparison, the results of $v_1(p_t)$ for protons from Fig. 7.1 (after rebinning) are shown by empty circles. Both results are corrected for the reaction plane resolution. The curves superimposed on deuteron data are fits using the function given by Eq. (7.5). The size of each p_t bin is 60 MeV/c.

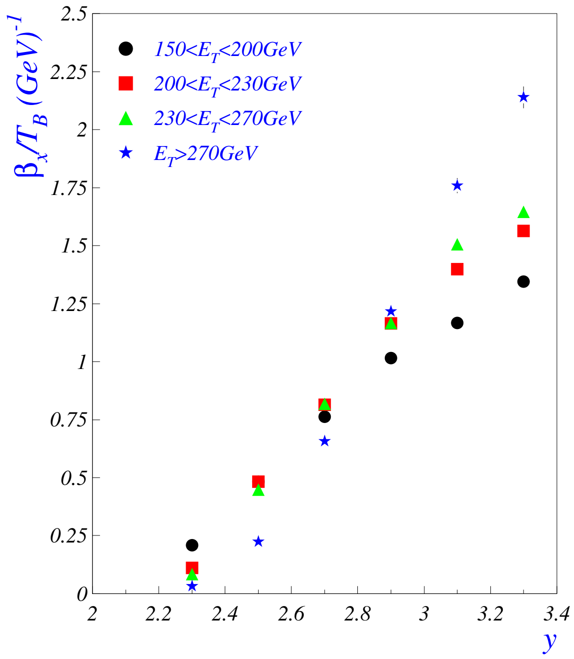

Figure 7.5: Fitted values of the β_x/T_B ratio of a deuteron moving thermal source. Values are extracted from the fits shown in Fig. 7.4.

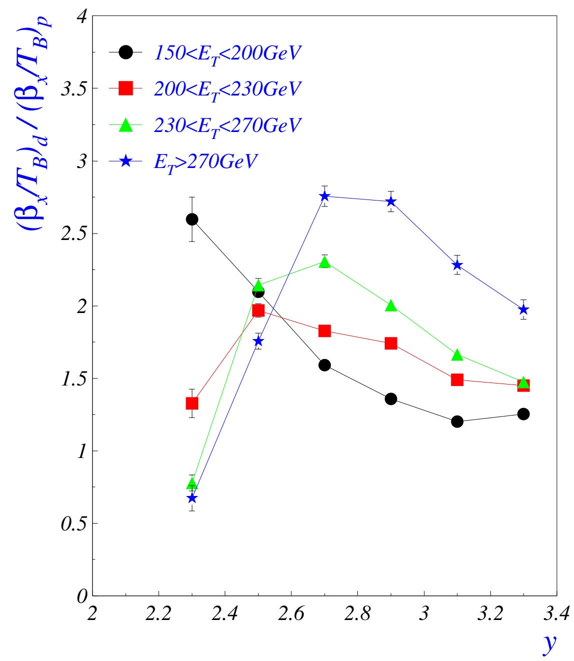

Figure 7.6: Comparison of the measured β_x/T_B ratio between a deuteron source and a proton source. Data points of each centrality region are connected by straight lines to guide the eye.

trometer. In the particle identification of deuterons, the main source of background is the admixture coming from protons on the left side of deuteron squared-mass distribution (see Fig. 5.4) in the momentum range 12$\sim$16 GeV/c. The deuterons falling into this contamination region are removed by requiring that an identified deuteron must NOT be within the $2\sigma_{m^2}$ range of the proton squared-mass distribution.

One observes that the p_t dependence of v_1 of deuterons is similar to that of protons. Moreover, the value of v_1 is systematically larger than that of protons. The centrality dependence of v_1 is somewhat different from that for protons: while at rapidity $y < 2.8$, v_1 decreases with increasing centrality, v_1 does not show such dependence at beam rapidity. In summary, the relative difference in v_1 between protons and deuterons depends on rapidity and centrality: at rapidity $y < 2.4$, no significant difference is observed; at rapidity $y > 2.8$, the difference increases with the increase in centrality.

The smooth curves shown in Fig. 7.4 are fits using the function (Eq. (7.5)) predicted for a deuteron moving thermal source model. Fig. 7.5 shows the fitted results for β_x/T_B for different centralities as a function of rapidity. The rapidity dependence of the β_x/T_B ratio for deuterons shows a similar dependence to that for protons (see Fig. 7.2). The maximum value of β_x/T_B for deuterons is nearly twice that of protons. However, the centrality dependence of the β_x/T_B ratio is quite different from that of protons.

Fig. 7.6 shows the ratio between the β_x/T_B value of protons and that of deuterons as a function of rapidity. The centrality and rapidity dependence of this ratio is rather complex: in particular, the centrality dependence at rapidity $y = 2.3$ is completely reversed compared to that at rapidity $y > 2.5$.

It has been shown that the production of protons (neutrons) is well described by a thermal model with an expansion in the transverse direction for central collisions[41]. Assuming the production of deuterons are due to the simple coalescence of nucleons

Table 7.1: Transverse velocity β_x of a deuteron moving thermal source. The values of β_x for deuterons extracted by using the modified moving thermal source model in the rapidity range $3.0 < y < 3.2$ are shown in the second row. The values of T_B are from Ref. [109]. For comparison, the values of T_B and the extracted β_x in the same rapidity range are shown in the third and fourth row. Values within brackets represent errors due to statistical uncertainties. Additional 10∼15% systematic uncertainty applies to both the β_x values of protons and deuterons.

Centrality(E_T)	150-200GeV	200-230GeV	230-270GeV	$>$ 270GeV
T_B(MeV)(deuteron)	80(3)	80(3)	60(2)	50(3)
β_x(deuteron)	0.099(0.003)	0.112(0.005)	0.090(0.005)	0.086(0.007)
T_B(MeV)(proton)	102(2)	102(2)	102(2)	102(2)
β_x(proton)	0.099(0.002)	0.095(0.002)	0.092(0.002)	0.071(0.002)

at freeze-out, it can be argued that the deuteron source would have the same sideward velocity β_x and the same transverse expansion velocity β_t as those of nucleons. Consequently $(\beta_x/T_B)_d/(\beta_x/T_B)_p$ can be simplified to $(T_B)_d/(T_B)_p$ which can be further approximated by $(T_0 + m_p\beta_t^2/2)/(T_0 + m_d\beta_t^2/2)$. This approximation predicts, that the ratio would drop to less than unity at mid-rapidity (∼0.6 if one assumes $\beta_t \simeq 0.5$ with $T_0 = 140$MeV) and would reach unity at beam rapidity (where $\beta_t \simeq 0$). In that case, similar values of v_1 would be observed at beam rapidity. This is contrary to what is observed in Fig. 7.6 or Fig. 7.4.

Since directed flow basically reflects the non-equilibrium aspect of the collision system and deuterons would be subject to the same collective potential as protons, we would argue that the sideward velocity of deuterons would not be very much different from that of protons. If true, we would expect that the complex dependence shown in Fig. 7.6 is due to the complicated non-equilibrium effects which are reflected at least partly in the behavior of the inverse slope T_B of the particle spectra. The behavior of T_B has been found to be complicated both in theoretical[108] and experimental studies[109].

Table 7.1 shows the extracted β_x at beam rapidity ($3.0 < y < 3.2$), using the modified sideward moving thermal source model with the "effective temperature" T_B measured by the E877 experiment[109]. The measured T_B for deuterons have a significant dependence on the collision centrality. This implies that non-equilibrium production of deuterons is important. In contrast, such effect is negligible in the proton production[64]. Most interestingly, in this analysis, deuterons show the same transverse velocity as that of protons.

7.1.3 Comparison with RQMD model

The relativistic quantum molecular dynamics (RQMD)[113] is a semiclassical transport theoretical approach to study the space-time evolution of heavy ion collisions at ultra-relativistic energies. It combines the classical propagation of particles with excitation of hadrons into resonances and strings. Secondaries (emerging from the decaying resonances and strings) undergo subsequent interactions, both with each other and with the ingoing baryons. This model predicts the production of a broad range of single particles (from nucleons to antibaryon and antihyperons) in heavy-ion collisions and has been successful in describing experimental single particle data[64].

The RQMD event generator running in a pure "binary collision" fashion is the so-called *cascade* mode[114]. The so-called *mean-field* mode[53] takes into account mean-field effects by simulating the nucleon-nucleon potential. Results of particle directed flow predicted by both RQMD event generators (Version 2.3) will be compared to the experimental data in this section (protons and deuterons) and the following sections (pions, kaons and antiprotons). In this analysis, the total number of generated RQMD

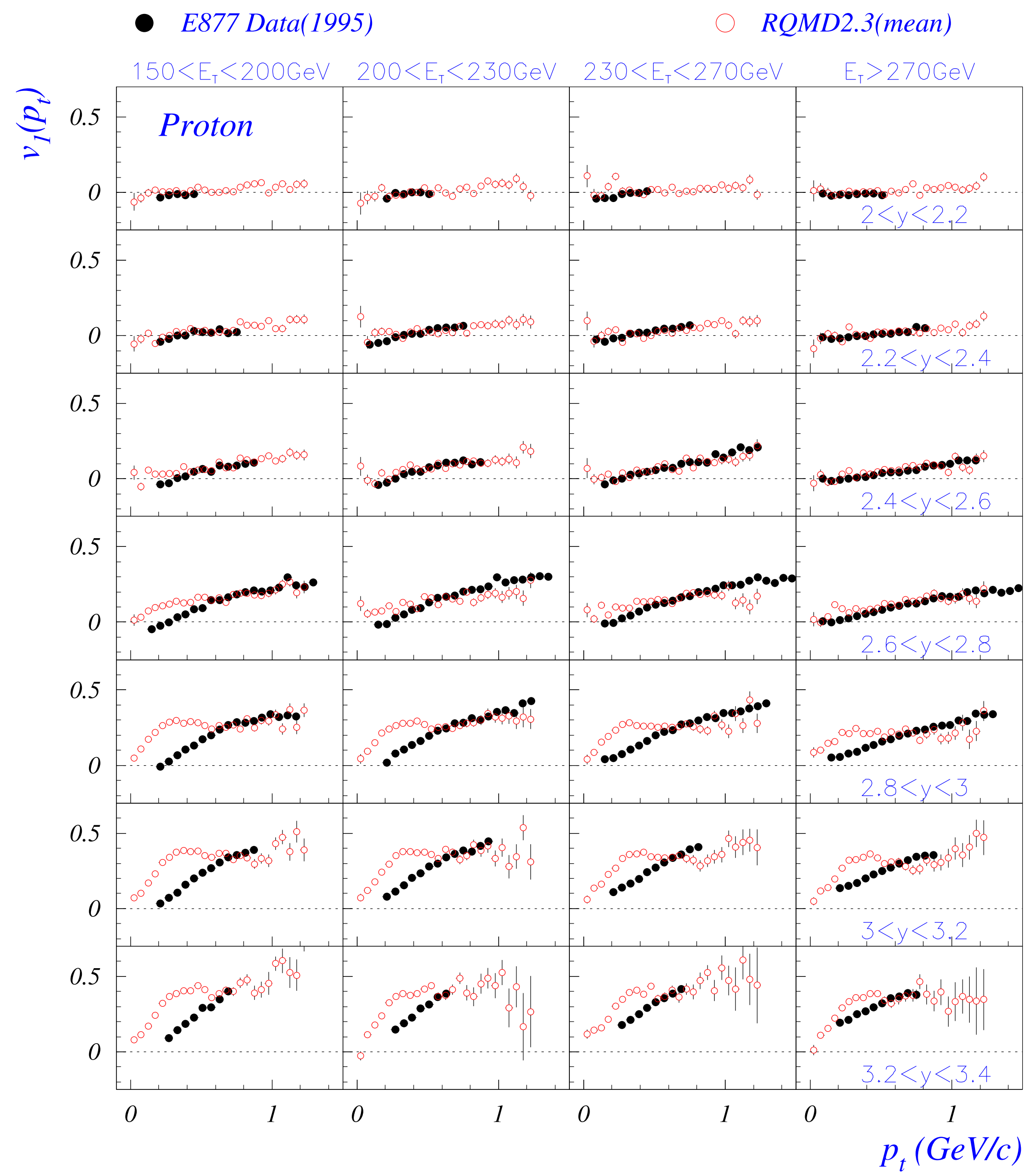

Figure 7.7: Comparison of the measured v_1 for protons with those predicted by RQMD 2.3 mean-field mode. The experimental measurements and model predictions are represented by solid and empty circles respectively.

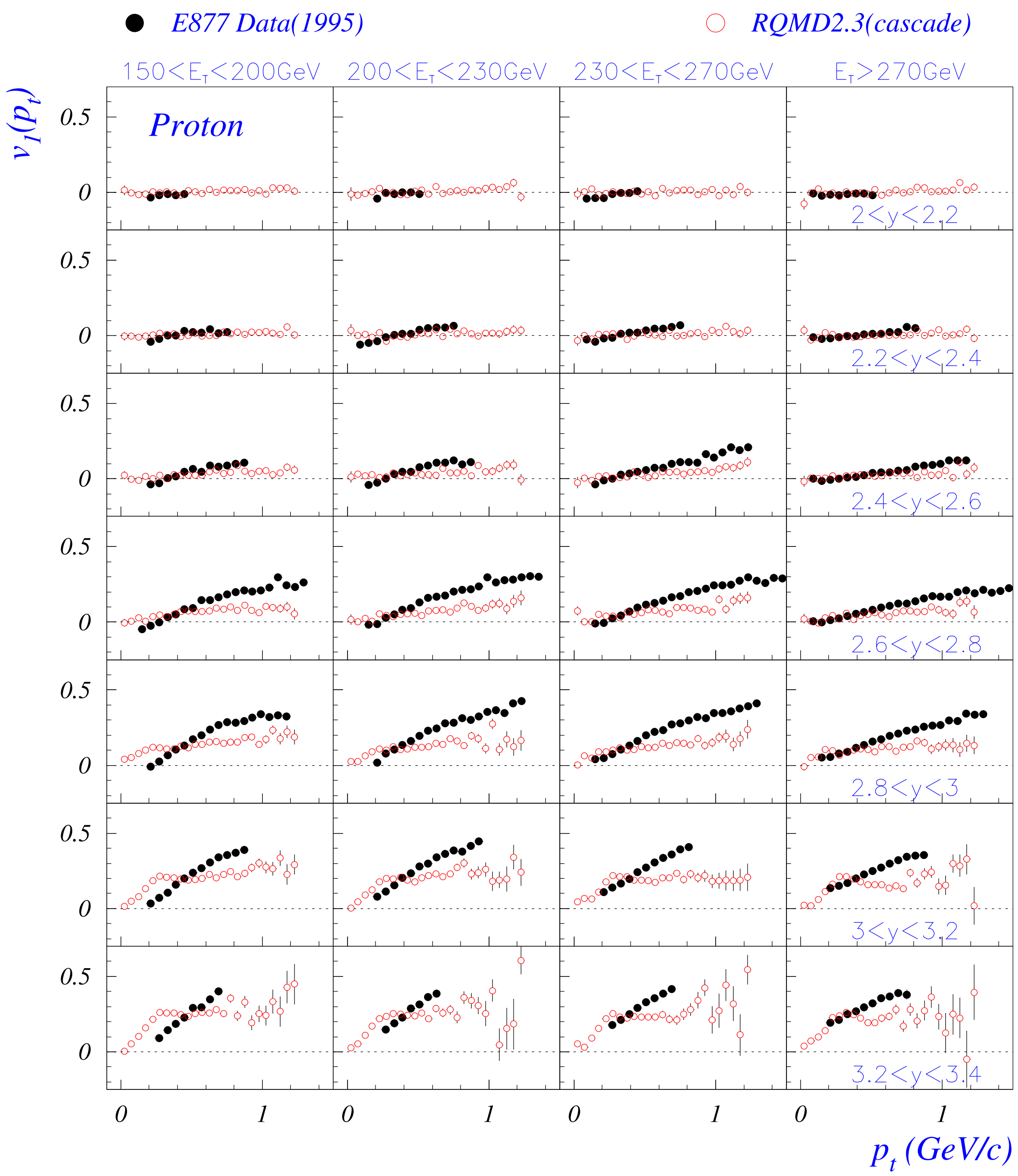

Figure 7.8: Comparison of the measured v_1 for protons with those predicted by RQMD 2.3 cascade mode. The experimental measurements and model predictions are represented by solid and empty circles respectively.

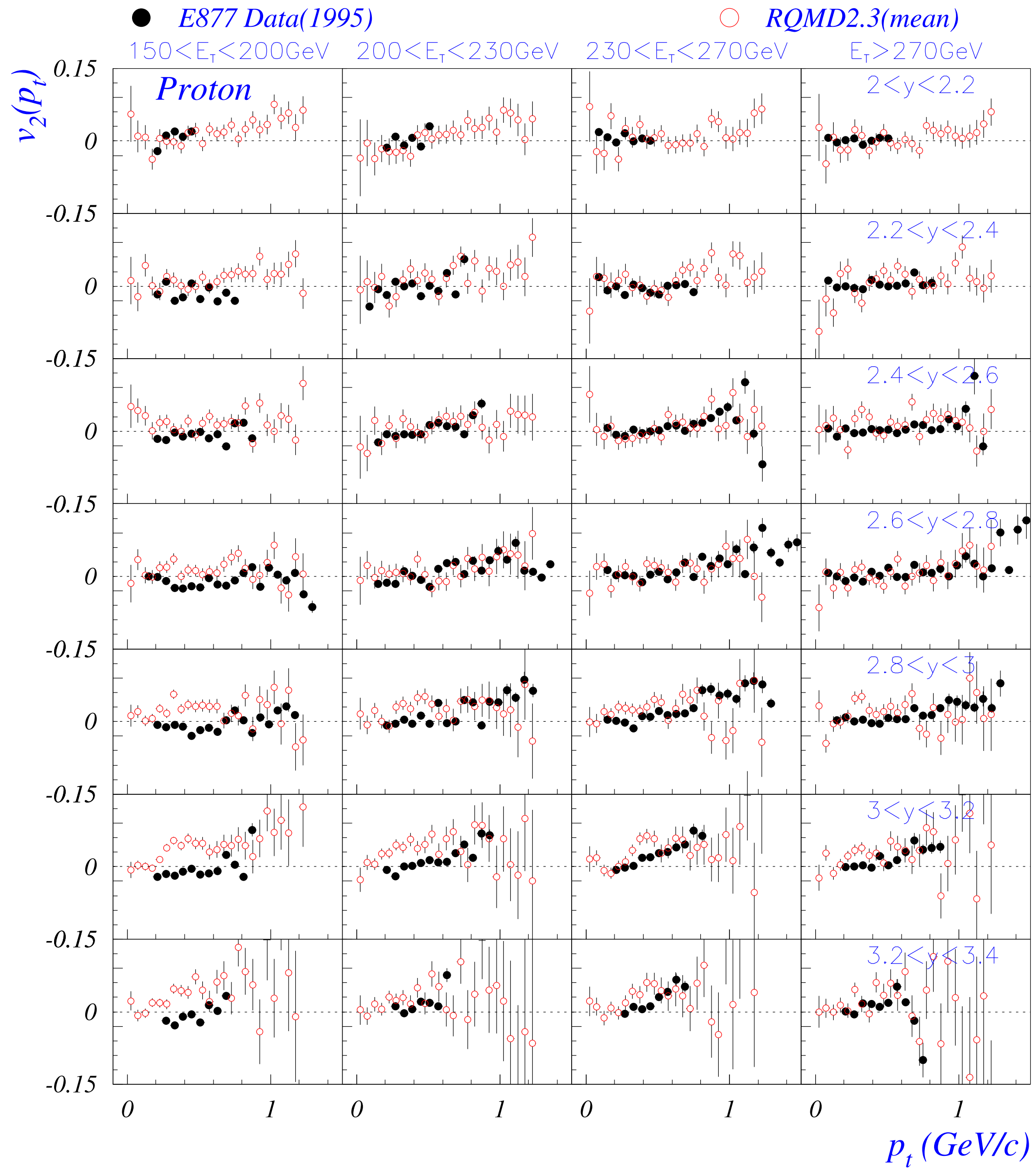

Figure 7.9: Comparison of the measured v_2 for protons with those predicted by RQMD 2.3 mean-field mode. The experimental measurements and model predictions are represented by solid and empty circles respectively.

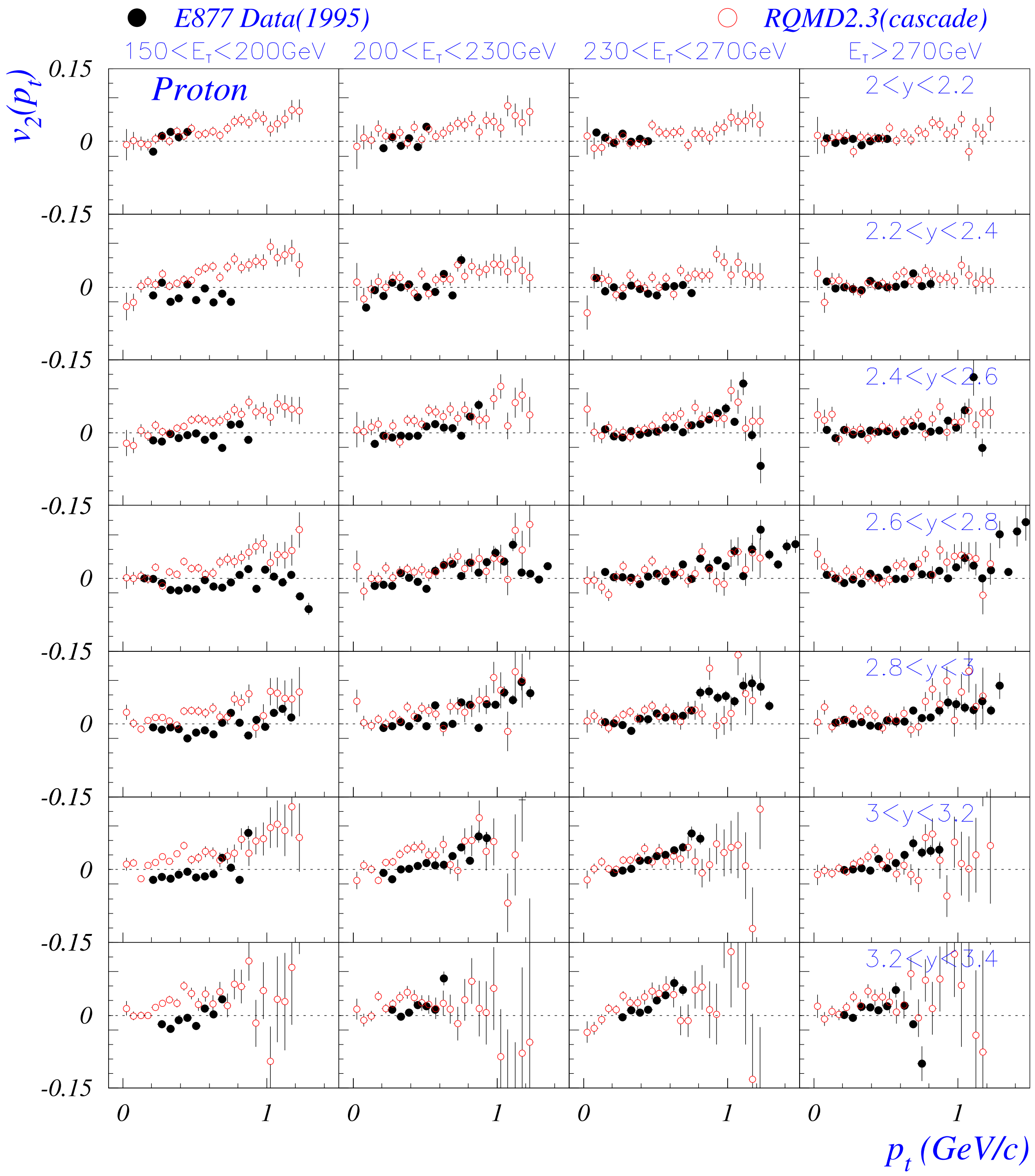

Figure 7.10: Comparison of the measured v_2 for protons with those predicted by RQMD 2.3 cascade mode. The experimental measurements and model predictions are represented by solid and empty circles respectively.

events is ~20,000 events for the mean-field mode and ~43,000 for the cascade mode. For all the model comparisons presented in this thesis, the RQMD events are subject to the same event selection criteria as that is applied to experimental data.

Fig. 7.7 shows the comparison of the measured values of v_1 for protons with those predicted by RQMD in the mean-field mode. At rapidity $y < 2.6$, the agreement between experimental data and model calculations is good. However, starting at rapidity $y > 2.6$, the deviation of model calculations from experimental data becomes significant: while for $p_t < 0.6$ GeV/c the model over-predicts v_1, it under-predicts v_1 at larger value of p_t. The model also predicts a faster saturation of v_1 in the projectile rapidity region ($2.6 < y < 3.2$). One can also notice that the deviation at $p_t < 0.5 \sim 0.6$ GeV/c depends on the rapidity and centrality, and this deviation is most significant at beam rapidity for the semi-central collisions ($150 < E_T < 200$ GeV). This interesting deviation may imply that the influence from spectators is not properly accounted for in the RQMD prescription [3].

Fig. 7.8 shows the comparison of the measured values of v_1 for protons with those predicted by RQMD in the cascade mode. The model under-predicts the proton flow by nearly a factor of 2 for rapidity $y > 2.2$ in all centrality regions. At low p_t around beam rapidity, a similar behavior to that shown in Fig. 7.7 is also observed.

Fig. 7.9 and Fig. 7.10 show the comparison of the measured values of the second component v_2 for protons with those predicted by RQMD in the mean-field mode and in the cascade mode respectively. Both models reproduce most of the features observed in the data, however, they both over-predict v_2 in the beam rapidity region. This over-prediction is most significantly observed in the mid-centrality region. It should be pointed out, that, in general case, the value of v_2 is not equivalent to the actual ellipticity of the particle distribution both experimentally and in the model.

[3] In the RQMD calculated events, spectator protons are excluded since they are not involved in any interaction with the collision zone.

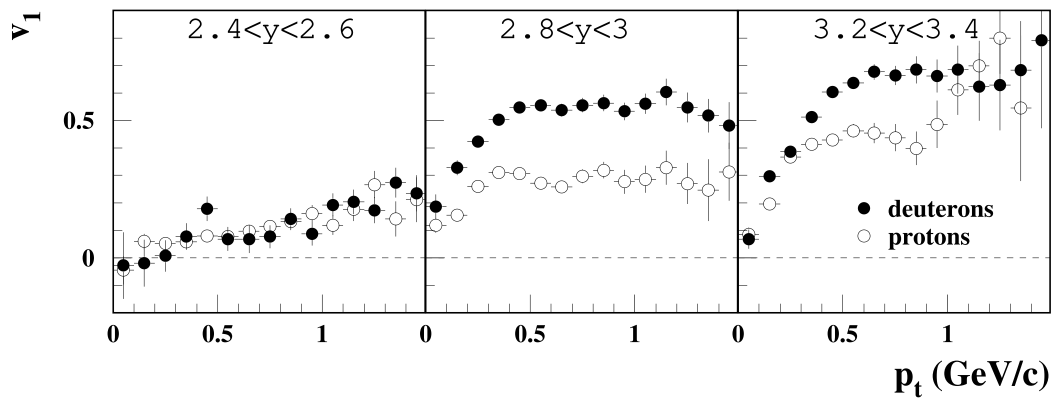

Figure 7.11: The p_t dependence of v_1 for deuterons and protons predicted by RQMD+coalescence model. The centrality corresponds to the region of $150 < E_T < 200$ GeV. The figure is taken from Ref. [110].

Similar to the case of v_1, v_2 also contains the coupling contribution from radial flow as well as that from directed flow. This is discussed in more details in Ref. [106].

Fig. 7.11 shows the results of $v_1(p_t)$ for deuterons and protons calculated using the coalescence model[108] combined with the RQMD (version 2.3 in the mean-field mode) event generator. This coalescence model includes volume effects by explicitly requiring the coalescing nucleons be close both in the momentum and in the configuration space. The model reproduces most of the features observed in the deuteron data (see Fig. 7.4). However, discrepancy between model calculations and experimental data is evident: similar to what is observed for protons, the model predicts for deuterons a faster saturation of v_1 in the beam rapidity region than what is observed in the data; at rapidity $2.4 < y < 2.6$, the model predicts almost no difference in v_1 for protons and deuterons whereas this difference is significant in the data; at rapidity $y > 2.8$, the model over-predicts the v_1 difference between protons and deuterons.

However, effects such as projectile fragmentation might be important to the production of deuterons particularly in the projectile rapidity region. Such contamination is not considered in RQMD.

7.2 Directed flow of Charged Pions

Fig. 7.12 and Fig. 7.13 show the comparison of the measured values of $v_1(p_t)$ for positive pions (π^+) with those predicted by RQMD in the mean-field and the cascade mode respectively. The missing data at low p_t is because of lack of acceptance in the spectrometer for the 1995 configuration. One observes that v_1 is negative at low p_t and gradually rises to positive at high p_t. The RQMD model in the mean-field mode reproduces well the data while in the cascade mode the model over-predicts the magnitude of v_1 at rapidity $y < 3.6$.

Fig. 7.14 and Fig. 7.15 show the results for negative pions. The p_t dependence of the v_1 data for π^- is similar to that for π^+. Although the predictions by the mean-field mode shows a good agreement with the data at rapidity $y < 3.6$, the model fails to reproduce the data at $y > 3.6$. In the cascade mode, the discrepancy between the model predictions and the data is similar to that observed for π^+.

More details are revealed from the comparison in the p_t dependence of the measured v_1 for both species of pions (see Fig. 7.16). One observes that at approximately $p_t < 0.3$ GeV/c, π^+ exhibits a more negative v_1 than π^- whereas at approximately $p_t > 0.3$ GeV/c, the difference in v_1 between these two pion species disappears. In both cases, v_1 gradually rises to positive values at highest p_t. Looking more closely at the very low p_t for π^- [4], one can notice that v_1 becomes positive near $p_t = 0$ [5].

[4] In the 1995 experimental configuration, the E877 spectrometer has the acceptance coverage at $p_t = 0$ for negative charged particles.

[5] v_1 should be zero at $p_t = 0$ just because of the continuity of the spectra. A more detailed plot

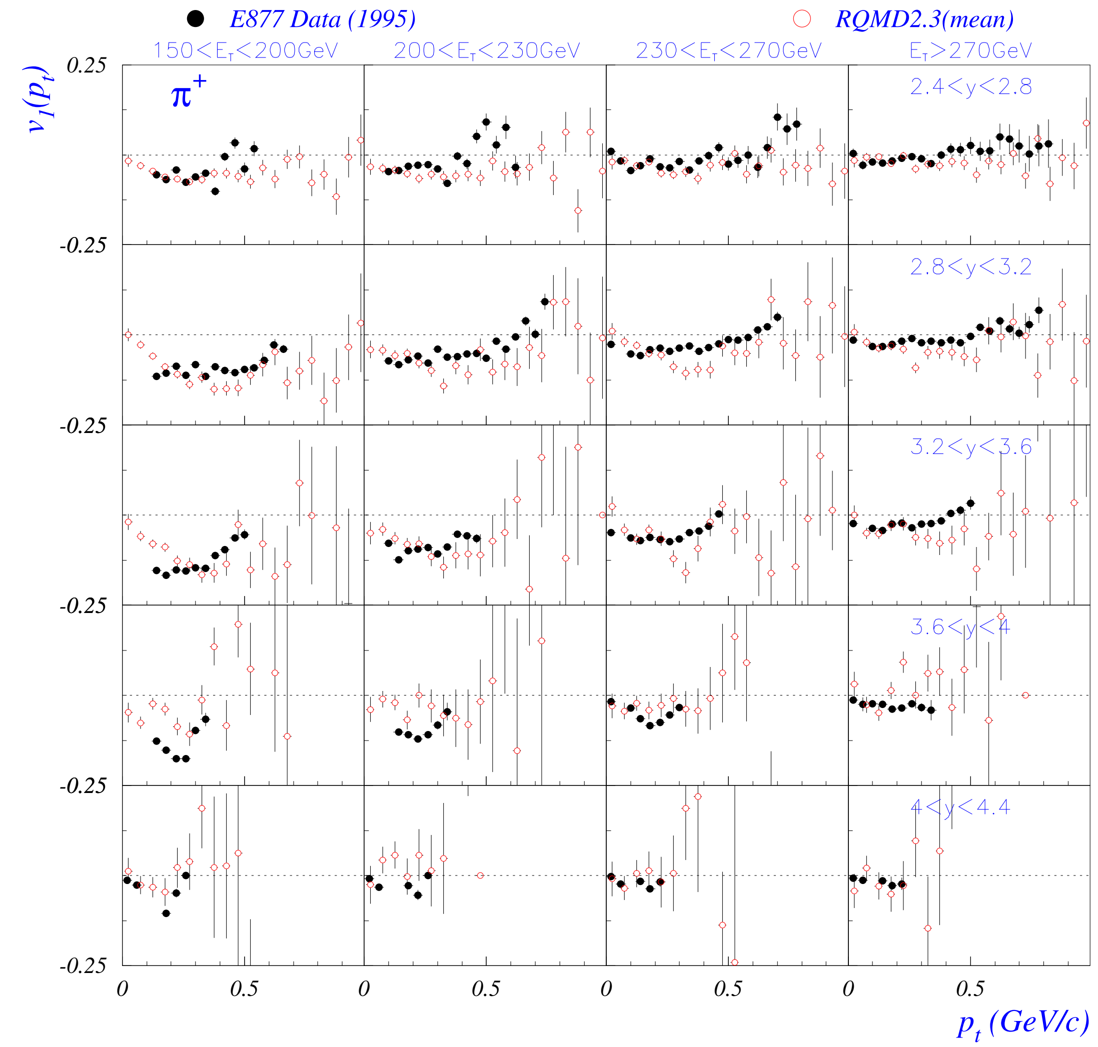

Figure 7.12: Comparison of the measured v_1 for positive pions with those predicted by RQMD 2.3 mean-field mode. The experimental measurements and model predictions are represented by solid and empty circles respectively.

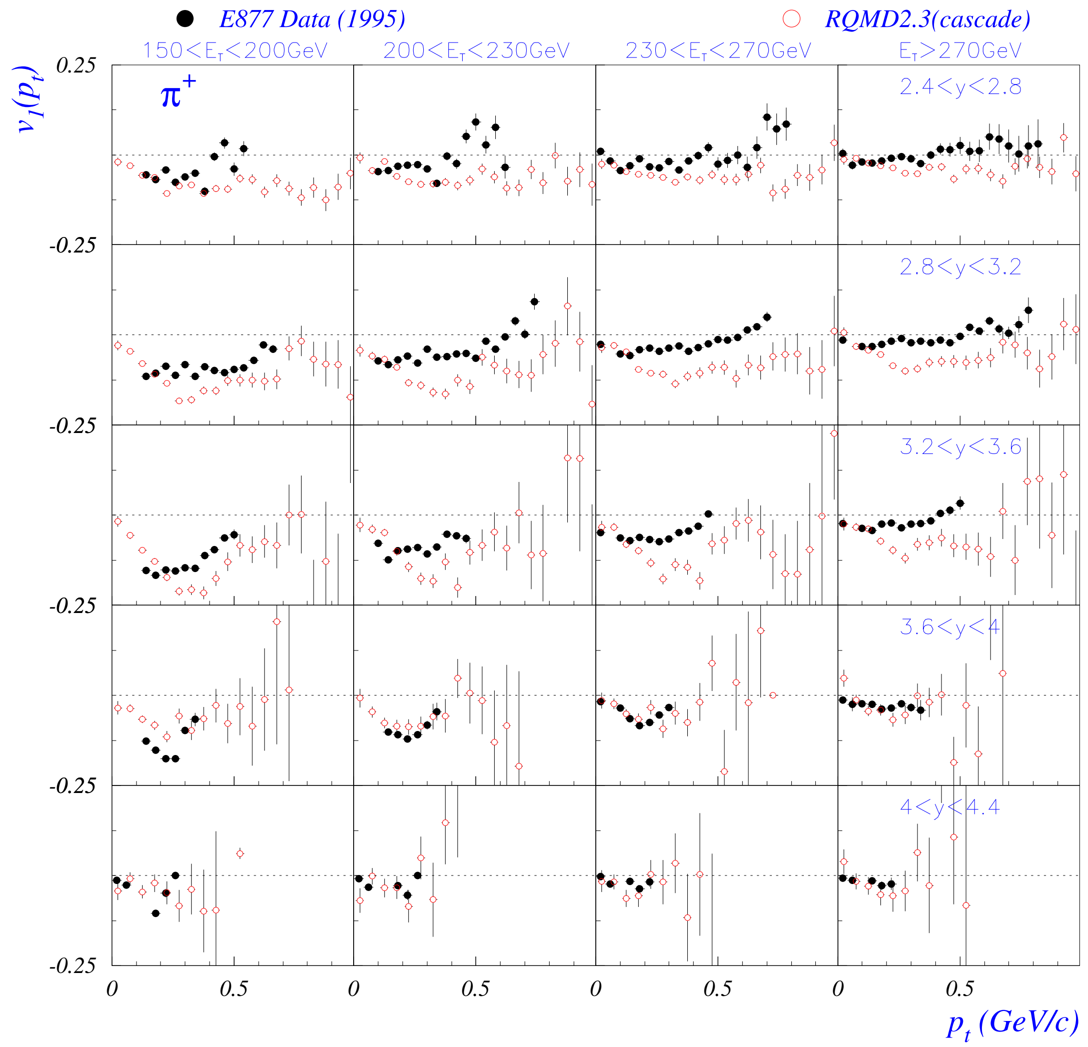

Figure 7.13: Comparison of the measured v_1 for positive pions with those predicted by RQMD 2.3 cascade mode. The experimental measurements and model predictions are represented by solid and empty circles respectively.

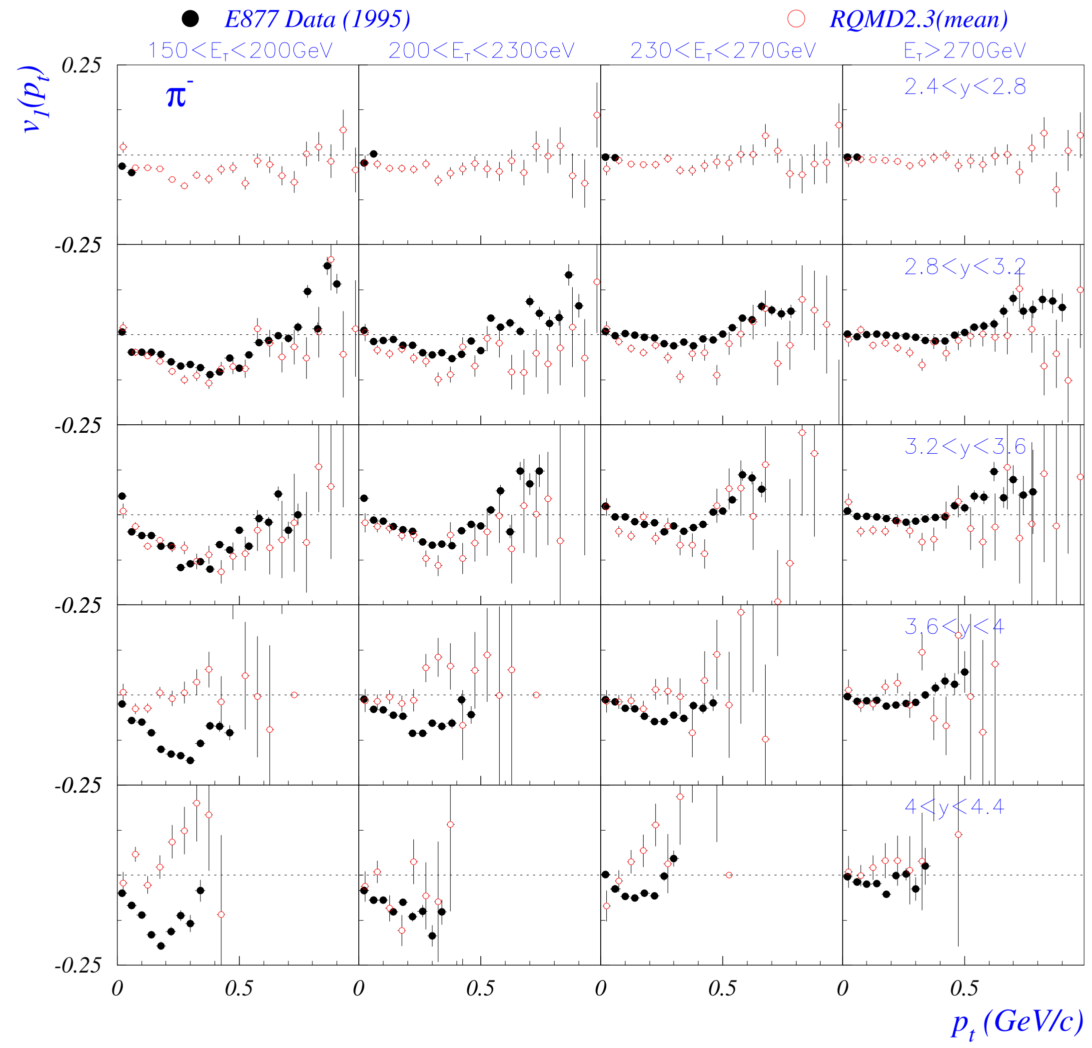

Figure 7.14: Comparison of the measured v_1 for negative pions with those predicted by RQMD 2.3 mean-field mode. The experimental measurements and model predictions are represented by solid and empty circles respectively.

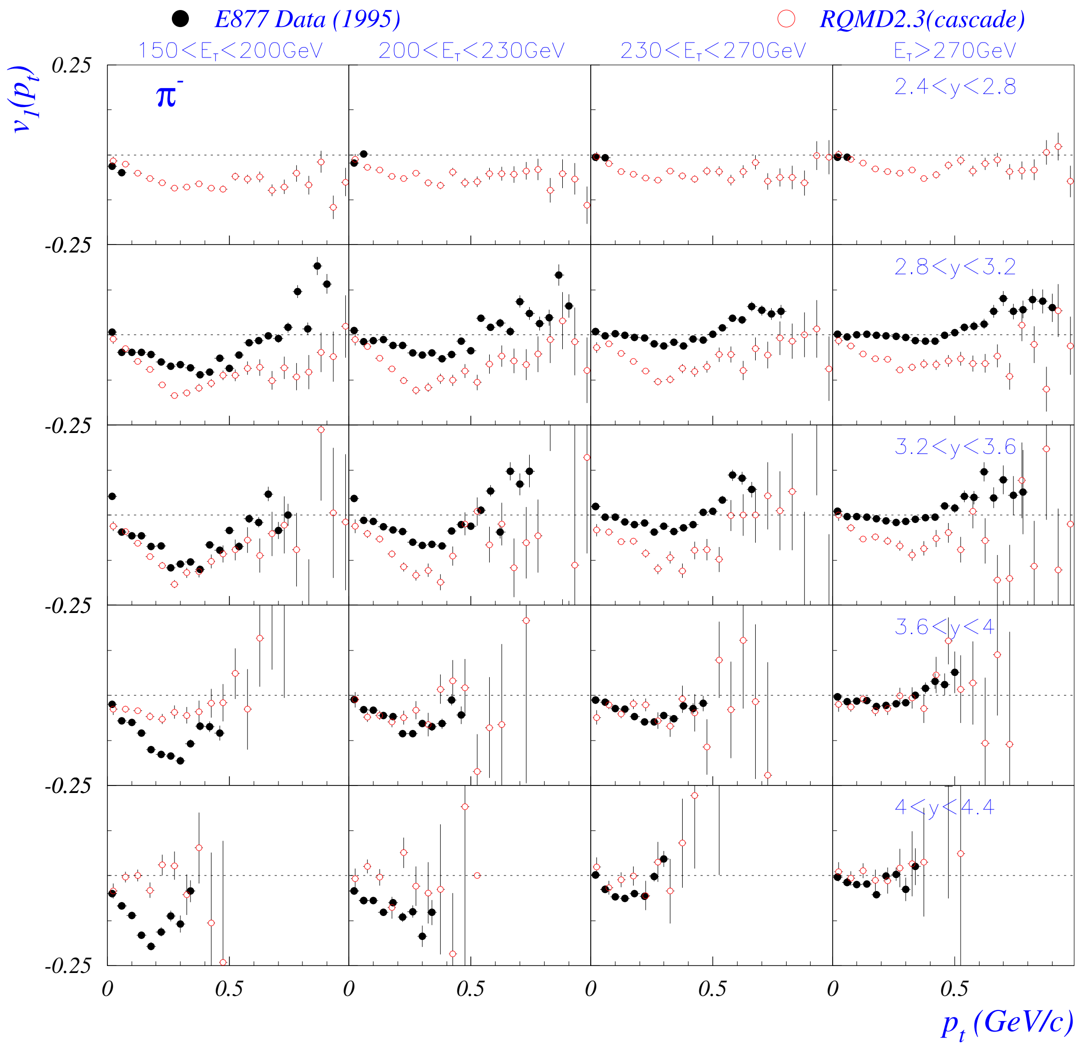

Figure 7.15: Comparison of the measured v_1 for negative pions with those predicted by RQMD 2.3 cascade mode. The experimental measurements and model predictions are represented by solid and empty circles respectively.

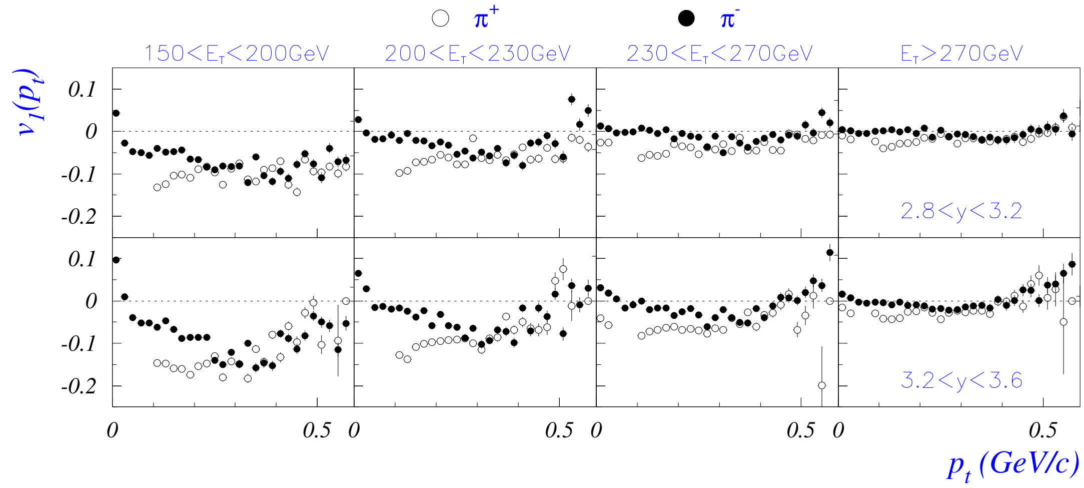

Figure 7.16: Comparison of the p_t dependence of the measured v_1 between positive and negative pions. The values of v_1 for π^- and π^+ are represented by solid and empty circles respectively.

This effect is observed to be more significant for less central collisions.

Pions are primarily created either in the inelastic nucleus-nucleus collisions ($NN \rightarrow NN\pi$) or emitted from decaying baryon resonances (N^*, Δ, Λ, etc)[118]. Pions created in NN collisions would be expected to be isotropic, and the emission from baryon resonance decays would create a positive v_1 for pions as resonances should retain a signature from the flow of nucleons[115]. Once pions are created, they can either escape, scatter, or be absorbed. In a high density baryonic environment, a created pion has a large probability to be absorbed due to its large absorption and rescattering cross section (its mean free path is about 5 fm at normal nuclear density or should be smaller at higher densities). Reabsorption, and more importantly rescattering[115, 117], off the "cold" spectator nucleons will reduce the pion flux in the directions of the spectators, and consequently tend to create a negative v_1 for pions (the so-called shadowing effect).

in Ref. [33] shows that point.

The observed feature of the p_t dependence of v_1 for both pions actually reflects the competition between the collective flow of baryon resonances and the shadowing of spectators. The low p_t pions which on average stay longer in the collision zone, have a greater chance to be rescattered or reabsorbed, and as a result, they exhibit an anticorrelation (negative v_1) to the directed flow of nucleons due to the dominance of the shadowing effect; as p_t increases, the portion of secondary pions (from the baryon resonance) escaped from the collision zone will increase and consequently, v_1 will rise and eventually display their intrinsic directed flow characteristics inherited from nucleons at highest p_t. While it does not reproduces the detailed behavior, this negative to positive behavior is in fact reproduced by RQMD. At very low p_t, the difference in v_1 between the two pion species might also be due to Coulomb effect and to the more important role of Δ and Λ decays in π^-. The observed positive v_1 of π^- at near $p_t = 0$ is probably due to attractive Coulomb interactions for π^-.

7.3 Directed Flow of Charged Kaons

The production of charged kaons (K^+ and K^-) [6] in heavy-ion collisions is of particular interest since the strangeness enhancement in heavy-ion collisions has been predicted to be a signature of the QGP formation[119]. The heavy strange s (and antistrange $\bar{s}$) quarks do not exist prior to the collisions. At the AGS, the probability for the annihilation of a produced $s\bar{s}$ pair is small since the abundance of strange and antistrange quarks is low (the ratio of the number of produced kaons to that of nucleons or pions is less than 0.1[40]). Most of the kaons and antikaons survive in the hot and dense hadronic reaction zone until they disappear by weak decays. Study of the production of kaons is expected to bring us useful information about the earlier

[6] K^- ($\bar{K}^0$) is also commonly called an antikaon since it is the charge conjugate of the kaon K^+ (K^0).

stages of the collision, and therefore help us to get a better understanding of the behavior of the strongly-interacting, highly-excited and dense matter[121].

The study of the directed flow of kaons is important to understand the properties of kaons in the dense nuclear medium. Theoretical studies with RQMD[132] and ARC[133] showed that the directed flow of K^- in heavy-ion collisions is predicted to exhibit "antiflow" due to the rescattering and absorption of the kaons in the dense nuclear matter. At lower energies ($<$2 AGeV), it is predicted, that in the dense nuclear medium ($\sim$2 times ρ_0, the density of the normal nuclear matter), an in-medium kaon-nucleon potential[122, 123], which is weakly repulsive for kaons and strongly attractive for antikaons, results in an increased effective mass for kaons and equivalently reduced mass for antikaons[126]. The recent observation of the disappearance of K^+ directed flow in Ni+Ni collisions at 1.93 AGeV[127] and an enhanced elliptic emission of the same particle species in Au+Au collisions at 1 AGeV[128] were interpreted as indication for in-medium modifications of kaon properties. For Au+Au collisions at 11.5 AGeV, the energy density achieved is much higher ($\sim 5\rho_0$ or higher) and the influence of kaon potential on the kaon (antikaon) directed flow could become more important due to a much stronger rescattering and absorption in the much denser nuclear medium. A study of the difference between the directed flow of K^+ and that of K^- would provide important information for the understanding of the influence from KN potentials, absorption and rescattering.

The directed flow of K^+ has been previously studied by the E877 using the data obtained during the 1994 running period[71]. Study of K^- flow has also been attempted in that analysis. Unfortunately, limited by the statistics, it is difficult to draw a definite conclusion from the comparison between both kaon species. In this section, the directed flow of K^+ and K^- will be re-investigated with the 1995 data set, which has nearly 4 times more statistics and better particle identification.

7.3.1 Kaon identification

Experimental study of the directed flow of particles requires good particle identification. Unlike protons or pions which are basically free of background, kaons suffer seriously from background contamination because of their low yields. A previous work on K^+ production spectra using 1993's data[64] carefully studied the background sources and found out that the so-called low m_t structure claimed by previous analyses was simply due to the improper handling of the backgrounds. Directed flow observables are more sensitive to background contamination: even a small amount of background contamination could, for example, reverse the sign of the observed v_1.

The track confirmation using VTX measurement information is important to reduce the background in the identification of K^+ and K^-. Fig. 7.17 show a contour plot of the squared-mass distributions for K^+ and K^- with and without VTX confirmation. One notices that even though the ridges corresponding to both kaons (m^2 ~0.24 GeV^2/c^4) are visible in the distributions with no VTX confirmation, the background contamination is quite significant for both kaon species over a large momentum range. With the track confirmation (within $\pm 2.5\sigma_{dx}$) at the VTXB, the backgrounds are reduced significantly particularly in the low momentum range.

Shown in Fig. 7.18 is a study of the background in the selection of positive kaons as a function of momentum. A track confirmation (within $\pm 2.5\sigma_{dx}$) at the VTXB is applied. One notices that the background contamination for K^+ is negligible until momentum gets higher than 2 GeV/c. The background consists of two major sources: the contamination from positive pions and the "false" tracks. The contribution from π^+ contamination (extending tail from the π^+ Gaussian distribution) is represented by an an exponential curve (see Fig. 7.18). The π^+ contamination is negligible until $p > 3.0$ GeV/c. The "false" tracks originate from the failure of the tracking system and their contribution is approximated by a linear function in the squared-mass

Table 7.2: Background contamination in the selection of positive kaons. The second row represents the contribution from π^+, the third row the contribution from "false" tracks and the fourth row the total of these two contributions. See text for details.

Momentum range (GeV/c)	0.5-1	1-1.5	1.5-2	2-2.5	2.5-3	3-3.5	3.5-4
π^+ background(%)	~ 0	~ 0	~ 0	< 1	< 2	< 5	< 10
"false" tracks(%)	< 15	< 5	< 5	< 8	< 15	< 20	< 30
Total background(%)	< 15	< 5	< 5	< 10	< 15	< 25	< 40

Table 7.3: Background contamination in the selection of negative kaons. The second row represents the contribution from π^-, the third row the contribution from "false" tracks and the fourth row the total of these two contributions. See text for details.

Momentum range (GeV/c)	0.5-1	1-1.5	1.5-2	2-2.5	2.5-3	3-3.5	3.5-4
π^- background(%)	~ 0	~ 0	~ 0	~ 0	< 1	< 3	< 30
"false" tracks(%)	~ 0	~ 0	< 4	< 6	< 10	< 15	< 20
Total background(%)	< 20	< 10	< 4	< 6	< 10	< 20	< 50

spectrum (straight lines in Fig. 7.18). At $p > 4$ GeV/c, the background exceeds the kaon peak.

Fig. 7.19 shows a similar background study in selecting K^-. As for K^+, the same confirmation at the VTXB is applied. The background mainly consists of the contamination from π^- whereas the contamination from "false" tracks is small. The background contribution in selecting K^+ and K^- for different momentum ranges are summarized in Table 7.2 and Table 7.3 respectively. The background contribution is calculated by comparing the area of each background falling within $\pm 2\sigma_{m^2}$ window about the center of each extracted Gaussian with that of the Gaussian in the same region. Kaons are selected with the criteria: $|m^2 - m_K^2| < 2.0\sigma_{m^2}$. The mass resolution of kaon peak is given in Fig. 5.5. To select clean kaons for the flow study, we apply a maximum momentum cut of 3.5 GeV/c for both kaons.

From Table 7.2 and Table 7.3, one notices that, at momentum less than 3.0 GeV/c, the contamination from pions is small for both kaons and the "false tracks" are the major source of the background. The azimuthal behavior of the "false tracks" is difficult to study. Basically, most of the "false tracks" are the tracks of those particles with incomplete or very poor tracking information. Therefore, we expect that "false tracks" mainly consist of incorrectly or poorly identified pions and kaons [7]. We estimate that the systematic error on average for the directed flow results of both kaons is about 10% of the values of the pion directed flow results by assuming that 50% of the "false tracks" are from incorrectly or poorly identified pions.

7.3.2 Kaon directed flow

The experimental analysis of the directed flow of kaons is limited by the statistics available in the data. The analysis strategy employed in this section is to study the average directed flow signal v_1 over a large acceptance region (e.g., the forward rapidity region) first. Then we will attempt to study the p_t dependence of v_1 as a function of rapidity and centrality using the Fourier analysis method as done in the previous sections. Though the average flow signal v_1 obtained over a large acceptance region usually does not reveal the detailed behavior of v_1 and also depends on the specific acceptance region chosen, it provides important systematic information such as centrality dependence. Since the influence from statistical fluctuations on the flow signal is minimized, v_1 can be used to understand the systematics. We will also use this strategy in the study of the directed flow of antiprotons in the next section.

[7]The contamination from protons for K^+ should be negligible at $p < 4$ GeV/c because of the large separation between the K^+ mass peak and proton mass peak. See also Fig. 7.17.

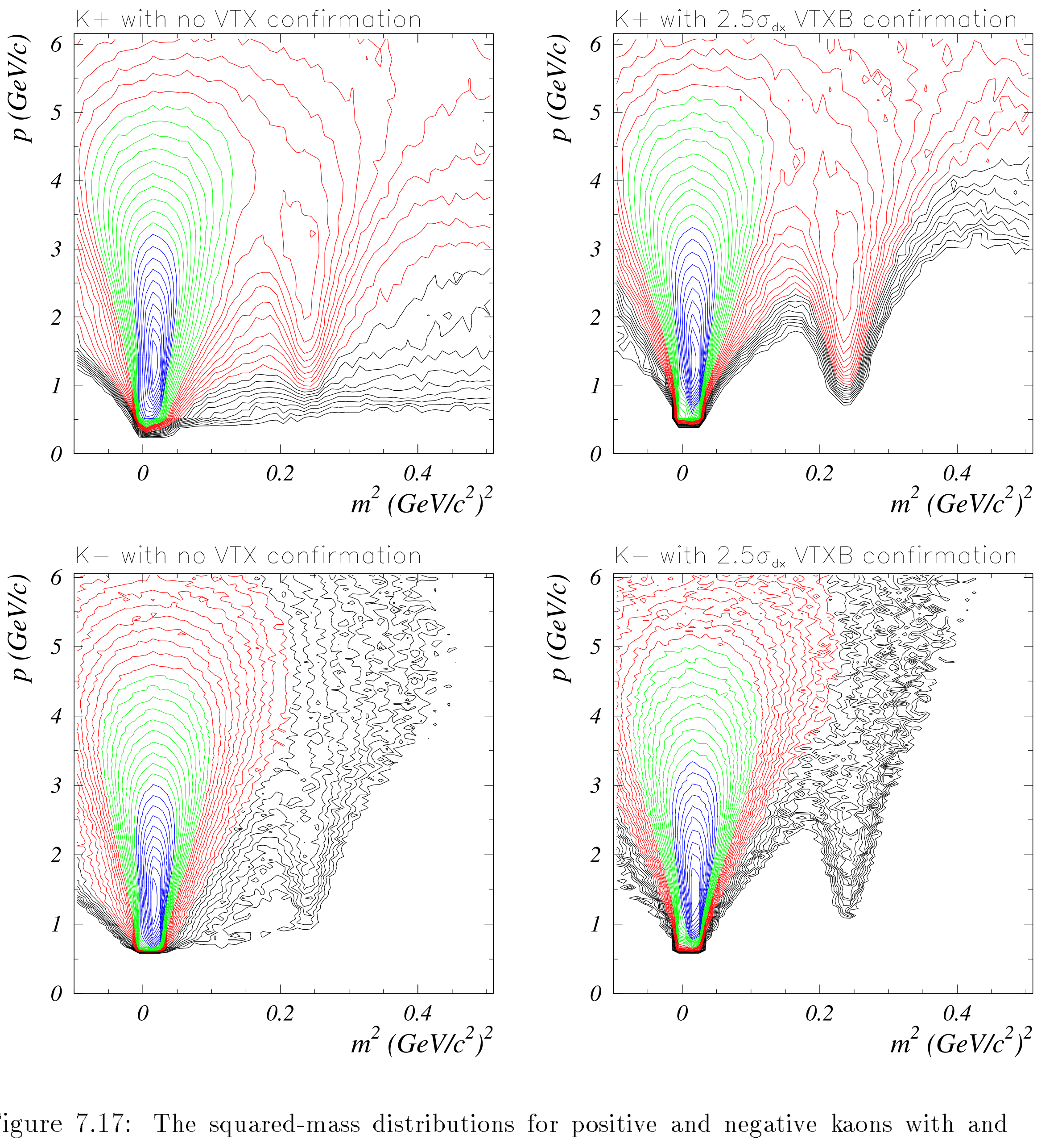

Figure 7.17: The squared-mass distributions for positive and negative kaons with and without VTX confirmation. The top two panels show the distributions for K^+ while the bottom panels show those for K^-. For the distributions with VTX confirmation, a $2.5\sigma_{dx}$ confirmation at VTXB is applied. See Section 5.2 in Chapter 5 for the description about VTX matching.

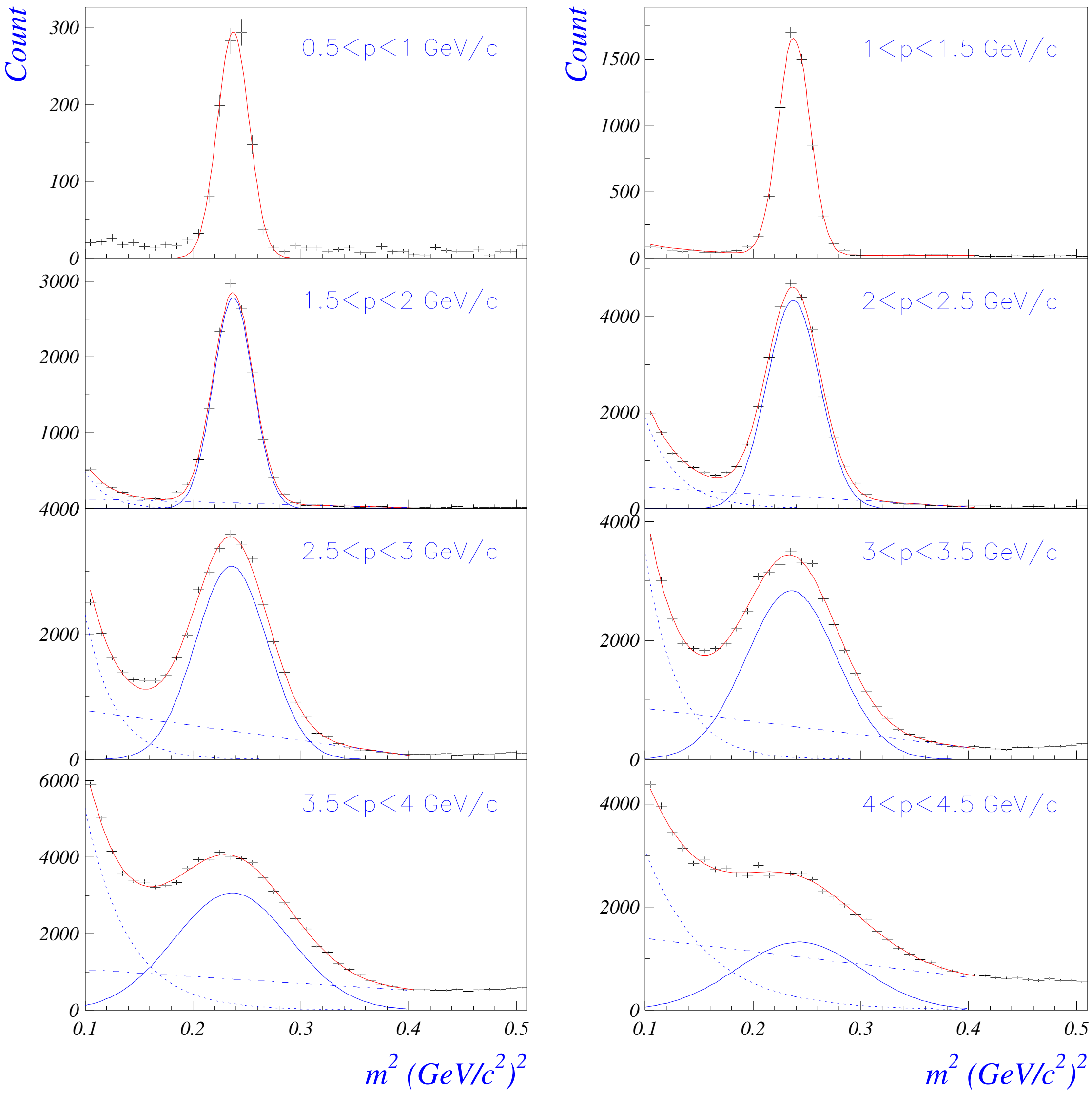

Figure 7.18: Study of the background contribution in the identification of positive kaons for different momentum ranges. The squared-mass distributions are fitted with a kaon mass function (Gaussian) and two background functions (an exponential one and a linear one). The exponential curves (dotted) represent the contamination from π^+; the straight lines (dot-dashed) are the estimated contributions from "false" tracks.

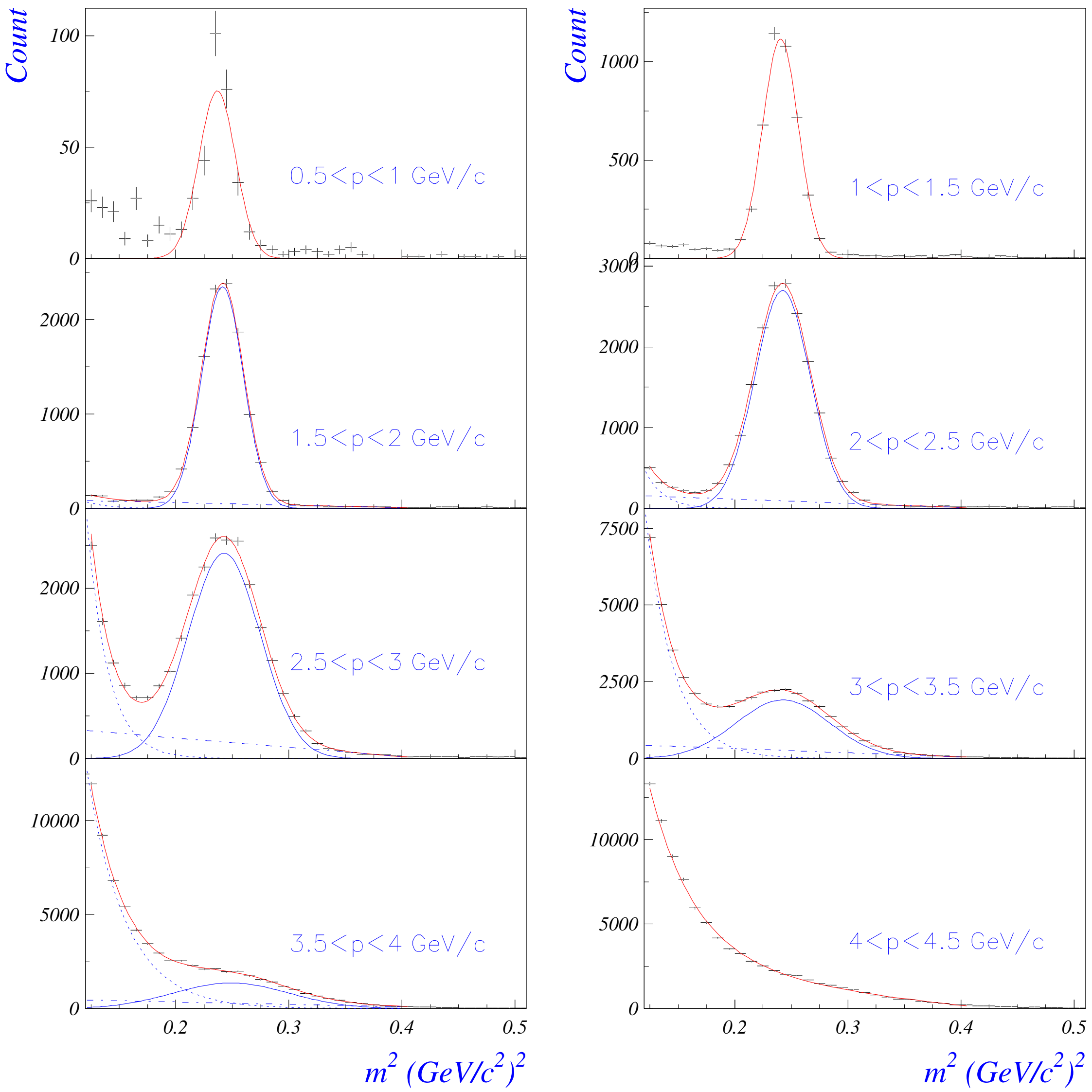

Figure 7.19: Study of the background contribution in the identification of negative kaons for different momentum ranges. Similar to Fig. 7.18, the Gaussians represent the kaon peaks; the dotted curves are the contamination from π^-; the straight lines (dot-dashed) are the estimated contributions from "false" tracks.

Fig. 7.20 and Fig. 7.21 show the azimuthal angular distributions of K^+ ($p_t < 0.7$ GeV/c) and K^- ($p_t < 0.5$ GeV/c) with respect to the reaction plane measured in the forward rapidity ($1.8 < y < 3.0$ for K^+ and $1.8 < y < 2.8$ for K^-) for four different collision centralities. The acceptance for both kaons in the phase space of rapidity and p_t is shown in Fig. 5.11 of Chapter 5. In these figures, ϕ is the emission angle of the particle and ψ_r is the reaction plane angle. All distributions are normalized to unity. The azimuthal distributions of both K^+ and K^- exhibit clear minima at $\phi - \psi_r = 0$ corresponding to an anisotropic emission antiparallel to the impact parameter vector.

For an emission dominated by directed flow, the azimuthal emission pattern can be parameterized by

$$\frac{dN}{d\varphi} = 1 + 2v_1' \cos\varphi \qquad \varphi = \phi - \psi_r \tag{7.6}$$

The parameter v_1' quantifies the directed flow of particles parallel ($v_1' > 0$) or antiparallel ($v_1' < 0$) to the impact parameter vector. The value after correction for the reaction plane resolution is $v_1 = v_1'/\langle\cos\Delta\phi\rangle$, where $\langle\cos\Delta\phi\rangle$ represents the uncertainty in the reaction plane as discussed in Chapter 6. The measured azimuthal distributions of both kaons are fitted with the function given in Eq. (7.6). The full lines in Fig. 7.20 and Fig. 7.21 are the results of such fits. The values of the fitted parameter v_1' shown in these figures are not corrected for the reaction plane resolution.

Table 7.4 gives the corrected directed flow parameter v_1. The "antiflow" of both K^+ and K^- display a strong dependence on centrality, being most pronounced in semi-central collisions ($E_T < 270$ GeV) and almost completely disappearing for central collisions. The K^- exhibits a somewhat stronger "antiflow" than the K^+ in semi-central collisions.

Fig. 7.22 and Fig. 7.23 show the p_t dependence of v_1 obtained from the Fourier analysis method for K^+ and K^- respectively. The strong centrality dependence of

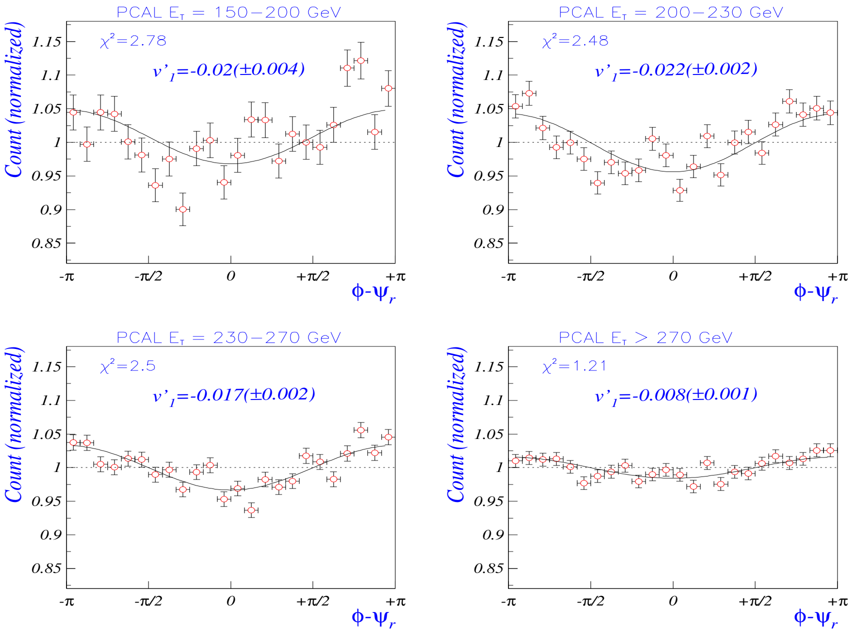

Figure 7.20: K^+ azimuthal angular distributions measured in the forward rapidity for different centralities. ϕ is the emission angle of the particle and ψ_r is the reaction plane angle. The smooth curves are the fits using Eq. (7.6). Also given in the figures are the values of the fitted parameter v_1'.

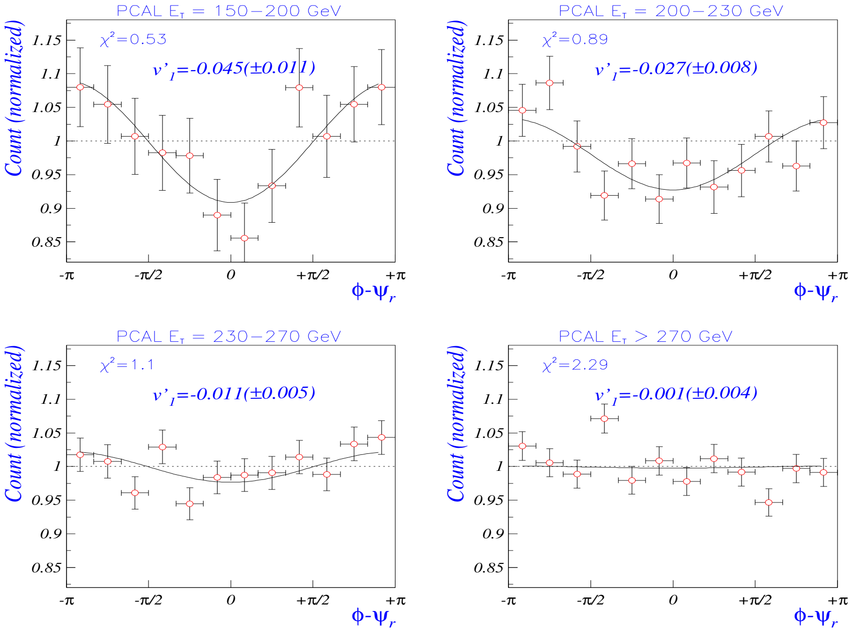

Figure 7.21: K^- azimuthal angular distributions measured in the forward rapidity for different centralities. See Fig. 7.20 for details.

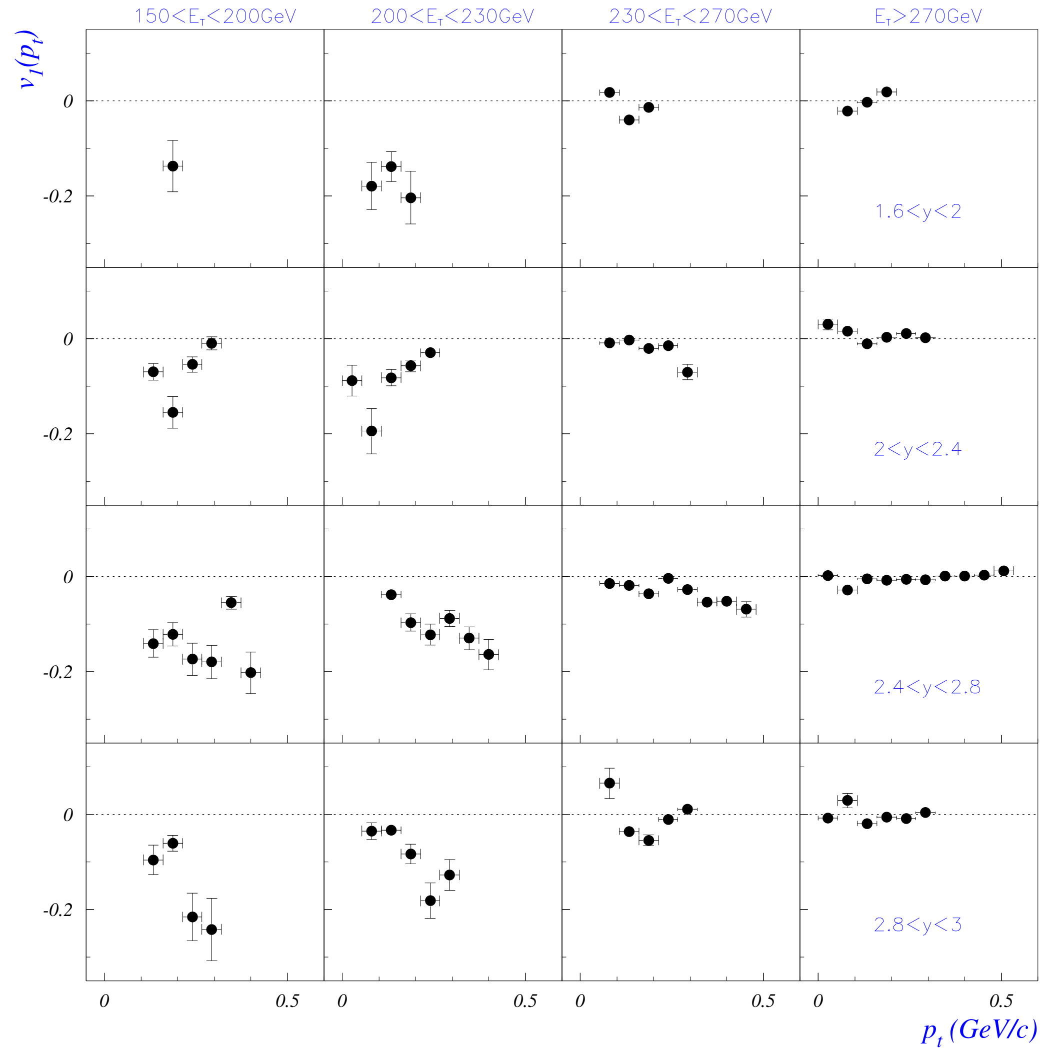

Figure 7.22: $v_1(p_t)$ for positive kaons. The values of $v_1(p_t)$ are corrected for the reaction plane resolution.

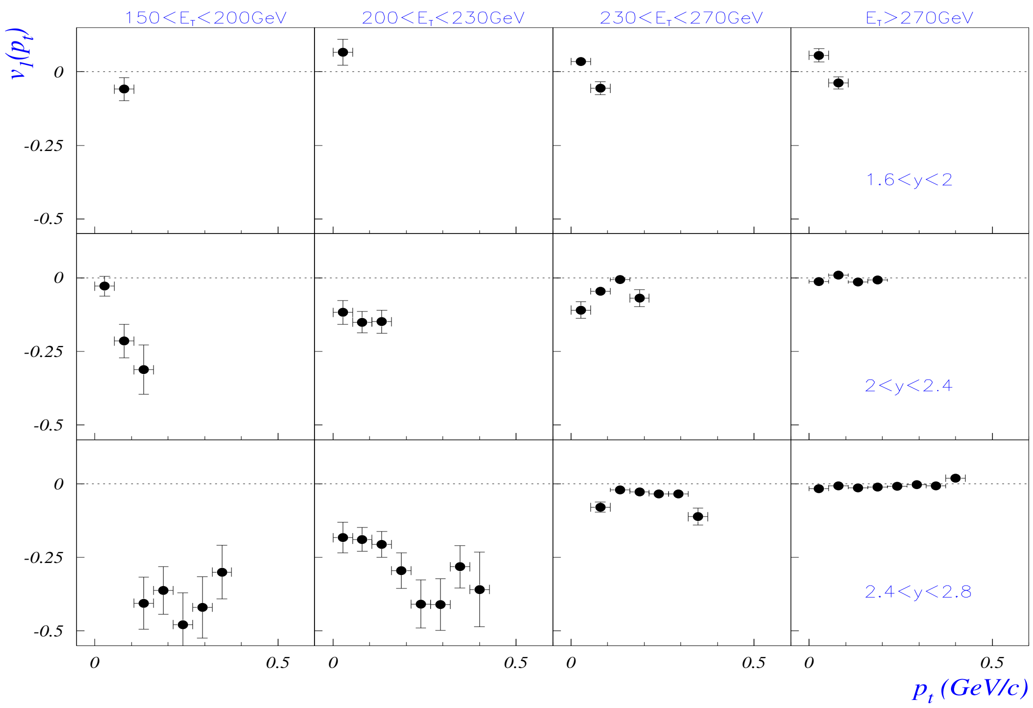

Figure 7.23: $v_1(p_t)$ for negative kaons. The values of $v_1(p_t)$ are corrected for the reaction plane resolution.

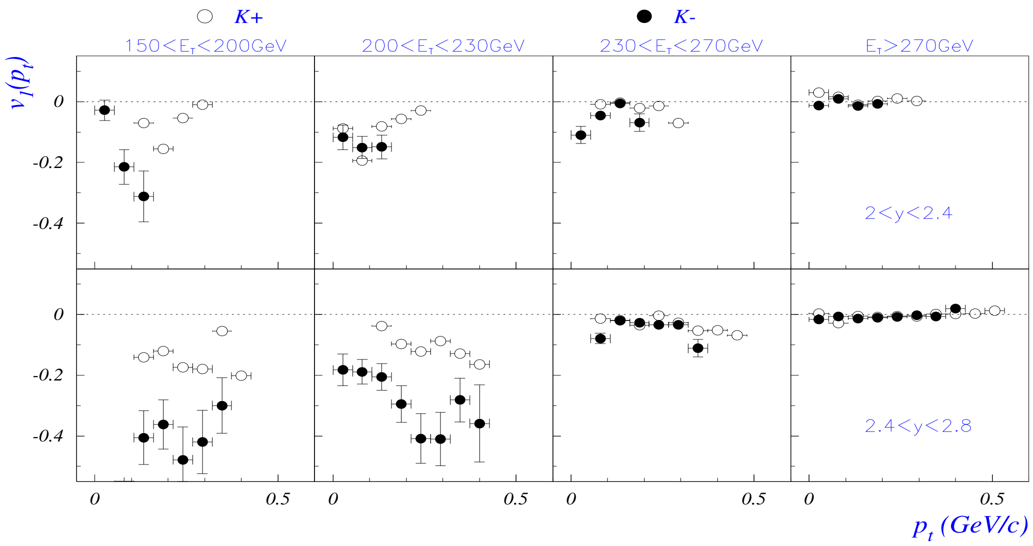

Figure 7.24: Comparison of $v_1(p_t)$ between positive and negative kaons.

Table 7.4: Results of directed flow parameter v_1 of $K^{\pm}$ for different centralities. The values of v_1 shown in this table are taken from the results of shown in Fig. 7.20 and Fig. 7.21, and are corrected for the reaction plane resolution. The values in the brackets represent the estimated errors.

PCAL E_T(GeV)	150-200	200-230	230-270	>270
v_1 (K^+)	-0.027(0.005)	-0.029(0.003)	-0.025(0.004)	-0.012(0.003)
v_1 (K^-)	-0.060(0.015)	-0.036(0.011))	-0.016(0.007)	-0.002(0.006)

the directed flow of both kaons is observed at all the rapidities covered by the E877 spectrometer. At rapidity $2.4 < y < 2.8$, the flow of K^- increases towards more negative values with increasing p_t and possibly reaches its minima at $p_t \sim 0.3$ GeV. The flow of K^+ seems to exhibit a similar trend. This conclusion is quite tentative due to the limited p_t coverage of the spectrometer. Because of the limited acceptance coverage and statistics, it is difficult to draw a conclusion regarding the rapidity dependence of v_1 for both kaons.

Fig. 7.24 shows the comparison of $v_1(p_t)$ between K^+ and K^-. Although the directed flow for both kaons is almost the same in central collisions ($E_T > 230$ GeV), it is observed to be much stronger for K^- in semi-central collisions.

7.3.3 Comparison with RQMD model

Fig. 7.25 shows the comparison of $v_1(p_t)$ for K^+ between the data and the predictions of RQMD (both in the mean-field and cascade mode). At forward rapidity ($2 < y < 2.8$) and low p_t ($p_t < 0.6$ GeV), both the data and the RQMD calculations display very small directed flow for the most central collisions. However, the data shows a significant negative directed flow in semi-central collisions whereas RQMD in the mean-field (cascade) mode predicts vanishing (small negative) directed flow. Similar discrepancy is also observed for K^- (see Fig. 7.26).

At the AGS, the primordial negative kaons are mainly produced through the channel $NN \to K^+K^-NN$ and are not expected to exhibit significant directed flow signature[123]. During the propagation, the primordial kaons undergoes elastic (such as $K^-N \to K^-N$) and inelastic (strange-exchange processes such as $K^-N \to \Lambda\pi$ and $K^-N \to \Sigma\pi$) collisions with baryons. These interactions eventually modify the distributions of K^- significantly because of the large baryon density reached at the AGS. In particular, in the projectile (or target) rapidity, the emission of K^- is expected to be strongly affected by the absorption and rescattering with the spectator nucleons. This probably explains the experimental observation of the strong centrality dependence of K^- directed flow in this rapidity region. The observed strong negative flow for K^- implies the important role of K^- absorption and rescattering in the dense nuclear medium.

At the AGS, positive kaons are mainly from the associate production mode $NN \to \Lambda K^+N$. The primordial positive kaons are thus expected to follow more closely the nucleon flow. However, the final flow pattern of the emitted positive kaons might be very much different because the produced positive kaons, as the negative kaons, suffer a lot of rescattering and/or absorption during their propagation in the dense nuclear matter. The difference of the directed flow between K^+ and K^- in semi-central collisions could indicate that K^+ suffers less from absorption and rescattering. It could also be due to the initial flow contribution carried by K^+ from nucleons.

It is possible that the actual rescattering and/or absorption might not as be significant as expected. This might be particularly true for K^+ since theoretical studies[125] at lower energies ($<$ 2 GeV) indicate that rescattering only explains part of the effect observed in the experimental data at these energies. If so, some other mechanism might have to be introduced. A possible candidate is the mean KN potential suggested by Refs.[122, 123]. The introduction of a strong repulsive

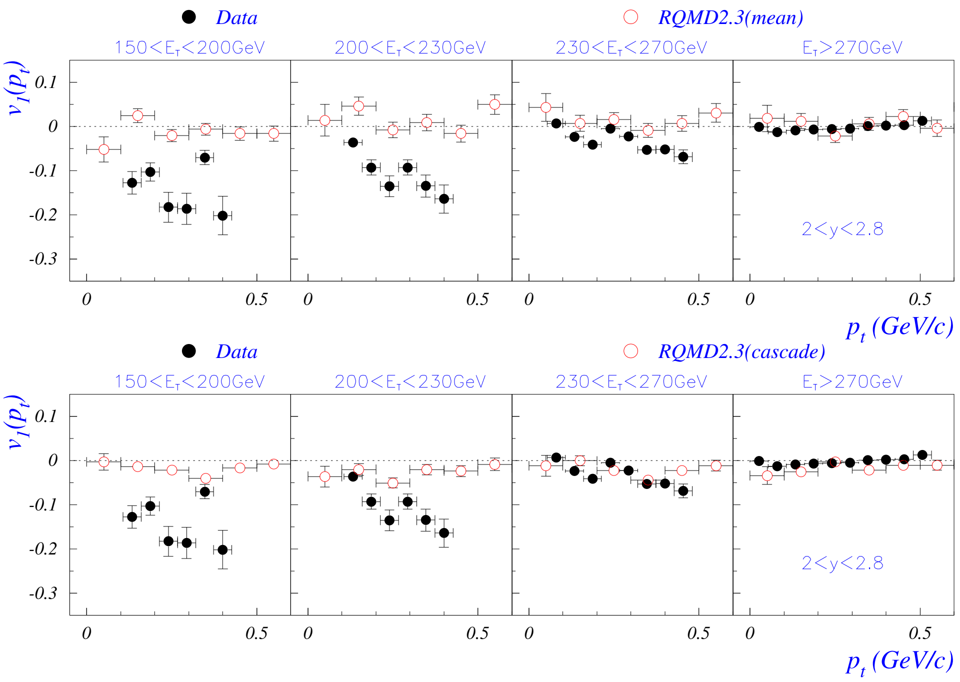

Figure 7.25: Comparison of $v_1(p_t)$ between the data and RQMD calculations for K^+. The upper panel shows the comparison between the data (filled circles) and RQMD calculations (empty circles) in the mean-field mode; the lower panel shows the same comparison with RQMD in the cascade mode.

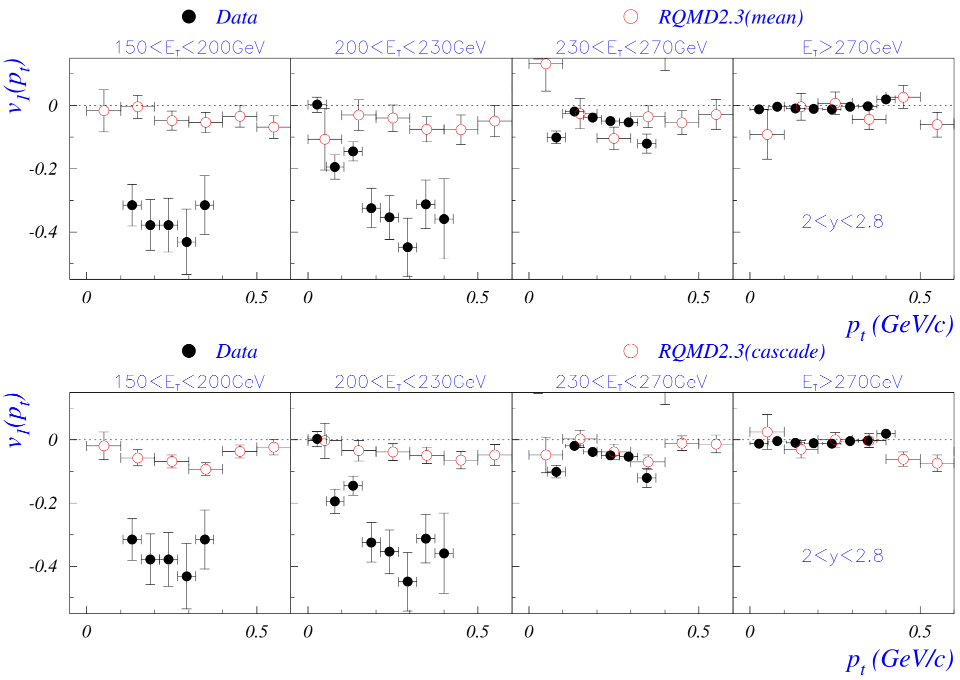

Figure 7.26: Comparison of $v_1(p_t)$ between the data and RQMD calculations for K^-. See Fig. 7.25 for the description.

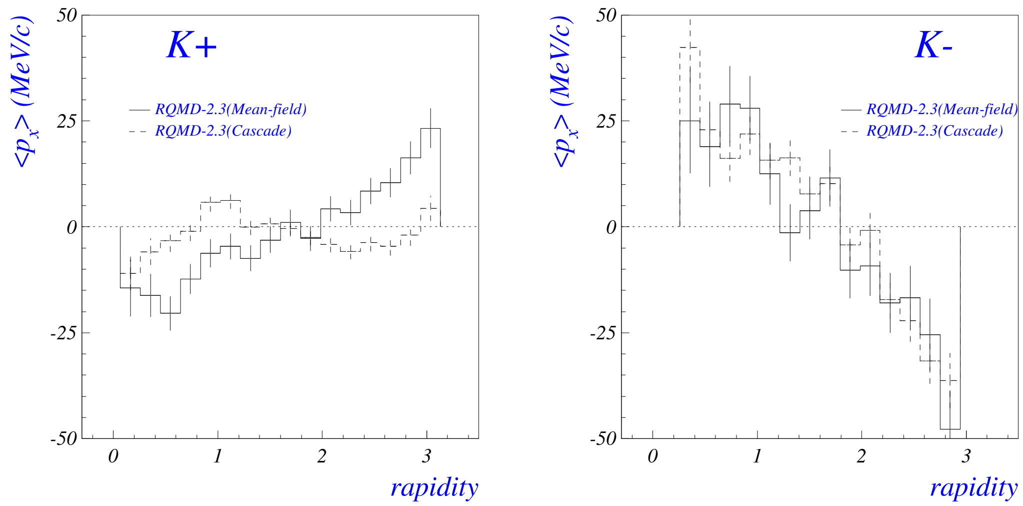

Figure 7.27: Directed flow ($\langle p_x(y)\rangle$) as a function of rapidity for K^+ and K^- predicted by RQMD-2.3 in Au+Au collisions ($b < 7$ fm) at 11.5 AGeV/c.

KN potential for K^+ could produce enough amount of "antiflow" for K^+, however, such potential would result in a stronger attractive force for K^- and thus reduce the "antiflow" for K^- by a significant amount. The role of the KN potential and the kaon absorption (and/or rescattering) needs to be further investigated particularly for the extreme dense nuclear matter achieved at the AGS. The present data may help in such investigation.

As is shown in Fig. 7.25 and Fig. 7.26, the present RQMD models simply fail to reproduce the significant "antiflow" for both kaons in semi-central collisions. Fig. 7.27 shows the average transverse momentum $\langle p_x(y)\rangle$ in the reaction plane as a function of rapidity calculated by RQMD for both K^+ and K^-. It is interesting to notice that in the forward rapidity region the inclusion of the mean-field potential in RQMD changes $\langle p_x\rangle$ of K^+ from small negative to positive whereas that potential has little effects on the directed flow of K^-. The change in behavior exhibited by the mean-field calculation for K^+ completely contradicts our directed flow results.

7.4 Directed Flow of Antiprotons

The enhanced production of antiprotons (and other antibaryons) in relativistic heavy-ion collisions has long been proposed as a possible signature of the phase transition from the hadronic matter to a quark-gluon plasma[48]. Enhanced production of antiprotons ($\bar{p}$) may also indicate strong, density independent mean field effects[129]. The final yield of antiprotons observed by experiments is, however, a result of both the elementary production in baryon-baryon interactions and the subsequent annihilation with baryons in the nuclear matter. The enhanced production of antiprotons might be significantly offset by the strong annihilation of antiprotons in the extreme dense baryon environment[130] reached at the AGS.

The large annihilation probability of antiprotons with baryons (particularly at low relative momentum) would result in a considerable distortion in the momentum distribution of antiprotons. In a non-central heavy-ion collision, nucleons are preferentially emitted along the impact parameter vector. Antiprotons co-moving with those nucleons would suffer a greater probability of annihilation and rescattering from them, resulting in an anticorrelation with the nucleon directed flow - the so-called "antiflow" of antiprotons in nuclear collisions predicted by A. Jahns et. al.[132]. Measurement of the directed flow of antiprotons is important to understand the role of annihilation in dense nuclear matter and would provide new insight into the dense baryon regions of the collision. Furthermore, measurement of the directed flow of antiprotons would also shed light on the understanding of anti-quark productions in dense nuclear matter, such as the $\bar{\Lambda}/\bar{p}$ ratio recently observed at the AGS and SPS [134, 135, 136, 137].

Measurement of the directed flow of antiprotons is a difficult task because of the extremely limited statistics of antiprotons available from the data. In this section, we will present the experimental study of the directed flow of antiprotons. This work is based on the statistics of nearly 60 million Au+Au central events.

7.4.1 Antiproton identification

Fig. 7.28(a) shows the acceptance in phase space covered by the E877 spectrometer for antiprotons. The E877 spectrometer mainly covers the low p_t region ($p_t < 0.5$ GeV/c) at forward rapidities ($1.6 < y < 2.5$). To reduce the background in the identification of antiprotons, tracks are required to have matching measurements (within $2.5\sigma_{dx}$, see Section 5.2 in Chapter 5) in the two upstream VTX detectors. Tracks are also required to have complete y-information in both drift chambers. Fig. 7.28(b) shows the mass distribution of antiprotons ($p < 4$ GeV/c) when these stringent track selection criteria are applied. The antiproton ($\bar{p}$) mass peak is centered at 932 MeV/c^2 and has a resolution of $\sim$40 MeV/c^2.

Table 7.5: Background contamination in the selection of antiprotons. The second row represents the contribution from background. The background contribution is calculated by comparing the area of the background falling within $\pm 1.5\sigma_{m^2}$ window about the center of each Gaussian peak.

Momentum range (GeV/c)	1-2	2-3	3-4	4-5	< 4
Background(%)	~ 0	< 25	< 45	> 150	< 30

Shown in Fig. 7.28 is also a study on the background in selecting antiprotons for different momentum ranges. The contribution of the background increases with momentum and becomes dominant at $p > 4$ GeV/c. A possible major source of the background is from K^-. A maximum momentum of 4 GeV/c is required in the identification of antiprotons based on a compromise between the signal and the background. The selected antiprotons are required to fall within $\pm 1.5\sigma_{m^2}$ around the center of the $\bar{p}$ mass peak. The assumed mass resolution used is that of the proton

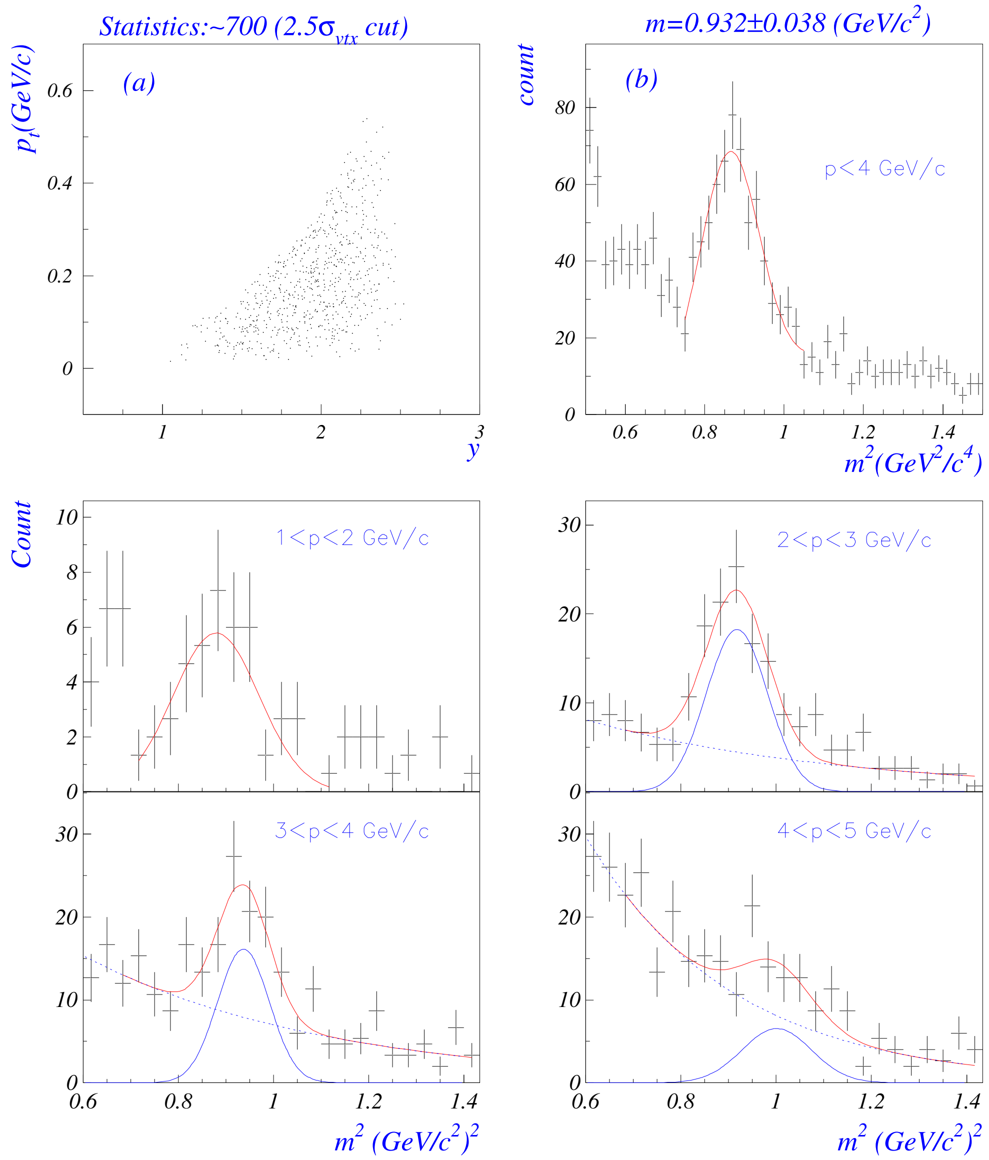

Figure 7.28: Particle identification of antiprotons for different momenta. (a) is the acceptance in phase space covered by the E877 spectrometer for antiprotons; (b) shows the squared-mass spectrum in the antiproton peak region. The other histograms show the same spectrum in different momentum ranges: the antiproton peak is represented by a Gaussian whereas the background is approximated by an exponential distribution.

peak given by Fig. 5.5 in Chapter 5. A total statistics of ~700 antiprotons have been selected. Table 7.5 shows the background contamination in selecting antiprotons for different momentum ranges. For $p < 4$ GeV/c, the average antiproton to background ratio is greater than 3:1.

7.4.2 Antiproton directed flow results and discussion

Fig. 7.29 shows the azimuthal distributions of antiprotons with respect to the reaction plane measured in the forward rapidity ($1.6 < y < 2.6$) for three different centralities. Taking into account that the resulting distributions have to be symmetric about $\phi - \psi_r = 0$ and to reduce statistical fluctuation the data from in the angular range $[-\pi,0]$ have been added to the data in the range $[0,\pi]$. For presentation purpose the resulting data have been reflected about $\phi - \psi_r = 0$ (open circles in Fig. 7.29). It should be pointed out that the application of this technique is based on the observation that the original (before reflection) distributions are symmetric within error about $\phi - \psi_r = 0$. The selection of the centrality window is done to equalize the statistics between different centrality regions. The definition of these centrality windows is given in Table 7.6. A pronounced minima at $\phi - \psi_r = 0$ are clearly observed in the azimuthal distributions for $E_T < 280$ GeV, indicating that antiproton production is strongly anti-correlated with that of nucleons in semi-central collisions.

Fig. 7.30 shows the same azimuthal distributions but with only one of the two upstream VTXs being used in track matching. This relaxed particle selection criteria increases the background by ~50%. Distributions in both figures are fitted with the function given by Eq. (7.6). Table 7.6 presents the extracted directed flow parameter v_1 after being corrected for the reaction plane resolution. At the forward rapidity, the antiproton directed flow is observed to be strongly negative in semi-central collisions whereas it becomes very small for the most central collisions. With more background

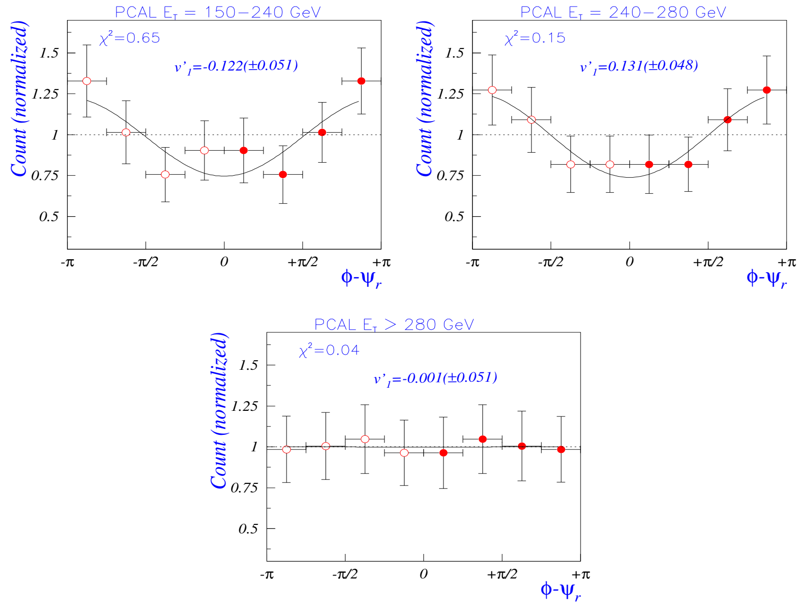

Figure 7.29: Antiproton azimuthal distributions measured in the forward rapidity for different centralities. The data are integrated over the phase space of $1.6 < y < 2.6$ and $p_t < 0.5$ GeV/c (see Fig. 7.28 for the acceptance coverage). Empty circles are the reflection of filled circles about $\phi - \psi_r = 0$.

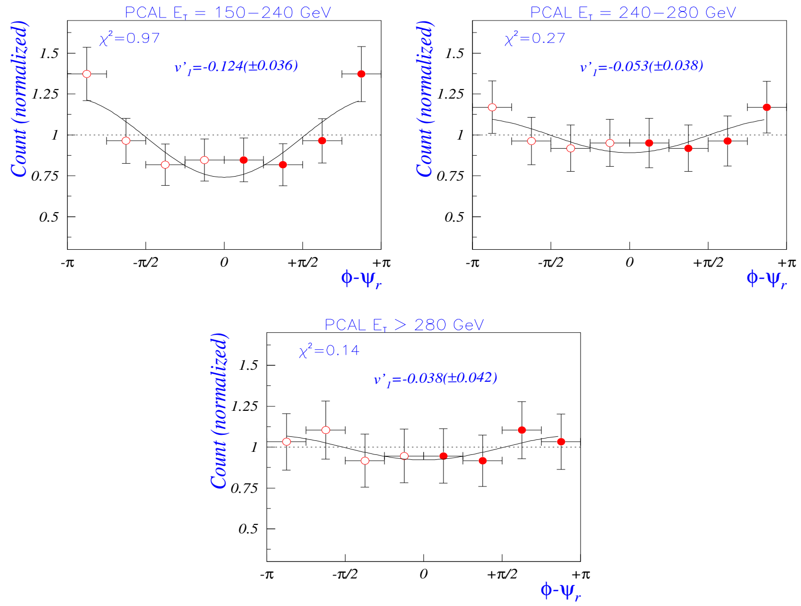

Figure 7.30: Antiproton azimuthal distributions measured in the forward rapidity for different centralities. Track matching is only required at one of the two upstream VTXs.

Table 7.6: Results of directed flow parameter v_1 of $\bar{p}$ for different centralities. The values of v_1 shown in this table are taken from the fitted results of v_1' shown in Fig. 7.29 (second row) and Fig. 7.30 (third row), and are corrected for the reaction plane resolution. The values in the brackets represent the errors.

PCAL E_T(GeV) ($\sigma_{top}/\sigma_{geo}$)	150-240 (23-8%)	240-280 (8-4%)	>280 (< 4%)
v_1 (both VTXs)	-0.16(0.07)	-0.20(0.07)	-0.00(0.09)
v_1 (One VTX)	-0.16(0.05)	-0.10(0.06))	-0.07(0.08)

contamination (mainly from K^-) using only one VTX for track matching, the flow signal remains nearly unchanged at the centrality $150 < E_T < 240$ GeV, but decreases by almost half at the centrality $240 < E_T < 280$ GeV. This behavior can be understood from the kaon flow result obtained in the previous section: the directed flow of K^- is comparable to that of antiprotons at the first centrality, but smaller for the second centrality window. This comparison makes us more comfortable to conclude that that the data in Fig. 7.29 indeed are dominated by the directed flow signal of antiprotons.

Fig. 7.31 shows the trend in the p_t dependence of the directed flow results of antiprotons. One notices that the flow signal first increases to a large negative value reaching a maximum at $p_t \sim 200$ MeV/c, and then decreases as a function of p_t. Fig. 7.32 shows the rapidity dependence in the antiproton directed flow results. The directed flow results for protons are shown on the same plot for comparison. It is observed that antiproton directed flow vanishes at mid-rapidity and its rapidity dependence is anti-correlated to that of the proton flow. It is also observed that the strength of antiproton flow is nearly $2 \sim 4$ times larger than that of the proton at the same rapidity. Note , however, that the observed rapidity and p_t dependence shown in Fig. 7.31 and Fig. 7.32 is acceptance biased since p_t acceptance changes rapidly with rapidity (see Fig. 7.28).

It is interesting to notice that the maximum asymmetry occurs at approximately $p_t \sim 200$ MeV/c. The annihilation probability for an antiproton mainly depends on two factors: the annihilation cross section which is strongly dependent on the relative kinetic energy of the antiproton, and the baryon density. Antiprotons at lower p_t (or lower energy for a prefixed rapidity) tend to have a greater probability to be absorbed and the strongest absorption (the most significant anisotropy) should occur where the highest baryon density has been reached.

Fig. 7.33 shows the directed flow ($\langle p_x(y) \rangle$) for antiprotons predicted by RQMD in the cascade mode. For comparison the same predictions by both the cascade and mean-field modes for protons are also shown. Due to insufficient statistics, the predictions by the mean-field mode for antiprotons are not shown here. One observes that the predicted directed flow for antiprotons is nearly three (six) times larger than that predicted by the cascade (mean-field) mode for protons at the same rapidity. This prediction seems consistent with our results even if due to poor statistics a direct comparison is not possible.

The directed flow of antiprotons measured here could be the sum of the flow from the primary antiprotons (directly produced in NN collisions or other production mechanisms) and antiprotons from antihyperon decays such as $\bar{\Lambda}$, $\bar{\Sigma}$. Due to the experimental setup, the E877 spectrometer is not able to separate the primary antiprotons and those fed down from antihyperon decays. A previous study[138] based on a Monte Carlo simulation has shown that the probability of a secondary antiproton from a $\bar{\Lambda}$ decay to be detected by the E877 spectrometer is ~70% of that of a primary antiproton. A complementary measurement of the directed flow of antihyperons such as $\bar{\Lambda}$ in the future combined with the present observation would provide necessary information for the decoupling of the flow contribution of primary antipro-

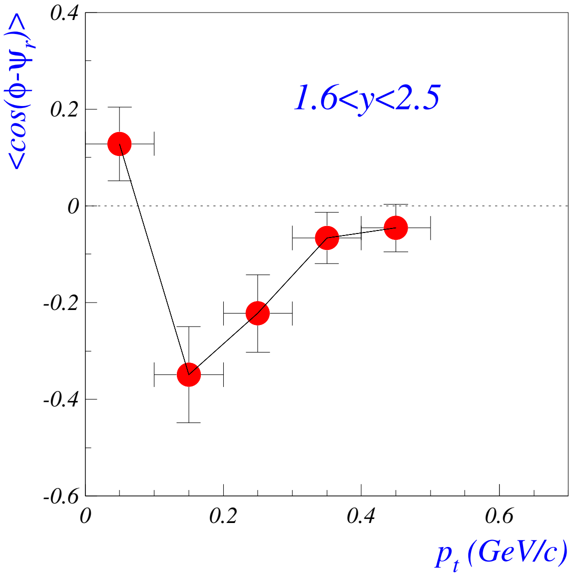

Figure 7.31: The p_t dependence of the directed flow ($\langle\cos(\phi - \psi_r)\rangle$) for antiprotons. The values of $\langle\cos(\phi - \psi_r)\rangle$ are integrated over the forward rapidity region $1.6 < y < 2.5$. Data points are connected by straight lines to guide the eye.

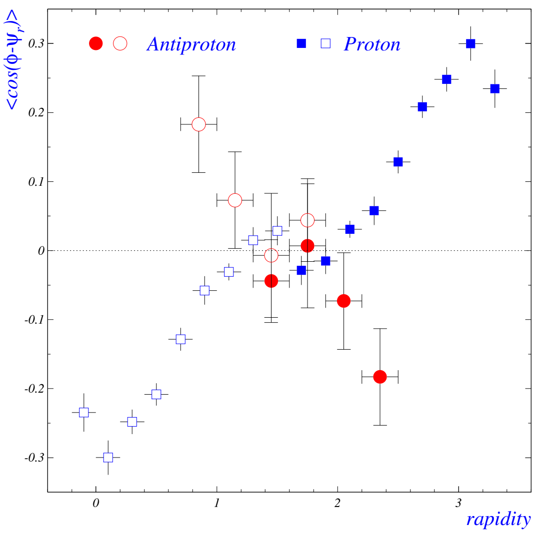

Figure 7.32: The rapidity dependence of the directed flow ($\langle\cos(\phi - \psi_r)\rangle$) for antiprotons. For comparison the results of the directed flow of protons are shown by squares. The values of $\langle\cos(\phi - \psi_r)\rangle$ for protons are corrected for both the reaction plane resolution and acceptance while those for antiprotons are corrected for the reaction plane resolution only. Empty symbols are the reflection of filled ones about mid-rapidity ($y = 1.6$).

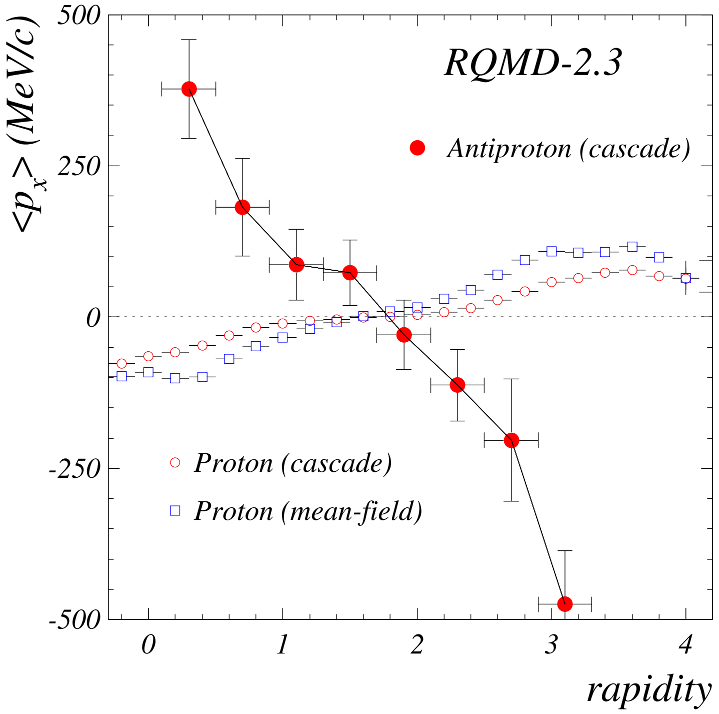

Figure 7.33: Directed flow ($\langle p_x(y) \rangle$) as a function of rapidity for antiprotons predicted by RQMD-2.3 (cascade) in Au+Au collisions (b <7 fm) at 11.0 AGeV/c. For comparison the predictions for protons are shown by empty symbols (circles for the cascade mode and squares for the mean-field mode). The lines connecting antiproton points are to guide the eye.

tons and that of antihyperons. Furthermore, the comparison between the directed flow behavior of these two contributions could give crucial information to understand the observed unexpected $\bar{\Lambda}/\bar{p}$ ratios[134, 135, 136, 137].

Chapter 8

Summary and Conclusions

In this thesis, the anisotropy in the azimuthal distributions of identified particles with respect to the reaction plane have been studied as a function of particle rapidity, particle transverse momentum and collision centrality in Au+Au collisions at 11.5 AGeV/c.

The present work includes the description of a new double-sided microstrip silicon detector used in the E877 experiment at the AGS. This detector provided a complete spatial information of the incident Au beam and its information was used in the study of Λ decay (not part of this thesis) and to improve the reaction plane determination as well as particle momentum measurements.

We have studied various experimental effects and developed new corresponding correction methods in the evaluation of the flow signal. In particular, the tracking efficiency loss due to the finite spatial resolution of the detectors is investigated and a method for recovering the lost efficiency on an event-by-event basis is developed. This correction strategy can also be applied to most tracking detectors used in other heavy-ion experiments. In the study of time-of-flight measurements, it is found that the systematic effect from 60Hz frequency have to be corrected for high-precision time measurements over a relatively long period of time. The unbiased transverse energy distributions are reconstructed from the measured distributions using the experimental trigger information to provide the event characterization information like collision centrality. Positional matching of reconstructed tracks using an new upstream vertex detector has been adopted to suppress backgrounds in the study of low-yield particles like kaons and antiprotons.

We have performed a systematic study on the resolution of the reaction plane and corrected the influence from nonflow effects including momentum conservation and calorimetric showers. The azimuthal distributions of identified particles with respect to the reaction plane are described by Fourier expansions and the anisotropy of the distributions is quantified by the Fourier moments corrected for the resolution of the reaction plane. The directed flow (the first Fourier component) is measured for a wide range of identified particles (protons, deuterons, charged pions, charged kaons and antiprotons). It is the largest in semi-central collisions and consistently decreases for the most central collisions.

The directed flow of protons and deuterons shows similar behavior and is observed to be strongly correlated with the reaction plane. Their directed flow signal (v_1) is interpreted in the hydrodynamic picture of a thermal source moving sidewards while expanding radially in the transverse plane. The transverse momentum and rapidity dependence of v_1 reflects the interplay between the radial expansion and the sideward motion, and the nearly linear p_t dependence of v_1 for both particles is well described by this simple model parameterized with the sideward velocity and the "effective temperature". Deuterons are found to have nearly the same average sideward velocity as protons and the systematically larger observed v_1 for deuterons is interpreted as due to the larger mass. The complicated rapidity and centrality dependence of the "effective temperature" for deuterons indicates that complex mechanisms are involved in the deuteron production.

The directed flow for both π^+ and π^- is observed to be anti-correlated to that of protons in the low p_t range. The complicated p_t dependence of v_1 for both pions reflects the complex reaction dynamics of pion production, reabsorption, rescattering as well as the flow characteristics of baryon resonances. The difference in v_1 between π^+ and π^- at p_t <200 MeV is qualitatively interpreted as the difference of the Coulomb interactions for the two pion species.

Based on nearly four times the statistics and higher quality data as compared to the previous work[71], we have re-investigated the directed flow of K^+ and K^-. We have observed a significant "antiflow" for both K^+ and K^- at forward rapidities in semi-central collisions. K^- exhibits a stronger "antiflow" probably due to the stronger absorption and/or rescattering during its propagation in the dense nuclear medium. The significant "antiflow" observed for K^+ at the AGS is contrary to the observations made at lower energies ($<$ 2 GeV) and indicates that a stronger KN potential might be needed to explain the data.

We have clearly observed, for the first time, a strong negative v_1 signal near projectile rapidity for antiprotons, showing that the emission of antiprotons is strongly anti-correlated with that of nucleons. The observed large "antiflow" for antiprotons indicates that a strong annihilation process is involved in the dense nuclear matter as predicted by previous theoretical studies[132, 133]. This observation will provide important information for the study of antimatter production in ultra-relativistic heavy-ion collisions both theoretically and experimentally.

RQMD (version 2.3) in the cascade mode correctly predicts the general trend of the directed flow observed for all the particles studied. In particular, the prediction of a strong "antiflow" for antiprotons is observed. However, this model fails to reproduce the strength of the flow for nearly all the particles. Including the mean-field mechanism, RQMD agrees better with the experimental results for protons and pions, but the discrepancy is still significant. The over-prediction of v_1 for protons (deuterons) at low p_t near the projectile rapidity indicates that the RQMD model (in both the cascade and mean-field modes) seems to underestimate the rescattering contribution from spectators. More importantly, the attractive characteristics exhibited by the mean-field potential for K^+ completely contradicts the significant "antiflow" we have observed for this particle species. The applicability or validity of the mean-field potential for particles other than nucleons and pions needs to be investigated.

The collision system at the AGS exhibits strong nuclear hydrodynamic effects. Directed flow of nucleons (light nuclei) and pions continues to be important for the study of the nuclear equation of state (EoS) or mean-field properties. However, the study of the flow phenomena for strange matter and antimatter starts to go beyond the hydrodynamics context. Due to the completely different interaction mechanisms, the initial directed flow signature carried by strangeness or antimatter might be completely lost due to the strong absorption and/or rescattering in the dense nuclear matter and in the end the directed flow pattern, or to say more precisely, the azimuthal asymmetry could carry little information about the EoS. Nevertheless, the study of the azimuthal asymmetry reveals the interplay between complicated mechanisms such as production, absorption, rescattering etc. The general method of directed flow will continue to be a powerful tool for the future experiments to study the non-equilibrium aspect of the collision system at RHIC and LHC.

Appendix A

Definitions of Some Global Variables

The rapidity variable y is defined as

$$y = \frac{1}{2} \ln \left(\frac{E + p_z}{E - P_z} \right) = \frac{1}{2} \ln \left(\frac{1 + \beta \cos \theta}{1 - \beta \cos \theta} \right) \tag{A.1}$$

The pseudorapidity variable η is defined by

$$\eta = \frac{1}{2} \ln \left(\frac{p + p_z}{p - p_z} \right) = \frac{1}{2} \ln \left(\frac{1 + \cos \theta}{1 - \cos \theta} \right) = - \ln \left(\tan \frac{\theta}{2} \right) \tag{A.2}$$

The relation between θ_{lab} and θ_{CM} is

$$\ln \left(\tan \frac{\theta_{CM}}{2} \right) = -(\eta_{lab} - \eta_0) = \ln \left(\tan \frac{\theta_{lab}}{2} \right) + \eta_0 \tag{A.3}$$

where η_0 is the center-of-mass pseudorapidity of the system.

Appendix B

Modified Bessel Functions

The modified Bessel function is defined by

$$I_\nu(z) = \sum_{k=0}^{\infty} \frac{1}{k!\Gamma(k+\nu+1)} \left(\frac{z}{2}\right)^{2k} \qquad (|z| < \infty, |\arg(z)| < \pi) \tag{B.1}$$

where $\Gamma(k+\nu+1)$ is the Gamma function.

In particular,

$$I_0(z) = \sum_{k=0}^{\infty} \frac{(\frac{z}{2})^{2k}}{(k!)^2} \qquad I_1(z) = I_0'(z) = \sum_{k=0}^{\infty} \frac{(\frac{z}{2})^{2k+1}}{k!(k+1)!} \tag{B.2}$$

and

$$I_{\frac{1}{2}}(z) = \sqrt{\frac{2}{\pi z}} \sinh(z) \qquad I_{-\frac{1}{2}}(z) = \sqrt{\frac{2}{\pi z}} \cosh(z) \tag{B.3}$$

Functions of higher orders can be derived by using the relation

$$zI_{\nu-1}(z) - zI_{\nu+1}(z) = 2\nu I_\nu(z). \tag{B.4}$$

Appendix C

Performance of the Beam Detectors and TOFU

In this appendix, the performance of two new Čerenkov Beam SCIntillators(BSCI) installed in the E877 setup in the fall of 1995 are described. The four signals from the two detectors have an intrinsic time resolution of around 30$\sim$50ps. The combination of all four time signals from the two detectors achieves a startup time resolution as good as $\sim$20ps for the Time-Of-Flight Upgrade (TOFU) System. With this start time, the average time-of-flight resolution obtained from identified pions is estimated to be $\sim$90ps for the whole TOFU hodoscope. Relevant effects on timing from the new detectors are studied. Finally, the corrections made for getting the optimum timing are discussed.

C.1 Čerenkov Beam Scintillators

C.1.1 Čerenkov beam scintillators

The Beam SCIntillator detector (BSCI) in the 1995's running period is composed of 4 detectors equipped with photo-multipliers. They are denoted as S1, S2, S3 and S4 in Fig. 2.1 (Chapter 2). These detectors are designated to provide a start time reference information for the event and to discriminate beam particles. S1 and S3 are plastic scintillators, having a "donut" shape with a hole at the center and working as veto counters. S2 and S4, being made of two Čerenkov quartz radiators, were upgraded for the 1995 experimental run. Each quartz crystal has a dimension of 3 *inch* long by 2 *inch* wide with a thickness of $(200\pm2)\mu$m[139]. S2 and S4 were used to define a 'good' beam particle. Each Čerenkov radiator is seen by two photomultipliers labeled as S_{21}, S_{22}, S_{41} and S_{42} respectively. These photomultipliers installed on each side (in the x direction) of the radiator (see Ref.[59] for details on these detectors).

C.1.2 Time-Of-Flight Upgrade electronics

Fig. C.1 shows a block diagram of the E877 time-of-flight electronics system. Beam logic module generates beam particle definition signal using the logic $\bar{\mathrm{S}}1\times\mathrm{S}2\times\bar{\mathrm{S}}3\times\mathrm{S}4$. Five FASTBUS TDC modules (LeCroy 1875A) are used to digitize signals from the TOFU system which consists of 148 scintillator slats with each slat having two phototubes at both ends. Each FASTBUS TDC module has 64 channels with a resolution of around 25ps. Four out of the 64 channels of each module are assigned to the time measurements from the four phototubes (S21,S22,S41 and S42) of S2 and S4, and the other 60 channels are left for the TOFU time signals. The time information from the BSCI was also measured using CAMAC TDC (Model 2228A) module with a time resolution of 50ps. This TDC unit was dedicated to the measurement of the 60Hz waveform for each event. In 1995 running period, the signal from S41 was used as the common start for all TDC modules.

C.1.3 Time calibration of FASTBUS TDCs

The FASTBUS TDCs are calibrated using pulses generated by a time calibrator. The calibrator generated precisely defined pulses in random at eight different time intervals expanded with a multiple of 10ns. The spread in the time measurement is mainly attributed to the noises of the electronic modules and jitters in the TDCs..

Time calibration constants are obtained with each 10ns interval divided by the average number of channels between any two adjacent peaks. The obtained constants shown in Fig. C.2 are between 24$\sim$26 ps/channel.

A comparison between the 1994's and 1995's calibration constants is also shown in Fig. C.2. The time calibration constants in 1995 are almost the same as those in 1994 except for a very small systematic shift in FASTBUS module No.1.

C.1.4 Beam scintillator: pulse height distributions

A sample of the four BSCI ADC outputs without any corrections is shown on Fig. C.3. The two pulse height distributions from S2 have Gaussian shapes while the two from S4 show very non-Gaussian distributions. Double beam effects are small but obvious. Single beam and double beam events are well-separated especially in S22.

The ADC pedestal (not shown in Fig. C.3) is estimated by acquiring MT events (those with no beam present in the apparatus). In the experiment, the signals from detectors picked up noises from power cables and caused signals (or pedestals) to fluctuate with 60Hz frequency. A timer with a 2.5MHz clock was used to keep track of 60Hz phase. It is observed that the pedestals of all four ADCs are quite stable against 60Hz with fluctuations of the order of one channel. Fig. C.4 shows the

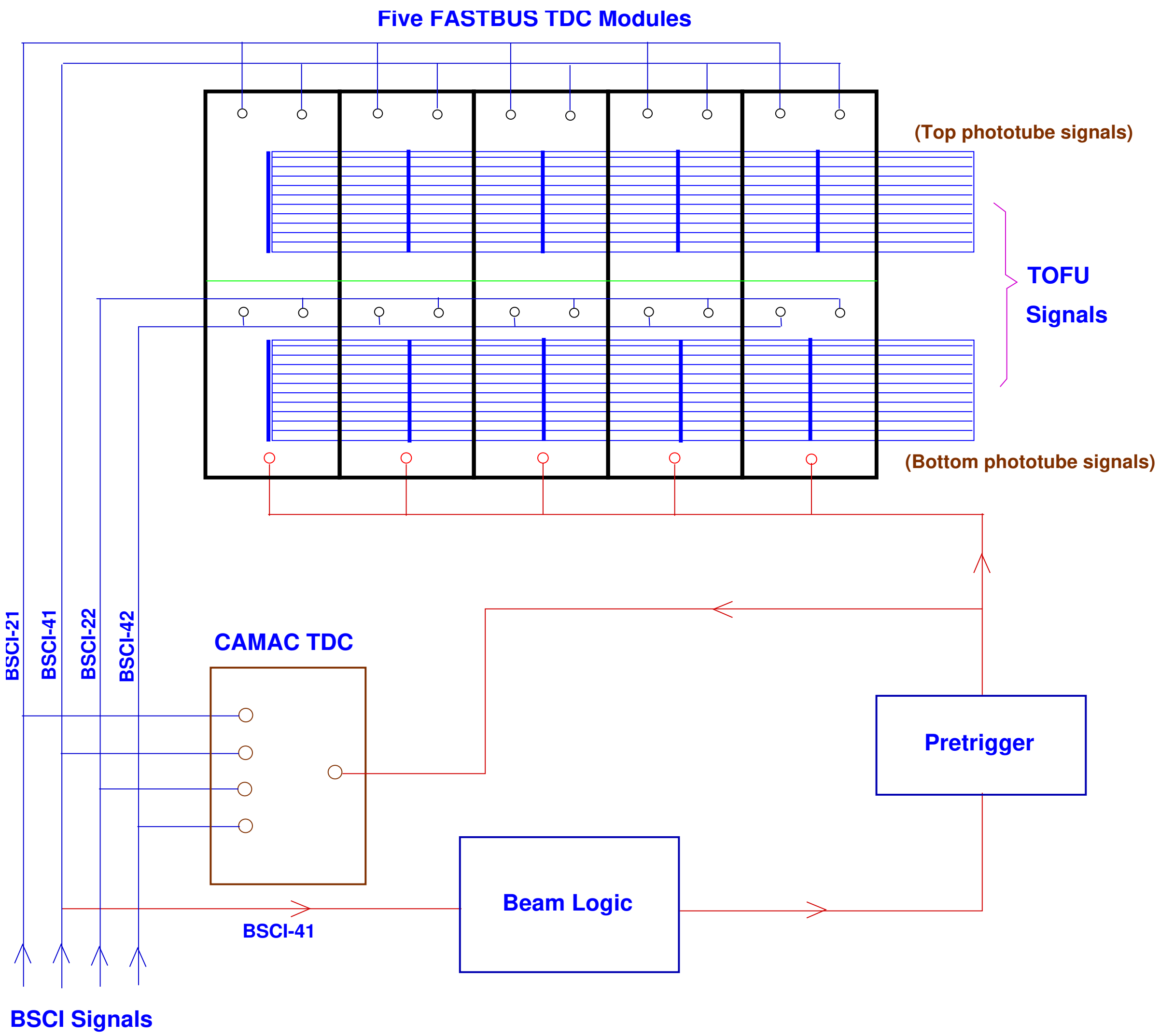

Figure C.1: Block diagram of E877 time-of-flight electronics system

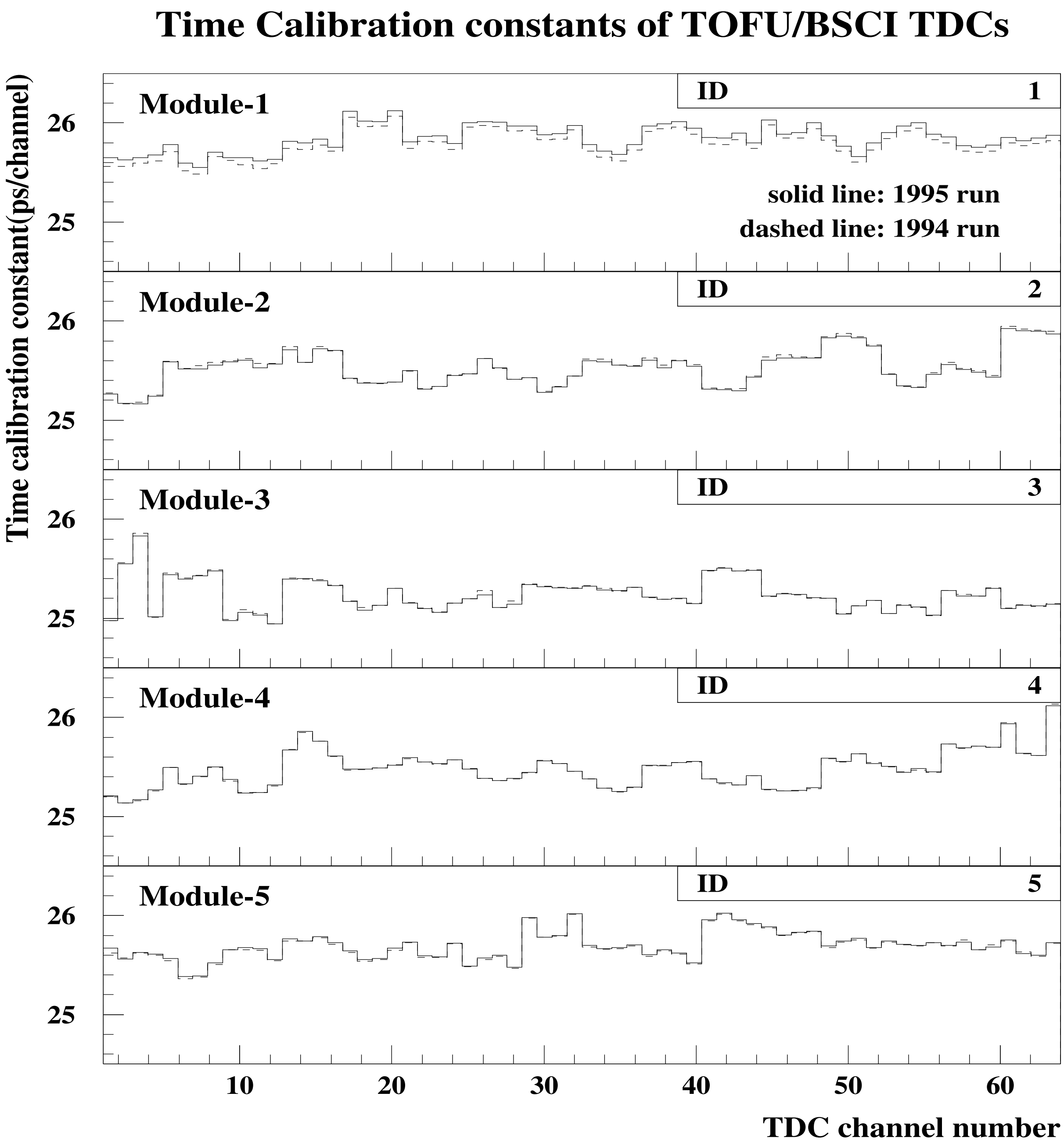

Figure C.2: FASTBUS TDC time calibration. Each FASTBUS module has 64 channels. For each module, the first two channels are assigned to S21 and S41 signals respectively and the following 30 channels for 30 TOFU top-end phototube signals. Channel-33 and Channel-34 are assigned to S22 and S42 signals respectively, and the last 30 channels for 30 TOFU bottom-end phototube signals.

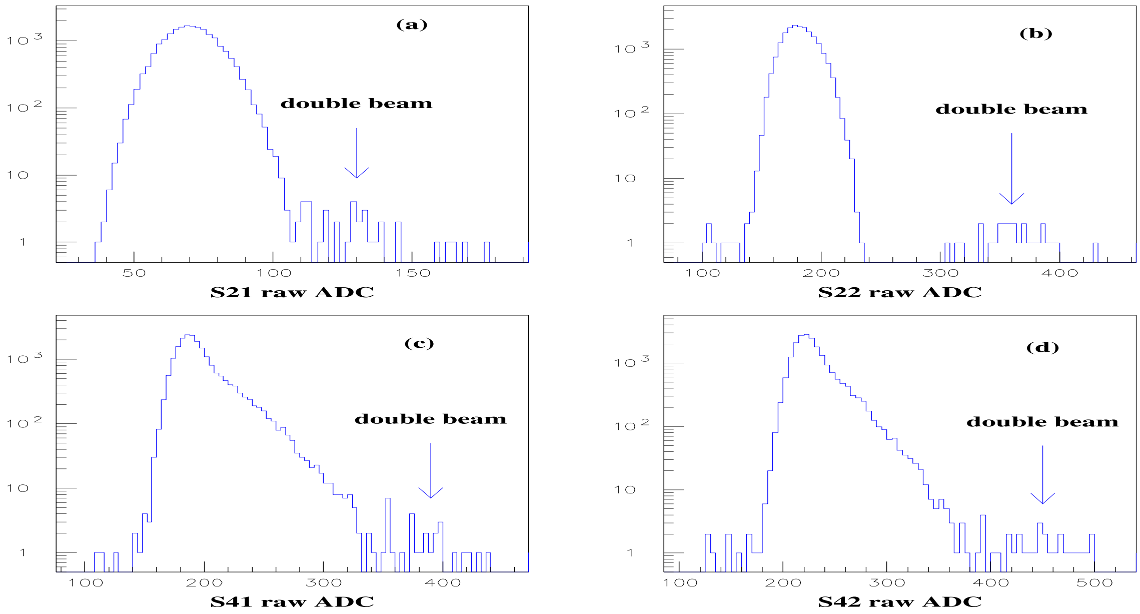

Figure C.3: Pulse height sum of four BSCI phototubes

pedestals of the four BSCI ADCs as a function of the 60Hz phase. The horizontal axis represents the relative 60Hz phase at the moment one event was recorded. The range from 0 to 1 of the 60Hz phase showed in Fig. C.4 represents an actual range from 0 to 2π.

Fig. C.5 shows the correlation between the pulse heights and the beam particle positions on the detectors. The positions are derived from the angular and positional information provided by the two-dimensional beam vertex (BVER) detector (see Chapter 3). From Fig. C.5, one observes that the positional effect on S4 is smaller than that on S2 since the beam is more focused on S4. Unexpectedly, one observes that the pulse heights of S21 and S22 show the same tendency with respect to beam particle positions. For an ideal scintillator with produced photons being collected at both ends, the end which is closer to the location where the beam particle hits is expected to collect more photons. In that case we would expect the pulse heights of S21 and S22 would show opposite tendencies with respect to the positions. Our

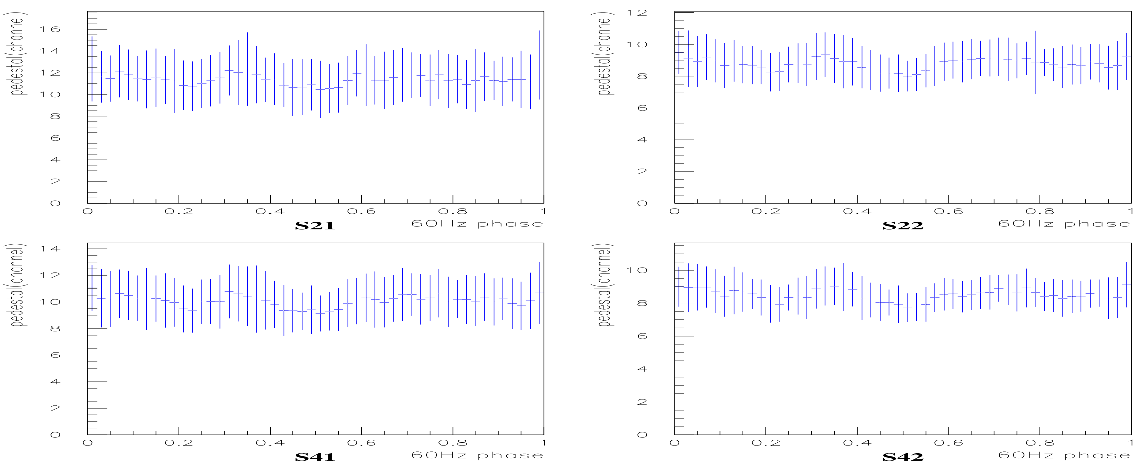

Figure C.4: Pedestals of the four BSCI ADCs vs 60Hz phase. The error bar represents the width of the pedestal peak.

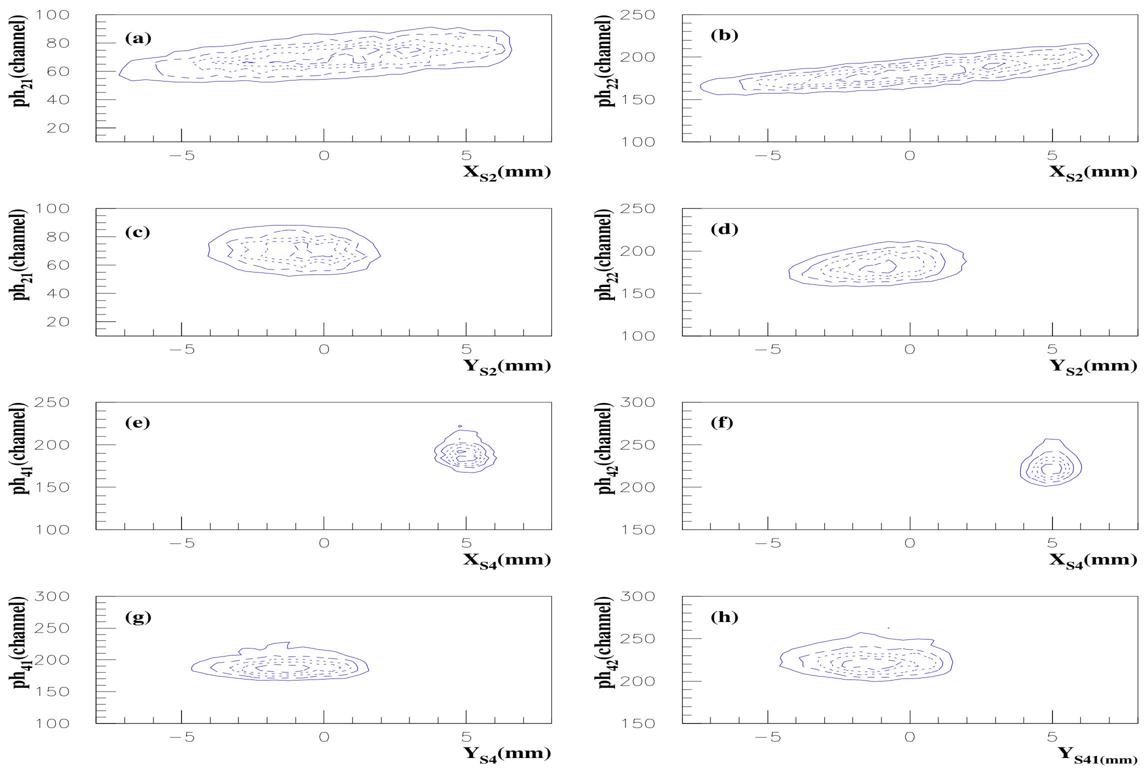

Figure C.5: Contour plots of correlations between BSCI pulse heights for each phototube of S2 and S4 and beam particle positions.

explanation of the present observation is that the effect is related to the properties of the S2 crystal itself. The non-uniformity of the crystal could make quantum efficiency of the production of Čerenkov photons position-dependent; the tilt of the quartz crystal (its surface not perpendicular to the beam axis) could also cause the unequal Čerenkov light collection at the two ends.

C.2 Beam Scintillator: Time Information

Leading-edge discriminators are used to generate time signals. A time signal is generated whenever the leading edge of a signal rises above the given threshold of a discriminator. The relative time to cross a given threshold becomes smaller when the signal becomes larger and vice versa. Consequently the measured time depends on pulse height; this effect is the so-called *slewing effect*. The time spread of a pulse height is mainly due to three factors. The first one is its intrinsic spread due to quantum efficiency. The second one is due to fluctuations in the PMTs. The change of HV or other working conditions would alternate the pulse height. The third one in our case is the beam positional spread on the detectors. Because the light collection efficiency is a function of the beam particle positions, the pulse height changes as a function of the positions.

An effective and widely-used method of correcting the slewing effect is by using a semi-empirical formula:

$$t^{corr.} = t - \frac{B}{\sqrt{ph^{corr.}}} + A \tag{C.1}$$

where

$$ph^{corr.} = ph - \text{pedestal} - f_{ped}(phase) \tag{C.2}$$

is the corrected pulse height (pedestal subtracted and 60Hz dependence corrected). A and B are constants to be determined. t and $t^{corr.}$ are the uncorrected and corrected

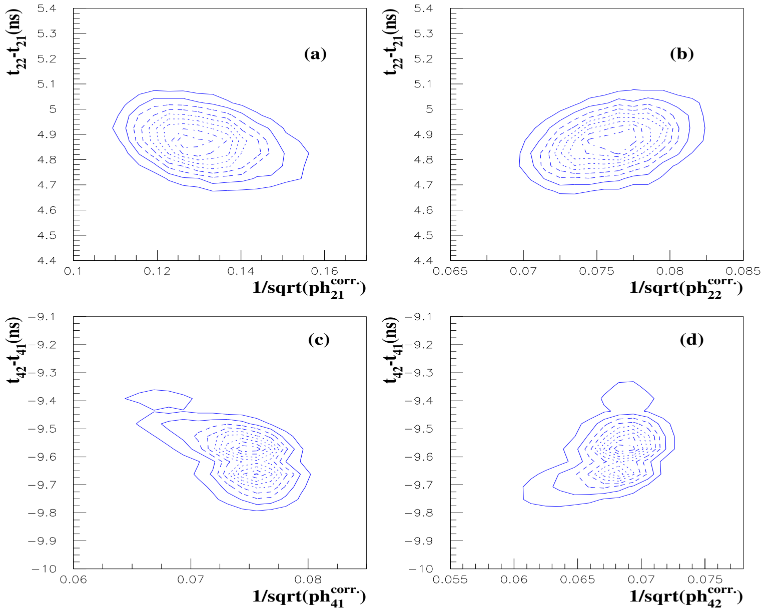

Figure C.6: Examples of slewing effects in BSCI time signals. $ph_{21}^{corr.}$, $ph_{22}^{corr.}$, $ph_{41}^{corr.}$ and $ph_{42}^{corr.}$ are the corrected pulse heights given by Eq. (C.2).

time measurements respectively.

In the experiment, the time signal from S41 was used as the startup reference for all the TDCs, i.e., all TDC time measurements are relative to it. Therefore one always needs to keep in mind that all time measurements except t_{41} unavoidably contain the information of S41 [1]. To avoid the complication due to the S41 involvement, the differences between two time measurements instead of each individual measurement are used in the discussions below.

Fig. C.6 are examples which portray the correlation between BSCI time measurements (calibrated) and the pulse heights. Slewing effects on timing are obvious. t_{22}-t_{21} shows opposite dependence on $ph_{21}^{corr.}$ and $ph_{22}^{corr.}$ as expected from Eq. (C.1) (Fig. C.6(a) and Fig. C.6(b)). The similar observation goes for t_{42}-t_{41}. The tails in

[1] t_{41} is the measured time difference of S41 time signal after going through FASTBUS module and that after passing through beam logic and pre-trigger modules, and is used as common start or stop for the TDCs.

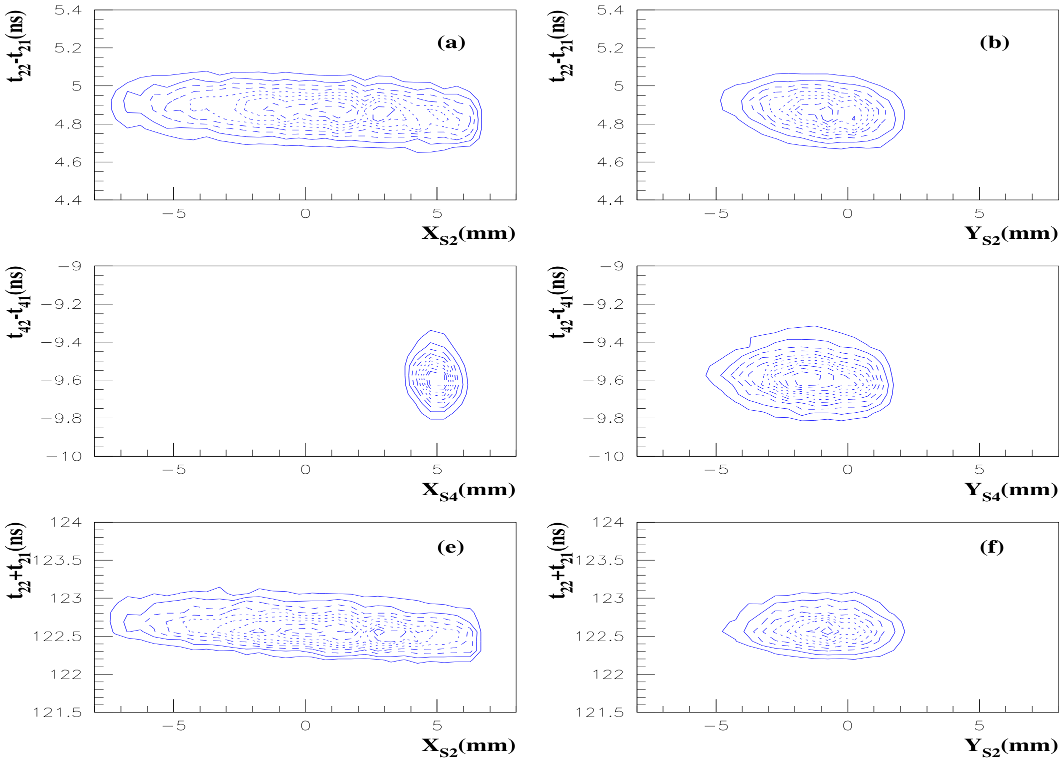

Figure C.7: Contour plots of the correlations between BSCI time measurements and beam particle positions.

Fig. C.6(c) and Fig. C.6(d) are due to the non-Gaussian distributions of ph_{41} and ph_{42} (Fig. C.3(c) and Fig. C.3(d)).

Fig. C.7 showd examples of the correlation between BSCI time measurements (calibrated) and the beam particle positions on the two detectors. t_{22}- t_{21} and t_{42}-t_{41} are used again instead of each individual time measurement. One sees that $t_{22} - t_{21}$ has a slight dependence on both x- and y-positions of the beam particles on S2 while t_{42}- t_{41} shows no dependence on the positions on S4. One can have a further look at the sum of t_{22}+ t_{21} which we expect to demonstrate no positional dependence for an ideal detector.[2] We indeed observe no dependence on y-position of S2. However,

[2]Assume a constant velocity v of light in the scintillator, the measured times at the two ends of PMTs can be expressed as $t_1 = t_0 + (s + x)/v + c_1$ and $t_2 = t_0 + (s - x)/v + c_2$, where t_0 and x are

t_{22}+t_{21} still shows same dependence on x-position of S2.

60Hz ripple on time measurement

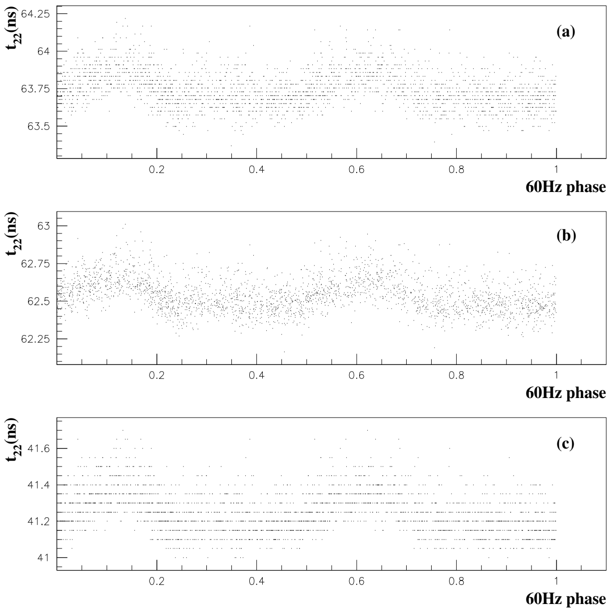

Figure C.8: Scatter plots of S22 time measurement vs 60Hz phase. (a).calibrated FASTBUS TDC time without the slewing correction; (b). calibrated FASTBUS TDC time after the slewing correction;(c).CAMAC TDC time without the slewing correction.

The dependence of time measurement on 60Hz can be partly understood as the influence of the varying pulse height with 60Hz. This correction is usually done through the slewing correction by using corrected pulse heights. In that procedure, the pedestal is first subtracted from the measured pulse height and then the 60Hz contribution is added on top of that.

Fig. C.2 shows an example of the dependence of time measurement over 60Hz phase. The amplitude of the S22 time fluctuations over 60Hz is $\sim$200ps. A comparison of the time measurement with and without slewing corrections is also shown. One can notice that the usual slewing correction does not reduce the 60Hz effect. One

the time of arrival and particle position at the detector, c_1 and c_2 are time offsets due to various delays. Thus $(t_1+t_2)/2 = t_0 + s/v + (c_1+c_2)/2$ is independent of x.

also notices that the CAMAC TDC unit displays the same 60Hz phase dependence as the FASTBUS TDCs, indicating that the origin of such 60Hz influence is from PMTs or the fast electronics itself.

C.3 Determination of Time Start

This part describes a proper procedure to get the optimum start time (Tstart) for the time-of-flight between the target and the TOFU. The spread in this start time contributes to the final TOF resolution which determines the particle identification quality.

C.3.1 Beam scintillator calibration

Before advancing the Tstart study, we need to minimize all effects that create the timing uncertainties. Based on above information on BSCI performance, we used the following procedure for the BSCI time measurement:

- We correct the measured pulse heights with the subtraction of pedestals and the inclusion of the 60Hz effect on pulse heights;
- We introduce a slewing correction on each phototube signal;
- We correct the dependence of time measurement on beam particle positions;
- We finally correct the effect of 60Hz on time measurement [3].

Pedestal and 60Hz corrections on pulse heights

Fig. C.9 shows the corrected pulse heights over 60Hz phase. The pulse heights exhibit a rather weak dependence on 60Hz phase. The centers of amplitude change

[3] This correction is new for the analysis 1995 data set.

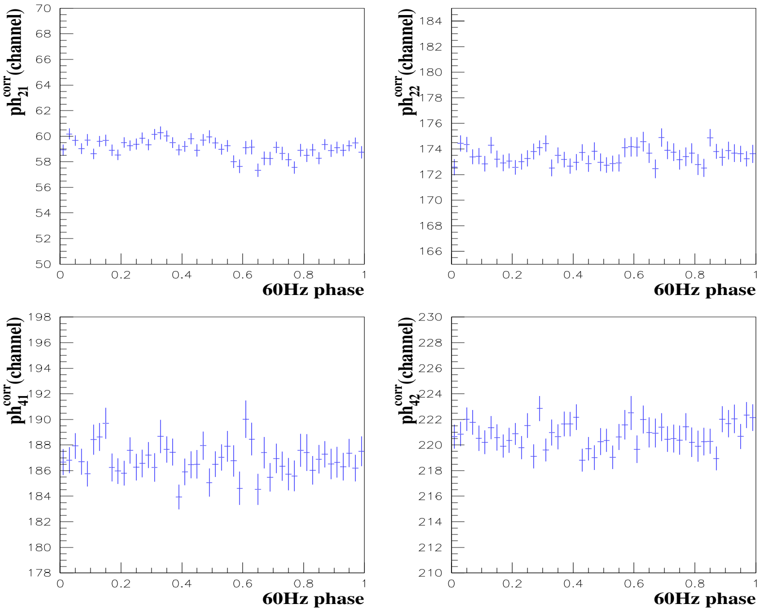

Figure C.9: Examples of calibrated BSCI pulse heights vs 60Hz phase

within 2$\sim$3 channels($\approx$1%). Since the rise times of pulse heights are $\leq 1ns$[140], the alteration due to pulse heights is estimated to be negligible compared to other effects [4].

Slewing correction

As we previously pointed out, the pulse height depends on the intrinsic quantum efficiency, PMT conditions and the beam particle positions on the scintillator. Consequently, one is also correcting or suppressing these effects on time measurements when one is doing slewing correction. We noticed that the slewing correction makes a very significant contribution to the improvement of time resolutions. S. Panitkin of Stony Brook[77] presented a detailed and systematic study on the slewing correction for '93 and '94 BSCI time measurement. Here we employed his method to get the

[4] Taking S21 which is the worst case(ph_{21} $\sim$70 channels), one estimates the fluctuation on time due to pulse height uncertainty is $\sim 20ps$.

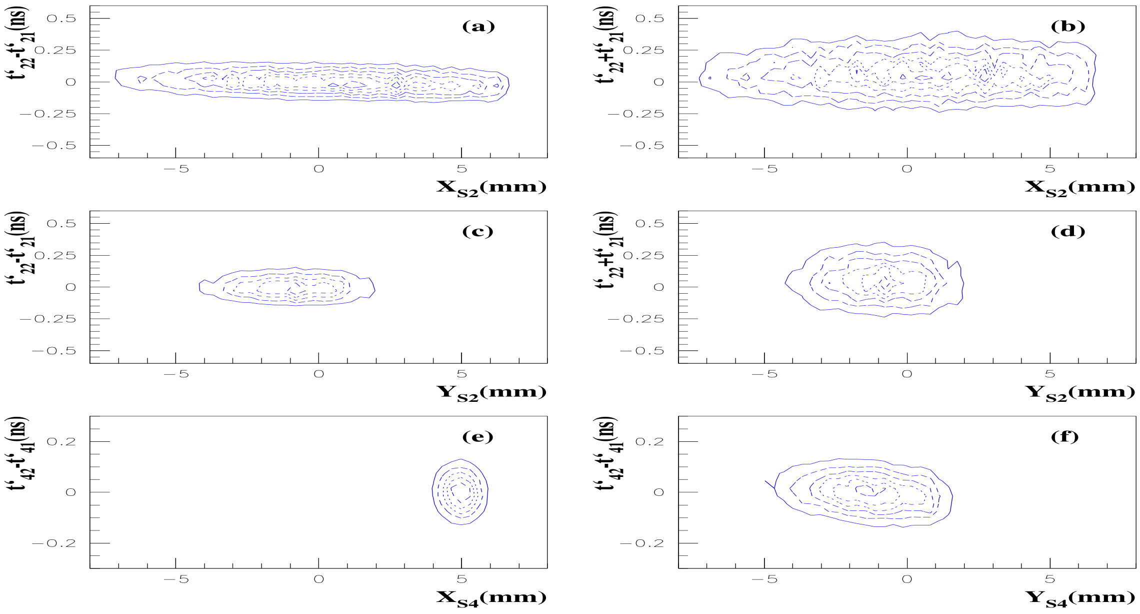

Figure C.10: Positional effects on time measurement after slewing corrections

proper slewing constants that are presented in Table. C.1.

In determining the correction, the formula used is as follows:

$$t'_i - t'_j = t_i - t_j - \frac{a_i}{\sqrt{ph_i^{corr.}}} + \frac{a_j}{\sqrt{ph_j^{corr.}}} + c_{ij} \qquad \text{(C.3)}$$

where t_i and $t_j (i \neq j, i, j = 21, 22, 41, 42)$ are the time measurements before slewing correction while t'_i and t'_j are the ones after slewing correction. a_i and a_j are the slewing constants. $ph_i^{corr.}$ and $ph_j^{corr.}$ are the corrected pulse heights. c_{ij} represents the time offsets due to PMT transit times, cable delays and electronic module delays.

Positional dependence correction

The positional dependence is expected to be partly accounted for by the slewing correction, however, it is still worthwhile to check the relation between the corrected time measurement and the beam particle positions. Fig. C.10 shows the residual effect of the slewingly corrected time measurement on the positions. After slewing

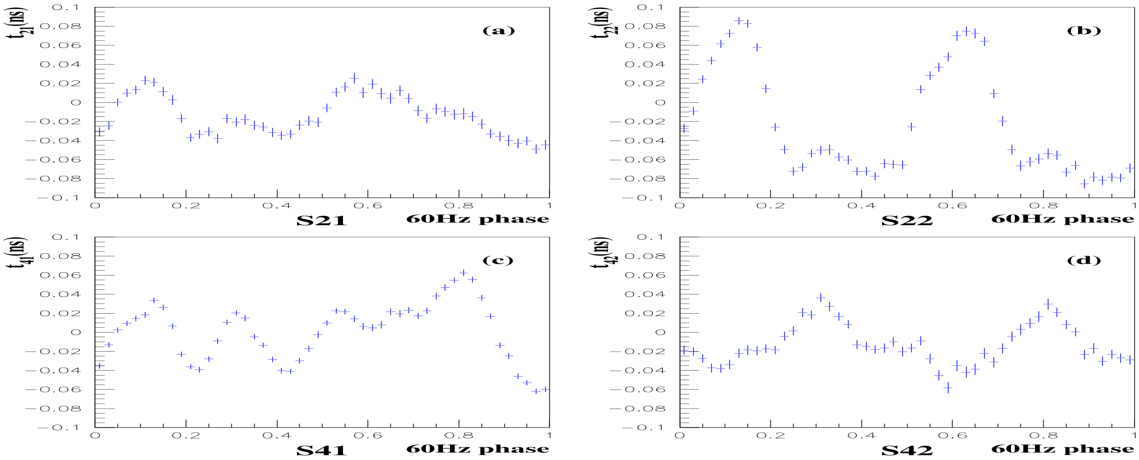

Figure C.11: 60Hz correction functions for BSCI time measurement

corrections most of the effect is gone . The remaining effect only contributes less than $2ps$ to the final time resolutions and the correction is actually trivial. This result is consistent with the observations from '93 and '94 BSCIs[77].

The new 60Hz corrections

The middle panel in Fig. C.2 which has been corrected for the slewing effect shows that the 60Hz effect on time doesn't disappear. This implies that the observed 60Hz here has a source other than that in pedestals as we already noticed from pulse heights. The source is the 60Hz ripple effect on TDC modules. To distinguish these two different effects, we call the present one the *timing 60Hz* (60Hz effect on TDC) and the other one the *pulse height 60Hz* (60Hz effect on ADC).

Fig. C.11 are profiles presenting the centroid positions of the time peaks for the four FASTBUS TDC time measurements. All time measurements in the figure have been corrected for pedestal, pulse height 60Hz, slewing and positions. In the calibration, these profiles are used as correction functions for time measurement. Here another important point must be emphasized. The timing 60Hz correction to be applied on time measurement is actually acted on the difference of the times between

Phototube	a_i (ns)	b_i (ps/mm)	d_i (ps/mm)
BSCI21	5.3	3.0	0.0
BSCI22	15.9	-3.0	0.0
BSCI41	15.3	3.0	3.3
BSCI42	18.6	-3.0	-3.3

Table C.1: Part of correction parameters used in Eq.(C.4).

one phototube and S41. Hence the corrections presented in Fig. C.11(a),(b) and (d) can be used to correct the timing 60hz effect in S21, S22, S42. The function in Fig. C.11(c) is used to correct electronic module noise. To correct the timing 60Hz effect from S41 itself, further information is needed. This issue will be discussed later in the TOFU calibration.

Summary of BSCI calibration

To summarize the calibration for BSCI time measurement, we propose the following calibration formula:

$$ct_i = t_i - \frac{a_i}{\sqrt{ph_i^{corr.}}} - b_i * x_i - d_i * y_i - f_i(phase) + c_i \tag{C.4}$$

where i=21,22,41 and 42. [5] x_i and y_i are the x- and y- positions of beam particles on the two scintillators. b_i and d_i are the corresponding positional correction coefficients on time measurement. $f_i(phase)$ represents the 60Hz correction on time measurement

[5] In fact, the measured t_{41} doesn't contain the information of S41 phototube. The treatment here is for the sake of the consistency of definitions. The S41 information will be canceled out anyway in the time-of-flight calculation.

as a function of the phase. All other variables in Eq. (C.4) have already been defined in Eq. (C.4). Some of the parameters for Eq. (C.4) are listed in Table. C.1.

C.3.2 The best *Tstart*

To find out the optimum *Tstart*, it is important to get an idea of the intrinsic time resolution of each phototube. To avoid the involvement of the S41 effect which makes things intricate, we instead use some combinations that are free of the S41 influence. Some of the combinations are $ct_{21} - ct_{22}$, $ct_{21} - ct_{42}$ and $ct_{22} - ct_{42}$. Fig. C.12 shows examples of the distributions of these time measurements. After all the discussed corrections, all time measurements show quite Gaussian distributions with resolutions varying from 38 to 69 ps.

Table. C.2 shows the measured time resolutions (one standard deviation) of the time measurements for all five FASTBUS modules. By making the assumption that all corrections has been properly applied and thus all the time measurements after the corrections would be independent, one can estimate the time resolution of each individual phototube from the measured time resolutions of their combinations with the following relations:

$$\sigma^2(ct_i - ct_j) = \sigma^2(t_i^0) + \sigma^2(t_j^0) \tag{C.5}$$

where i,j=21,22,41,42($i \neq j$);$\sigma(t_m^0)$ (m=21,22,41,42) are the intrinsic resolutions of phototube S21,S22,S41 and S42 respectively.

One can further make an estimation of the intrinsic resolution t_{41}^0 of S41 from the derived values of S21,S22 and S42. There are three ways to evaluate t_{41}^0. All are presented in Table. C.2 and they agree with one another. To check the quality of the evaluations(also the effectiveness of the applied corrections), one can check the time-of-flight between S2 and S4, i.e., $(t_{21} + t_{22})/2 - (t_{41} + t_{42})/2$. The estimated resolution (line 14 in Table C.2) using the derived intrinsic resolutions agrees well

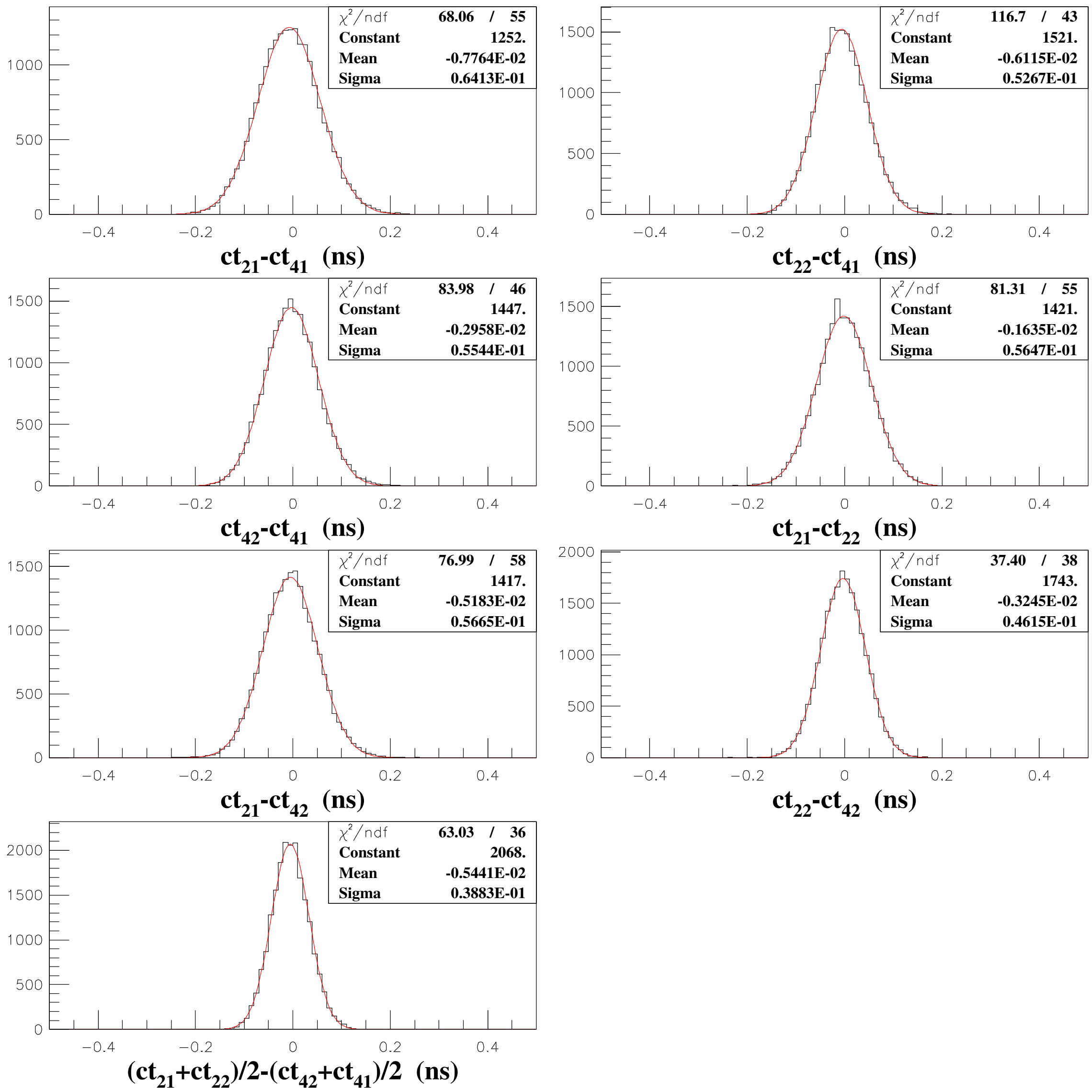

Figure C.12: Various BSCI time distributions from FASTBUS TDCs. All time measurements have undergone the slewing, position and timing 60Hz corrections. For convenience, the distributions have been centered at zero.

the measured ones. The estimated time resolutions are $50ps$, $36ps$, $44ps$ and $46ps$ for S21, S22, S41 and S42 respectively.

One can therefore evaluate the time resolution of a possible Tstart with the derived time resolutions of the four phototubes. Table. C.2 presents three possible $Tstart$s. If one uses the signals of S2 or S4 only, one will get a $Tstart$ time resolution of about 30 ps. Both scintillators show the same quality in timing. These two options have been adopted by the analyses of previous years. However, if one makes full use of all four phototube signals, one would achieve a resolution of the order of 20 ps which is almost negligible compared to that of TOFU, which has an intrinsic time resolution of $\sim 85ps$ on average.

$$Tstart = \frac{ct_{21} + ct_{22} + ct_{41} + ct_{42}}{4} \tag{C.6}$$

is the Tstart we have used for '95 data analysis.

C.4 TOFU Calibration

TOFU calibration has been discussed in details by R. Lacasse[64]. Here only a brief review is provided and the focus is put on the procedures which are related to the Time-of-Flight(TOF) measurement.

The time of arrival of a particle at the TOFU is estimated by the average of the two time measurement given by the two phototubes(up and bottom) at both ends of a TOFU scintillation counter. The TOF of a particle having flown between the target and TOFU is evaluated as[6]

$$TOF = \frac{t^i_{up} + t^i_{btm}}{2} - T_{start} \tag{C.7}$$

where Tstart is given by Equation.(3) and i is the TOFU counter number.

[6]Actually it differs by a constant because of various delays.

Table C.2: Time resolutions of BSCI.

BSCI Time Resolution (in ps)	Module-1	Module-2	Module-3	Module-4	Module-5	Average
$\sigma(ct_{21}-ct_{22})_{mea.}$	56.4	60.5	61.8	62.6	67.3	61.7
$\sigma(ct_{21}-ct_{42})_{mea.}$	56.6	65.1	71.5	71.1	76.6	68.2
$\sigma(ct_{22}-ct_{42})_{mea.}$	46.1	55.6	63.4	63.2	61.7	58.0
$\sigma(ct_{21}-ct_{41})_{mea.}$	64.1	64.5	66.2	65.9	69.5	66.0
$\sigma(ct_{22}-ct_{41})_{mea.}$	52.7	56.3	58.8	57.9	57.2	56.6
$\sigma(ct_{42}-ct_{41})_{mea.}$	55.4	61.4	67.2	65.8	65.1	63.0
$\sigma(t^0_{21})_{est.}$	46.1	49.0	49.6	49.9	57.4	50.4
$\sigma(t^0_{22})_{est.}$	32.4	35.5	36.9	37.8	35.1	35.5
$\sigma(t^0_{42})_{est.}$	32.8	42.8	51.5	50.6	50.7	45.7
$\sigma(t^0_{41})^{[1]}_{est.}$	44.5	41.9	43.8	43.0	39.2	42.5
$\sigma(t^0_{41})^{[2]}_{est.}$	41.6	43.7	45.8	43.8	45.2	44.0
$\sigma(t^0_{41})^{[3]}_{est.}$	44.6	44.0	43.1	42.1	40.8	42.9
$\sigma(t^0_{41})_{avg.}$	43.6	43.2	44.2	43.0	41.7	43.1
$\sigma(\frac{ct_{21}+ct_{22}}{2}-\frac{ct_{41}+ct_{42}}{2})_{est.}$	39.2	42.9	45.9	45.6	47.0	44.1
$\sigma(\frac{ct_{21}+ct_{22}}{2}-\frac{ct_{41}+ct_{42}}{2})_{mea.}$	38.8	42.5	48.0	46.4	48.0	44.7
$\sigma(\frac{t^0_{21}+t^0_{22}}{2})_{est.}$	28.2	30.3	30.9	31.3	33.6	30.9
$\sigma(\frac{t^0_{41}+t^0_{42}}{2})_{est.}$	27.3	30.3	34.5	34.1	34.6	32.1
$\sigma(\frac{t^0_{21}+t^0_{22}+t^0_{41}+t^0_{42}}{4})_{est.}$	19.6	21.4	23.1	23.1	24.1	22.2

[Note]:$\sigma(t^0_{41})$ of case [1],[2] and [3] are the values derived from $\sigma(ct_{21}-ct_{41})$, $\sigma(ct_{22}-ct_{41})$ and $\sigma(ct_{42}-ct_{41})$ respectively.

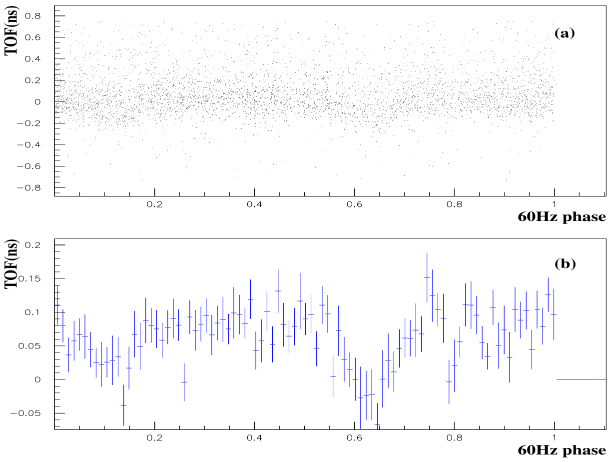

Figure C.13: Evidence for the *timing 60Hz* in TOFU. (a) shows the 60Hz ripple in the TOF of one TOFU counter. The ripple is the same for all the TOFU counters. (b) is the correction function for the final TOF.

t^i_{up} and t^i_{btm} are the respective time measurements from the phototubes at the two ends and they are undergone the following corrections.

- *Pedestal and pulse height 60Hz corrections.* Pedestals are subtracted and the pulse height 60Hz influence is rectified by using the information derived from pedestals to get the corrected pulse height $ph^{corr.}$;

- *Slewing corrections.* Pulse height effect on timing is minimized by using the correction function $1/\sqrt{ph^{corr.}}$. New slewing constants are found for the 1995 TOFU (see Fig. C.14);

- *Timing 60Hz corrections.* It has been already pointed out in Section C.1.4 that the TOFU time signals like all other time measurement are relative to the S41 startup signal and unavoidably embrace the effects from S41. In our calculation of the TOF (Eq. (C.7)), all other effects from S41 are canceled out except the timing 60Hz from S41. Remember that the timing 60Hz correction on *Tstart* is only done on the relative time between the phototube and S41. The timing 60Hz effect from S41 still remains in the time measurements from TOFU phototubes and is transfered to TOF given by Eq.(C.7). Fig. C.13(a) shows such 60Hz ripples in TOFU time measurement. This effect is the same

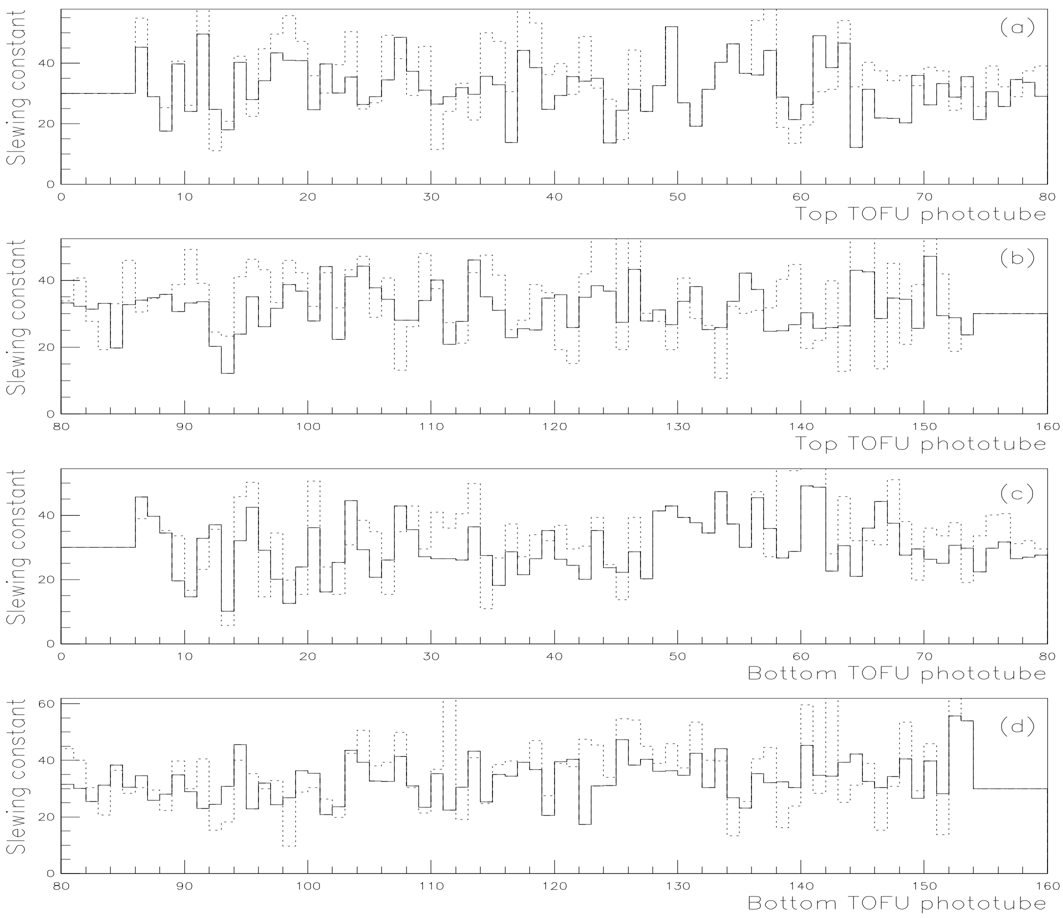

Figure C.14: Slewing constants for TOFU phototubes. (a) and (b) show the slewing constants of top TOFU phototubes while (c) and (d) show those of bottom TOFU phototubes. Solid lines stand for 95's while dotted lines for 94's. For units, time measurement are in *ns* and pulse heights are in *channel*s.

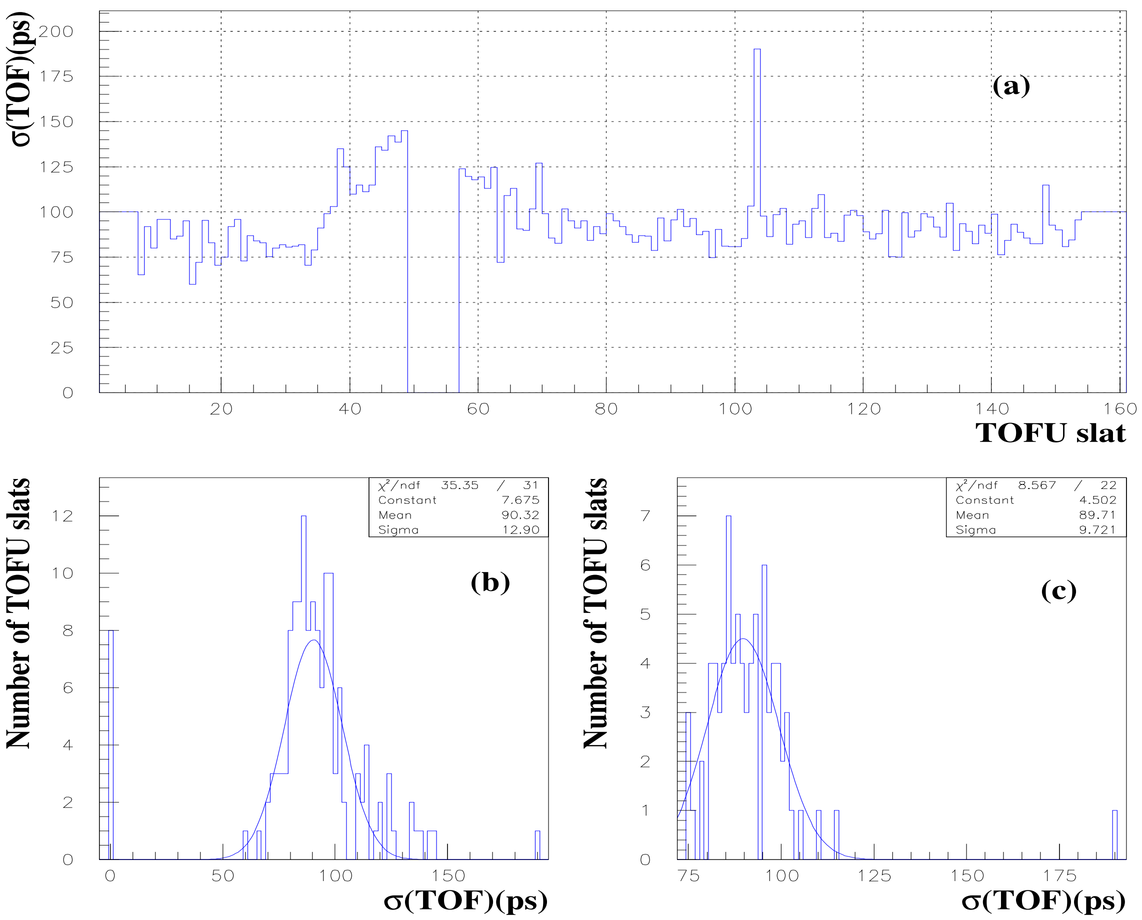

Figure C.15: TOF resolutions estimated by using identified pions. (a) displays the resolutions of all 148 TOFU counters. (b) shows the resolution distribution of the whole wall. (c) shows the resolution distribution of the section of the wall(from Slat#75-Slat#153) where negative pions can be well separated.

for all TOFU phototubes. Fig. C.13(b) shows the correction function for the final TOF [7].

Fig. C.15 shows the derived TOF resolution for the entire TOFU hodoscope. Identified particles were chosen for the study. Slat number 103 is a bad one. All other TOFU counters look good. The *worse* resolution for the section from Slat#35 to Slat#70 is due to the difficulty in separating identified particles. The counters falling within the beam region were turned off during operation(see Fig. C.15(a)). It shows that the overall resolution of TOFU is of the order of $90ps$(Fig. C.15(b) and (c)).

[7]This final step correction can be also applied to phototube time measurements t^i_{up} and t^i_{btm} first,which is equivalent to the above way it is done on TOF directly.

Bibliography

[1] J. W. Harris and Berndt M*ü*ller, Annu. Rev. Nucl. Part. Sci., **46**, 71(1996).

[2] J. Pochodzalla, *et al.* Phys. Rev. Lett. **175**, 1040(1995).

[3] C. M. Hung and E. V. Shuyak, Phys. Rev. Lett., **75**, 4003(1995).

[4] J. D. Bjorken, Acta Phy. Polon., **B23**, 637(1992).

[5] A. B. Migdal, Nucl. Phys., **A210**, 421(1993).

[6] G. E. Brown and W. Weise, Phys. Rep., **27C**, 2(1976).

[7] T. D. Lee and G. C. Wick, Phys. Rev., **D9**, 2291(1974).

[8] S. Chin and A. Kerman, Phys .Rev. Lett., **43**, 1292(1979).

[9] E. P. Gilson, *et al.*, Phys. Rev. Lett., **71**, 332(1993).

[10] T. A. Armstrong, *et al.*, the E864 Collaboration, Phys. Rev. Lett., **79**, 3612(1997).

[11] R. Kllingenberg for the NA52 Collaboration, Nucl. Phys., **A610**, 306c(1996).

[12] E. Kolb, M. S. Turner, The Early Universe, Redwood City, CA, Addison-Wesley(1990).

[13] V. Bernard, Quark-Gluon Plasma Signatures, Paris, Editions Frontières(1990); B. Müller, Rep. Prog. Phys., **58**, 611(1995).

[14] L. von Hove, Phys. Lett., **118B**, 138(1982).

[15] K. A. Bugaev *et al.*, Phys. Lett., **B255**, 18(1991).

[16] R. Ganz, nucl-ex/9808007 26 Aug 1998.

[17] M. Gyulassy *et al.*, Nucl. Phys., **B237**, 477(1984).

[18] D. H. Boal *et al.*, Rev. Mod. Phys., **62**, 553(1990).

[19] T. Matsui, H. Satz, Phys. Lett., **178B**, 416(1986).

[20] L. Ramello for the NA50 Collaboration, Quark Matter 97, Tokyo(December 1997).

[21] W. Scheid, H. Müller, and W. Greiner, Phys. Rev. Lett., **32**, 741(1974).

[22] S. Z. Belenkij and L. D. Landau, Usp. Fiz. Nauk, **56**, 309(1955).

[23] A. .E. Glassgold *et al.*, Ann. Phys. (NY), **6**, 1(1959).

[24] H. Å. Gustafsson *et al.*, Phys. Rev. Lett., **52**, 1590(1984).

[25] R. E. Renfordt *et al.*, Phys. Rev. Lett., **53**, 763(1984).

[26] J. Barrette *et al.*, E814 Collaboration, Phys. Rev. Lett., **64**, 1219(1990).

[27] J. Barrette *et al.*, E814 Collaboration, Phys. Rev. Lett., **70**, 2996(1993).

[28] F. Videbaek *et al.*, Proceedings of the International Workshop of Heavy Ion Physics at the AGS '93, edited by G. Stephans *et al.*, 89(1993).

[29] S. Eisman *et al.*, Phys. Lett. **B292**, 10(1992).

[30] Jean-Yves Ollitrault, Phys. Rev., **D46**, 229(1992).

[31] J. Barrette *et al.*, E877 Collaboration, Phys. Rev. Lett., **73**, 2532(1994).

[32] J. Barrette *et al.*, E877 Collaboration, Phys. Rev., **C55**, 1420(1997).

[33] J. Barrette *et al.*, E877 Collaboration, Phys. Rev., **C56**, 3254(1997).

[34] H. Appelshäuser *et al.*, NA49 Collaboration, Phys. Rev. Lett., **80**, 4136(1998).

[35] M. M. Aggarewal *et al.*, WA98 Collaboration, nucl-ex/9807004 21 Jul 1998.

[36] G. D. Westfall *et al.*, Phys. Rev. Lett., **37**, 1202(1976); J. Gosset *et al.*, Phys. Rev., **C18**, 844(1978).

[37] M. L. Lisa *et al.*, EOS Collaboration, Phys. Rev. Lett., **75**, 2662(1995).

[38] M. Petrovic *et al.*, FOPI Collaboration, Phys. Rev. Lett., **74**, 5001(1995).

[39] P. J. Siemens and J. O. Rasmussen, Phys. Rev. Lett., **42**, 880(1979).

[40] P. Braun-Munzinger *et al.*, Phys. Lett., **B344**, 43(1995).

[41] J. Stachel, Nucl. Phys., **A610**, 509c(1996).

[42] N. Herrmann, FOPI Collaboration, Nucl. Phys., **A610**, 49c(1996).

[43] Nu Xu for the NA44 Collaboration, Nucl. Phys., **A610**, 175c(1996); I. G. Bearden *et al.*, NA44 Collaboration, Phys. Rev. Lett., **78**, 2080(1997).

[44] W. Reisdorf and H. G. Ritter, Annu. Rev. Nucl. Sci., **47**, 663(1997).

[45] Heng Liu, for the E895 Collaboration, Nucl. Phys. **A630**, 549c(1998).

[46] C. Ogilvie *et al.*, Nucl. Phys., **A638**, 57(1998).

[47] H. Stöcker and W. Greiner, Phys. Rep., **137**, 278(1986).

[48] T. DeGrand, Phys. Rev., **D30**, 2001(1984).

[49] D. H. Rischke, nucl-th/9505014 11 May 1995.

[50] J. Brachmann *et al.*, Nucl. Phys., **A619**, 391(1997).

[51] M. Demoulins *et al.*, Phys. Lett., **B241**, 476(1990).

[52] H. H. Gutbrod *et al.*, Phys. Rev., **C42**, 640(1990); H. H. Gutbrod *et al.*, Phys. Lett., **B216**, 267(1989).

[53] H. Sorge, Phys. Rev. Lett., **78**, 2309(1997).

[54] P. Danielewicz *et al.*, Phys. Rev. Lett., **81**, 2438(1998).

[55] P. Braun-Munzinger and J. Stachel, Nucl. Phys., **A638**, 3(1998).

[56] Jean-Yves Ollitrault, nucl-ex/9802005 12 Feb 1998.

[57] R. Bersch, M.S. thesis, SUNY at Stony Brook, 1995.

[58] W. E. Cleland, M. Clemen, U. Sonnadara and S. Voloshin, E877 Note#PITT-95-002, 1995

[59] R. Lacasse *et al.*, Nucl. Instr. and Methods, **A408**, 408(1998).

[60] M. Fatyga, D. Makowiecki, and W.J. Llope, Nucl. Inst. Methods, **A184**, 322 (1989).

[61] D. Fox, *et al.*, Nucl. Inst. and Methods, **A317**, 474(1992).

[62] S. V. Greene, Ph.D. thesis, Yale University, 1992.

[63] B. Hong, Ph.D. thesis, SUNY at Stony Brook, 1995.

[64] R. Lacasse, Ph.D. thesis, McGill University, 1998.

[65] J. Simon-Gillo et al., Nucl. Inst. and Methods. **A309**, 427(1991).

[66] Thongbay Vongpaseuth, Ph.D. thesis, SUNY at Stony Brook, 1998.

[67] B. Yu, Ph.D. thesis, University of Pittsburg, 1991.

[68] Z. Z. Zhang, Ph.D. thesis, University of Pittsburg, 1993.

[69] Upul Jayasiri Sonnadara, Ph.D. thesis, University of Pittsburg, 1992.

[70] James Dee, Ph.D. thesis, SUNY at Stony Brook, 1995.

[71] Mark Pollack, Ph.D. thesis, SUNY at Stony Brook, 1997.

[72] W.E. Cleland *et al.*, E877 Note#PITT-95-002(Febuary 8, 1995).

[73] G. Lutz and A. S. Schwarz, Annu. Rev. Nucl. Part. Sci., **45**, 295(1995).

[74] G. Batignani *et al.*, Nucl. Inst. and Meth., **A277**, 147(1989).

[75] L. Hubbeling *et al.*, Nucl. Inst. and Meth., **A310**, 197(1991).

[76] P. Weilhammer, Nucl. Inst. and Meth., **A342**, 1(1994).

[77] Sergei Y. Panitikin, Ph.D. thesis, SUNY at Stony Brook, 1997.

[78] LeCroy Research Systems, 1996 Catalog.

[79] Yujin Qi, Ph.D. thesis, McGill University (in preparation).

[80] HBOOK Reference Manual, Version 4.21, CERN.

[81] PAW The Complete Reference, Version 2.03, CERN.

[82] D. G. Cassel *et al.*, Nucl. Inst. and Meth., **A185**, 235(1981).

[83] J. Barrette *et al.*, the E814 Collaboration, Phys. Rev., **C45**, 819(1992).

[84] J. Barrette *et al.*, the E814 Collaboration, Phys. Rev., **C50**, 1077(1994).

[85] Timothy William Piazza, Ph.D. thesis, SUNY at Stony Brook, 1997.

[86] K. Shigaki, Ph.D. thesis, University of Tokyo, 1995.

[87] Review of Particle Physics Part I, Phys. Rev. **D54**,134(1996).

[88] Dariusz Miśkowiec, Momentum Resolution of the E877 Spectrometer, E877 Note(Febuary, 1996).

[89] S. Voloshin, Occupancy correction, E877 Note #HD-96/08/15 and #HD-96/08/27 (unpublished).

[90] M. Gyulassy *et al.*, Phys. Lett., **B110**, 185(1982); P. Danielewicz and M. Gyulassy, Phys. Lett., **B129**, 283(1983).

[91] Jean-Yves Ollitrault, Phys. Rev., **D48**, 1132(1993).

[92] P. Danielewicz and G. Odyniec, Phys. Lett., **B157**, 146(1985).

[93] A. M. Poskanzer and S. A. Voloshin, Phys. Rev., **C58**, 1671(1998).

[94] Wen-chen Chang, Ph.D. thesis, SUNY at Stony Brook,1997.

[95] S. Voloshin and Y. Zhang, Z. Phys., **C70**, 665(1996).

[96] Jean-Yves Ollitrault, nucl-ex/9711003 v2 13 Nov 1997.

[97] J. H. Friedman *et al.*, Phys. Rev. Lett., **28**, 191(1972).

[98] M. C. Foster *et al.*, Phys. Rev., **D6**, 3135(1972).

[99] P. Danielewicz *et al.*, Phys. Rev., **C38**, 120(1988).

[100] Jean-Yves Ollitrault, Nucl. Phys., **A590**, 561c(1995).

[101] M. M. Affarwal *et al.*, WA93 Collaboration, Phys. Lett., **B403**, 390(1997).

[102] C. A. Ogilvie *et al.*, Phys. Rev., **C40**, 2592(1989).

[103] W. K. Wilson *et al.*, Phys. Rev., **C45**, 738(1992).

[104] Private communication with Dr. Jean-Yves Ollitrault.

[105] W. Cleland and S. Voloshin, E877 Note #PITT-95-003(April 24, 1995).

[106] K. Filimnov, Ph.D. thesis, McGill University (in preparation).

[107] S. Voloshin, Phys. Rev., **C55**, R1630(1997).

[108] R. Mattiello *et al.*, Phys. Rev. Lett., **74**, 2180(1995); Phys. Rev., **C55**, 1443(1997).

[109] Stephen Craig Johnson, Ph.D. thesis, SUNY at Stony Brook, 1997.

[110] J. Barrette *et al.*, nucl-ex/9805006 v2 6 Aug 1998 (to be published in Phys. Rev. **C**).

[111] Claude Pruneau, for the E864 Collaboration, Quark Matter '97, Tsukuba, Japan.

[112] Ziping Chen, for the E866 Collaboration, HIPAGS '96, 1996, Detroit.

[113] H. Sorge, H. Stöcker and W. Greiner, Nucl. Phys., **A498**, 567c(1989).

[114] H. Sorge, Phys. Rev., **C52**, 3291(1995).

[115] S. A. Bass *et al.*, Phys. Rev., **C51**, 3343(1995).

[116] J. C. Kintner *et al.*, Phys. Rev. Lett., **78**, 4165(1997).

[117] Bao-An Li and C. M. Ko, Phys. Rev., **C53**, R22(1996).

[118] S. A. Bass *et al.*, nucl-th/9803035 v2 19 Mar 1998.

[119] J. Rafelski, Phys. Rep., **88**, 331(1982); P. Koch *et al.*, Phys. Rep., **142**, 167(1986).

[120] G. E. Brown *et al.*, Phys. Rev., **D37**, 2042(1988).

[121] C. A. Ogilvie, nucl-ex/9809004 27 Sep 1998.

[122] G. Q. Li, C. M. Ko, and Bao-An Li, Phys. Rev. Lett., **74**, 235(1995).

[123] G. Q. Li and C. M. Ko, Phys. Rev., **C54**, R2159(1996).

[124] G. Q. Li, C.-H. Lee and G. E. Brown, Phys. Rev. Lett., **79**, 5214(1997).

[125] G. Q. Li and G. E. Brown, nucl-th/9804018 8 Apr 1998.

[126] J. Schaffner-Bielich *et al.*, Nucl. Phys., **A625**, 325(1997)

[127] J. Ritman *et al.*, Z. Phys., **A352**, 355(1995).

[128] Y. Shin *et al.*, Phys. Rev. Lett., **81**, 1576(1998).

[129] V. Koch *et al.*, Phys. Lett., **B265**, 29(1991).

[130] A. Jahns *et al.*, Phys. Rev. Lett., **68**, 2895(1992).

[131] S. H. Kahana *et al.*, Phys. Rev., **C47**, R1356(1993).

[132] A. Jahns *et al.*, Phys. Rev. Lett., **72**, 3464(1994).

[133] D. E. Kahana *et al.*, Phys. Rev. Lett., **74**, 4404(1995).

[134] T. Alber *et al.*, Phys. Lett., **B366**, 56(1996).

[135] Y. Akiba *et al.*, Nucl. Phys., **A610**, 139c(1996).

[136] P. G. Jones *et al.*, Nucl. Phys., **A610**, 188(1996).

[137] T. A. Armstrong *et al.*, nucl-ex/9811002 4 Nov 1998.

[138] Youngil Kwon, Ph.D. thesis, SUNY at Stony Brook, 1997.

[139] E877 collaboration,Transparencies of the E877 collaboration meeting, SUNY at Stony Brook, June 9-10, 1995.

[140] Private communication with Dr. Craig Woody of BNL.